Creation, trapping and manipulation of a cold argon gas

Conor Maher-McWilliams

A thesis submitted to University College London
in partial fulfilment of the requirements for the
degree of Doctor of Philosophy

Department of Physics and Astronomy
University College London
August 2012

I, Conor Maher-McWilliams, confirm that the work presented in this thesis is my own. Where information has been derived from other sources, I confirm that this has been indicated in the thesis.

Signed .... Date ....

Abstract

This thesis describes the construction and characterisation of a unique cold argon atom source for sympathetic cooling of molecules. Argon atoms were laser cooled from their lowest lying metastable state using the $4s[3/2]_2 \rightarrow 4p[5/2]_3$ transition at 811.5 nm. A magneto-optical trap (MOT) was used to cool the metastable argon (Ar*) atoms to 73.2 ± 0.4 μK and trap them at a density of 3.93×10^9 cm^{-3}. Cooling was facilitated using an external-cavity diode laser which was frequency-stabilised to the cooling transition using a magnetic dichroism technique. This was the first application of this technique to a plasma operated at our pressures where the applied magnetic field affected the gas behaviour.

The Ar* atoms in the MOT were used to demonstrate chirped optical Stark acceleration for the first time. Atoms were accelerated up to velocities of 191 ± 1 ms^{-1} while maintaining narrow energy spreads in the accelerated ensemble (30-100 mK). The acceleration occured over tens of nanometres and on micrometre length scales. Control over the number of particles accelerated was achieved by tailoring the depth of the optical lattice potential. Monte Carlo numerical simulations of acceleration were used to fit experimental results and study the dynamics of particles over the acceleration duration.

Trapping of Ar* atoms in a quasi-electrostatic trap (QUEST) has also been demonstrated. The QUEST was formed at the focus of a 100 W laser beam with a wavelength of 10.6 μm. A trap lifetime of 18.3 ± 0.3 ms was measured.

Contents

Acknowledgments

I would like to thank my supervisor Professor Peter Barker for his guidance and support over the course of my PhD. His enthusiasm for our work has been a great motivation. I would also like to thank my second supervisor Dr Jonathan Underwood for his contribution to this work. I owe a huge thanks to Dr Peter Douglas with whom I worked closely for the first three years of my PhD. Peter's insight, experimental skill and perseverance provided the impetus for a productive and enjoyable working relationship. Thanks are also due to the other members of our research group for their assistance, insight and collaboration over the past four years. In particular, I would like to thank Dr Nicholas Coppendale for guidance during my early days in the lab and Alexandros Gerakis for his assistance and patience during experiments using shared equipment. I would also like to acknowledge the contribution of Pete Edmunds with whom I worked closely during my final months in the laboratory. Pete will now take over the experiment and I am confident it is in good hands.

I owe a massive debt of gratitude to my family, particularly my parents, for their support throughout my PhD which has been invaluable. I would also like to thank my colleagues and friends at UCL and friends from outside the university for their support. A special mention must go to Dr Arne Wickenbrock who has always kept things at UCL interesting.

Publications

1. C. Maher-McWilliams, P. Douglas and P. F. Barker, *Laser-driven acceleration of neutral particles*, Nat Photon **6**, 386, (2012)
2. P. Douglas, C. Maher-McWilliams and P. F. Barker, *Frequency stabilization of an external-cavity diode laser to metastable argon atoms in a discharge*, Review of Scientific Instruments **83**, 063107 (2012)
3. P. F. Barker, S. M. Purcell, P. Douglas, P. Barletta, N. Coppendale, C. Maher-McWilliams and J. Tennyson, *Sympathetic cooling by collisions with ultracold rare gas atoms, and recent progress in optical Stark deceleration*, Faraday Discuss. **143**, 175, (2009)

Chapter 1

Introduction

Cold atomic and molecular gases (< 1 K) are widely used in modern physics research as they offer highly controllable systems which are ideal for studying and manipulating physical and chemical interactions. The development of atomic Doppler cooling techniques has enabled researchers to trap and accumulate dense samples (10^9-10^{12} cm^{-3}) of atoms at ultracold temperatures below 1 mK. Doppler cooling is a dissipative technique which removes kinetic energy from atoms through the resonant scattering of photons from laser beams. The success of this method is reliant on the presence of a closed cycle of electronic transitions, which is found in many atomic species. The electronic structure of molecules is much more complex than atoms and Doppler cooling cannot generally be applied to molecular species. This has led to the development of a wide range of more exotic techniques using electric, magnetic and optical fields, as well as collisions with a cold buffer gas to produce cold molecular samples. Temperatures in the mK regime can be readily achieved but a general scheme for reaching ultracold temperatures, where much of the interesting physics and chemistry takes place, has yet to be demonstrated. The work in this thesis is part of a larger project to sympathetically cool molecules, initially at mK temperatures, to the ultracold regime through collisions with laser cooled, ultracold rare gas atoms.

1.1 Ultracold atoms

A number of methods are used to cool, trap and manipulate atoms in ultracold atom experiments. One of the most important techniques is Doppler cooling which uses near-resonant laser light to dissipatively cool atomic motion [1]. Doppler cooling can be used to both cool and trap atoms in a magneto-optical trap (MOT) at temperatures as low as a few μK [2]. The low energy of MOT atoms allows transfer of the atoms to shallow conservative optical and magnetic potentials. Ultracold atoms trapped in a conservative potential can be further cooled evaporatively by lowering the trap depth [3]. In this method intra-trap collisions kick the hottest atoms out of the trap and also act to rethermalise the remaining trapped atoms, thus lowering the temperature. Optical traps can also be used to arrange trapped atoms in various lattice geometries created by the interference pattern of two or more laser beams [4]. These cooling and trapping techniques have provided the foundation for a multitude of ground breaking experiments spanning many disciplines such as many-body physics [5], metrology [6], collisional physics [7] and quantum information [8]. MOTs have been used for high precision measurements of atomic lifetimes [9, 10, 11], to study cold collisions [7] and for atomic clocks [12]. Many experiments now use MOTs as a starting point before further manipulation of the ultracold ensemble in conservative traps. Rubidium (^{87}Rb) atoms transferred from a MOT to a magnetic trap have been evaporatively cooled to form a Bose-Einstein condensate [13]. This was a major achievement in experimental physics and led to the award of the 2001 Nobel prize to E. A. Cornell, W. Ketterle and C. E. Wieman. A Fermi-degenerate gas of ^{40}K atoms has been realised in a similar way [14]. Interactions in these novel phases of matter are governed by particle statistics rather than individual atom or photon interactions. Fascinating quantum phenomena and other novel matter phases have been observed in quantum degenerate gases. Interference between two BECs has been used to demonstrate the interaction of two coherent matter waves [15]. By transferring quantum gases to optical lattices condensed matter systems can be studied. In these experiments the system parameters can be very well controlled and are free from defects common in condensed matter crystals [16]. For example, a phase transition from an incompressible superfluid to Mott insulator has been observed in a BEC transferred to a three-dimensional optical lattice [17]. A BEC transferred to a two-dimensional optical lattice led to the creation of a strongly correlated one-dimensional Tonks-Girardeau gas [18]. Optical transitions of atoms confined in an optical lattice are now used in metrology to keep time with a fractional accuracy at the 10^{-18} level [19]. In quantum information the entanglement of individual qubits, required in many quantum information processes, has been demonstrated by entangling pairs of ^{87}Rb atoms confined in a double well optical lattice [20].

1.2 Cold and ultracold molecules

Doppler cooling techniques, so successfully applied to atoms, cannot be directly transferred to molecules due to their complex electronic structure which makes finding a closed cycle of transitions almost impossible. A variety of other methods, which will be outlined in the next section, have been developed to produce cold molecular samples. Although the rich internal structure of molecules makes them more difficult to manipulate than atoms it also opens up an exciting range of potential experiments beyond the scope of ultracold atomic physics. Cold and ultracold molecules have the potential to make a major contribution to fields such as few-body physics and chemistry, precision spectroscopy and tests of fundamental constants and many-body physics [21].

Cold chemistry

Cold molecules offer the opportunity to study and control chemical reactions with unprecedented precision in a temperature regime where quantum mechanical effects become important. Molecular beams with mK temperatures and tuneable velocities have been used to study near-threshold inelastic collisions between OH radicals and Xe atoms in high resolution crossed-beam experiments [22]. Evidence of quantum threshold phenomena has also been observed in collisions of cold OH with both He and D_2 [23]. In this experiment the cold OH radicals were initially confined in a magnetic trap and the collision energy was tuned by varying the velocity of the He or D_2 beam.

Chemical reactions between cold molecules can be controlled through the application of external electric and magnetic fields or via manipulation of the initial quantum state of the reactants [24, 25]. The application of an external electric field has been observed to strongly affect collisions between ultracold Rb atoms and cold NH_3 molecules [26]. In this work the measured inelastic collision rates were faster than those predicted from field-free calculations.

At ultracold temperatures certain chemical reaction rates have been predicted to increase significantly [24]. The large de Broglie wavelength of ultracold molecules changes the dynamics in reactions and quantum mechanical effects govern collisions. Barriers on the collisional potential energy surfaces play a different role at such low energies as tunneling phenomena dominate the interaction while threshold phenomena accelerate barrierless reactions. Control of reactions between ultracold KRb molecules has been demonstrated by changing the initial quantum state of the colliding molecules [27]. By changing the collision pairs from identical molecules to molecules in different initial quantum states the reaction rates were observed to be enhanced by a factor of between 10 and 100. The collisions between same state molecules were p-wave dominated threshold collisions. These collisions involved tunneling through an angular momentum barrier on the potential energy surface. When the colliding molecules were in different states s-wave scattering dominated where there was no angular momentum barrier and the reaction rates were higher. As yet, ultracold chemistry remains a relatively unexplored domain experimentally and the production of a wide range of ultracold molecular species will allow further study of reactions presenting the opportunity to demonstrate further controlled reactions.

High resolution spectroscopy

High resolution spectroscopy is an important tool in metrology, for the measurement of fundamental constants and in the testing of fundamental theories. The spectroscopic resolution in measurements is often limited by the interaction time. For ions, long interaction times are achieved by confinement in electrostatic traps, while laser cooling techniques have allowed high resolution measurements on certain species [28]. The development of methods to produce cold, slow molecules has played an important role in molecular high resolution spectroscopy. A beam of cold $^{15}ND_3$ molecules at a velocity of 50 ms^{-1} has been used to determine the molecular hyperfine structure by measuring the microwave inversion tunneling spectrum [29]. The production of cold OH molecules confined in an electrostatic trap has enabled the measurement of the radiative lifetime of one of the molecules metastable states [30]. In a similar experiment the radiative lifetime of CO metastable rotational levels was measured, again with a cold sample in an electrostatic trap [31].

There is currently a large experimental effort focusing on using cold molecules to measure the electric dipole moment (edm) of the electron which would serve as a test of the standard model of physics [32]. The permanent edm of any elementary particle would imply physics beyond the standard model as it requires violation of both parity (P) and time-reversal (T) invariance. The electron edm can be measured by applying an external electric field to an atom or molecule and measuring the change in energy of the particle. The energy change of an atom/molecule in an external field E due to the electron edm d_e is given by $d_e P(E) E_{int}$, where E_{int} is the effective electric field from the molecule and $P(E)$ is the degree of polarisation of the atom/molecule in the applied field. The magnitude of E_{int} scales with the cube of the nuclear charge and heavy atoms and molecules offer the highest sensitivity in experiments. The most accurate measurement of the edm, $d_e = (6.9 \pm 7.4) \times 10^{-28}$ ecm, to date has been made using a beam of ^{205}Tl atoms [33]. The E_{int} of ^{205}Tl atoms is large but $P(E)$ is small for realistically achievable fields. Polar molecules are much more polarisable in external fields and can offer much higher sensitivity. Production of a sample of cold, trapped polar molecules would allow sensitive measurement over long interaction times and therefore a more precise measurement of the electron edm.

Cold molecules have potential application in other fundamental experiments such as the search for parity violation in chiral molecules. The mirror image of these molecules cannot be superimposed. Observing different physical properties between left and right handed *enantiomers* would imply a parity violation. An experiment has been carried out to look for differences in the frequencies of rovibrational transitions in the two CHFClBr enantiomers [34]. No parity violation was observed at the 2.5×10^{-13} level but this experiment was carried out on a room temperature gas and by using a cold molecular beam or a trapped sample the precision of the measurement could be significantly increased.

Many body physics

In the previous section the realisation of novel phases of matter in atomic quantum degenerate gases was discussed. Many-body quantum phases, including superfluid, supersolid, Mott insulator, checkerboard, and collapse phases are predicted in an ultracold dipolar gas where dipole-dipole interactions dominate over van der Waals interactions [35]. Although such a gas could be realised with atoms, large electric fields are required to induce a dipole moment and polar molecules are more suitable requiring only moderate fields to polarise the sample. Diatomic polar molecules have also been proposed for use in quantum computation where the qubit is the orientation of a molecule's electronic dipole moment with respect to an external electric field [36].

1.3 Cooling and slowing molecules

Association of ultracold atoms

A large experimental effort has gone into developing techniques to produce cold and ultracold molecules. In this section these methods will be reviewed and their advantages and disadvantages discussed. There are currently only two techniques which have been successful in producing ultracold molecules. These methods use photoassociation [37] and Feshbach resonances [38]. Photoassociation produces molecules by resonantly pumping two colliding ultracold atoms to a bound molecular state. The first molecules produced with this technique were Na_2 [39]. From the subset of atoms which have been laser cooled a variety of homo- and heteronuclear molecules have now been produced in this way. In most cases the favoured decay channel from the bound molecular state is dissociation and the molecules tend to be short lived (ns timescales). This problem can be solved using optical pumping techniques to transfer the excited molecules to deeply bound, low lying vibrational levels in the electronic ground state. This two stage process has been used to produce K_2 [40] and RbCs [41] molecules at temperatures well below 1 mK. Caesium molecules (Cs_2) produced in this way have been further cooled to the $v = 0$ vibrational ground state using broadband shaped femtosecond laser pulses and adiabatic passage techniques [42].

Ultracold molecules have also been created by exploiting magnetically controlled scattering resonances. These Feshbach resonances occur when the total energy of two colliding atoms is equal to the energy of a bound molecular state. This can lead to creation of a molecule. Provided the magnetic moments of the scattering and bound states differ, an applied magnetic field can be used to Zeeman shift the potential curves and the energy difference between the bound state and the dissociation continuum can be tuned. Thus, if this energy difference is small for two colliding atoms the applied magnetic field can be tuned to resonantly couple to the bound state producing Feshbach molecules. Most Feshbach molecules also have short lifetimes; however, deeply bound Cs_2 [43], KRb [44] and Rb_2 [45] molecules have been produced by inducing adiabatic transfer to the ground state via two or more optical transitions.

The main advantage of these association techniques is that the molecules produced inherit the temperature of the constituent ultracold atoms which usually lies in the μK-nK range. The principle drawback is that the set of molecules that can be produced using these techniques is limited by the atoms which can be laser cooled. Nonetheless, these methods have proved very useful in studying ultracold molecular physics and led to the first experimental observation of molecular BEC [46].

Buffer gas cooling

Buffer gas cooling dissipatively cools atoms and molecules through elastic collisions with a cold buffer gas [47]. The species to be cooled is introduced into a helium cryostat where the gas has a temperature of a few hundred mK. Elastic collisions between the buffer gas and the species to be cooled dissipates their vibrational, rotational and translational energy. The first molecular species to be cooled and trapped using this technique was CaH [48]. In this experiment the CaH molecules were produced via laser ablation of a CaH_2 solid target placed inside a copper cell filled with ^{3}He. The ^{3}He buffer gas was maintained at approximately 300 mK by a dilution refrigerator. The molecules were trapped in a quadrupole magnetic trap at a density of 8×10^7 cm^{-3} at a temperature of 400 ± 50 mK. Isolating the cold molecular sample by pumping out the buffer gas was not possible as the pumping techniques require times of $\sim$10 s while the CaH trap life time is $\sim$2 s. More recently, this technique has been used to cool and trap NH molecules which were injected into the buffer gas cell from a room temperature beam [49]. The temperature to which molecules can be cooled using this technique is fundamentally limited by the temperature of the buffer gas ($>$ 100 mK). Even with evaporative cooling, reaching the ultracold regime may not be possible.

Stark and Zeeman deceleration

Stark deceleration is a widely used technique to slow cold molecules from a molecular beam. This method uses inhomogeneous quasi-electrostatic fields to decelerate polar molecules from a supersonic beam [50]. It exploits the interaction between the permanent dipole moment of a molecule and the applied electric field. This interaction results in the gain of potential energy, due to the Stark effect, provided the molecule's dipole moment is anti-parallel to the applied field. Such molecules are said to be in *low-field seeking* states and on entering an inhomogeneous electric field will lose kinetic energy as they climb the resultant potential hill. A Stark decelerator consists of a series of electrode rods across which tens of kilovolts are applied to produce an inhomogeneous electric field.

The molecules are generally introduced as intense pulsed beams undergoing supersonic expansion such that they are translationally cold (≈ 1 K) in the centre-of-mass reference frame but with a velocity on the order of 100 ms^{-1}. While the molecular jet is traveling down the decelerator the electrodes are switched on and off in a precise timing sequence such that, in an ideal case, as the molecules reach the top of the potential hill produced by each electrode pair the electric field is switched off and the molecules do not regain the kinetic energy lost on their descent. In reality only a small portion of the bunch of molecules remains in phase with the field switching and are decelerated to the desired final velocity. This technique is quantum state selective as only molecules in the right state will be decelerated.

The first experimental realisation of Stark deceleration succeeded in decelerating a beam of metastable CO from 225 ms^{-1} to 98 ms^{-1} [51]. The technique has now been widely implemented for a variety of other molecules including NH_3 [52], OH [53, 54], H_2CO [55] and SO_2 [56]. All molecules are high-field seeking in their absolute ground state and all these experiments were carried out with the molecules in an excited, low-field seeking state. Stark decelerators are capable of producing samples of molecules with translational energy distributions on the order of tens of millikelvin at densities of approximately 10^7 cm^{-3}. It is important to note that these temperatures are not achieved through dissipation, although the final energy distribution is narrower than the initial distribution. A narrower distribution is achieved through velocity selection. As only molecules with the right phase and velocity will be decelerated successfully the slowed sample has a narrower energy distribution. Stark decelerated molecules have successfully been loaded into an electrostatic trap at a temperature of 350 mK [57]. The technique has also been used to study low energy collisions in high resolution crossed-beam experiments [22]. Although Stark deceleration has proved a very useful tool in cold molecular physics the technique is limited to deceleration of polar species in low-field seeking states and is not capable of producing samples in the ultracold temperature regime.

Zeeman deceleration is an analogous method to Stark deceleration which uses magnetic fields to decelerate paramagnetic molecules. The technique was first applied to H and Ne atoms [58, 59]. Subsequent experiments have decelerated ground state O_2 molecules, which are uniquely paramagnetic in their ground state, from 389 ms^{-1} to 83 ms^{-1} [60].

Optical Stark deceleration

Optical Stark deceleration is a technique developed in our research group which uses intense, pulsed optical fields to rapidly decelerate molecules from a supersonic jet. This method exploits the interaction between a far detuned optical field and the induced dipole moment of a molecule [61, 62]. Such experiments involve spatially overlapping two nearly counter-propagating intense laser pulses ($> 10^{11}$ Wcm^{-2}) to create an interference pattern. This interference pattern is aligned with molecules creating a deep periodic optical lattice potential. A non-zero frequency difference between the two lattice beams creates a moving lattice with a velocity which is dependent on the magnitude of the frequency difference. Molecular deceleration can be achieved using either a constant-velocity [61] or decelerating lattice [62].

Currently the only optical Stark deceleration experiments which have been demonstrated have used a constant-velocity lattice traveling slower than the molecular jet. The intensity and duration of the lattice pulses were carefully controlled such that a portion of the molecules in the jet with the right phase with respect to the lattice underwent a half oscillation in the lattice sites and experienced maximum deceleration. The first demonstration of optical Stark deceleration was with NO molecules and achieved deceleration from 400 ms^{-1} to 321 ms^{-1} [61]. In subsequent work C_6H_6 molecules were decelerated from 380 ms^{-1} to 191 ms^{-1} [63]. Deceleration to rest has been achieved for C_6H_6 using a lattice traveling at half the molecular beam velocity [64]. The decelerated samples in these experiments had densities of greater than 10^{10} cm^{-3} while the temperatures were on the order of 1K.

Although a constant-velocity lattice can be used to achieve deceleration there are some drawbacks. This method requires precise control of the lattice beam intensities and precise switching of the optical fields on nanosecond timescales, which is technically demanding. Another limitation is that the final velocity spread of the decelerated molecules is at best equal to that in the supersonic jet (≈ 1 K). An improved optical Stark deceleration scheme has been proposed which uses a decelerating lattice [62]. In these experiments the lattice will be turned on with a velocity equal to that of the molecular jet and then be decelerated to rest by chirping the frequency difference between the lattice beams to zero. The final velocity of the decelerated packet in this technique requires control over the relative frequency of the two lattice pulses. A laser system has been developed in our research group which can produce two pulses with energies of up to 700 mJ whose intensity and frequency can be controlled over a duration of 20 ns to 10 μs [65]. Using a chirped lattice it is possible to achieve final velocity spreads in the decelerated sample which are narrower than in the molecular jet by selecting only a small velocity class of molecules in the jet. A chirped lattice has been used to accelerate argon atoms from a MOT to velocities of 191 ± 1 ms^{-1} while maintaining a narrow energy spread 30-100 mK [66]. These experiments will be presented in this thesis and demonstrate the feasibility of optical Stark deceleration. One of the main advantages of this technique is its generality as it does not rely on a molecule having a permanent electric or magnetic dipole moment as is the case with Stark and Zeeman deceleration.

Doppler cooling

Applying Doppler cooling to molecules is problematic due to the scarcity of closed cycling transitions. However, Doppler cooling of SrF molecules in a cryogenic beam has been demonstrated using three lasers [67]. The cooling scheme was based around the $\mathrm{X}^2\Sigma^+ \rightarrow \mathrm{A}^2\Pi_{\frac{1}{2}}$ electronic transition which ensured spontaneous decay back to the initial electronic state as the $\mathrm{A}^2\Pi_{\frac{1}{2}}$ state is the lowest lying excited electronic state. Favourable Franck-Condon factors dictated that only three vibrational levels ($v = 0, 1, 2$) were populated after 10^5 transitions. The $v = 1$ and $v = 2$ states were re-pumped to the $v = 0$ state using two of the three lasers. Spontaneous decay lead to the population of Zeeman sublevels not resonant with the laser. Molecules in these sublevels were returned to resonant level by applying a magnetic field which forced the molecules to Larmor precess into the resonant level. All ground-state hyperfine and spin-rotation substructure was addressed by radio frequency sidebands on the lasers. Although this experiment was successful in cooling the molecular beam to millikelvin temperatures it is clear that the method is considerably more complex than atomic laser cooling. Furthermore, this technique is not widely applicable to other molecular systems and there are only about ten other diatomic molecules which are candidates to be cooled in this way [68].

Cavity cooling

Cooling of molecules in high-finesse optical cavities has also been proposed as a potential method for achieving microkelvin temperatures [69]. In this cavity cooling scheme the molecules' kinetic energy would be dissipated by a frictional force arising from the coupled molecule-field dynamics. The energy is dissipated via loss from the cavity field and no closed cycle electronic transitions are required. Cavity cooling to microkelvin temperatures has been demonstrated for single rubidium atoms [70] and an ensemble of caesium atoms [71], but as yet molecular cooling using this technique has not been achieved. Any such future experiments will require cooling/slowing of the molecules using one of the aforementioned techniques prior to cavity cooling.

Sympathetic cooling

Another technique which has been proposed to cool molecules below the millikelvin barrier is sympathetic cooling. This scheme involves co-trapping a cold molecular species with ultracold atoms and allowing the two species to thermalise through collisions. The cooling mechanism is the same as in buffer gas cooling. This technique is important in the realisation of a Fermi degenerate gas as evaporative cooling fails for identical fermions at low temperatures. Sympathetic cooling has been demonstrated between Rb atoms in different spin substates confined in a magnetic trap [72]. One of the substates was evaporatively cooled while the other was cooled sympathetically through thermal contact with the evaporatively cooled atoms. In another experiment fermionic ^{6}Li atoms have been cooled by collisions with co-trapped ^{7}Li atoms which are bosons [73]. Interspecies sympathetic cooling has also been achieved in a magnetic trap confining evaporatively cooled rubidium atoms and potassium atoms which lead to the first observation of a potassium BEC [74].

The success of sympathetic cooling experiments is reliant on a favourable rate of elastic to inelastic collisions. Inelastic collisions can lead to loss of trapped atoms through state transfer to untrappable states or reactions between the two species. If inelastic collisions are too prominent the species to be cooled will be depleted before thermalisation occurs. There are two main proposals for sympathetic cooling of molecules with ultracold, laser cooled atoms. One of these schemes proposes to use alkali atoms and a magnetic trap [75] while the other involves using rare gas atoms co-trapped with molecules in an optical trap [76]. When assessing the validity of a sympathetic cooling scheme detailed calculations of the elastic and inelastic collisional cross-sections are required in order to predict trap losses and the thermalisation time. Theoretical studies have been carried out to investigate the prospects of sympathetically cooling OH with Rb [77] and NH_3 with various alkali and alkaline-earth species, as well as xenon [78]. The cross-sections were calculated using *ab initio* potential energy surfaces and showed that the interacting systems will show strong inelasticity when inelastic collisions are energetically allowed. Sympathetic cooling could only potentially work in these systems if the two species involved are in their absolute ground states. This has experimental implications on the type of trap that can be used as electrostatic and magnetic traps cannot trap molecules in their absolute ground states. One potentially successful sympathetic cooling experiment using a magnetic trap involves cooling NH with Mg atoms where elastic collision rates are predicted to be much faster than inelastic rates [79]. Although this sympathetic cooling system may be successful, Mg atoms have not yet been trapped at temperatures below 1 mK [80]. Another proposed experiment involves co-trapping LiH and Li in a microwave trap [81]. Although these schemes may yet produce ultracold molecules, general applicability to a wide range of species will be difficult due the high reactivity of the atomic species used. Also, apart from the LiH scheme which proposes to use a microwave trap, the other schemes all intend to use a magnetic trap which can only trap specific molecular states.

The sympathetic cooling scheme using rare gas atoms, which are much less reactive than alkali-metal atoms, has been proposed in our research group and will be discussed in the next section.

1.4 Sympathetic cooling of molecules with rare gas atoms

The work presented in this thesis is part of an experimental project to sympathetically cool molecules via collisions with ultracold rare gas atoms in an optical trap [76]. Rare gas atoms are an attractive coolant species as they are very unreactive in their ground state which makes the elastic to inelastic collision ratio more favourable. Using an optical trap is attractive as it is capable of trapping all molecular ro-vibrational levels in the electronic ground state, unlike magnetic and electrostatic traps. Therefore, trap loss due to state-changing collisions is not a problem in an optical trap.

This sympathetic cooling scheme involves first preparing the atoms at ultracold temperatures via laser cooling and the molecules at cold temperatures using optical Stark deceleration before loading both species into a deep optical lattice potential. The two main considerations when selecting the best of the rare gas candidates for the first experiments were their collisional interaction with the molecules to be cooled and the ease with which the species can be produced and trapped at ultracold temperatures in its ground state. Of the rare gas elements helium, neon, argon, krypton and xenon have all been laser cooled [82] and the species selected for sympathetic cooling experiments was chosen from this subset. Theoretical elastic scattering cross-sections were calculated for Rg-H_2 and Rg-C_6H_6 complexes (where Rg denotes rare gas atom) [83, 84]. Collisions of para-H_2 and five rare gas species (He, Ne, Ar, Kr and Xe) were also studied [83]. The largest elastic scattering cross-sections were calculated for He-H_2 and Ar-H_2 and compared with those in the successful alkali atom sympathetic cooling experiments mentioned earlier. The Rg-C_6H_6 interaction was studied for ^{3}He, ^{4}He and Ne [84]. The elastic cross-section was largest for neon although all cross-sections calculated were comparable with the alkali atom sympathetic cooling experiments.

Preparation of ultracold rare gas atoms in their ground state is a two stage process which involves first laser cooling the atoms in an excited, metastable state before optically quenching them back to their ground state. Laser cooling from the ground state is not feasible as the nearest dipole allowed transitions are in the vacuum ultraviolet, beyond the reach of ordinary continuous wave laser systems. From their lowest lying metastable state $n\mathrm{s}[3/2]_2$ the rare gas atoms can be cooled using transitions to the $n\mathrm{p}[5/2]_3$ state. Table 1.1 shows the wavelengths that are used to cool the metastable rare gas atoms. Also shown is the Doppler temperature for each species which is the cooling limit for Doppler cooling. Laser cooling can readily achieve lower temperatures due to polarization gradient cooling [85]. Optical quenching of the metastable atoms can be achieved by exciting the atoms to an excited state from which they favourably decay to the ground state via one or more dipole transitions. The metastable states are high lying (the lowest is Xe at 8.3 eV above the ground state) and the momentum kick associated with emitting high energy photons during quenching acts to heat the atomic sample. Table 1.1 shows the quenching wavelengths and the heating induced from the photon recoil. Helium cannot be optically quenched but can be returned to the ground state using Stark induced transitions [86]. The recoil effect heats helium by over 1 mK which rules it out as a suitable candidate for sympathetic cooling to ultracold temperatures.

The molecular species will be prepared for sympathetic cooling experiments using the chirped optical Stark deceleration technique discussed in the previous section. This method has not yet been used to decelerate molecules but is predicted to produce sta-

	^{4}He*	^{20}Ne*	^{40}Ar*	^{84}Kr*	^{132}Xe*
λ_{cool} (nm)	1083.0	640.2	811.5	811.3	881.9
T_{Doppler} (μK)	39	203	141	133	116
λ_{quench} (nm)	-	633.4	801.4	810.4	979.9
T_{recoil} (μK)	1216	261	66	25	11
Ground state U_0 (mK)	2.0	3.8	15.7	23.8	38.7

Table 1.1: Data on transitions used to laser cool and optically quench rare gas atoms. All data for the levels were taken from the NIST atomic spectra database and the wavelengths given are for an atom in air [87]. Also shown are the peak trap depths, U_0, for the different species in their ground states in a high finesse cavity with a finesse of 6000 where a 15 W beam is focused to a waist of 78 μm.

tionary molecular samples at temperatures of tens of millikelvin [62]. In order to trap a significant fraction of these molecules in an optical trap, high field intensities are required. The required intensities can be achieved using high finesse build-up cavities which have been used in ultracold atom trapping experiments [88, 89]. Trap depths of 9 mK have been achieved in a high finesse cavity for Rb atoms [89]. In our group a confocal cavity with a finesse of 6000 is currently under development which will achieve a circulating power inside the cavity 2000 times that of the input beam. A laser input of 15 W focused to a waist of 78 μm at the centre of the cavity will give a trap depth of 45 mK for H_2 and 98 mK for C_6H_6. The corresponding trap depths for the rare gas species in their ground states are shown in table 1.1.

After consideration of the Rg-molecule elastic scattering cross-sections, the recoil heating effects and achievable trap depths, argon was chosen for the first sympathetic cooling experiments. A theoretical study of Ar-H_2 and Ar-C_6H_6 sympathetic cooling has been carried out in order to predict the thermalisation temperature and timescales [90]. The thermalisation was evaluated using the direct simulation Monte Carlo method and considering collisions in a single optical lattice site. The number densities of the atoms and molecules and the depth of the trap were carefully selected to correspond to expected experimental parameters. Atom-molecule, atom-atom and molecule-molecule collisions were considered. At the beginning of the simulation, the atoms and molecules were given initial coordinates and there trajectories under the influence of the trapping forces were then calculated. At each time step in the simulation inter-particle collisions were considered. The trap was divided into cells and only particles within the same cell were allowed to collide. A random number, assigned from the collision probability distribution, was used to determine whether a given pair collided or not. The collision probability is dependent on the relative velocity of the particles, their elastic cross-section and the volume of the cell considered. Elastic s-wave scattering dominates at the collision energies considered and higher-order scattering was neglected from the simulation. These simulations estimated achievable final temperatures of 330 ± 30 μK for H_2 and 600 ± 100 μK for C_6H_6, which would be reached on a timescale of less than ten seconds.

This sympathetic cooling scheme is currently being developed in our research group. This thesis presents experimental progress towards realising this general method for producing ultracold molecules. There are three main experimental elements of the project which involve (i) the development of a source of ultracold ground state argon atoms, (ii) the production of cold stationary molecules using chirped optical Stark deceleration and (iii) the construction of a high finesse optical cavity to co-trap the atoms and molecules. The work in this thesis focuses on the production of the ultracold argon source and describes intermediary experiments before sympathetic cooling which have been carried out.

Chapter 2

Laser cooling and trapping

The experimental work presented in this thesis involves the manipulation of argon atoms using laser fields. This chapter introduces the forces experienced by atoms in laser fields, discussing their physical origin, and outlines their application in the laser cooling and trapping experiments reported in this thesis.

2.1 Light forces on atoms

There are two fundamentally different forces an atom can experience in a light field. The *scattering force* results from the isotropic scattering of photons from a near-resonance laser field. This force is dissipative and is crucial in laser cooling of atoms. The second force is the *optical dipole force* which derives from the A.C., or optical Stark effect.

2.1.1 Scattering force

The scattering force can be understood by considering a two level atom, with a lower level $|g\rangle$ and upper level $|e\rangle$, at rest in a single laser field which has a frequency ω_L close to the resonant frequency of the atomic transition ω_0. The lower and upper levels are coupled by a dipole transition and the atom will absorb photons from the laser field, exciting it from $|g\rangle$ to $|e\rangle$. Ignoring stimulated emission, the atom will decay from $|e\rangle$ back to $|g\rangle$ via spontaneous emission at a rate characterized by the natural linewidth of the transition Γ ($= 1/\tau$ where τ is the lifetime of the excited state). As photons have a momentum $\hbar\boldsymbol{k}$ ($\boldsymbol{k} = 2\pi/\lambda\hat{\boldsymbol{z}}$ is the photon wavevector) there is a momentum transfer to the atom associated with absorption and emission due to the conservation of momentum. Absorption of the laser beam photons occurs in the $\boldsymbol{z}$ direction only, while photons are spontaneously emitted isotropically in all directions. Thus the net momentum transfer from many emitted photons averages to zero and there is a net force in the direction of the laser beam over many absorption-emission cycles. The magnitude of the scattering force is the product of the momentum of a single photon and the photon scattering rate Γ_{scatt} and is given by,

$$\boldsymbol{F_{scatt}} = \hbar \boldsymbol{k} \Gamma_{scatt}. \tag{2.1}$$

The photon scattering rate depends on the frequency and intensity of the laser field and the natural linewidth of the atomic transition and is given by

$$\Gamma_{scatt} = \frac{s_0 \Gamma/2}{1 + s_0 + (2\Delta/\Gamma)^2}, \tag{2.2}$$

where $s_0 = I/I_s$ is the on-resonance saturation parameter, $I_s = \frac{\pi h c}{3\lambda^3 \tau}$ is the saturation intensity and $\Delta = \omega_L - \omega_0$ is the frequency detuning of the laser field from the atomic transition. At high intensities the scattering force saturates to a maximum value of $F_{max} = \hbar \boldsymbol{k} \Gamma/2$.

If we now consider that the atom is not at rest but has a velocity $\boldsymbol{v}$ the detuning is Doppler shifted to $\Delta + \boldsymbol{k}\boldsymbol{v}$. The scattering rate, and therefore the force, become velocity dependent which leads to dissipation and cooling.

2.1.2 Optical dipole force

The optical dipole force derives from the energy shifts of atomic energy levels in a laser field. The energy shifts are caused by the Stark effect of the electric field of the light. Consider a two level atom in a laser field given by $\boldsymbol{E} = E_0 \boldsymbol{\epsilon} \cos(\boldsymbol{k} z - \omega_L t)$, where $\boldsymbol{\epsilon}$ is the polarisation vector of the light. If the detuning of the laser field from the atomic resonance is large, the energy shifts of the ground $|g\rangle$ and excited $|e\rangle$ states can be written as

$$\Delta E_g = \frac{\hbar \Omega^2}{4\Delta} \qquad \text{and} \qquad \Delta E_e = -\frac{\hbar \Omega^2}{4\Delta}, \tag{2.3}$$

where Δ is the detuning of the light field from the atomic transition and Ω is the *Rabi frequency*. The Rabi frequency is a function of the transition dipole moment $\langle g|\boldsymbol{d}|e\rangle$ and the amplitude of the electric field $\boldsymbol{E}$ and is given by

$$\Omega = \frac{\langle g|\boldsymbol{d}|e\rangle \boldsymbol{E}}{\hbar}. \tag{2.4}$$

In the limit of large detunings $\Omega \ll \Delta$. This result is derived using a semiclassical approach where the atom is considered a two level quantum system and the light is a classical wave. The rotating wave approximation is also applied which neglects terms oscillating with the laser frequency ω_L and keeps slower oscillating terms (i.e. $\omega_L - \omega_o$). The magnitude of the energy shift is dependent on the coupling to the light field and is proportional the to the light intensity ($I \propto \Omega^2$). In a typical laser field the intensity $I(\boldsymbol{r})$ is not homogeneous and produces a spatially-dependent light shift. The dipole force is due to the energy gradients in the light field. The sign of the force is dependent on the detuning of the laser field and attracts atoms to regions of high intensity in a red-detuned field ($\Delta < 0$) while in a blue-detuned field ($\Delta > 0$) the force is repulsive. Unlike the scattering force the dipole force does not saturate and can, in principle, be large in high intensity laser fields. The result presented here is for the simplified case of a two level atom and the situation in a multilevel atom is more complicated although the physical origin of the force remains the same.

2.2 Optical molasses

In laser cooling experiments the scattering force is used to cool atomic motion in a technique called *Doppler cooling.* We consider a one-dimensional case where an atom with a small velocity $\boldsymbol{v}$ can be cooled by two red-detuned ($\Delta < 0$) laser beams counter-propagating along the same axis as the atomic velocity. The detuning of the atom from the beam which opposes its motion is $\Delta + k\boldsymbol{v}$ while the detuning from the beam propagating in the same direction is $\Delta - k\boldsymbol{v}$. The Doppler effect acts to shift the beam opposing the atom's motion closer to resonance and the other beam further from resonance. The atom experiences a force opposing its motion given by the sum of the scattering forces from each laser beam,

$$\boldsymbol{F}(v) = \frac{\hbar \boldsymbol{k} \Gamma s_0}{2} \left(\frac{1}{1 + s_0 + (2(\Delta + \boldsymbol{k}\boldsymbol{v})/\Gamma)^2} + \frac{1}{1 + s_0 + (2(\Delta - \boldsymbol{k}\boldsymbol{v})/\Gamma)^2} \right). \tag{2.5}$$

In the low velocity limit ($\boldsymbol{k}\boldsymbol{v} \ll \Gamma$) this equation can be expanded to the first order in v to give

$$\boldsymbol{F}(v) = -\hbar \boldsymbol{k}^2 \frac{8 s_0 \left(\Delta/\Gamma\right)}{\left(1 + \left(2\Delta/\Gamma\right)^2\right)^2} \boldsymbol{v}, \tag{2.6}$$

which is a damping force and can be rewritten

$$\boldsymbol{F}(v) = -\beta \boldsymbol{v} \tag{2.7}$$

where β is the damping coefficient. This force is analogous to viscous drag and hence is named *optical molasses*. The velocity distribution of an atomic sample is compressed in an optical molasses while damping the mean velocity to zero. Equation 2.7 represents a simplified picture and implies that cooling to 0 K is possible which would violate thermodynamics. This model does not take into account the spread in momentum of the spontaneously emitted photons which results from the natural linewidth of the transition. This leads to a low temperature limit called the *Doppler temperature* which is given by

$$T_D = \frac{\hbar \Gamma}{2 k_B}. \tag{2.8}$$

This temperature is limited by the linewidth of the cooling transition. Optical molasses can readily be extended to three dimensions using three pairs of laser beams. Although successful cooling can be achieved in three-dimensional optical molasses it is not a trap and atoms will eventually diffuse out of the molasses region. In order to achieve both cooling and trapping, a spatially varying force is required.

2.3 Magneto-optical trap

A magneto-optical trap combines a quadrupole magnetic field with an optical molasses which can both cool and trap atoms. The diagram in figure 2.1 illustrates, in one dimension, the mechanism by which the spatially-dependent force is generated for a two level atom with $J_g = 0 \rightarrow J_e = 1$ cooling transition. The quadrupole magnetic field applies a linear B-field gradient across the trapping region which crosses zero at the trap centre ($z = 0$). The applied B-field splits the excited state into its three Zeeman sublevels ($m_e = -1, 0, +1$). If we consider an atom moving away from the trap centre towards the σ^- laser beam the m_e = -1 excited state sublevel is shifted downwards in energy and the $m_e = +1$ sublevel is up shifted in energy. Thus, as the atom moves away from the trap centre the $\Delta m = -1$ transition is tuned closer to resonance with the laser beam while the $\Delta m = +1$ transition is tuned further from resonance. Conservation of angular momentum dictates that the $\Delta m = -1$ transition is pumped by σ^- photons and the $\Delta m = +1$

transition is pumped by σ^+ light. Therefore, the atom moving towards the σ^- beam will scatter more photons from the σ^- beam than the σ^+ beam and experience a force towards the centre of the trap. If the atom moves in the opposite direction, towards the σ^+ beam, the roles of the $m_e = \pm 1$ states are reversed and the atom scatters more photons from the σ^+ beam again experiencing a force towards the trap centre.

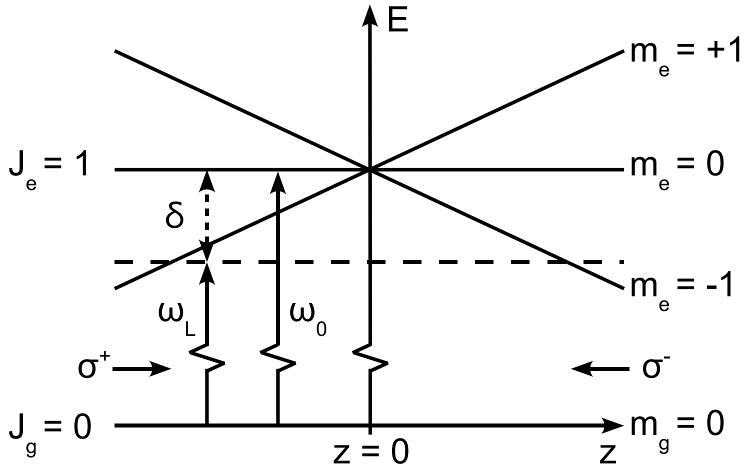

Figure 2.1: A MOT arrangement in 1D showing the Zeeman splitting of the excited state sublevels due to the quadrupole magnetic field, the directions of the σ^+ and σ^- laser beams and their detuning from resonance. The laser beam polarisations are defined in the $+z$ direction.

The effective detuning of an atom in a MOT is $\Delta + \boldsymbol{kv} + \mu' \boldsymbol{B}(z)/\hbar$ where μ' is the magnetic moment of the transition and $\boldsymbol{B}(z)$ is the magnetic field strength. The magnetic moment of the transition is given by $\mu' = (g_g m_g + g_e m_e)\mu_B$ where g_g and g_e are the Landé g-factors of the ground and excited state respectively and μ_B is the Bohr magneton. The force on the atom is given by equation 2.5 with the modification of the effective detuning. In the low intensity and low velocity limit the force can be expanded to

$$\boldsymbol{F} = -\beta v - \kappa z \tag{2.9}$$

where the spring constant κ is given by

$$\kappa = \frac{\mu' \frac{\partial B}{\partial z}}{\hbar k} \beta \tag{2.10}$$

In a three-dimensional MOT, counter-propagating σ^+ and σ^- beams along each axis confine the atoms in three dimensions.

2.4 Sub-Doppler cooling

Temperatures colder than the Doppler limit can readily be achieved in laser cooling experiments [91]. *Sub-Doppler* cooling processes derive from polarisation gradients in the optical field and the multiplicity of energy levels of the cooling transition [85, 92]. The most simple sub-Doppler cooling scheme involves cooling via a $J_g = \frac{1}{2} \rightarrow J_e = \frac{3}{2}$ transition in a light field formed by two orthogonal, linearly polarised counter-propagating beams. The polarisation of this light field will vary over half a wavelength from linearly polarised at 45° to the two beam polarisations, to σ^+, to linearly polarised but perpendicular to previous linear polarisation, to σ^-. In this light field the atom will be optically pumped to the $m_g = +\frac{1}{2}$ sublevel when in the purely σ^+ field region and to the $m_g = -\frac{1}{2}$ sublevel when the field is purely σ^-. Thus in traveling through the light field the atoms will have their population pumped backwards and forwards between the ground state sublevels every half wavelength.

The light field will also act to light shift the $m_g = +\frac{1}{2}$ and $m_g = -\frac{1}{2}$ levels, an effect which is crucial to this cooling mechanism. For low intensity beams the light shifts of the ground magnetic sublevels are given by

$$\Delta E_g = \frac{\hbar \Delta s_0 C_{ge}^2}{1 + (2\Delta/\Gamma)^2} \tag{2.11}$$

where C_{ge} is the Clebsch-Gordan coefficient that describes the atom-light field coupling. This expression is similar to equation 2.3 but the light shift is now twice as large as there are two traveling waves, the Clebsch-Gordan coefficients rather than the Rabi frequency describe the atom-light field coupling and spontaneous emission has been taken into account in the derivation. In the purely σ^+ field the $m_g = +\frac{1}{2}$ state will be more strongly coupled to the light field and will accordingly have a larger light shift, by a factor of three in this case, than the $m_g = -\frac{1}{2}$ state. In the pure σ^- the light shifts of the states are reversed. If the laser field is red-detuned the magnetic substates will be negatively shifted in energy and optical pumping will shift the atomic population to the substate with the largest light shift and the lowest energy.

Figure 2.2 illustrates how the optical pumping and the light shift combine to cool the atom. At the $z = 0$ position the field is purely σ^+ and thus the atom is optically pumped to the $m_g = +\frac{1}{2}$ sublevel. As the atom moves in the z direction it climbs the potential

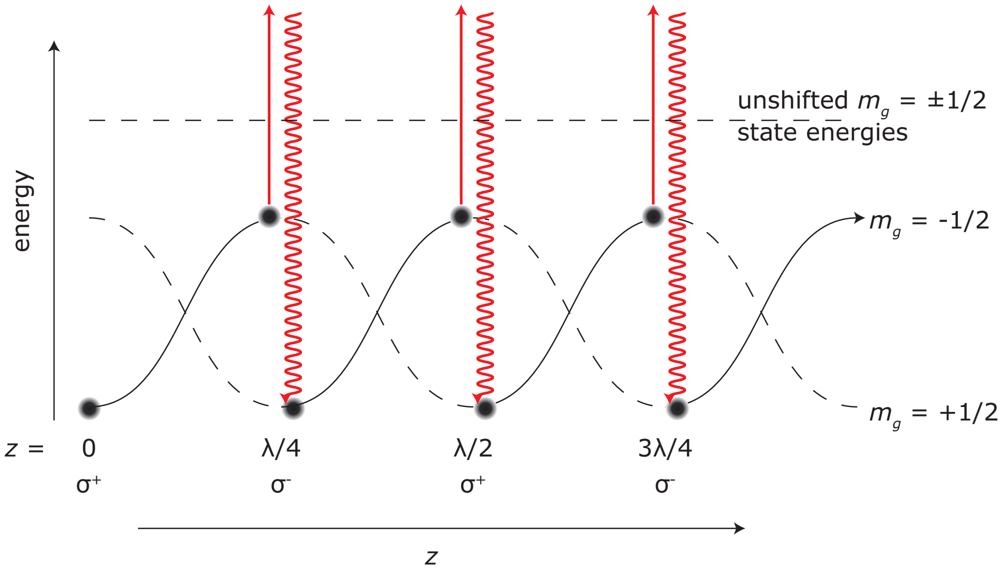

Figure 2.2: An illustration of the sub-Doppler cooling mechanism in a light field formed by two orthogonal, linearly polarised counter-propagating laser beams. Each absorption emission cycle results in the loss of kinetic energy.

hill created by the light shift and gains potential energy and loses kinetic energy (i.e. it experiences the dipole force). When the atom reaches the $z = \frac{\lambda}{4}$ position the light field is purely σ^- and the atom is pumped into the $m_g = -\frac{1}{2}$ substate which is now lower in energy than the $m_g = +\frac{1}{2}$ state. The atom continues to move in the z direction and again begins to climb the potential hill until it reaches $z = \frac{\lambda}{2}$ and is optically pumped to the, now lower energy, $m_g = +\frac{1}{2}$ substate. The potential energy gained in climbing the potential hills is radiated during the optical pumping thus removing kinetic energy from the atom. The process will continue until the kinetic energy of the atom is too low to overcome the upcoming potential hill and it becomes localised between two potential maxima. The efficiency of this cooling process for an atom is dependent on the atomic velocity and is maximum for atoms that travel a distance of $\frac{\lambda}{4}$ during one optical pumping process. The low temperature limit for sub-Doppler cooling derives from the momentum kick associated with emitting a single photon and is given by

$$T_{recoil} = \frac{(\hbar k)^2}{2m}. \tag{2.12}$$

The sub-Doppler cooling scheme discussed here is the simplest and similar cooling processes are observed in other light field configurations (e.g. a σ^--σ^+ field) [93]. In all cases the cooling mechanism relies on differential scattering from counter-propagating beams.

2.5 Dipole trap

2.5.1 Far off resonance trap (FORT)

The dipole force can be used to spatially confine atoms which have been laser cooled using inhomogeneous laser fields. When an atom is in a laser field the electric field of the laser will act to induce an atomic dipole moment given by $\boldsymbol{p}(\boldsymbol{r}, t) = \alpha(\omega)\boldsymbol{E}(\boldsymbol{r}, t)$, where $\alpha(\omega)$ is the complex polarisability of the atom. The electric field is given by $\boldsymbol{E}(\boldsymbol{r}, t) = \boldsymbol{\epsilon} E_0(\boldsymbol{r})\exp(-i\omega t) + c.c.$ and the induced dipole will oscillate at the driving frequency ω. The induced dipole will interact with the electric field to give a potential

$$U_{dip}(\boldsymbol{r}) = -\frac{1}{2}\langle \boldsymbol{p}(\boldsymbol{r}, t) \cdot \boldsymbol{E}(\boldsymbol{r}, t)\rangle = -\frac{1}{2\epsilon_0 c}\mathrm{Re}(\alpha)I \tag{2.13}$$

where the angular brackets denote the time average over fast oscillating terms and $I = \frac{1}{2}\epsilon_0 c|E_0|^2$ is the intensity of the laser field. The factor of $\frac{1}{2}$ takes into account that the dipole is induced in an AC field rather than a permanent dipole in a DC field. The dipole force is then given by the gradient of this potential

$$\boldsymbol{F}_{dip}(r) = -\nabla U(r) = -\frac{1}{2\epsilon_0 c}\mathrm{Re}(\alpha(\omega))\nabla I(r). \tag{2.14}$$

The power absorbed by the dipole from the laser field, and re-emitted as dipole radiation, is given by

$$P_{abs} = \langle \dot{\boldsymbol{p}} \cdot \boldsymbol{E}\rangle = \frac{\omega}{\epsilon_0 c}\mathrm{Im}(\alpha(\omega))I(r). \tag{2.15}$$

The absorption arises from the out-of-phase component of the dipole oscillation and can be thought of as absorption of photons from the light field followed by spontaneous emission. The scattering rate in this model is the ratio of the power scattered to the energy of a single photon,

$$\Gamma_{scatt}(r) = \frac{P_{abs}}{\hbar\omega} = \frac{1}{\hbar\epsilon_0 c}\mathrm{Im}(\alpha(\omega))I(r). \tag{2.16}$$

The dipole force and the scattering rate are the most important quantities when considering a dipole trap and are given here as functions of the atomic polarisability and the laser field intensity. These expressions are valid for near-resonant or far off-resonant fields, where the detuning ($\Delta = \omega - \omega_0$) is a significant fraction of the atomic transition frequency (ω_0). When far off-resonant fields are used the saturation, and therefore the scattering rate, is very low and the polarisability can be well approximated by a classical damped harmonic oscillator subject to a classical radiation field. The following expressions for the dipole potential and the scattering rate can then be obtained

$$U_{dip}(r) = -\frac{3\pi c^2}{2\omega_0^3}\left(\frac{\Gamma}{\omega_0 - \omega} + \frac{\Gamma}{\omega_0 + \omega}\right) I(r) \tag{2.17}$$

$$\Gamma_{scatt}(r) = \frac{3\pi c^2}{2\hbar\omega_0^3}\left(\frac{\omega}{\omega_0}\right)^3 \left(\frac{\Gamma}{\omega_0 - \omega} + \frac{\Gamma}{\omega_0 + \omega}\right)^2 I(r) \tag{2.18}$$

where ω_0 is the resonance frequency of the classical oscillator and Γ is the damping rate. The damping rate is determined by the dipole coupling of the ground and excited state and is given by

$$\Gamma = \frac{\omega_0^3}{3\pi\epsilon_0\hbar c^3}|\langle e|\boldsymbol{d}|g\rangle|^2. \tag{2.19}$$

In a red-detuned field ($\Delta < 0$) the dipole force acts to push particles towards regions of high intensity while in a blue detuned field ($\Delta > 0$) the force attracts atoms to regions of low intensity. Red-detuned traps are simpler to implement experimentally as it is easier to create three-dimensional field maxima, for example at the focus of a Gaussian beam or in a standing wave. In near-resonant optical fields, where $\Delta \ll \omega_0$, the second term in equations 2.17 and 2.18 can be neglected by applying the *rotating wave approximation.* The dipole potential then scales as $I(r)/\Delta$ and the scattering rate as $I(r)/\Delta^2$. Near-resonant, red-detuned dipole traps usually use large detunings and high intensities to minimise photon scattering which acts to heat the trapped atomic sample. While these traps are effective for atom trapping the detuning can switch sign for ground and excited states meaning that only certain states can be trapped.

2.5.2 Quasi-electrostatic trap

An alternative dipole trapping potential to a FORT can be formed using long wavelength light fields whose wavelengths differ by hundreds of nanometres from any atomic resonances. In this regime the rotating wave approximation does not hold as $\omega \ll \omega_0$ and both terms in equations 2.17 and 2.18 contribute equally. The dipole force and scattering rate then simplify to

$$U_{dip}(r) = -\frac{3\pi c^2}{\omega_0^3}\frac{\Gamma}{\omega_0} I(r) \tag{2.20}$$

$$\Gamma_{scatt}(r) = \frac{6\pi c^2}{\hbar\omega_0^3}\left(\frac{\omega}{\omega_0}\right)^3\left(\frac{\Gamma}{\omega_0}\right)^2 I(r). \tag{2.21}$$

This potential is a good approximation to the quasi-electrostatic trap (QUEST) [94] potential which is given by

$$U_{dip}(\boldsymbol{r}) = -\frac{1}{2}\alpha_{stat}|E(\boldsymbol{r})|^2 \tag{2.22}$$

where α_{stat} is the static polarizability of the atom. This trapping potential is very general and can be applied to any polarisable particle whether that be an atom, molecule or some mesoscopic particle. The spontaneous photon scattering rate in a quasi-electrostatic potential is very low and is on the order of 10^{-3} s^{-1} for a typical trap. The QUEST therefore represents a good approximation of a purely conservative trapping potential.

2.6 Laser cooling argon

So far in this chapter we have discussed laser cooling of a simple two-level atom. Real atoms have a more complex electronic structure which needs to be considered in cooling experiments. In order for an atom to be cooled effectively it must have a closed cycle of electronic transitions so that many photons are scattered. The most commonly cooled species are the alkali-metal atoms (Li, Na, K, Rb, Cs) as they all have a closed cycle of transitions from their ground states at optical and near-infrared wavelengths. Many of the wavelengths required can readily be produced in the laboratory using diode lasers. Cooling of alkali-metal atoms' is complicated somewhat by their hyperfine structure. The upper level of the atoms' cooling transition can decay to a hyperfine ground state that is not resonant with the cooling laser. This requires the use of *re-pumper* lasers which optically pump the atoms back to the lower level of the cooling transition.

Laser cooling of rare gas atoms differs from the cooling of alkali atoms. Ground state rare gas atoms have a closed shell of outer electrons and the nearest excited states are 8-20 eV away. Laser cooling from the ground state requires VUV photons which cannot be produced using current continuous wave laser technology. Instead, rare gas atoms are cooled from high-lying metastable states via near-infrared transitions.

2.6.1 Electronic structure of argon

Argon atoms are cooled from a high-lying metastable state. When in this excited state the outer shell of the argon atoms' core is unfilled and therefore possesses spin and orbital angular momentum. The electronic structure of the atom is then governed by the interaction of the core's spin and orbital angular momentum with the spin and orbital angular momentum of the valence electron. Although the LS coupling scheme, readily applicable to alkali atoms, describes some argon states well (e.g. the ground state) it breaks down for others. Instead, the $j\ell$ coupling scheme is used when the spin orbit interaction of the electrons in the atomic core is larger than the electrostatic interaction between the valence electron and the core electrons [95]. This scheme is applicable to the excited states of rare gas atoms as the mean distance of the valence electron from the core is large. In the $j\ell$ coupling scheme the spin S and orbital angular momentum L of the core are first coupled together to give the total angular momentum of the core $j = L + S$. The total angular momentum of the core is then coupled to the orbital angular momentum of the valence electron ℓ to give $K = j + \ell$ which is then coupled to the spin of the valence electron s to give the total angular momentum $J = K + s$. Argon does not have a nuclear spin and therefore has no hyperfine structure which simplifies its structure in comparison with other commonly cooled species (e.g. alkali atoms). The spectroscopic notation used in this thesis is $n\ell[K]_J$ where n is the principal quantum number of the valence electron.

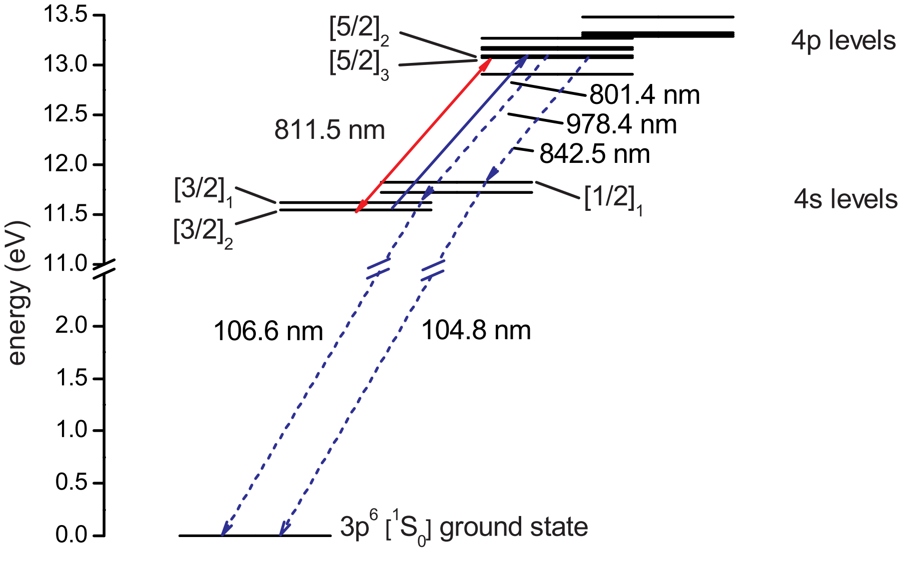

Figure 2.3: Grotrian energy level diagram showing the atomic states of argon important in our experiments. The red arrow shows the 811.53 nm laser cooling transition. The lower level of the cooling transition ($4s[3/2]_2$) is 11.5 eV above the ground state. The solid blue arrow shows the 801.48 nm quench transition used to return metastable atoms to their ground state. The dashed blue lines show the two possible decay routes to the ground state. The ionisation potential is not shown but is 15.8 eV for argon. All data for the levels were taken from the NIST atomic spectra database and the wavelengths given are for an atom in air [87].

Figure 2.3 shows the relevant argon energy level structure for the experiments presented in this thesis. The closed cycle 4s$[3/2]_2$ → 4p$[5/2]_3$ transition at 811.53 nm is used for laser cooling. As argon has no hyperfine structure this is the only laser wavelength required. Electric dipole transitions are forbidden from the 4s$[3/2]_2$ to the ground state, as well as other lower energy states, and it is metastable with a measured lifetime of 38 s [9]. Also shown in figure 2.3 is the 4s$[3/2]_2$ → 4p$[5/2]_2$ quench transition at 801.48 nm which is used to return metastable atoms to their ground state. Once in the 4p$[5/2]_2$ state the atoms can decay to the ground state via either the 4s$[1/2]_1$ state or the 4s$[3/2]_1$ state. The transition strengths for the three possible decay routes from the 4p$[5/2]_2$ state suggest that after three absorption cycles 98 % of a given atomic sample will be in the ground state.

Chapter 3

Construction of the Ar* MOT

This chapter details the design, construction and characterisation of a metastable argon (Ar*) MOT for use as an atomic source in molecular sympathetic cooling experiments. In this chapter the Ar* source, the vacuum system and the frequency-stabilised diode laser system used for cooling are described as well as characterisation measurements of the trapped atomic cloud.

3.1 Vacuum system

In atomic and molecular trapping experiments the background gas pressure is of critical importance as collisions between background gas atoms and those in the trap cause depletion of the trapped sample. This loss process limits the trap lifetime and can hinder experiments requiring long confinement times if the pressure is too high. It has already been mentioned in section 1.4 that thermalisation in molecular sympathetic cooling experiments is predicted to require timescales of a few seconds. In light of this our trap must have a long confinement time and requires a low background gas pressure, ideally in the ultra-high vacuum (UHV) regime ($< 10^{-9}$ mbar). The vacuum system described here was designed to satisfy these pressure requirements and incorporate all experimental elements required for sympathetic cooling experiments.

Figure 3.1 shows a schematic diagram of the vacuum system designed. There are three main chambers in the system which were pumped by four magnetically-levitated turbomolecular pumps (TMPs). The TMPs are backed by two Edwards XDS10 scroll pumps. At the source end of the system, argon gas was introduced via a 12 mm glass tube where the pressure is typically in the mid 10^{-2} mbar range. The reasons for operating at this pressure are explained in section 3.2. The glass tube was coupled to the first stainless steel vacuum chamber which was pumped by a 1000 ls^{-1} Edwards STP-1003 TMP. On exiting the glass tube the argon gas formed an effusive beam which was collimated by a skimmer before entering a second vacuum chamber. The skimmer was a stainless steel tube of outer diameter 12 mm, length 70 mm and thickness 2 mm. The end of the skimmer facing the exit of the glass tube was tapered down to a fine edge to minimise back scattering of atoms into the atomic beam. Most of the gas exiting the glass tube did not pass through the skimmer and was pumped out of the system in the first chamber. A mechanical shutter (see section 3.5.2) in front of the skimmer was used to block the atomic beam during experiments. The pressure in this chamber was measured using a magnetron gauge and was typically on the order of 10^{-5} mbar. The second vacuum chamber was pumped by 1000 ls^{-1} Shimadzu TMP-1003M which achieved pressures, measured with another magnetron gauge, on the order of 10^{-8} mbar. After passing through the second chamber the gas beam entered the 75 cm long Zeeman slower tube (see section 3.4.1) at the end of which there was another skimmer. The second skimmer had an inner diameter of 20 mm, was 40 mm long and was also tapered down to a fine edge facing the atomic beam. On the other side of the skimmer the atomic beam entered the science chamber where all experiments took place.

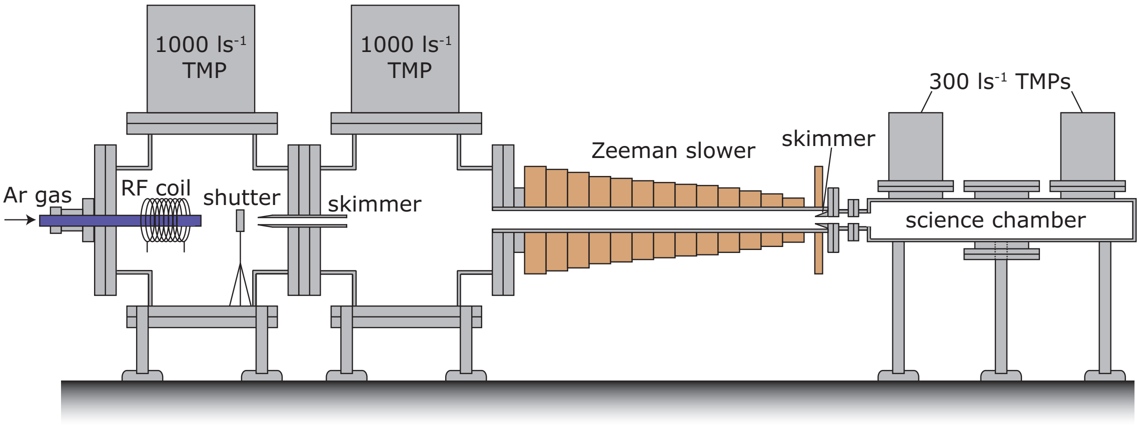

Figure 3.1: Schematic diagram of the vacuum system designed for Ar* MOT and sympathetic cooling experiments. The system is differentially pumped by four magnetically-levitated turbomolecular pumps. The pressure drops from 10^{-2} mbar in the glass tube where the Ar gas is introduced to to the low 10^{-8} mbar range in the science chamber when the experiment is running without the atomic beam shuttered.. The vacuum system was constructed from stainless steel and ConFlat (CF) flanges and copper gasket seals were used throughout.

3.1.1 Science chamber

The science chamber was carefully designed to facilitate sympathetic cooling experiments which require incorporation of the MOT, a high-finesse optical cavity, a molecular jet and the high intensity optical Stark deceleration laser pulses. Further access was required for pumping, pressure measurement, imaging, ion detection and optical cavity electronics among other things. Figure 3.2 shows a schematic of the science chamber and illustrates the principal port requirements for future sympathetic cooling experiments. The chamber is cylindrical with a radius of 28 cm and a height of 7 cm. The chamber was pumped by two 300 ls^{-1} TMPs, one Shimadzu TMP-303M and an Edwards STP-301. A high precision Edwards EBEAM (electron beam) ion gauge was used for pressure measurement. Before being connected to the rest of the vacuum system the science chamber was sealed off and pumped down to determine the base pressure of the chamber. After baking at 100 °C for 3 days a pressure of 1×10^{-9} mbar was measured. This study was carried out during initial set up of the experiment when only one TMP was mounted on the science chamber. The addition of the second TMP should enable pumping to a lower pressure but this has not yet been verified. For a typical operating pressure in the discharge of 5×10^{-2} mbar the pressure measured in the science chamber was 3×10^{-8} mbar with the atomic beam shutter open. Shuttering the atomic beam reduced the pressure in the science chamber from 3×10^{-8} mbar to 6×10^{-9} mbar.

3.2 Ar* source

In order to produce Ar*, we used a RF discharge based on a design developed for use in other rare gas, laser cooling experiments [96, 97]. This design has been measured to produce metastable fluxes of 4×10^{14} $\text{s}^{-1}\text{sr}^{-1}$. Figure 3.3 shows a schematic diagram of the discharge set-up. Research grade Ar gas was delivered to the glass tube (O.D. = 12 mm) via 1/4 inch copper pipe. A needle valve in the backing line was used to control the pressure in the glass tube which was measured with a Pirani gauge connected to the 1/4 inch copper pipe just before the connection to the glass tube. A bellows valve connected in parallel with the needle valve allowed pumping out of the backing line around the needle valve as the pump rate through the needle valve is slow. O-ring connectors were used to connect the glass tube to the copper pipe at one end and to the vacuum system at the other. The glass tube was pumped by the TMP mounted on the first stainless steel

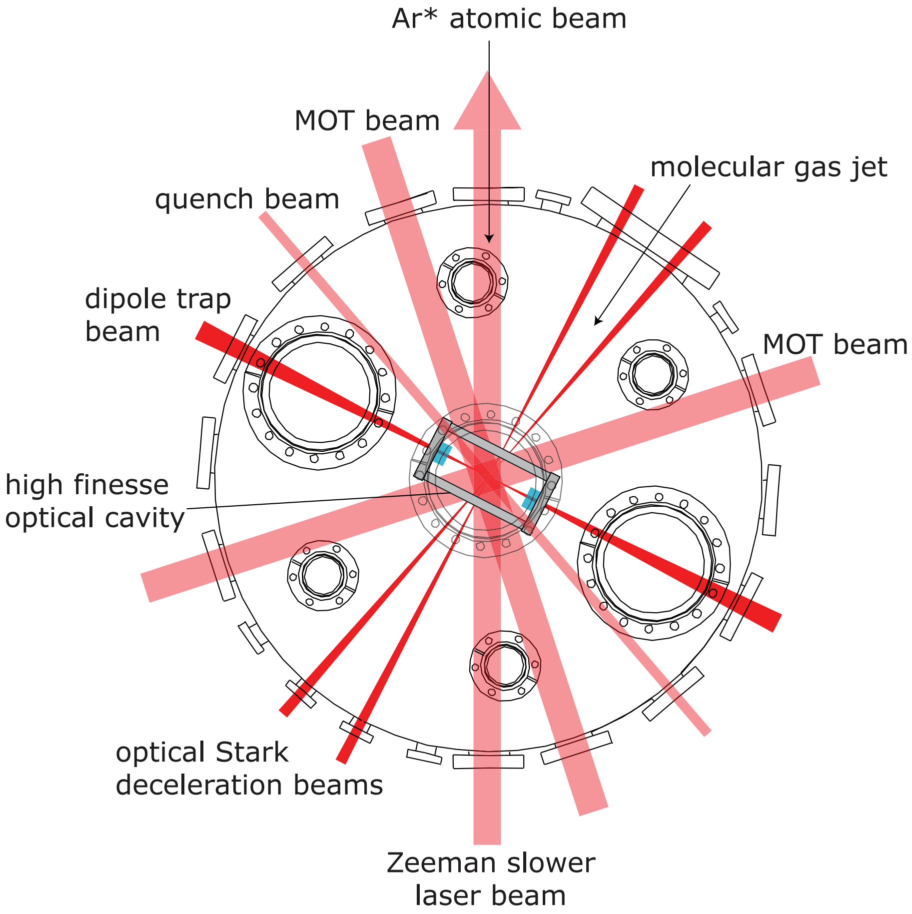

Figure 3.2: Schematic diagram of the science chamber designed to incorporate all experimental elements required for sympathetic cooling experiments. Laser beam access is required for the MOT (7 beams, 2 vertical), optical Stark deceleration (2 beams), quenching (1 beam) and optical dipole trap (1 beam). Access is also required for the Ar* atomic beam and the molecular jet. The unassigned ports in this diagram are used for detection, pumping, pressure measurement and electronic feedthroughs. The chamber was constructed from non-magnetic 316LN stainless steel.

vacuum chamber.

On entering the glass tube the Ar gas is excited by a coaxial resonator consisting of a helical coil encased in a cylindrical brass shield. The coil is wound from 1.6 mm diameter enameled copper wire, is 7 cm long, has 11 turns and a diameter of 3.2 cm. Figure 3.3 shows the complete dimensions of the resonator. An impedance matched circuit was used to drive between 5 W and 25 W of RF power at ≈ 155 MHz through the coil. The coil was mounted inside the vacuum system to optimise the Ar* production efficiency at the exit of the glass tube. The vacuum chamber also acts to shield the RF power radiated by the coil which can interfere with other laboratory equipment. Initial ignition of the discharge requires tuning of the impedance matching until the discharge glow extends into the glass tube outside the vacuum chamber. The discharge can be operated at pressures ranging

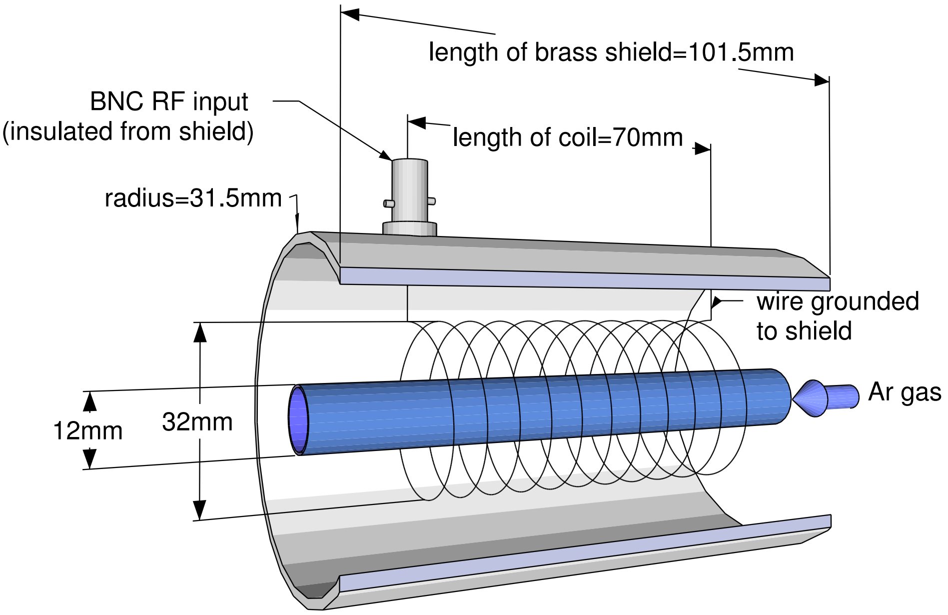

Figure 3.3: Schematic diagram of the RF discharge coil with part of the brass shield encasing the coil cut away. The coil has 11 turns and its dimensions are shown in the diagram. RF is delivered from an impedance matched circuit to the coil via the insulated BNC connection on the brass shield.

from a few mbar down to the 10^{-3} mbar range. During typical operation the discharge pressure is in the mid 10^{-2} mbar range. At this pressure the discharge is 35 cm long with the plasma extending 10 cm outside the vacuum chamber.

An external cavity diode laser (discussed in section 3.3) was used for spectroscopy of the metastable atoms in the discharge. The laser beam was passed through the discharge and its frequency was repetitively scanned around the laser cooling transition at 811.53 nm. The resultant absorption curves were determined using a photodiode. Figure 3.4 shows the efficiency of producing atoms in the desired metastable state, as well as the density of metastable atoms as a function of discharge pressure. The Ar* density was determined by analysing the absorption profiles using the Beer-Lambert law. The ratio of Ar* in the gas was then obtained by dividing the Ar* density by the total number density in the gas calculated from the measured pressure. It is clear that the production efficiency peaks at 1×10^{-2} mbar while the Ar* density plateaus at $1.2 \pm 0.2 \times 10^{18}$ m^{-3} above 3×10^{-2} mbar. We typically operated the discharge at $4 - 6 \times 10^{-2}$ mbar where the metastable production is constant and the discharge operates stably.

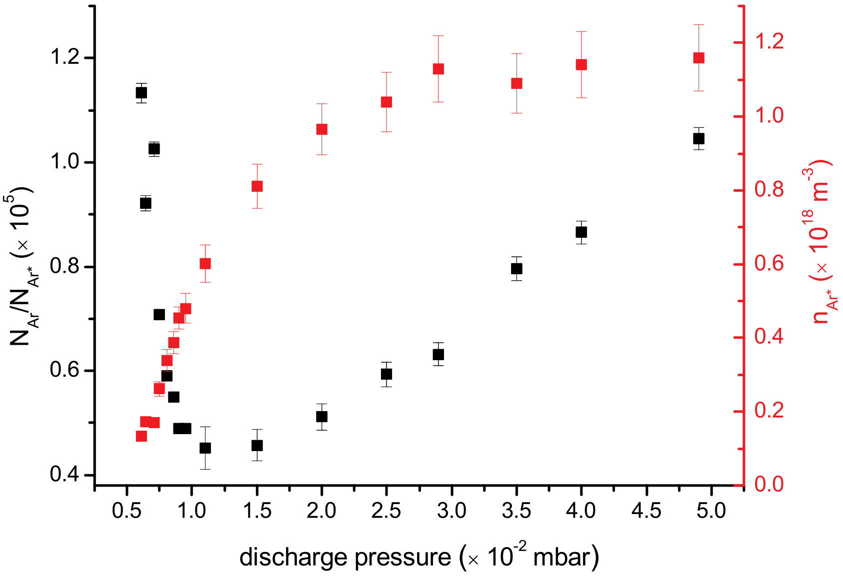

Figure 3.4: A plot of the fraction and overall density of metastable argon atoms as a function of pressure in a stable RF discharge.

3.3 Laser system

The laser system for a MOT is required to provide a narrow linewidth, frequency stable output with sufficient optical power. Our MOT laser system consisted of two diode lasers set up in a master-slave configuration. The master laser was frequency-stabilised to the 811.53 nm cooling transition but could not provide the power required. The slave laser produced the required optical power and was injection locked to the frequency of the master laser. The desired detunings for the MOT and Zeeman slower beams were achieved using acousto-optic modulators (AOMs). A third laser was constructed to quench the metastable atoms back to their ground state via the 801.48 nm quench transition shown in figure 2.3.

3.3.1 Master laser frequency stabilisation

Our master laser was a commercial Toptica DL 100 external-cavity diode laser (ECDL). ECDLs have a reflective diffraction grating to provide frequency selective feedback to the laser diode [98]. A piezoelectric transducer (PZT) is typically used to control the angle of the grating and can be used to tune the output frequency of the laser. ECDLs can be frequency-stabilised to an atomic or cavity resonance by producing a linear error signal which crosses zero voltage at the desired frequency reference. This signal is fed back, via a servo loop, to the voltage control of the PZT and can maintain the laser on resonance for a long period of time.

A common technique used to generate an error signal uses the dichroism induced in an atomic vapor when a magnetic field is applied. Methods based on dichroic atomic vapor laser lock (DAVLL[99]) rely on the dichroism of atomic gases when a magnetic field is applied which gives a differential absorption for σ^+ and σ^- polarized light. The magnetic field is applied along the same direction as the laser beam and splits the lower and upper levels of the resonant transition into their m_J Zeeman sublevels with σ^+ light optically pumping $\Delta m_J = +1$ transitions and σ^- light pumping $\Delta m_J =$ -1 transitions. The upper levels of the σ^+ transitions are Zeeman shifted up in frequency with respect to the lower levels while there is a net shift down in frequency for the σ^- transitions. Absorption profiles for σ^+ and σ^- light are therefore frequency shifted by equal and opposite amounts. Subtracting one from the other gives an error signal crossing zero at the unshifted resonant frequency of the transition ω_0. This error signal is fed back to the grating PZT in the ECDL via a servo loop. When the laser output frequency is on resonance the error signal feeds back 0 V to the PZT and the laser frequency remains at ω_0. If the laser frequency drifts away from resonance the magnitude of the error signal increases and a voltage is fed back to the PZT to force the laser frequency back towards ω_0. The error signal is linear around the zero crossing point and the voltage fed back to the PZT is proportional to the magnitude of the frequency drift.

We used a DAVLL based method to stabilise our ECDL to the 811.53 nm argon laser cooling transition shown in figure 2.3. Previous work on stabilizing lasers to noble gas atoms in discharges has used frequency/phase modulation techniques where the error signal is produced by obtaining the derivative of a spectroscopic signal using phase sensitive detection [100, 101, 102]. Although these methods produce a stable lock, DAVLL based techniques have the advantage they do not necessitate frequency/phase modulation or phase sensitive detection and require only a few simple optical elements and a servo controller.

In most experiments where magnetic dichroism has been used for laser locking the spectroscopic frequency reference has been derived from an atomic vapor and the applied magnetic field had no effect on the bulk behavior of the gas. In our work the magnetic field was applied to a plasma and through the Lorentz force this field affected the plasma behavior. DAVLL has been successfully applied to gallium atoms in an argon buffer plasma [103] where no effects of the magnetic field on the plasma were noted. We operated at over two orders of magnitude lower pressure than this case and observed, and studied, the effects of the magnetic field on the plasma.

Saturated absorption spectroscopy

We used saturated absorption spectroscopy to produce Doppler-free (DF) absorption profiles for our error signal. Figure 3.5 shows a typical saturated absorption spectroscopy curve which was obtained by aligning two counter-propagating beams, a pump and a probe beam, through the RF discharge and measuring the probe transmission on a photodiode. This signal was obtained with a homogeneous magnetic field of 2.6 Gauss applied to the plasma. The absorption profile shows the narrow DF peak at the centre of the much broader Doppler-broadened lineshape. The peak absorption, at the bottom of the Doppler profile, is 27% while the absorption contrast between the DF peak and the Doppler profile is 21%.

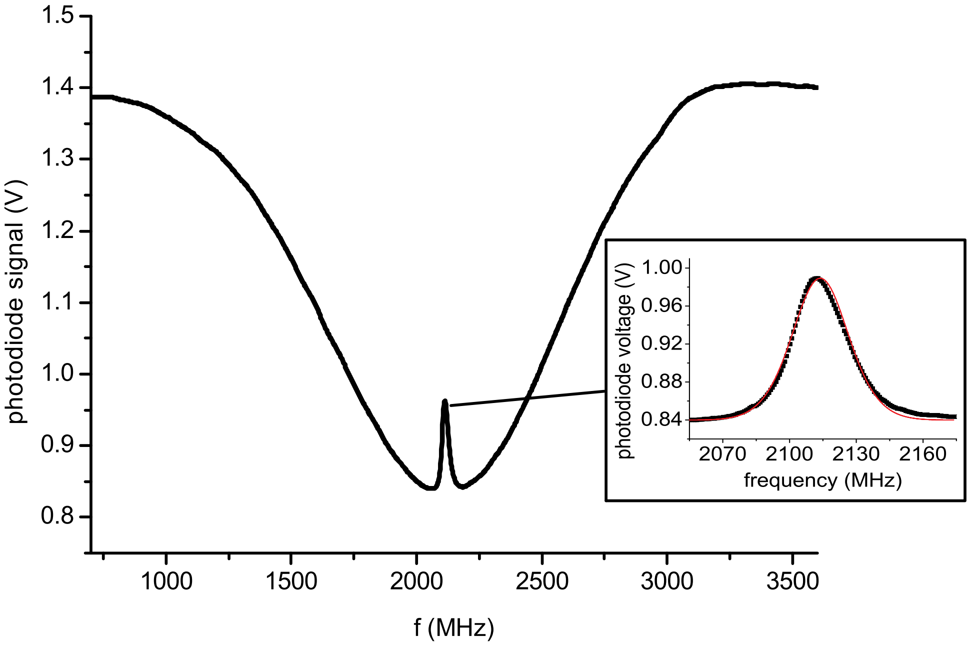

Figure 3.5: Saturation absorption spectroscopy signal showing full Doppler-broadened absorption profile with a Doppler-free peak at the centre of the lineshape. This signal was obtained with a homogeneous magnetic field of 2.6 Gauss applied to the plasma. The width of the Doppler-free peak is $\Delta\nu_{\mathrm{FWHM}} = 28$ MHz and the plot inset shows a Voigt profile fit to the observed profile. The observed width is larger than the natural linewidth $\Gamma = 5.87$ MHz of the transition due laser frequency fluctuations, Zeeman broadening, power broadening and pressure broadening. The contribution of these broadening mechanisms is discussed further in the text. The frequency calibration was obtained using a Fabry-Perot etalon with a free spectral range of 2 GHz.

The DF peak was measured to have a width of $\Delta\nu_{FWHM} = 26$ MHz, considerably broader than the natural linewidth of the transition ($\Gamma = 5.87$ MHz). The observed broadening was partially due to the unequal Zeeman shifts for the different $\Delta m_J = \pm 1$ transitions. The lower level of the $4s[3/2]_2 \rightarrow 4p[5/2]_3$ has five Zeeman sublevels ($m_J = 0, \pm 1, \pm 2$) and the upper level has seven ($m_J = 0, \pm 1, \pm 2, \pm 3$). There are five $\Delta m_J = +1$ transitions between the ground and excited sublevels and five $\Delta m_J = -1$ transitions. The applied magnetic field shifts the energy of the sublevels by different amounts ($\Delta E_B \propto B m_J$) and the frequencies of the different $\Delta m_J = \pm 1$ transitions are shifted by unequal amounts. For example, the $m_J = 2 \rightarrow 3$ transition was shifted by 4.5 MHz while the $m_J = -2 \rightarrow -1$ transition was shifted by 6.1 MHz. The probe intensity ($I = 4$ mWcm^{-2}) also contributed to the observed width as we operated above the saturation intensity of the transition ($I_S = 1.44$ mWcm^{-2}). This gave power broadening of 11 MHz. Pressure broadening constants measured in other work for nearby argon transitions indicate that at our operating pressure the lineshape would be broadened on the order of a few MHz [104]. The remaining broadening (approximately 10 MHz) was a result of frequency jitter in the probe beam caused by mechanical resonances driven by turbomolecular pumps on our vacuum system. Figure 3.6 shows a fast Fourier transform of the laser frequency fluctuations which shows that the two main mechanical resonances were much faster (1.4 kHz and 2.2 kHz) than our scan time (31 Hz). As a result of this the frequency jitter is averaged over the duration of the scan and acted to broaden the observed DF peak.

Error signal generation

Figure 3.7 shows the experimental set-up used to generate our error signal. The magnetic field required was produced by a pair of Helmholtz coils mounted on either side of the discharge tube. The coils had 17 turns of 14 gauge copper wire, a radius of 26 mm and required currents of less than 1 A to generate the required fields. The pump and probe beams used to produce the saturated absorption signals were aligned through the centre of the Helmholtz coils just outside the vacuum chamber approximately 10 cm from the edge of the RF coil. The probe beam was linearly polarized which is equivalent to an equal combination of σ^+ and σ^- polarizations. After passing through the discharge tube the probe passed through a quarter-wave plate which converted the σ^+ and σ^- polarizations to two orthogonal linear polarizations which were then separated using a polarizing beam splitter and aligned onto two separate photodiodes. The applied magnetic field shifts the

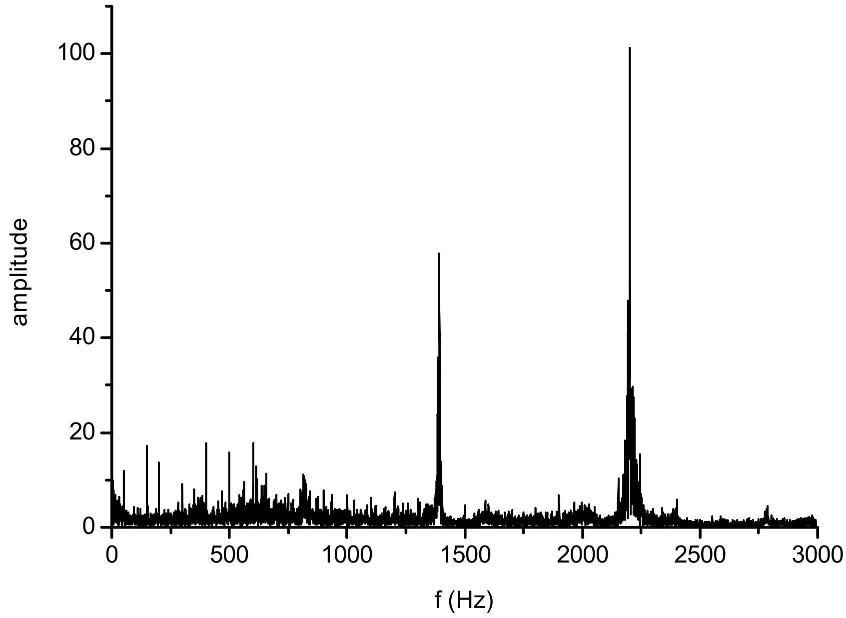

Figure 3.6: Fast Fourier transform (FFT) of the error signal frequency fluctuations. The two main mechanical resonances were at 1.4 kHz and 2.2 kHz and were driven by the turbo molecular pumps. The sampling time of the FFT was 1.67×10^{-4} s and the data analysed were acquired over 10.67 s.

DF peaks by equal amounts in opposite directions and subtracting the two absorption profiles with a servo controller (New Focus LB1005 Servo Controller) produces the error signal shown in figure 3.8. This signal was generated with an applied magnetic field of 2.6 Gauss which Zeeman shifted the centre of the observed DF peaks by ± 5.3 MHz.

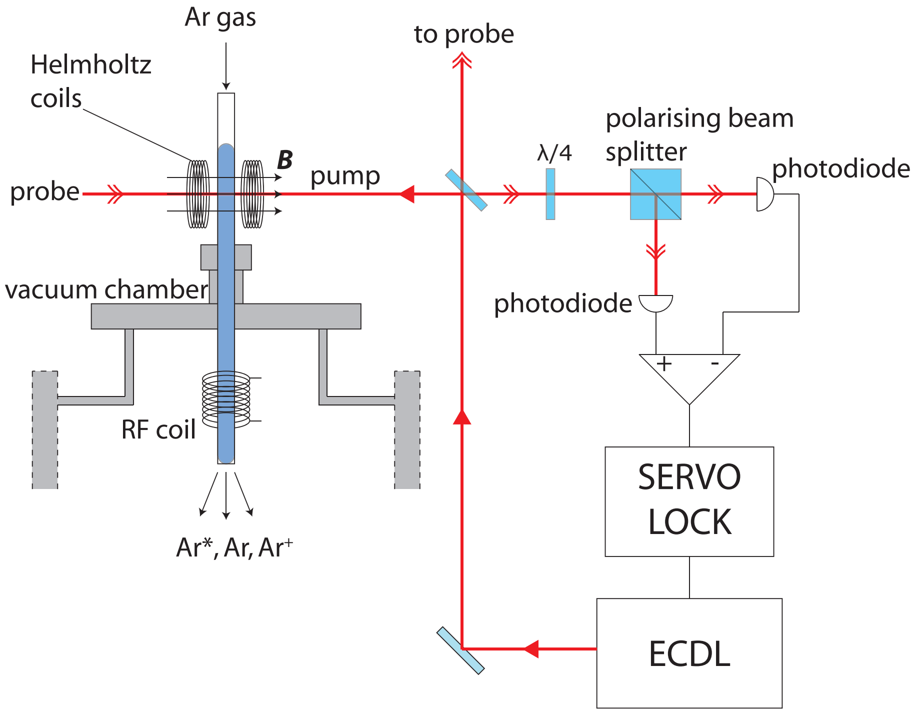

Figure 3.7: Schematic diagram of experimental set-up to stabilise the master ECDL to Ar* atoms in the RF discharge.

The error signal generated is fed back by a servo controller to the voltage controlling the diffraction grating PZT and keeps the ECDL laser frequency on resonance when locked. Locking to a DF peak is more precise than locking to a Doppler-broadened absorption profile at the cost of a reduced locking range [105, 106]: the error signal shown in figure 3.8 gives a locking range of 20 MHz. In the half hour after switching on the laser and discharge equipment the lock point drifts by approximately 2.5 MHz due to a change in the birefringence of the glass tube as its temperature rises from 21.0 °C to 23.1 °C.

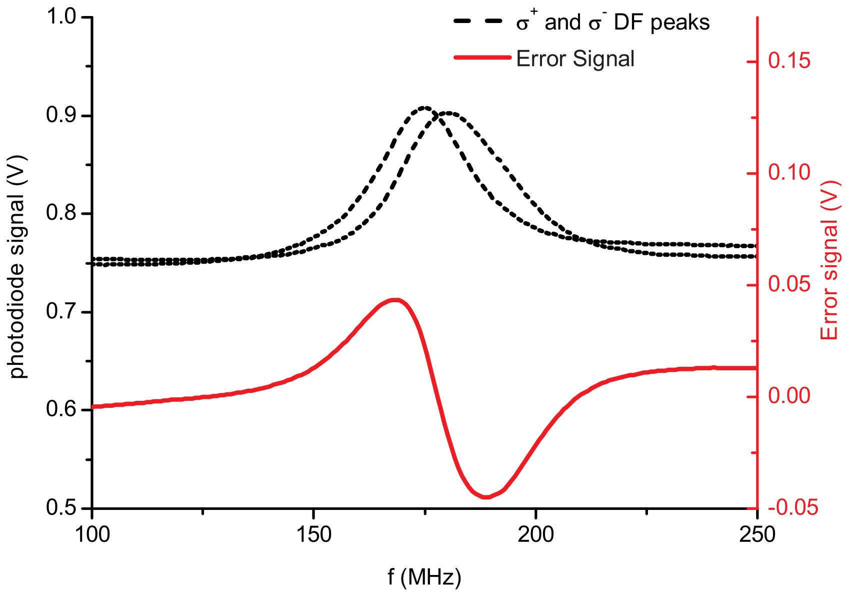

Figure 3.8: Oscilloscope signals of the shifted σ^+ and σ^- absorption profiles (dashed line) and the error signal (solid red line) produced by subtracting the σ^+ absorption profile from σ^-. The magnetic field applied to generate this signal was 2.6 Gauss and the pressure in the discharge was 5.2×10^{-2} mbar.

Frequency stability characterisation

The stability of the lock, after the glass temperature had stabilised, was measured by analyzing frequency fluctuations of the locked laser to determine the square root Allan variance (SRAV) [107]. The frequency fluctuation data were determined from the error signal fluctuations when the laser was locked. The error signal amplitude was converted to frequency using a calibration obtained with a Fabry-Perot etalon (free spectral range = 2 GHz). The SRAV $\sigma_y(\tau)$ was then be determined for different averaging times τ from

$$\sigma_y(\tau) = \left[\frac{1}{2(2N+1)} \sum_{k=1}^{N-1} (\bar{y}_{k+1} - \bar{y}_k)^2 \right]^{1/2} \tag{3.1}$$

where $\bar{y}_k$ is kth the fractional frequency (i.e. the measured average frequency $\bar{\nu}_k$ divided by the nominal frequency of the laser ν_0) averaged over a time τ and N is the number of data points. Figure 3.9 shows the SRAV as a function of averaging time over the range 10^{-4}-10^1 s. The features observed in the SRAV spectrum at $\tau < 10^{-2}$ s are due to mechanical resonances which drive oscillations in the error signal. At longer τ ($> 10^{-1}$ s) these fast oscillations are averaged out and the SRAV drops to 1.8×10^{-10}. Considering the nominal frequency of the laser is $\nu_0 = 370$ THz the laser stability is 3.2 MHz at $\tau = 3 \times 10^{-4}$ s and 129 kHz at $\tau = 1$ s. With this stability the laser remains locked over the course of a typical day operating the MOT. The long term stability compares with previous DF DAVLL schemes applied to Rb atoms in an atomic vapor where frequency instabilities of 200 kHz [105] and 120 kHz [106] were quoted. Although these locking characteristics are suitable for our laser cooling experiments for other applications the frequency fluctuations due to the mechanical resonances could be suppressed by mechanical damping/isolation of the vacuum pumps or the laser, or feedback to the laser diode current which can respond much faster than the PZT.

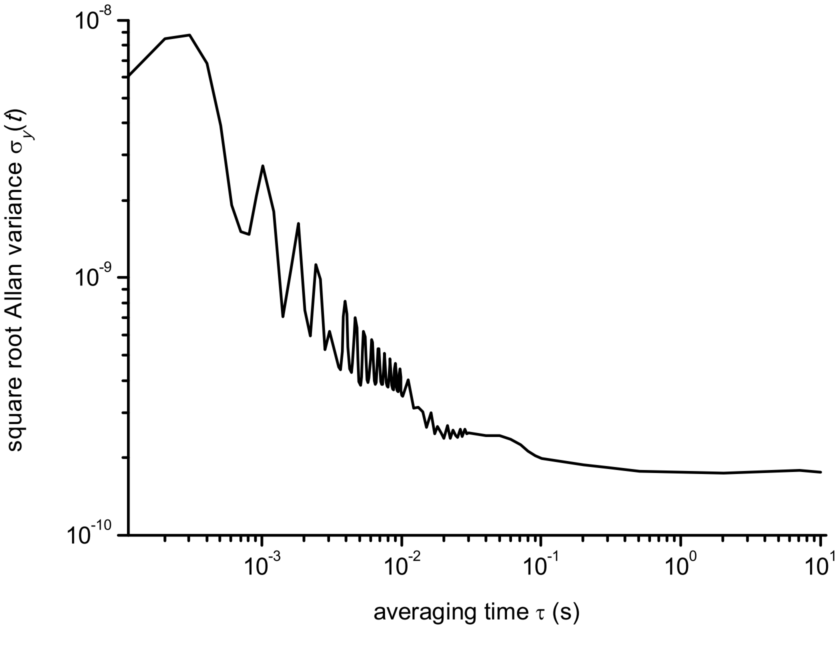

Figure 3.9: The square root Allan variance $\sigma_y(t)$ as a function of averaging time τ. The data analysed were acquired at a sampling rate of 10^4 s^{-1} over a time of 6000 s. The acquisition period began 1 hour after equipment had been switched on.

Pressure and magnetic field effects on lock

The pressure in the discharge has an effect on the error signal and locking through changing the depth of the absorption profiles. This effect was investigated between the pressures of 4×10^{-2} mbar and 2×10^{-1} mbar. Although tuning the discharge pressure lead to variations in both the slope (± 30%) and amplitude (± 10%) of the error signal the lock point was shifted by less than 1 MHz. There were two contributions to this frequency shift. The first was due to a mismatch in the absorption depths of the σ^+ and σ^- DF peaks caused by alignment imperfections. As the pressure in the discharge changed the absorption depth of the DF peaks did not increase/decrease by the same amount and the zero point of the error signal was shifted. The other contributing factor was the change in heat load on the glass tube at different pressures which caused a change in the tube's birefringence. A frequency shift of 1 MHz did not have a deleterious effect in our experiment as laser cooling is effective over a frequency range spanning several natural linewidths ($\Gamma = 5.87$ MHz for the Ar* cooling transition). However, the lock point shift could be compensated by adding a voltage offset to the error signal fed back to the PZT or by adjusting the angle of the quarter-wave plate.

As mentioned earlier, the applied magnetic field had an effect on the behaviour of the plasma through the Lorentz force. We observed the effects of the magnetic field on both the bulk behaviour of the plasma and our spectroscopic signals. The applied field reduced the length of the plasma in the glass tube but for all applied magnetic fields there was always a discharge inside the Helmholtz coils. The applied magnetic field also affected the metastable density in the probe region and the absorption of the beam was observed to increase from 27% to 36% as the field was increased from 0 to 10 Gauss. At low pressures ($< 10^{-2}$ mbar) the ions and electrons in the plasma are deflected onto the walls of the glass tube producing a glow on the glass. At these pressures the mean free path of the charged particles was approximately equal to the diameter of the glass tube and they collided with the glass walls before colliding with other gas atoms. The laser could still be locked under these conditions.

The slope of the error signal could be adjusted by tuning the magnetic field strength. We measured the steepest slope at an applied magnetic field strength of 4 Gauss which produced a corresponding locking range of just under 20 MHz. Although the strongest lock will be achieved with the steepest slope, figure 3.10 shows that this method produced a linear slope to which the laser could be locked over a range of magnetic fields up to about 6 Gauss. As the magnetic field is increased beyond this range strong Zeeman effects became important and lead to spectrally resolvable frequency shifts between different $\Delta m_J = +1$ and $\Delta m_J = -1$ transitions which severely distorted the error signal as shown for an applied field of 39.2 Gauss in figure 3.10).

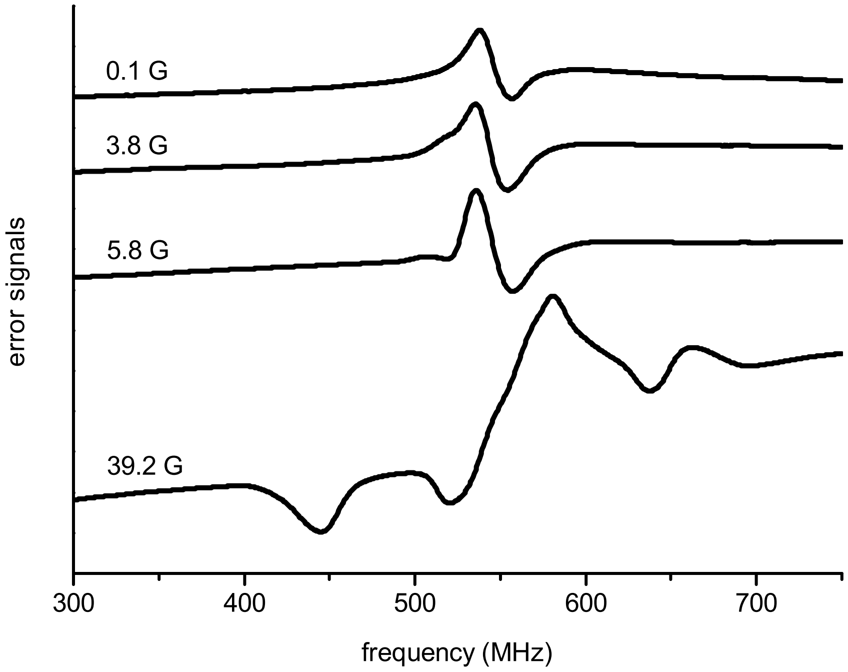

Figure 3.10: The shape of the error signal at different magnetic field strengths, including a heavily distorted signal at 39.2 G.

3.3.2 Injection locked slave laser

The output of the frequency-stabilised ECDL did not provide sufficient laser power for all the beams required for the MOT. In order to increase the optical power available, we injection locked a second, higher power diode laser to the ECDL in a master-slave set-up. The slave laser was a temperature stabilised, free-running diode laser. The laser consisted of a commercial diode (Sanyo DL-8141-035A) mounted in a custom-built mechanical mount. The portion of the master laser output that was not used for frequency stabilisation was seeded into the slave to injection lock its frequency to that of the master [108]. Figure 3.11 shows the optical set-up for injection locking the slave. Before being injected into the slave the master beam was aligned in double-pass through an 80 MHz AOM and shifted by -160 MHz from resonance to obtain the frequency required for the Zeeman slower laser beam (see 3.4.1). The beam was then expanded to match the size of the slave output before being aligned through the side port of an optical isolator and injected into the slave diode. The power injected into the slave diode was 6 mW. During initial alignment the slave output was aligned into a wavemeter (WavePro 7300) and the diode temperature and current were tuned to set the wavelength to 811.53 nm.

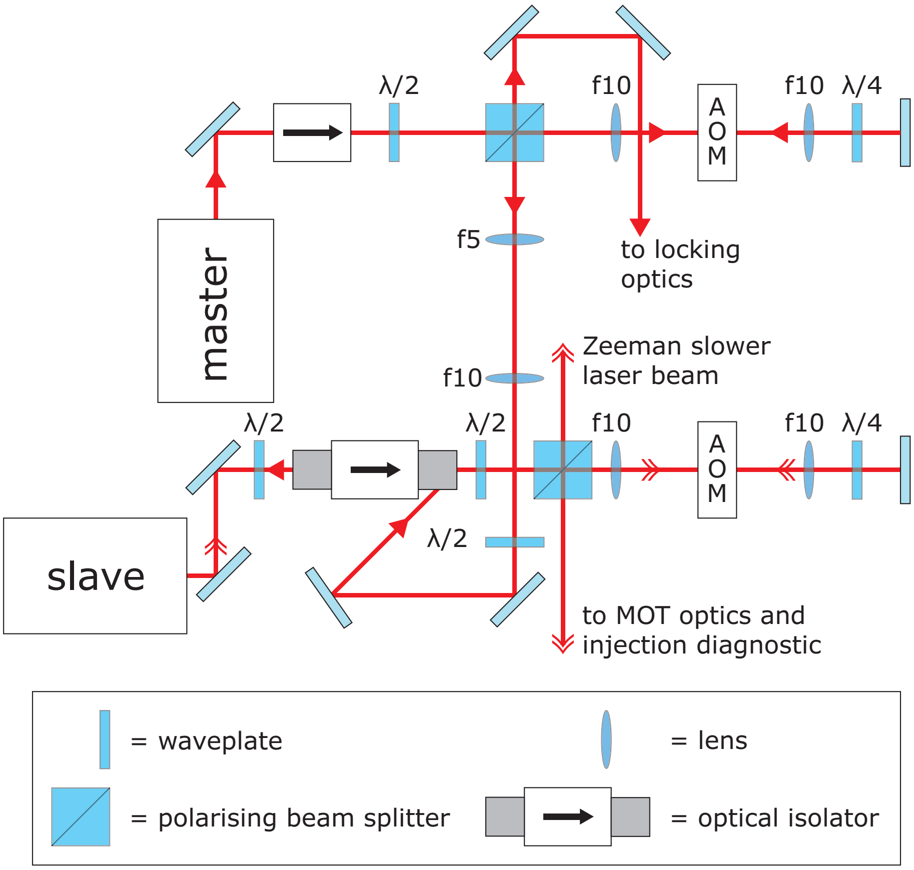

Figure 3.11: Optical set-up for injection locking the slave laser to the master. The diagram also shows the two AOMs used to generate the frequencies required for the MOT and Zeeman slower laser beams.

A portion of the slave output was aligned through the discharge cell and onto a photodiode as an injection diagnostic. By locking the frequency of the master laser and adding a current modulation to the slave laser diode current the absorption signal shown in figure 3.12 was observed which is characteristic of injection locking. The output from the slave was split into two beams, one for the Zeeman slower and one for the MOT. The frequency of the slave was as required for the Zeeman slower beam but not the MOT and the beam for the MOT was double-passed through another AOM. The beam was shifted back towards resonance and the detuning from resonance Δ was set by this AOM according to $\Delta = -160 + 2f$, where f is the frequency shift applied by the AOM in single pass. The frequency shift applied by the AOMs was controlled by tuning the voltage applied to the voltage controlled oscillators (VCOs) (Mini-Circuits ZX95-100-S+) which provided the RF frequency to the AOMs.

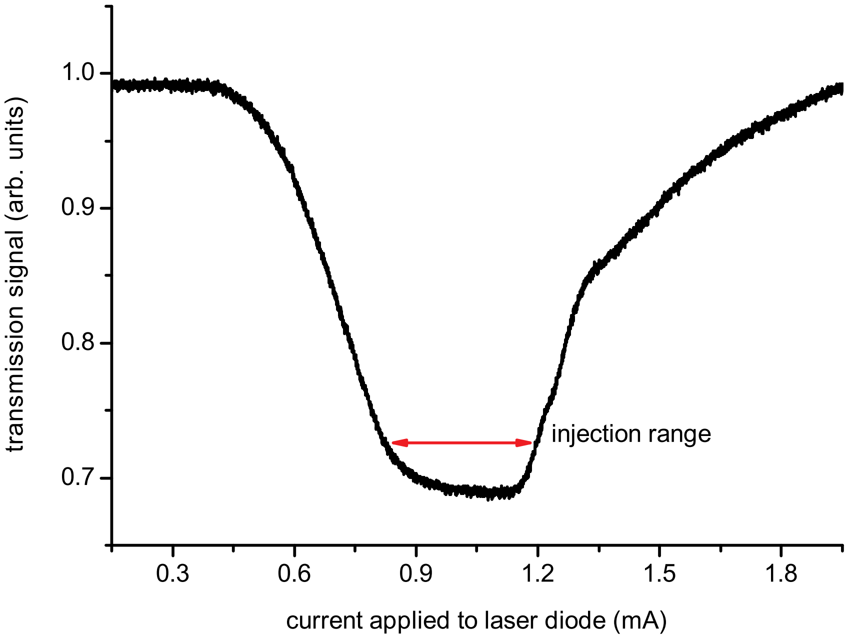

Figure 3.12: Characteristic absorption signal of the slave laser injection locking diagnostic. The absorption occurs when the frequency of the slave is dragged to match that of the frequency-stabilised master laser i.e. onto resonance. The plateau at the bottom of the absorption curve is the current region where the injection locking is stable and is called the *injection range*. The current applied was a modulation added to the offset current ($\approx$ 240 mA).

3.3.3 Quench laser

The quench laser was also a temperature stabilised, free-running diode laser. A free-running diode laser was suitable as a narrow linewidth was not required. In fact, a broader linewidth laser was actually useful in reducing the sensitivity of the quenching to laser frequency drifts. The sensitivity to frequency drifts was also reduced by power broadening due to the high laser power ($>$ 100 mW). The quench laser consisted of a commercial diode (Sanyo DL-8141-002) housed in a mount identical to that built for the slave laser. The output frequency was controlled by tuning the diode temperature and current. During initial set up of the laser the output was aligned into the wavemeter and tuned to the 801.48 nm quench transition.

3.4 Magnetic fields

As well as the quadrupole magnetic field required for the MOT, further magnetic field coils were needed for a Zeeman slower and to cancel out background fields in the MOT region. This section describes the design and construction of these three sets of magnetic field coils.

3.4.1 Zeeman slower

In section 3.2 the RF discharge used to populate the desired argon metastable state for laser cooling was described. On leaving the discharge tube the argon formed an effusive beam with a thermal velocity distribution. Only a small fraction of the atoms in this beam had velocities within the capture velocity of the MOT ($v_c \approx 60$ ms^{-1} for Ar* with typical MOT parameters). Assuming a room temperature Ar* beam, less than 0.5% of the atoms passing through the MOT would have been trapped. To improve this fraction we slowed the atoms before they reached the MOT region using the Zeeman slowing technique [109]. This is a Doppler cooling method which uses a spatially varying magnetic field to keep the atoms on resonance with a counter-propagating laser beam. Without the slower, the atoms would detune from resonance as their velocity decreased and deceleration would cease. To achieve constant slowing along the length of a Zeeman slower the magnetic field profile must follow

$$B(z) = B_0 \pm B_1\sqrt{1 - z/z_0} \tag{3.2}$$

where B_0 is a constant bias field, B_1 is the magnitude of the spatially varying field and z_0 is the length of the solenoid. The sign of the $\pm$ is dependent on the polarisation of the slowing laser and is positive for σ^+ light and negative for σ^- light. The quantisation axis is defined along the direction of the atoms' velocity and the polarisations are reversed with respect to the laser wave vector $\boldsymbol{k}$. In a σ^+ slower the B-field decreases along the atoms' trajectory while in a σ^- slower the B-field increases. We chose to design a σ^+ slower where the field decreased to zero and then reversed. The change in polarity of the B-field gives a non-zero field at the end of the slower and the atoms were quickly detuned from the slowing laser as they exited. The maximum field required was also reduced by using this design which eased the solenoid's power requirements.

The length of the slower is governed by the deceleration of the atoms which, from equation 2.2, is given by

$$a = \frac{\hbar k \Gamma}{2m}\frac{s_0}{1 + s_0 + (2\Delta/\Gamma)^2}. \tag{3.3}$$

The detuning of the laser with respect to the atomic transition is given by $\Delta = (\omega_{laser} - \omega_0) - \mu' B(z)/\hbar + kv$. In a Zeeman slower the magnetic field is designed to keep the laser on resonance (i.e. $\Delta = 0$) and at high intensities the acceleration then saturates to a maximum of

$$a_{max} = \frac{\hbar k \Gamma}{2m}. \tag{3.4}$$

When designing a Zeeman slower it is sensible to assume that only some fraction η of a_{max} will be achievable due to imperfections in the B-field profile. The length of slower required to decelerate an atom from an initial velocity v_i to a final velocity v_f is then given by Newton's laws of motion as

$$z_0 = m\frac{v_f^2 - v_i^2}{\eta \hbar k \Gamma} \tag{3.5}$$

We assumed $\eta = 0.5$ which gave a z_0 of 67 cm for an Ar* atom with an initial velocity of 390 ms^{-1} (the peak of Maxwell-Boltzmann at room temperature) slowed to 40 ms^{-1}. There are a variety of designs which have been implemented in Zeeman slowers: almost all use electromagnets although slowing with a permanent magnet slower has also been demonstrated [110].

We opted to design a multi-section tapered solenoid to allow tuning and optimisation of the B-field profile after construction. It is important to consider that the Zeeman slower laser beam must pass directly through the MOT and select a large detuning such that the beam does not perturb the trapped atoms. We choose a detuning of $\Delta = -160$ MHz $\approx -27\Gamma$ which is easily achieved using an 80 MHz AOM as discussed in section 3.3. The slower was designed using a computer model which calculated the B profile generated by a user-defined slower using the Biot-Savart law for a single loop (see appendix A in reference [111]). The input parameters which defined the slower were the inner diameter of coil, wire dimensions, positions of coil sections, number of turns in each coil section and the current passing through each coil. The model summed the contribution from each individual loop at every z position along the length of the slower. The position of each loop was determined by the wire dimensions and 5 mm spaces were included between the coil sections to accommodate coil formers during construction. The field produced by the model was fitted to the desired B profile, given by equation 3.2, by varying the number of coil sections, the positions of the sections, the number of loops in each section and the current through the coils. The optimum design consisted of 14 coils driven by 4 power supplies and yielded a rms deviation of 3.7 Gauss between the modeled and desired fields.

Construction of the slower was relatively straightforward. The vacuum tube was mounted on a rod about which it was free to rotate and each coil was wound between two 5 mm thick formers. The first and last coils were wound with 1 mm diameter enameled copper wire while 4 mm × 2 mm flat enameled copper wire was used for the other coils. A Gaussmeter was used to measure and optimise the B-field profile produced by the slower. Figure 3.13 shows the modeled, measured and desired B profiles. The rms deviation between the measured and desired $B(z)$ was calculated to be 7.4 Gauss. The Zeeman slower was water-cooled by pumping water through a jacket in the vacuum tube design.

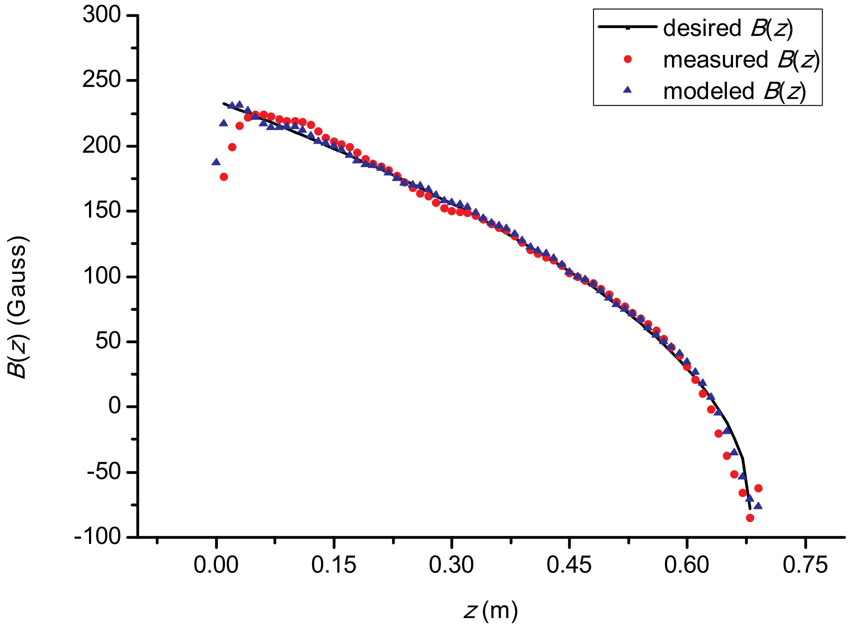

Figure 3.13: The measured magnetic field produced by the Zeeman slower compared with the ideal field and that calculated in the design model.

3.4.2 MOT coils

The quadrupole magnetic field for the MOT was generated by a pair of 94 turn coils set up in anti-Helmholtz configuration. The coils had a radius of 7.6 cm and produced a B-field gradient in the MOT region of 10 Gcm^{-1} with a current of 7 A passing through them. A modified version of the computer model used to design the Zeeman slower was used to determine the number of turns required. The coils were wound from 1 mm enameled copper wire on to water-cooled copper formers which were then attached to the viewports on the top and bottom of the science chamber. A MOSFET solid state relay (Power IO HDD-06V75), connected between the power supply and the MOT coils, was used for fast switching of the MOT magnetic field during experiments.

3.4.3 Compensation coils

Another set of magnetic field coils was required to nullify stray magnetic fields in the trapping region. Stray fields can shift the position of the magnetic zero and cause problems during experiments. The dimensions of these coils had to be quite large such that they could be mounted around the science chamber. The coils were designed using a modification of the Zeeman slower design model where the field was calculated for a square loop rather than a circular loop (see appendix A in reference [111]). The coils were wound from 15-way ribbon cable onto a cubic frame with a width of 29 cm. Three pairs of compensation coils were wound to address stray fields along each axis. The background fields in the MOT region could be nullified by driving currents on the order of 1 A through the compensation coils.

3.5 Shutters, detection and experimental control

3.5.1 Laser beam shutters

Switching of laser beams in experiments was achieved using both acousto-optic and mechanical shutters. Beams which passed through AOMs were switched by switching the RF power supply to the AOM. This was achieved using a commercial RF switch (Mini-Circuits ZX80-DR230-S+) connected between the VCO and the RF amplifier which supplied the RF power to the AOM. The switch was triggered by a 5 V input signal and could achieve sub-μs switching times.

AOMs could have been installed to switch other beams as well but this would have been an expensive solution. Instead we used a mechanical shutter constructed in-house from defunct hard disk drives according to an established design [112]. These shutters were constructed by attaching a razor blade to the read/write arm in the hard disk drive and driving the voice-coil actuator which controlled the motion of the arm. The circuit used to drive the shutter is detailed in reference [113] and accepts TTL level trigger pulses.

The performance of the shutter was tested using a He:Ne laser focused with a $f = 10$ cm lens. The transmission of the beam was monitored as the shutter interrupted it at its focus. Figure 3.14 shows the extinction of the beam. Switching from $90-10\%$ transmission was achieved in 400 μs. Faster switching times have been achieved using this design but as this was fast enough for our puposes no attempt was made to optimise this performance.

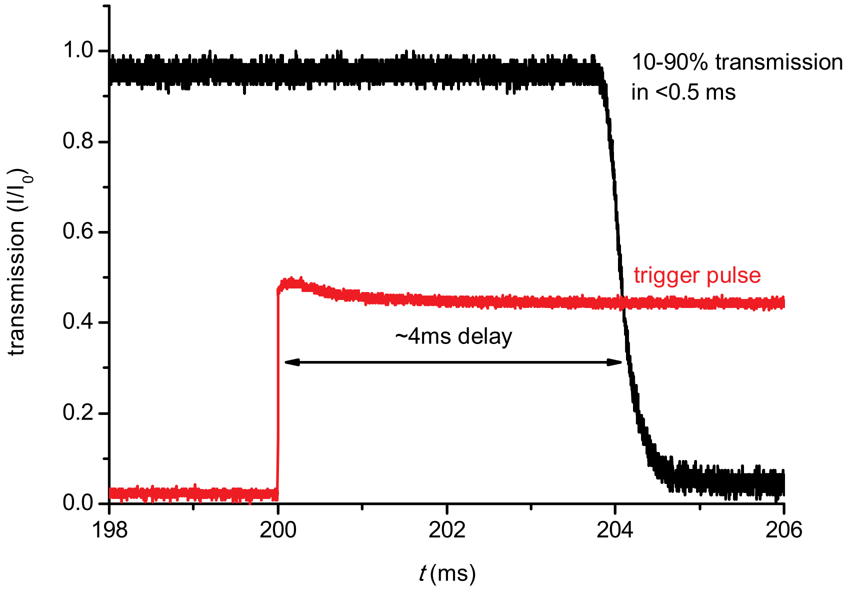

Figure 3.14: The extinction of a focused He:Ne laser beam by a mechanical shutter constructed from a defunct hard disk drive.

3.5.2 Atomic beam shutter

The mechanical shutter design was also used to construct the atomic beam shutter, shown mounted in the vacuum system in figure 3.1. A custom-built mount was designed such that the shutter could be secured at the bottom of the vacuum chamber. The razor blade used in the laser shutter design was replaced by a 25 mm × 25 mm thin aluminum shutter flag. The shutter was positioned in front of the skimmer separating the first two chambers at the RF discharge end of the vacuum system. When closed the shutter blocked the atomic beam from passing through the skimmer and entering the rest of the vacuum system. Shuttering the atomic beam reduced the pressure in the science chamber from 3×10^{-8} mbar to 6×10^{-9} mbar when the pressure in the discharge was 5×10^{-2} mbar. It was not possible to measure the timescale of the pressure drop, as it appeared almost instant on the ion gauge controller. However, a lower limit of 10 ms can be estimated by considering the velocity distribution of the beam. The shuttering of the beam could be monitored in the science chamber by detecting the ions in the beam using a micro-channel plate (MCP, described in section 3.5.4). Figure 3.15 shows the shutter trigger signal and the MCP signal as the beam is shuttered. The atomic beam ion signal is shuttered 5 ms after the trigger signal is sent to the shutter. The beam does not remain shuttered though and after 25 ms is unblocked again for 35 ms as the shutter bounces when it is closed. This shutter delay was taken into account when shuttering the atomic beam during experiments.

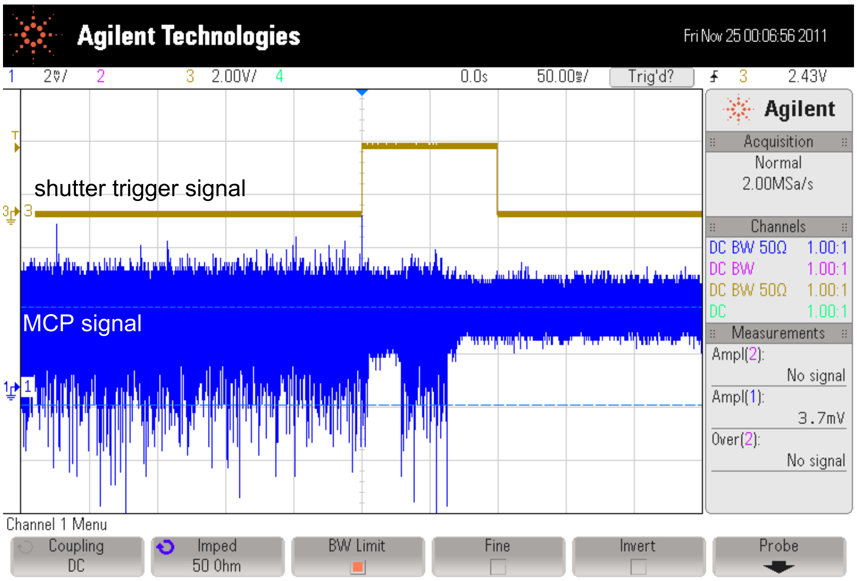

Acquisition
Normal
2.00MSa/s

Channels
DC BW 50Ω 1.00:1
DC BW 1.00:1
DC BW 50Ω 1.00:1
DC 1.00:1

Measurements
Ampl(2): No signal
Ampl(1): 3.7mV
Over(2): No signal

Coupling DC
Imped 50 Ohm
BW Limit
Fine
Invert

Figure 3.15: Screen grab from an oscilloscope showing the trigger signal for the atomic beam shutter and the ion signal recorded on an MCP in the science chamber as the shutter is closed. The shutter bounced when it closed causing the beam to be shuttered briefly before reopening for 35 ms and then being shuttered permanently.

3.5.3 Imaging

Imaging measurements were acquired using different CMOS and CCD cameras. Simple diagnostic and monitoring images were obtained using a Thorlabs DCC1645C CMOS camera or a triggerable Thorlabs DCU223C CCD camera. Sensitive imaging measurements were acquired using a thermo-electrically cooled Andor iXon$^{\mathrm{EM}}$+ electron multiplying CCD camera. A Computar MLH-10X zoom lens was used for imaging at the centre of the science chamber.

3.5.4 Ion detection

As argon atoms in their metastable state are close in energy to the ionisation potential (4.2 eV) they can be detected by ionisation using pulsed lasers. An El-Mul micro-channel plate (MCP) detector was used to measure the ion signal produced. A large negative voltage was applied to the MCP and it attracted positive ions onto its surface. Upon impact the ions trigger an avalanche of electrons in the carbon tubes which make up the MCP's surface. The resulting ion signal is detected using a circuit (given in the El-Mul catalogue) which is connected to an oscilloscope where the signal is recorded. A voltage of -2.5 kV was applied to the MCP achieving a gain of 10^6. The MCP was attached to a UHV electrical feedthrough which was attached to one of the small flanges shown on top of the science chamber in figure 3.2. Figure 3.16 shows how Ar* can be ionised by non-resonant multiphoton processes with 1064 nm and 532 nm laser light from either state of the cooling transition. These ionisation processes will be important in later chapters.

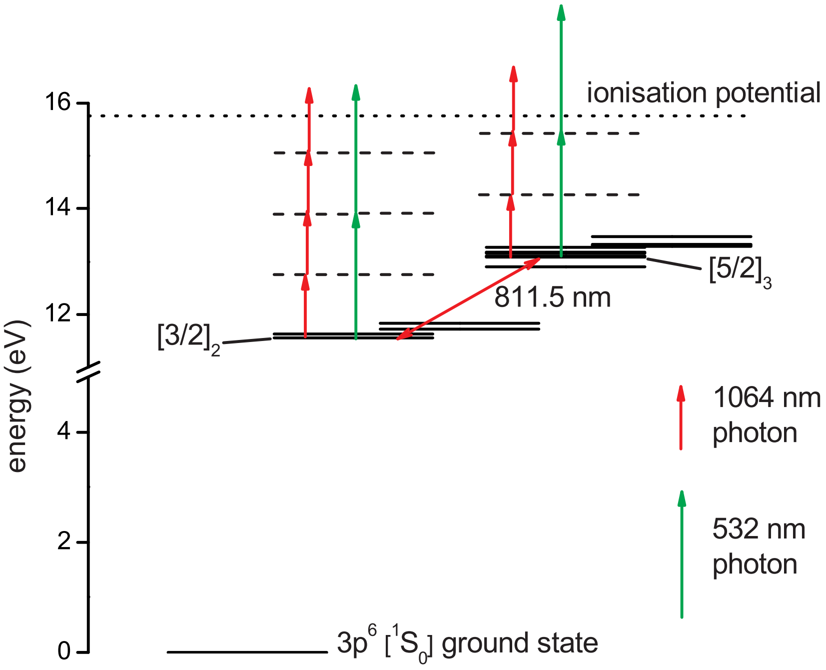

Figure 3.16: Non-resonant multiphoton ionisation of Ar* by 1064 nm and 532 nm laser light. Ionisation paths from both the lower 4s$[3/2]_2$ and upper 4p$[5/2]_3$ states of the laser cooling transition are shown. Four 1064 nm photons are required to ionise the atom from the 4s$[3/2]_2$ state and 3 from 4p$[5/2]_3$ while two 532 nm photons are required to ionise from either state.

3.5.5 Experimental control

Control of the experimental equipment during experiments was managed using an digital delay pulse generator (Quantum Composer 9520 series) which had 8 output channels capable of outputting up to 20 V. This box was used to control the triggering of the laser and atomic beam shutters, the MOSFET connected to the MOT coils, the EMCCD camera and the oscilloscope for recording the ion signals.

3.6 MOT characterisation measurements

The equipment described in this chapter was integrated to produce the Ar* MOT. The beam from the slave laser AOM (see figure 3.11) was split into three equal intensity beams which were used as the MOT beams. Each of the three beams was passed through a quarter-wave plate to achieve the desired circular polarisation and then aligned through the science chamber to cross at the magnetic field zero as shown in figure 3.17. The counter-propagating MOT beams were generated by retro-reflecting the beams and double-passing them through a quarter-wave plate. The MOT beams typically had an intensity of 1.5 mWcm^{-2} and the frequency detuning varied between -1.7Γ to -3.5Γ in different experiments. Figure 3.17 also shows a fluorescence image of the MOT obtained with the Thorlabs CCD camera. Initial experiments characterised the trap loading and lifetime and measured the density and temperature of the MOT. Quenching of the MOT atoms to their ground state was also tested.

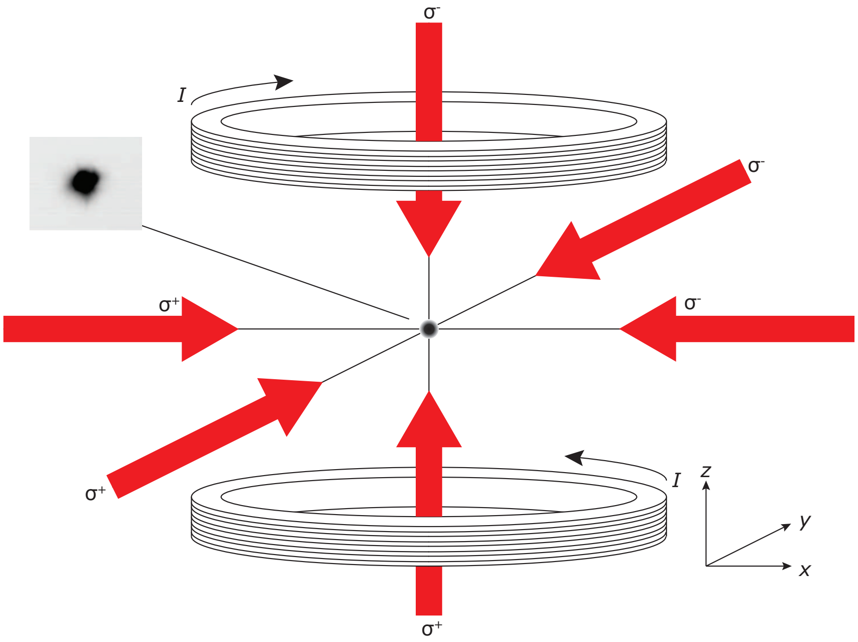

Figure 3.17: Schematic diagram of MOT showing 3 pairs of counter-propagating MOT beams and MOT coils. Also shown inset is an inverted colour fluorescence image of the MOT.

3.6.1 MOT loading and lifetime

The MOT loading time and lifetime were measured by recording the MOT fluorescence at different delays after switching on/off the trap loading. Switching on the loading of the trap was achieved by turning on the MOT B-field with all other experimental elements required for the MOT permanently on. For the lifetime measurement the trap loading was switched off by shuttering the Zeeman slower laser beam with a mechanical shutter. The loading measurements were taken by completely unloading the MOT by switching off the B-field for 2 seconds and then acquiring images at a variable delay after switching the MOT back on. Each image acquired was averaged over 20 accumulations and had a background image, acquired under the same experimental conditions but with the MOT magnetic field off, subtracted from it. Figure 3.18(a) shows a typical loading curve which shows that the MOT loads in 2.5 s. Figure 3.18(b) shows a lifetime curve obtained by loading the MOT for 3 s before switching off the trap loading and acquiring background-subtracted images at variable delays. The trap decay constant was measured from this lifetime curve to be 554 ± 7 ms.

Due to the large internal energy of Ar* atoms they are inherently fragile and intra-trap collisions lead to Penning ionisation reactions and loss from the trap [82]. This two body loss mechanism is density-dependent and thus the loading and lifetime curves will depend on the density in the trap. MOT lifetimes of less than 150 ms have been measured at higher trap densities. The density dependency of the MOT lifetime could quickly be observed by monitoring the decay of the trap at different MOT B-field gradients. By ramping down the B-field gradient the MOT became bigger and more diffuse and by blocking the Zeeman slower beam the lifetime was observed to be longer than at a normal operating gradient. These intra-trap, Penning collisions are discussed in more detail in chapter 7.

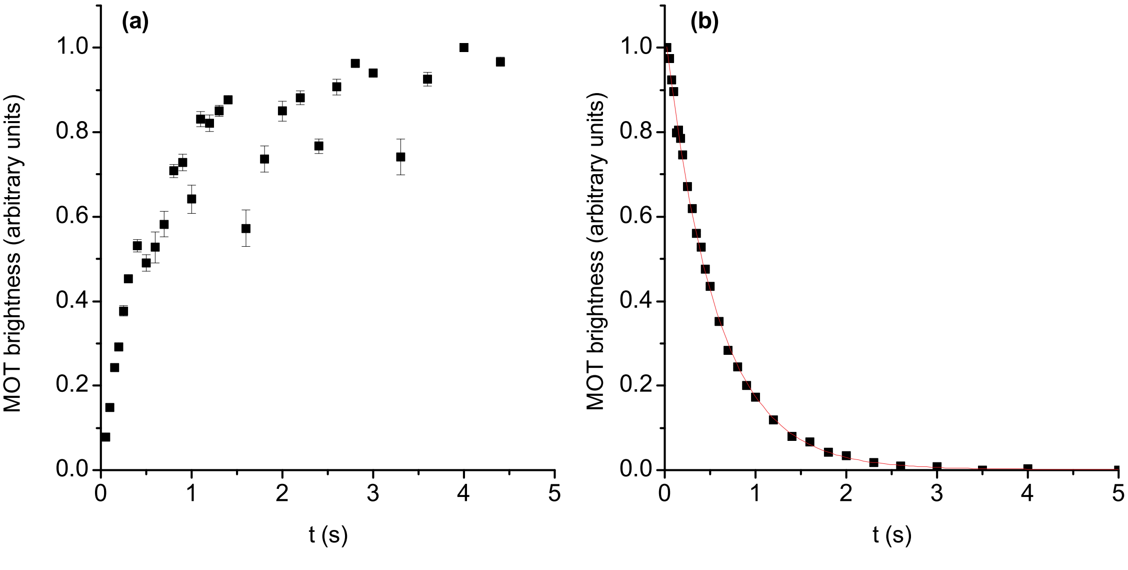

Figure 3.18: (a) Fluorescence signal from the MOT as a function of time after switching on the trap loading. The fluorescence is directly proportional to the atom number and shows that the MOT loads in approximately 2.5 s. The noise on the data was caused by instabilities in the RF discharge during the data acquisition. (b) Typical lifetime curve of the MOT obtained after switching off the trap loading. The time constant for the trap decay was determined from the exponential fit to be 554 ± 7 ms. The error bars on both plots are the standard error from the 20 measurements analysed for each data point.

3.6.2 MOT density

The number of atoms N_{Ar^*} trapped in a MOT can be determined using absorption or fluorescence imaging techniques. We imaged the photons scattered from the cooling beams on the EMCCD camera and determined N_{Ar*} from this signal. Considering the photon scattering rate and the experimental measurement conditions we can determine $N_{\mathrm{Ar}*}$ from

$$N_{\mathrm{Ar}*} = \frac{1 + 6s_0 + (2\Delta/\Gamma)^2}{6s_0(\Gamma/2)\Omega_d \ell} \frac{N_{counts}\eta}{t_{exp}} \tag{3.6}$$

where N_{counts} is the number of counts on the CCD chip in pixel units, t_{exp} is the image exposure time and ℓ is an attenuation factor through the imaging optics, Ω_d is the fraction of total light emitted incident on the lens and η is the camera efficiency. Figure 3.19 shows a MOT fluorescence image obtained with the Thorlabs CCD camera. In order to determine the number of atoms in the MOT from this image ℓ, Ω_d and η were first determined. An attenuation factor of $\ell = 0.67$ was measured by aligning a 811.53 nm laser beam through the imaging lens and measuring the power transmitted on a photodiode. The camera efficiency η was determined by aligning a very weak laser beam onto the CCD chip and calibrating the pixel count value to incident power and then number of photons incident to obtain $\eta = 21.4$ photon.pix^{-1}. The fraction of total light emitted incident on the lens was $\Omega_d = 6.94 \times 10^{-4}$ for a lens of diameter $d = 32.6$ mm at a distance of 32 cm from the MOT. The MOT shown in figure 3.19 was produced using 1.5 mWcm^{-2} beams detuned by 1.7Γ and the number of atoms was calculated to be $N_{\mathrm{Ar}*} = 8.88 \times 10^4$. The $1/\sqrt{e}$ radius of the MOT was measured from the image to be 176 μm and the density in the trap was then 3.93×10^9 cm^{-3}. This is one example of a density measurement and higher atom numbers, on the order of 10^5, and densities, of up to 10^{10} cm^{-3}, were measured with different trapping parameters. Our densities are comparable with previously measured Ar* MOT densities of $n_0 = (3 \pm 1) \times 10^9$ cm^{-3} [114] and $n_0 = 1.2 \times 10^{10}$ cm^{-3} [115].

3.6.3 MOT temperature

The temperature of the Ar* atomic cloud trapped in the MOT was determined using a fluorescence time-of-flight technique [91]. This method involves imaging the ballistic expansion of the atomic cloud after switching the MOT off. Assuming that the atomic

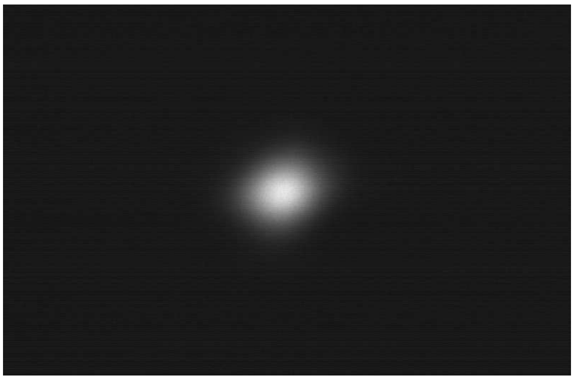

Figure 3.19: Fluorescence image of the MOT.

cloud is symmetric and has a Gaussian width it will expand according the following relation

$$\sigma^2(t) = \sigma_0^2 + \frac{k_B T}{m} t^2 \tag{3.7}$$

where $\sigma(t)$ is the Gaussian radius of the cloud at a time t, σ_0 is the initial Gaussian radius, T is the temperature of the cloud and m is the atomic mass. By measuring the width of the cloud at various expansion times this relation can be used to determine the temperature of the cloud. Nullification of the background magnetic fields is crucial when measuring the MOT temperature as stray fields can result in atoms being kicked from the trapping region when the B-field is ramped down. The stray fields were nullified by careful adjustment of the compensation coil currents while observing the MOT atoms being released into a 3D optical molasses. The atoms expanded slowly and the compensation coil currents were adjusted until the expansion was symmetric, a diagnostic of zero background field.

The experimental sequence for measuring the temperature began by loading the MOT for 2.5 s before shuttering the Zeeman slower beam and then, after 5 ms, switching off the MOT coils. After another 2 ms the MOT laser beams were switched off allowing the atomic cloud to expand freely. Images were acquired at different times t by switching the MOT beams back on and triggering the camera. Figure 3.20a shows images of the expanding cloud at delays of 1-9 ms. Gaussian curves were fitted to the cloud width to determine $\sigma(t)$. Figure 3.20b shows the corresponding plot of $\sigma^2(t)$ versus t^2 used to determine the temperature. The linear fit in the plot shown yielded a temperature of $T = 73.2 \pm 0.4$ μK. This is well below the Doppler limit ($T_D = 140.9$ μK), as expected due to polarisation gradient cooling. Our temperature is comparable with previously measured Ar* MOT temperatures [114] of ≈ 40 μK for similar MOT parameters.

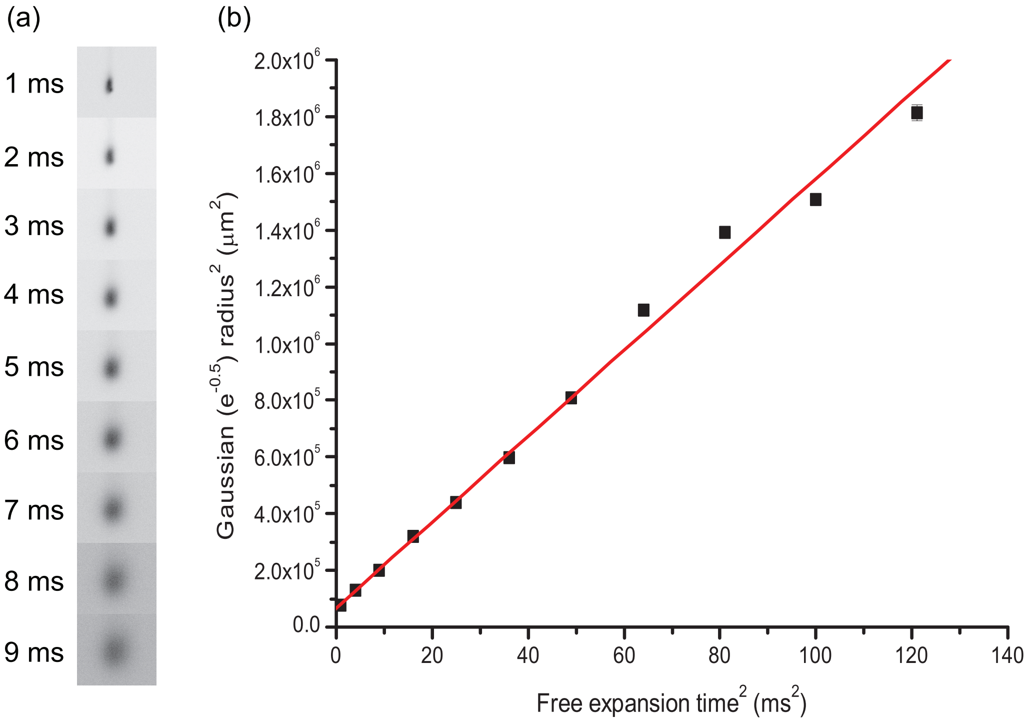

Figure 3.20: (a) Fluorescence images of the expanding atomic cloud released from the MOT. The images are background-subtracted and are the accumulation of 20 individual images obtained with an exposure time of 1 ms. (b) Plot of $\sigma^2(t)$ versus t^2 corresponding to the expansion images shows. The temperature of the MOT was determined from the linear fit using equation 3.7 to be $T = 73.2 \pm 0.4$ μK.

3.6.4 Quenching MOT atoms

Quenching of the ultracold Ar* atoms to their ground state was tested by aligning the quench beam through the MOT and tuning the laser to the 801.48 nm quench transition. By tuning the laser diode current the MOT could be seen to disappear and reappear as the laser frequency was tuned over quench transition. Figure 3.21 shows an image of the MOT with a focused quench beam aligned through it which causes the stripe through the middle of the MOT. In section 2.6.1 it was mentioned that after three absorption cycles 98% of the atoms in the quench beam will be in the ground state. Thus quenching occurs quickly and the laser beam imparts little momentum to the atomic cloud.

3.7 Conclusions

The design and construction of a Ar* MOT experiment has been described in this chapter. The vacuum system constructed for the MOT was designed such that it can facilitate future sympathetic cooling experiments. As well as access for the MOT laser/atomic beams the science chamber has ports which will be used to integrate the molecular optical

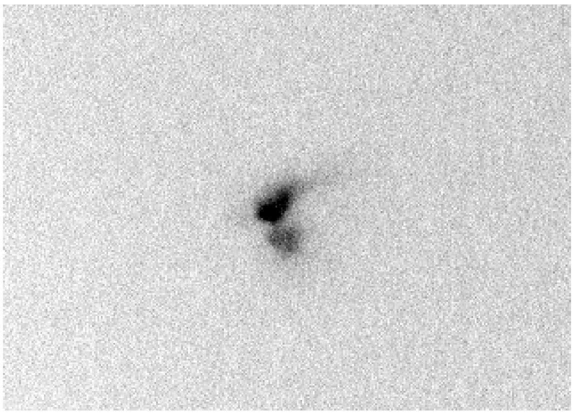

Figure 3.21: Inverted colour fluorescence image of the MOT with a focused quench beam at 801.48 nm aligned through it. Atoms in the quench beam region are optically pumped to their ground state and are lost from the MOT hence the stripe in the centre of the MOT.

Stark deceleration experiment and the high finesse optical cavity trap with the MOT. During operation the pressure in the science chamber was 6×10^{-9} mbar when the atomic beam was shuttered. Although this pressure was suitable for the experiments presented in this thesis further work may be required to achieve a lower pressure before sympathetic cooling experiments. One potential solution could be to reduce the gas load on the science chamber. This could be achieved by moving the science chamber off-axis from the atomic beam and directing the Ar* atoms in the beam through the science chamber skimmer which would reduce the number of atoms entering the chamber by approximately 10^4. Directing the Ar* atoms into the science chamber could be achieved using either a 2D MOT [116] or a magnetic guide [117]. The gas load could also be reduced using a double MOT system [118] where the first MOT acts as an atomic source for the second which would be located in the science chamber.

The other apparatus used to produce and detect the Ar* MOT has also been described. Our laser frequency stabilisation scheme has been presented demonstrating the application of a magnetic dichroism technique to Ar* atoms in a weak plasma. This method achieved a laser frequency stability of 129 kHz at 1 s averaging times.

The MOT was characterised and the loading time and lifetime of the trap were investigated. The data presented in section 3.6.1 gave a trap decay time of 554 ± 7 ms and a loading time of approximately 2.5 s. These are important characteristics for experiments where many repetitions are required and the MOT is repetitively loaded and unloaded. As mentioned previously the trap loading and lifetime are heavily influenced by the trap density due to two-body losses and the times given here can vary. The density and temperature of the trapped atomic sample were also measured to be 3.93×10^9 cm^{-3} and 73.2 ± 0.4 μK respectively. These are important characteristics of the atomic cloud for sympathetic cooling and the temperature measured here was lower than that used in simulations of Ar-H_2 and Ar-C_6H_6 sympathetic cooling [90]. Sympathetic cooling requires ground state, rather than metastable, argon atoms and quenching of the ultracold Ar* atoms to their ground state has been demonstrated here using a laser at 801.48 nm. This represents the completion of one of the key experimental elements, the ultracold atomic source, for molecular sympathetic cooling experiments. The Ar* MOT and apparatus described in this chapter are central to the experiments presented in the rest of this thesis.

Chapter 4

Optical Stark acceleration

Optical Stark deceleration is crucial to future sympathetic cooling experiments and there are also important applications for optical Stark acceleration such as producing low energy, highly monoenergetic beams [50]. These beams find application in, for example, reactive scattering experiments [119] and atomic nanafabrication [120]. Beams produced by Stark deceleration (see section 1.3) have been used to study near-threshold inelastic collisions between OH radicals and Xe atoms in high resolution crossed-beam experiments [22]. Similar crossed-beam experiments have observed Feshbach resonances in the $F + H_2 \rightarrow HF + H$ reaction using a molecular beam produced by a liquid-nitrogen-cooled valve assembly [119]. Beams with a narrow energy spread also find application in atomic nanofabrication where atoms or molecules are transported to a surface via an atomic or molecular beam [120].

Optical Stark acceleration could also be applied in controlled chemistry experiments. Chemical reactions depend on the translational energy as well as internal state of the reactants. Although much work has gone into using the optical phase and intensity of laser fields to control internal motion [121, 122] there have been no general optical techniques for controlling the translational motion of the reactants over a wide range. Optical acceleration has been achieved using optical tweezers in ultracold atomic scattering experiments [123]. The final velocities required in these experiments are on the order of 10's of millimeters per second and the technique demonstrated is not applicable to higher energy collisional experiments. Another experiment has achieved neutral particle acceleration using high intensity ($\approx 10^{12}$ Wm^{-2}) femtosecond laser pulses [124]. Acceleration of metastable helium up to velocities of 55 ms^{-1} was demonstrated but the velocity spread was very broad, precluding its use in experiments where high energy resolution is required.

Chirped optical Stark deceleration, which uses accelerating optical potentials to accelerate particles, has the potential to produce near monoenergetic atomic and molecular beams with precisely tunable velocities. Optical Stark deceleration of molecules with a constant-velocity lattice has been demonstrated where control over the final beam velocity was achieved [61]. In these experiments the beam was extracted from a low temperature, supersonic molecular beam. One major limitation of using a constant-velocity lattice is that the velocity, or energy spread of the decelerated beam was limited to that of the initial molecular beam (> 1 K). Chirped optical Stark acceleration/deceleration is a more powerful technique as it offers control over both the beam velocity and the velocity width of the beam [125].

We have performed optical Stark acceleration experiments on the Ar* atoms confined in our MOT which will be presented in the next chapter. This chapter serves as a prelude to the experimental chapter and will introduce the theory of acceleration and discuss some background experimental information. Firstly, the theory behind producing an accelerating optical potential will be discussed. Previous constant-velocity lattice molecular deceleration experiments will then be reviewed before focusing solely on acceleration by chirped, accelerating lattices. The laser system developed to achieve chirped optical Stark acceleration will also be described. Finally, we will present some simulations of acceleration and deceleration for different species.

4.1 Theoretical introduction

Optical Stark acceleration/deceleration uses the optical dipole force to manipulate the translational motion of atoms and molecules. This technique uses optical fields which are far off-resonance from the nearest optical dipole transition such that potential experienced by a polarisable particle is quasi-electrostatic and given by $U = -\frac{1}{2}\alpha_{stat}|\epsilon|^2$, as discussed in section 2.5.2. The force on a particle in this potential, $F = -\nabla U$, is dependent on the intensity gradient in the optical field. Optical Stark acceleration uses an interference pattern created by two, near counter-propagating laser beams where the intensity gradients are much steeper than in a single beam field. Overlapping this interference pattern with polarisable particles creates a periodic potential called an *optical lattice.*

The optical lattice potential can be derived by first considering two laser fields given by

$$\begin{aligned}
\epsilon_1(r,\boldsymbol{z},t) &= E_1(r,t)\mathrm{sin}(\boldsymbol{k}_1\boldsymbol{z}-\phi_1) \\
&= \frac{E_1(r,t)i}{2}\left(\mathrm{e}^{-i(\boldsymbol{k}_1\boldsymbol{z}-\phi_1)}-\mathrm{e}^{i(\boldsymbol{k}_1\boldsymbol{z}-\phi_1)}\right) \\
\epsilon_2(r,\boldsymbol{z},t) &= E_2(r,t)\mathrm{sin}(\boldsymbol{k}_2\boldsymbol{z}-\phi_2) \\
&= \frac{E_2(r,t)i}{2}\left(\mathrm{e}^{-i(\boldsymbol{k}_2\boldsymbol{z}-\phi_2)}-\mathrm{e}^{i(\boldsymbol{k}_2\boldsymbol{z}-\phi_2)}\right)
\end{aligned} \tag{4.1}$$

where $E_{1,2}(r,t)$ are the electric field amplitudes, $\boldsymbol{k}_{1,2}$ are the wavevectors and $\phi_{1,2}$ are the instantaneous phases of the beams. In experiments the beams intersect at a large full angle and we only consider the wavevectors in the z direction. The instantaneous phases are given by $\int \omega_{1,2}\,dt$ where $\omega_{1,2}$ are the frequencies of the laser beams. The total electric field is calculated by summing the fields from each beam $\epsilon = \epsilon_1 + \epsilon_2$ and the $|\epsilon|^2$ term in the equation for the potential can then be written as

$$\begin{aligned}
|\epsilon|^2 =&1/2\{E_1^2+E_2^2-E_1^2\mathrm{cos}[2(\boldsymbol{k}_1\boldsymbol{z}-\phi_1)]-E_2^2\mathrm{cos}[2(\boldsymbol{k}_2\boldsymbol{z}-\phi_2)]\} \\
&-E_1E_2\mathrm{cos}[(\boldsymbol{k}_1+\boldsymbol{k}_2)\boldsymbol{z}-(\phi_1+\phi_2)]+E_1E_2\mathrm{cos}[(\boldsymbol{k}_1-\boldsymbol{k}_2)\boldsymbol{z}-(\phi_1-\phi_2)].
\end{aligned} \tag{4.2}$$

This equation can be simplified by first ignoring the constant terms as they do not contribute to the intensity gradients. If we assume that the instantaneous phases are constant, such that $\phi_{1,2} = \omega_{1,2}t$, we can see that the third and fourth terms oscillate at twice the spatial ($2\boldsymbol{k}_{1,2}$) and optical ($2\omega_{1,2}$) frequencies and can be neglected. We can now write

$$|\epsilon|^2 = -E_1E_2\mathrm{cos}[(\boldsymbol{k}_1+\boldsymbol{k}_2)\boldsymbol{z}-(\omega_1+\omega_2)t]+E_1E_2\mathrm{cos}[(\boldsymbol{k}_1-\boldsymbol{k}_2)\boldsymbol{z}-(\omega_1-\omega_2)t]. \tag{4.3}$$

For atomic/molecular acceleration only the slowly varying term is important and the first term can be ignored giving

$$|\epsilon|^2 = E_1E_2\mathrm{cos}[(\boldsymbol{k}_1-\boldsymbol{k}_2)\boldsymbol{z}-(\omega_1-\omega_2)t]. \tag{4.4}$$

By substituting this equation for $|\epsilon|^2$ into the quasi-electrostatic potential and using a trigonometric identity we can obtain a useful form of the potential

$$U(r,\boldsymbol{z},t) = -\alpha_{stat}E_1(r,t)E_2(r,t)\mathrm{cos}^2[(1/2)(q\boldsymbol{z}-\Delta\omega t)] \tag{4.5}$$

where $q = |\boldsymbol{k}_1 - \boldsymbol{k}_2|$ is the amplitude of the lattice wavevector and $\Delta\omega$ is the frequency difference between the two beams. A finite frequency difference $\Delta\omega$ creates a moving lattice with a velocity given by $v_L = \Delta\omega/q$. Through tuning of $\Delta\omega$ the velocity of the lattice potential and any particles confined within it can be controlled. Equation 4.5 can be rewritten in terms of the measurable lattice beam intensities $I_{1,2}(r,t)$ as

$$U(r,\boldsymbol{z},t) = -\frac{2\alpha_{stat}}{\epsilon_0 c}\sqrt{I_1(r,t)I_2(r,t)}\cos^2[(1/2)(q\boldsymbol{z} - \Delta\omega t)]. \tag{4.6}$$

Acceleration/deceleration can be achieved using either a constant-velocity lattice, generated with a fixed $\Delta\omega$ [126], or with an accelerating lattice which is produced by rapidly sweeping, or *chirping*, the frequency difference between the two beams[127, 62]. In both cases we consider the lattice wavevector to be constant with time. This assumption can be justified by considering the equation for the lattice wavevector

$$q = |\boldsymbol{k}_1 - \boldsymbol{k}_2| = 2\pi\sin\left(\frac{\theta}{2}\right)\left(\frac{1}{\lambda_1} + \frac{1}{\lambda_2}\right) \tag{4.7}$$

where θ is the separation angle between the two lattice beams and $\lambda_{1,2}$ are their respective wavelengths. If we consider that the laser beam frequencies may have a time dependence we can rewrite this equation as

$$q(t) = \frac{2\pi}{c}\sin\left(\frac{\theta}{2}\right)(f_1(t) + f_2(t)). \tag{4.8}$$

It is clear that for a constant-velocity lattice q will be constant and in the chirped case this equation implies $\Delta q/q = \Delta f/f$ where $\Delta q = q_{t=0} - q_{t=T}$, $\Delta f = f_{t=0} - f_{t=T}$ and T is the duration of the frequency sweep. Laser beams with a wavelength of 1064 nm are used in experiments and for a chirp of 1 GHz we get $\Delta q/q = \Delta f\lambda/c \approx 4 \times 10^{-6}$ which shows that the lattice wavevector is effectively constant over the duration of the chirp. As the wavelengths of the two lattice beams are approximately equal we can write the lattice wavevector as

$$q(t) = \frac{4\pi\sin\left(\frac{\theta}{2}\right)}{\lambda}. \tag{4.9}$$

The force exerted on a particle in the lattice potential can be determined from equation 4.6 to be

$$F(r,\boldsymbol{z},t) = -\frac{\alpha_{stat}}{\epsilon_0 c}\sqrt{I_1(r,t)I_2(r,t)}\sin(q\boldsymbol{z} - \Delta\omega t). \tag{4.10}$$

Although this force is used in both constant-velocity and chirped lattice acceleration the mechanism by which acceleration is achieved is different in each case, as will be discussed in the next sections.

4.2 Constant-velocity lattice acceleration

Acceleration of particles within a constant-velocity lattice exploits the particle's oscillatory motion within the optical potential. Figure 4.1 illustrates, for a single particle, the mechanism by which acceleration and deceleration is achieved. In order to accelerate a particle (figure 4.1(a)), the frequency difference between the lattice beams is set such that the lattice has a velocity v_L that is larger than the initial velocity of the particle v_0. The illustration shows how over the course of a half oscillation in the lattice site the particle is accelerated from v_0 to $v_0 + 2\Delta v$, where $\Delta v = |v_L - v_0|$. After a quarter oscillation the particle is stationary with respect to the lattice and has gained a velocity of Δv. On returning to the bottom of the potential well and completing a half oscillation the particle has gained another Δv in velocity and has a velocity of $v_0 + 2\Delta v$. Figure 4.1(i) shows the velocity evolution of the accelerating particle over the half oscillation. If allowed to continue on its trajectory the particle will loose its velocity gained over the next half oscillation of the lattice site. Thus acceleration requires precise switching of the lattice laser beams such that the particles undergo an integer number of half oscillations over the lattice duration. Also, it is essential that the potential well is sufficiently deep such that the particles cannot overcome the potential barrier and remain localised within a single lattice site. Figure 4.1(b) illustrates particle deceleration where the lattice is initially traveling slower than the particle. In this case the particle will be decelerated in the lab frame from an initial velocity of v_0 to $v_0 - 2\Delta v$ over the course of a half oscillation. The final velocity in either acceleration or deceleration experiments is determined by the lattice velocity relative to the initial particle velocity. In the simple cases which have been outlined here we have considered a single particle initially positioned at the bottom of the potential well; in experiments, particles will distributed across the lattice site and acceleration/deceleration will only be effective for a small proportion of the particles in the lattice.

When setting up an acceleration or deceleration experiment the lattice velocity is chosen as $v_L = v_0 \pm \Delta v$ where the desired velocity change is $\Delta v_{total} = \pm 2\Delta v$. The potential well depth, and lattice beam intensities, required to achieve this velocity change must then be considered. The minimum well depth required is equal to half the kinetic energy removed/added from the particle. The factor of a half comes from the fact that

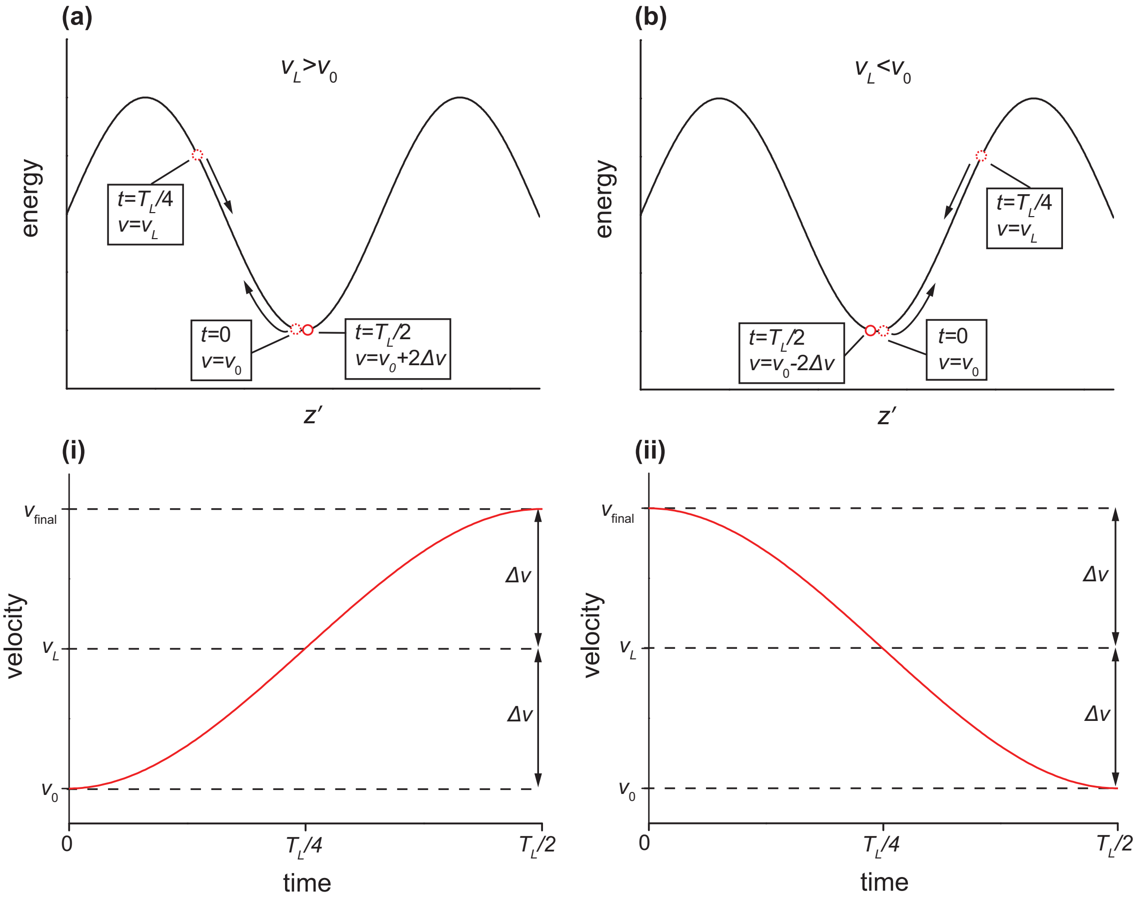

Figure 4.1: Illustration of acceleration (a) and deceleration (b) in a constant-velocity lattice in the reference frame of the moving lattice. In (a) the lattice velocity v_L is greater than the initial velocity of the particle v_0 and in the lattice frame the particle has a velocity $v' = v_0 - v_L = -\Delta v$ where $\Delta v = |v_L - v_0|$. The particle is initially located at the bottom of the potential well and it moves in the $-z'$ direction experiencing a dipole force back towards the potential minimum. After a quarter oscillation period the particle is stationary in the lattice frame $v' = 0$ and the dipole force then acts to accelerate the particle back towards the potential minimum. Once the particle has completed a half oscillation, and is back at the potential minimum, it will have a velocity of $v' = +\Delta v$. This velocity change is translated into the lab frame as acceleration of the particle from v_0 to $v_0 + 2\Delta v$. The velocity evolution of the particle in the lab frame over a half oscillation is shown in (i). The plots in (b) and (ii) show the corresponding plots to (a) and (ii) for the reciprocal case of deceleration where the lattice is initially traveling slower than the particle. Over the course of a half oscillation the particles velocity in the lab frame is reduced from v_0 to $v_0 - 2\Delta v$.

both ascending and descending the potential hill result in a velocity change in the same direction. For lattice beams of equal intensity I the minimum beam intensities required are [63]

$$I_{min} = \frac{\epsilon_0 c m \Delta v_{total}^2}{8\alpha}, \tag{4.11}$$

where m is the mass of the particle and $\Delta v_{total} = 2\Delta v$. From this equation we can see that the ease with which a particle can be decelerated is dependent on its polarisability to mass ratio. It is important to stress that the intensity given by this relation is a minimum and experiments use larger intensities, up to twice this value. In order to achieve a half oscillation in the lattice site, the lattice duration must be set by considering the oscillation period of a particle in the lattice. For deeply trapped particles in the lattice, where $\sin(q\boldsymbol{z} - \Delta\omega t) \approx (q\boldsymbol{z} - \Delta\omega t)$, the force is to a good approximation harmonic. Equation 4.10 then becomes

$$F(\boldsymbol{z}, t) \approx -\frac{\alpha_{stat} I}{\epsilon_0 c}(q\boldsymbol{z} - \Delta\omega t), \tag{4.12}$$

and the oscillation period in the lattice frame is

$$T_L = \frac{2\pi}{q}\sqrt{\frac{\epsilon_0 c m}{\alpha I}}. \tag{4.13}$$

In order to examine typical experimental lattice parameters, we can consider an experiment to accelerate Ar* ($m = 40$ a.m.u., $\alpha = 47.9 \times 10^{-40}$ Cm^{2}V^{-1}) from rest to 200 ms^{-1}. This would require a lattice with a velocity of 100 ms^{-1} formed by beams with intensities greater than 1.8×10^{14} Wm^{-2}. If we choose beam intensities of 2.7×10^{14} Wm^{-2}, which are 1.5 times the minimum limit, the oscillation period of an atom in the lattice is 6.1 ns. In order to achieve a half oscillation a lattice duration of 3.05 ns, or $NT_L + 3.05$ ns where N is an integer number, would be required.

Deceleration of molecules from a molecular beam has been demonstrated using a constant-velocity lattice. Figure 4.2 shows a schematic diagram of the experimental set-up. The molecules were prepared for deceleration in a supersonic jet, with a backing gas of xenon (95% by volume), where the molecules were translationally cold (on the order of 1 K) but had a mean centre-of-mass velocity of approximately 400 ms^{-1}. The lattice beams were produced by two Q-switched Nd:YAG pulsed lasers which output pulse energies of up to 350 mJ. Pulse durations of less than 15 ns were used in these experiments with the duration for a given experiment determined by the time required for a half oscillation in the lattice. The frequency of the lattice beams was controlled by tuning the temperature of the lasers and their relative frequency was monitored on a spectrum analyser. The beams were focused into the vacuum chamber into which the molecular beam was also introduced. At their foci the lattice beams had a 1/e^2 radius of 60 μm giving local intensities on the order of 10^{11} Wcm^{-2}. The foci of the lattice beams were overlapped at a full angle of 167.5° and superimposed onto the molecular beam to create the deep periodic lattice potential. In the first experiments nitric oxide (NO) molecules with an initial velocity of 400 ms^{-1} were decelerated to 270 ms^{-1} and accelerated to 500 ms^{-1} using a lattice with a duration of 5.8 ns [61]. Deceleration of benzene (C_6H_6) molecules from 380 ms^{-1} to 191 ms^{-1} has also been demonstrated [63]. These experiments did not manage to achieve the maximum velocity change for the respective lattice velocities due to finite switch off times of the lattice which meant that the molecules underwent more than a half oscillation in their respective lattice sites. By introducing a fast Pockels to optically chop one of the pulses, which improved the lattice switch off, C_6H_6 molecules were decelerated to rest [64].

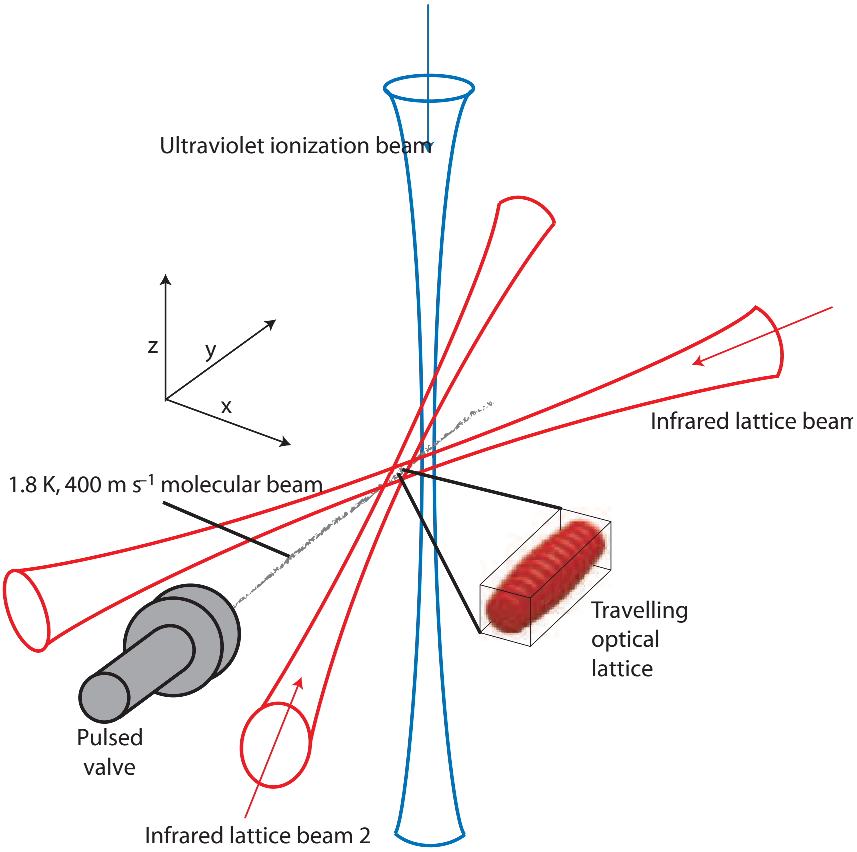

Figure 4.2: Schematic diagram of the experimental set-up used for constant-velocity lattice optical Stark deceleration. The lattice beams were overlapped at their foci and superimposed onto the molecular beam to create the deep lattice potential. This diagram was taken from reference [61].

Despite the success of this technique in achieving molecular deceleration there are some drawbacks. Precise switching of the optical fields is technically demanding and imperfections in the lattice switch off result in the desired final velocity not being achieved. Also, the high intensities required prohibit acceleration of easily ionised species, such as Ar* which is 4.2 eV from the ionisation continuum. More importantly, the velocity spread of the decelerated portion is fundamentally limited to be equal to or broader than velocity width of the initial distribution. This precludes the use of constant-velocity lattice acceleration/deceleration in some potential applications such as high resolution collision experiments. Narrower velocity distributions can be achieved by using an accelerating lattice which does not rely on the oscillatory motion of trapped particles. The following section will explain the acceleration mechanism in chirped lattice acceleration. The rest of the chapter will then describe the laser system used in experiments and discuss simulation of the acceleration process showing examples of the methods capability.

4.3 Chirped lattice acceleration

A chirped optical lattice is produced by rapidly changing the frequency difference between the two laser beams which results in an acceleration or deceleration of the lattice. Particle acceleration with a chirped lattice is achieved by trapping particles in the potential wells of the lattice and carrying them with the potential as it accelerates. In order to do this, the lattice is switched on with a velocity equal to that of the particles and then accelerated to the desired final velocity. As this method does not rely on the oscillatory motion of the trapped particles, acceleration can be carried out over longer durations and requires lower intensities. Using a chirped lattice also removes the fundamental limit on the velocity width of the accelerated distribution which prohibits the use of constant-velocity lattice acceleration in certain applications.

The form of the lattice potential given by equation 4.5 must be modified for a chirped lattice to include the time dependent aspect of the frequency difference between the lattice beams. For a linear chirp the potential is then written as

$$U(r, \boldsymbol{z}, t) = -\alpha_{stat} E_1(r,t) E_2(r,t) \cos^2[(1/2)(q\boldsymbol{z} - (\omega_0 t - 1/2\beta t^2))] \tag{4.14}$$

where ω_0 is the initial frequency difference between the beams and $\beta = \Delta\omega/\Delta t$ is the chirp rate where $\Delta\omega$ is the total frequency excursion and Δt is the duration of the chirp. A decelerating potential requires a negative chirp rate $(-\beta)$ while a positive chirp rate $(+\beta)$ generates an accelerating potential. The equation of motion for a particle in the lattice potential is given by

$$\frac{d^2 z}{dt^2} = -a(t) \sin[(q\boldsymbol{z} - (\omega_0 t - 1/2\beta t^2))], \tag{4.15}$$

where $a(t) = -\frac{1}{2}\alpha_{stat}qE_1(t)E_2(t)/m$ is the maximum force per unit mass. In order to study the trajectories of particles in the lattice, we calculate their motion in the reference frame of the accelerating lattice. The equation of motion in the accelerating reference frame becomes

$$\frac{d^2\theta}{dT^2} = -\frac{2aq}{\beta}\sin\theta - 2, \tag{4.16}$$

where $\theta = Z - T^2 - C$ is the phase of the particle with respect to the lattice and $T = \sqrt{\beta/2}t$ and $Z = qz$ are the dimensionless temporal and spatial variables respectively and $C = \omega_0 t$. Particle trajectories in velocity phase space $[\eta, \theta]$ can be derived from this equation of motion [127]. This system of equations is given by

$$\frac{d\eta}{dT} = \frac{-2aq}{\beta}\sin\theta - 2, \tag{4.17}$$

$$\frac{d\theta}{dT} = \eta. \tag{4.18}$$

By letting these equations equal zero we find the critical points of the system at $\eta = 0$ and $\sin\theta = -\beta/aq$. Linear stability analysis of equations 4.17 and 4.18 reveals a series of points $[\eta, \theta] = [2n\pi - \sin^{-1}\psi, 0]$ that are stable equilibrium points where n is an integer and $\psi = \beta/aq$. Another series of points found at $[\eta, \theta] = [(2n-1)\pi + \sin^{-1}\psi, 0]$ are unstable equilibrium points.

In the accelerating lattice frame the lattice potential appears modified from the sinusoidal potential observed in the lab frame and is given by $U(\theta) = -\int (m/q^2) d^2\theta/dt^2 \, d\theta$, which can be evaluated to

$$U(\theta) = -\frac{m\beta}{2q^2}\left(2\theta + \frac{2}{\psi}\cos\theta\right). \tag{4.19}$$

Figure 4.3 shows the modified lattice potentials in the accelerated frame for $\psi = 0.3$, 0.5 and 0.7. The parameter $\psi = \beta/aq$ is a measure of the ratio of the chirp rate to the lattice intensity and different values of ψ can be generated by either varying the chirp or the lattice intensity. The depth of the modified potential well ΔU is the difference between the bottom of the well and the nearest peak. Figure 4.3 shows that the well depth decreases with increasing ψ. The potential well depth is given by

$$\Delta U = \frac{ma}{q}[2\cos(\sin^{-1}\psi) - \psi(\pi - 2\sin^{-1}\psi)]. \tag{4.20}$$

From this equation we can see that no potential well exists for $\psi > 1$ as $\sin^{-1}\psi$ becomes unphysical. This gives an important condition for acceleration

$$\left|\frac{\beta}{aq}\right| < 1 \tag{4.21}$$

which implies that the chirp rate β must be less than aq. Physically this means that the acceleration of the lattice $a_L = \beta/q$ must be less than the maximum force per unit mass m applied by the potential gradient. The maximum well depth ΔU_{max} occurs when there is no chirp ($\psi = 0$) and the lattice is either stationary or traveling with a constant velocity. The potential wells shown in figure 4.3 have well depths of $0.58\Delta U_{max}$, $0.36\Delta U_{max}$ and $0.24\Delta U_{max}$ for $\psi = 0.3$, 0.5 and 0.7 respectively.

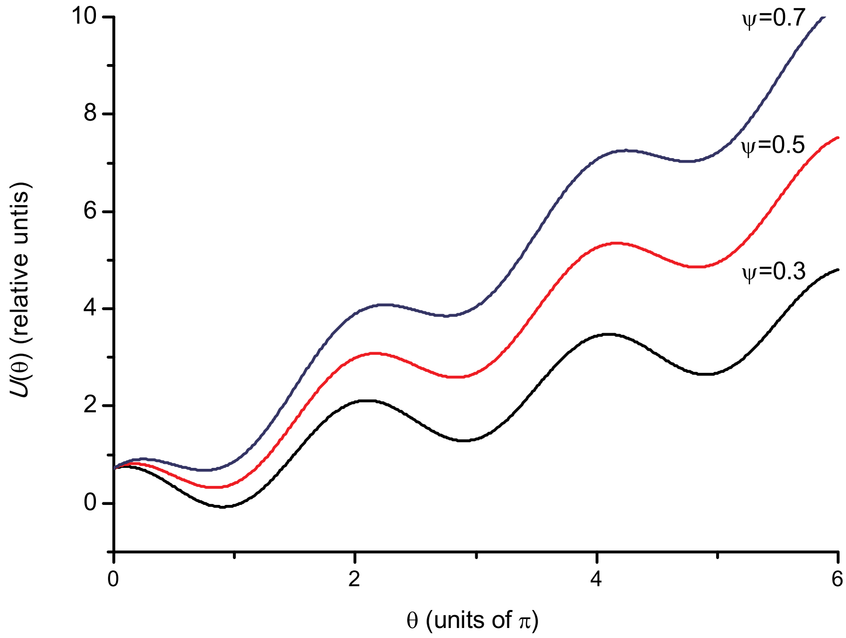

Figure 4.3: Chirped lattice potentials in the accelerated reference frame. The three curves shown were calculated from equation 4.19 for accelerating lattices ($+\beta$) with values of ψ of 0.3, 0.5 and 0.7.

The trajectories of particles within an accelerating lattice can be calculated by solving the equations of motion given in equations 4.17 and 4.18 numerically. Figure 4.4 shows a velocity phase space diagram mapping out particle trajectories across two lattice sites of a lattice with $\psi = 0.8$. Along the horizontal axis is the phase in the accelerated frame θ and the vertical axis corresponds to the phase velocity which can be converted to the actual velocity via $v = \frac{\eta\sqrt{\beta/2}}{q}$. The solid contour lines illustrate the trajectories that will be followed for particles with different initial $[\theta, \eta]$ phase coordinates. In this phase space a particle that is initially stationary and is not perturbed by the lattice would move in a parabolic trajectory centered on the θ axis. The tear drop shaped, almost closed, contour lines are the seperatrices which draw the boundaries between particles which are trapped by the potential and those that are untrapped. Particles within a separatrix remain trapped as the lattice accelerates and follow orbits of the local equilibrium point indefinitely, assuming no collisions take place. Untrapped particles, initially outside the separatrix, have their velocity perturbed but are not stably trapped. The maximum velocity a particle can have and be trapped is phase dependent and is given by [62]

$$v_c(\theta) = \pm V[\cos\theta - \cos(\pi + \sin^{-1}\psi) - \psi(\theta - \pi - \sin^{-1}\psi)]^{1/2} \tag{4.22}$$

where $V = \frac{2\sqrt{\beta/\psi}}{q}$.

Also shown in figure 4.4 are the trajectories of three particles (A, B and C) which have equivalent initial velocities ($\eta = 1.3$) but different phases ($\theta = -\pi, 0, +0.6\pi$) with respect to the lattice. The trajectories shown were followed over an equal time. Particle B is located within the separatrix and begins to map out the orbit it will follow over the duration of the lattice. Particles A and C are initially outside the separatrix but experience different perturbations by the lattice. Particle A is initially located close to the unstable equilibrium point at $[\theta, \eta] = [-0.83\pi, 0]$ and is strongly perturbed by the lattice. Its velocity is increased with respect to the lattice over the acceleration duration shown but as it is not stably trapped over longer durations it will follow the contour lines and its velocity will decrease with respect to the lattice. In comparison with particle A, particle C is weakly perturbed by the lattice and follows a near-parabolic trajectory.

The number of particles stably accelerated can be estimated for given initial velocity and spatial distributions by calculating the fraction of particles that lie within the separatrix. Figure 4.5 shows another phase space diagram for a lattice with $\psi = 0.8$, which in this case corresponds to an acceleration of 200 ms^{-1} in 100 ns with lattice beam intensities of 7.8×10^{12} Wm^{-2}. The phase space diagram is overlaid on the 1D velocity distribution of argon atoms with a temperature of $T = 100$ mK running along the z axis. The velocity values on the y axis are relative to the lattice velocity (i.e. a particle with a velocity 0 ms^{-1} is moving at the same velocity as the lattice).

The critical velocity given by equation 4.22 can be written as $v(x) = \pm\frac{\sqrt{\beta/2\psi}}{q}[\psi^{-1}\cos(qz) - qz - \pi + \psi^{-1}\sqrt{1-\psi^2} + \sin^{-1}\psi]^{1/2}$. The roots of this equation determine the spatial spread of trapped particles for particular experimental parameters

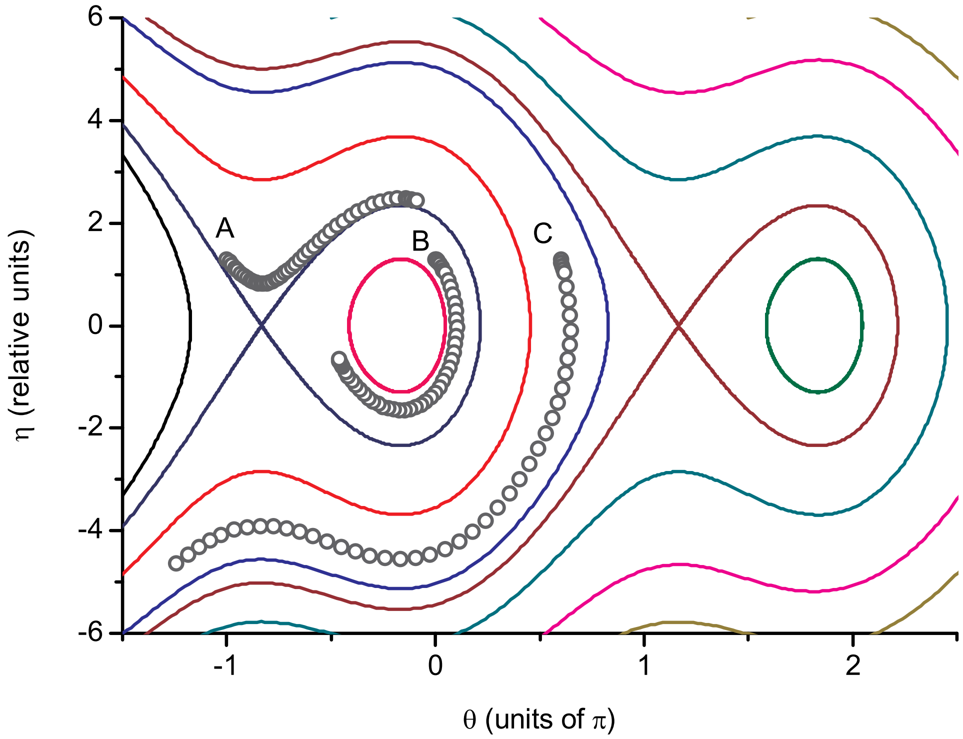

Figure 4.4: Velocity phase-space diagram for particles in an accelerating lattice with $\psi = 0.8$ [127]. The solid lines map out trajectories across two lattice sites centered at the stable equilibrium points $[\theta, \eta] = [-0.17\pi, 0]$ and $[\theta, \eta] = [1.83\pi, 0]$. The almost closed, tear drop shaped trajectories are the separatrices between trapped and untrapped particles in the potential. The three open circle trajectories A, B and C represent particles which have the same initial velocity ($\eta = 1.3$) but different phases ($\theta = -\pi, 0, +0.6\pi$) with respect to the lattice.

ψ, β and q. The first root can be determined analytically to be $z_1 = q^{-1}(-\pi + \sin^{-1}\psi)$ while the second root z_2 must be determined numerically. Assuming that the particles are initially in thermal equilibrium, the fraction that will be stably accelerated is given by

$$\kappa = \frac{\int_{z_1}^{z_2} \int_{v(z_1)}^{v(z_2)} \sqrt{\frac{m}{2\pi k_B T}} \mathrm{e}^{-mv^2/2k_B T}\, dv dz}{\int_0^{\lambda/2} \int_0^{\infty} \sqrt{\frac{m}{2\pi k_B T}} \mathrm{e}^{-mv^2/2k_B T}\, dv dz}, \tag{4.23}$$

where m is the particle mass, T is the temperature of the sample and k_B is the Boltzmann constant. For the case shown in figure 4.5 we find $\kappa = 0.24$. Figure 4.6(a) shows the fraction of accelerated Ar* as a function of ψ for an initial gas temperature of 100 mK. The decrease in κ is approximately linear from $\psi = 0.2$ to $\psi = 0.6$ and above $\psi = 0.8$. The κ values shown represent a maximum since for a real optical lattice the fraction will fall off in the radial direction due to the decrease in intensity of the lattice. Figure 4.6(b) shows the variation of κ with initial gas temperature for $\psi = 0.2, 0.5, 0.8$ and 0.9. The fraction accelerated is relatively constant until the initial velocity distribution becomes broader

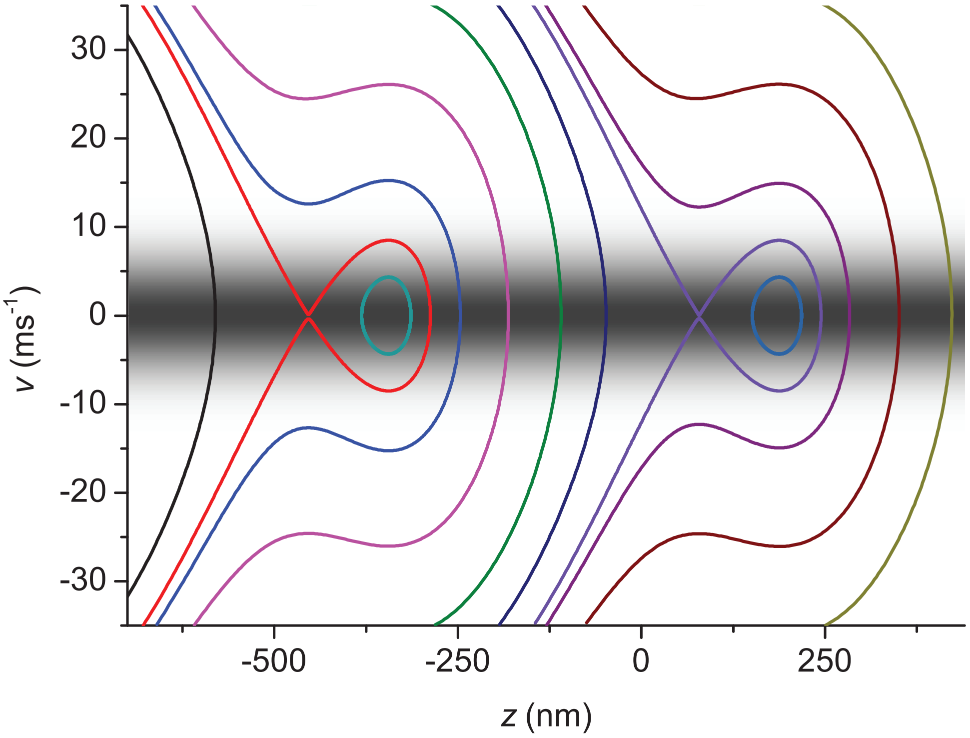

Figure 4.5: Phase space diagram for a lattice with $\psi = 0.8$ overlaid on the velocity distribution of Ar* atoms at a temperature of 100 mK. By calculating the number of atoms that lie within the separatrix we can determine the fraction κ of the initial distribution that will be accelerated.

than the velocity width of the separatrix. The lower the ψ parameter, and therefore the deeper the potential wells, the larger the fraction of warmer atoms that can be accelerated.

Although a large ψ parameter might seem attractive due to the larger number of particles that can be accelerated it is also important to consider the effect of ψ on the velocity distribution of the stably accelerated particles. The velocity width of the accelerated particles is determined by the well depth ΔU given by equation 4.20. The maximum velocity spread of the trapped and accelerated particles is given by

$$\Delta v = 2\sqrt{\frac{2\Delta U}{m}}. \tag{4.24}$$

This corresponds to the maximum kinetic energy a particle can gain in its oscillation around the local stable equilibrium point. Thus the velocity distribution of the accelerated particles can be controlled by tuning the potential well depth ΔU. However, there is a trade off between obtaining a narrow distribution and trapping a significant proportion of the distribution. Although a shallow potential well will produce a narrow velocity width the number of particles accelerated may be too low.

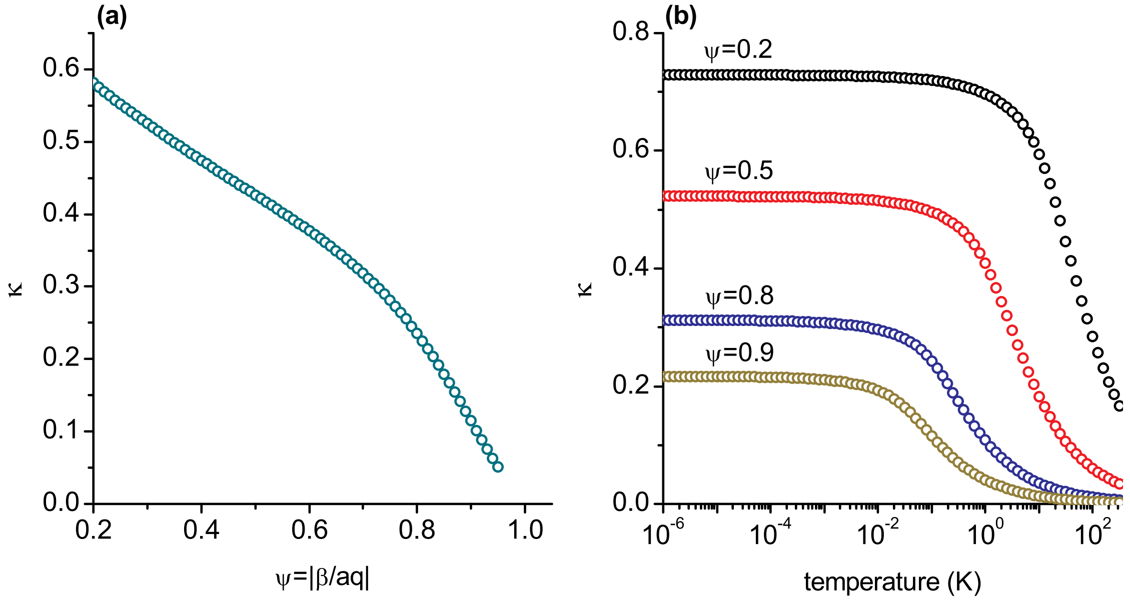

Figure 4.6: (a) Fraction, κ, of the initial 100 mK Ar* distribution stably accelerated as a function of ψ. (b) Fraction, κ, accelerated as a function of the initial temperature of the gas for $\psi = 0.2, 0.5, 0.8, 0.9$.

4.3.1 Radial motion in lattice

Unlike acceleration with a constant-velocity lattice there is no fundamental limit on the timescale for acceleration with a chirped lattice. However, one important consideration for the acceleration duration is the radial motion of particles in the lattice. Acceleration in the radial direction can lead to a large divergence of the particle beam. The intensity gradients in the radial direction are much more gradual than in the axial direction but over long enough times can still produce significant acceleration. The potential varies in the radial direction as

$$U(r) = U_0 \mathrm{e}^{\frac{-2r^2}{w_0^2}}, \tag{4.25}$$

where $U_0 = \frac{2\alpha_{stat} I_0}{\epsilon c}$ is the peak well depth, r is the radial coordinate and w_0 is the $1/\mathrm{e}^2$ radius of the beam. The force exerted by the potential is then

$$F(r) = \frac{4rU_0}{w_0^2} \mathrm{e}^{\frac{-2r^2}{w_0^2}}. \tag{4.26}$$

If we assume that the temperature of the gas is low in comparison with the depth of the potential, and the particles oscillate in the harmonic part of the potential, we can use a second order Taylor expansion to rewrite the force as $F(r) = -U_0 r/w_0^2$. Under this force the particles will undergo simple harmonic motion with an angular frequency given by

$$\omega = \sqrt{\frac{U_0}{w_0^2 m}}. \tag{4.27}$$

If we again consider a lattice produced by beam intensities of 7.8×10^{12} Wm^{-2} and a 1/e^2 radius of $w_0 = 75$ μm the oscillation period of an Ar* atom will be 24.3 μs. In experiments we want an acceleration time much less than this oscillation period such that acceleration in the radial direction is minimal.

The maximum force a particle in a given lattice can experience in the radial direction can be found by letting $\nabla F(r)$ equal zero. We find the maximum at $r = w_0/2$, where $\nabla F(w_0/2) = 2U_0/w_0 \mathrm{e}^{-1/2}$. If we again consider an experiment to accelerate Ar* by 200 ms^{-1} in 100 ns with lattice beams with intensities of 7.8×10^{12} Wm^{-2} and 1/e^2 radii of 75 μm, an atom experiencing the maximum radial force will be accelerated by 0.6 ms^{-1}.

4.4 High energy, chirped laser system

The laser system for optical Stark acceleration experiments must be capable of producing two high intensity ($10^{12} - 10^{14}$ Wm^{-2}) pulses with flat top temporal intensity profiles and controllable relative frequencies over durations of 10's to 100's of ns. No such laser is commercially available and instead a custom-built laser system was developed in our research group. The laser system was designed primarily for molecular deceleration experiments where the molecules are prepared in a molecular beam with mean particle velocities of 100's ms^{-1} (typically $\sim$ 400 ms^{-1}). If we assume a beam velocity of 550 ms^{-1}, deceleration to rest requires a laser capable of frequency chirping by $\Delta f = qv/2\pi \approx 1030$ GHz over the pulse duration. Flat top temporal intensity profiles are required so that the potential well depths in the lattice remain constant over the acceleration duration. Variation of the well depth can result in stably trapped particles being lost from the acceleration process or an increase in the velocity width of the accelerated particles, both of which are undesirable effects. The design, construction and characterisation of the chirped laser system has been well documented elsewhere [65, 125] and only an overview will be given here.

Figure 4.7 shows a schematic diagram of the laser system. The two output pulses of the laser are initially derived from a single 1064 nm Nd:YVO$_4$ microchip laser that can be rapidly frequency tuned by an electro-optic crystal in the cavity. The output from the microchip laser injection locks the frequency of a 1064 nm laser diode. The beam from the laser diode is coupled into a commercial fibre amplifier (IPG model no. YAR-1K-LP-SF) that amplifies the power to 1 W. A commercial electo-optic pulse shaper (Kentech Instruments) is used to chop the fibre amplifier output into two pulses of 20-1000 ns duration. The pulsed beam is split in two and coupled into two optical fibres, one 55 m longer than the other. The resulting path difference creates a time delay of 275 ns between the pulses at the exits of the fibres which allows the creation of a well-defined frequency difference when the microchip laser is chirped. On exiting the fibres, the pulses are amplified by two flash-lamp pumped, pulsed Nd:YAG amplifiers to produce the required intensities for optical Stark deceleration/acceleration. The following sections further describe the chirped microchip laser, the pulse amplification and the generation of an accelerating lattice.

4.4.1 Microchip laser

The microchip laser was constructed to provide a chirped master laser for pulsed amplification to the energies required for optical Stark deceleration. Figure 4.8 shows a schematic diagram of the microchip laser. The laser cavity is formed by one side of the Nd:YVO$_4$ microchip, which has a high reflecting reflective coating at 1064 nm, and a partially reflective output coupling mirror. The cavity length is 4.5 mm which produces the required free spectral range of well over 1 GHz. The Nd:YVO$_4$ microchip is pumped by an 808 nm laser diode and outputs at approximately 1064 nm. At the centre of the cavity is a 3 mm electro-optic lithium tantalate (LiTa0$_3$) crystal. Applying a voltage to the crystal changes the optical path length in the cavity allowing the rapid tuning of the microchip laser output frequency. A chirping efficiency of 15.4 ± 0.3 MHzV^{-1} was measured by varying a D.C. voltage applied to the LiTa0$_3$ crystal [65]. The microchip laser output is single mode and has a power of approximately 10 mW.

In order to generate rapid frequency changes, an arbitrary waveform generator (TTi: TGA12101) is used which is capable of applying voltage ramps of up to 20 V on 10's of ns timescales. The application of a rapid chirp induces relaxation oscillations which are observed as a large periodic modulation in the output intensity ($\approx 30\%$) of the laser. These oscillations are caused by the large difference between the cavity lifetime ($\tau \approx 300$ ps) and the lifetime of the excited state in the Nd:YVO$_4$ microchip ($\tau = 90$ μs) [128].

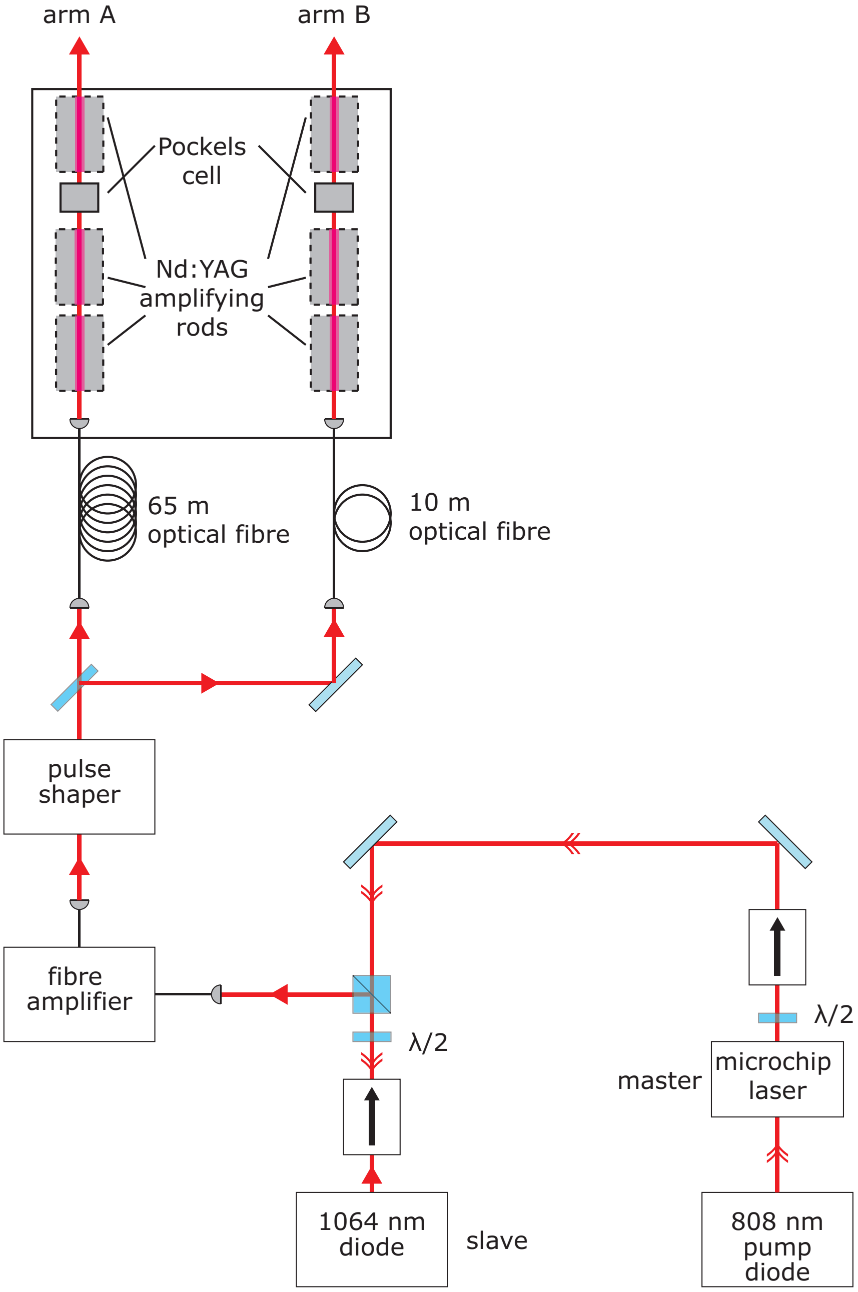

Figure 4.7: Schematic diagram of the high energy, chirped laser system constructed for optical Stark deceleration experiments.

In order to suppress these intensity oscillations, the microchip laser output is seeded into a 1064 nm diode laser in a master-slave configuration, similar to that described for the MOT lasers in section 3.3.2. The frequency output of the slave laser can match that of the master up to chirps of ≈ 1.4 GHz and exhibits an intensity modulation of less than 2%. The output of the slave laser is aligned through the fibre amplifier to increase the power to 1 W before the pulse amplification stage.

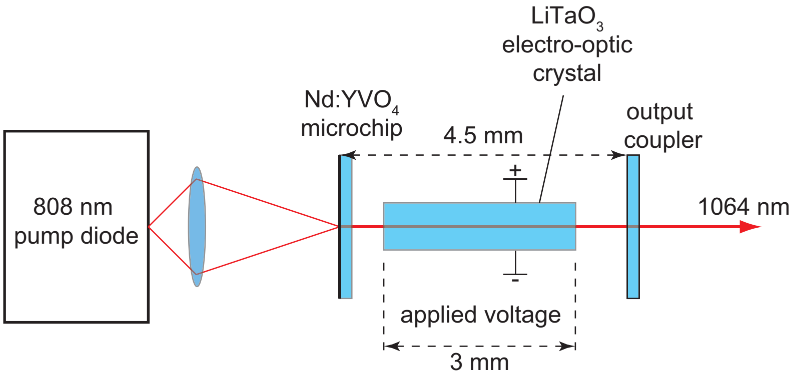

Figure 4.8: Schematic diagram of the microchip laser showing the LiTaO$_3$ electro-optic crystal that is used to chirp the laser output frequency.

4.4.2 Pulse shaping and amplification

The output beam from the fibre amplifier is aligned through the pulse shaper and then split into two beams. The pulsed beams are coupled into two optical fibres, of lengths 10 m and 65m, which creates a time delay between the pulses of 275 ns at the exits of the fibres. A custom-built Nd:YAG system (Continuum lasers) amplifies the pulses exiting the fibres to the required energies. Each arm of the amplifier consists of three Nd:YAG rods flash-lamp pumped at 10 Hz. The gain in each arm is on the order of 10^7. In order to produce flat top temporal profiles at the exit of the amplifier, an input pulse shape that is well approximated by an exponential rise is used to compensate for the temporally varying gain of the Nd:YAG rods during amplification. The pulse shaper produces two pulses ($\tau = 100 - 200$ ns) which are turned on 275 ns apart such that the first pulse exits the long fibre in coincidence with the second pulse from the short fibre.

The time delay allows us to overlap pulses with frequencies which are derived from different parts of the chirp applied to the microchip laser and thus control the frequency difference between the pulses. The first pulse from the shorter fibre is blocked by a Pockels cell and a polariser before the final Nd:YAG amplification rod. The amplifier is capable of producing pulse energies of 700 mJ for μs pulse durations. At pulse durations of 100-200 ns the output pulse energies are typically 350-400 mJ. Focusing these output pulses to beam waists of 100 μm or less allows the creation of intensities on the order of 10^{14} Wm^{-2}. Figure 4.9 shows the temporal intensity profile of a 140 ns flat top pulse measured by picking off a small portion of one of the high energy output pulses and aligning it onto a photodiode. In the next section we refer to the long arm of the laser system as arm A and the short arm as arm B, as shown in figure 4.7.

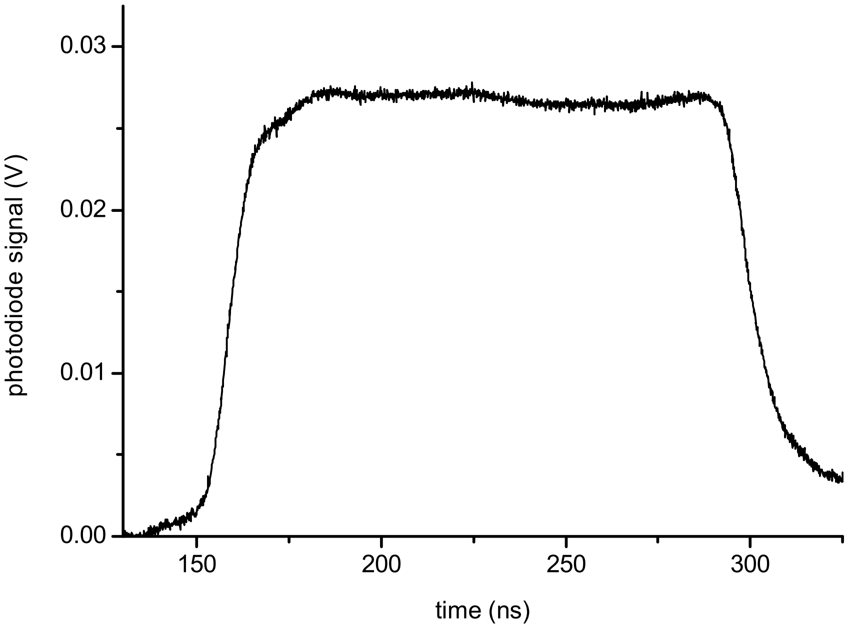

Figure 4.9: Temporal intensity profile of an output pulse from on arm of the high energy, chirped laser system.

4.4.3 Generating an accelerating lattice

In order to generate an accelerating lattice, we need to overlap the beams to create the interference pattern and then chirp the frequency difference between them by applying a voltage to the electro-optic crystal in the microchip laser. The waveform generator can be used to apply arbitrary voltage ramps of up to 20 V to the electro-optic crystal. Figure 4.10 shows how a frequency difference can be created between the output pulses by applying either a linear or sinusoidal chirp. In figure 4.10(a) the frequency is chirped linearly from 0 MHz to 308 MHz in 100 ns. This frequency excursion corresponds to a voltage ramp of 20 V applied to the electro-optic crystal, assuming a chirping efficiency of 15.4 MHzV^{-1}. The temporal position of the chirp is delayed by 275 ns between the arms of the laser system and when the frequency of arm A is ramped up, between 200 ns and 300 ns, the frequency difference between the pulses increases. Once the frequency difference reaches 308 MHz it remains fixed until 475 ns when the frequency of arm B is chirped and the frequency difference decreases. If we use a 140 ns pulse we can sychronise the chirp such that over the pulse duration the frequency difference can be swept from 0 MHz to 308 MHz. If the lattice is turned on 20 ns before the chirp begins and turned off 20 ns after the chirp ends we create a lattice which is initially stationary for 20 ns, then accelerates to 164 ms^{-1} over 100 ns before traveling at a constant velocity for the remaining 20 ns before the lattice is switched off. This frequency chirp corresponds to a lattice acceleration from rest to 164 ms^{-1}. If we synchronise the chirp such that the frequency difference is decreasing over the duration of the lattice pulse we create a decelerating lattice.

A lattice velocity of 164 ms^{-1} is the maximum that be achieved using the 20 V output of the waveform generator. To achieve higher frequency excursions and faster lattice velocities we use a sinusoidal voltage ramp amplified by a tank circuit. The tank circuit had an amplification factor of 3.5 at our operation frequency of 1.82 MHz (for details of the tank circuit see reference [125]). Figure 4.10(b) shows a 1 GHz sinusoidal chirp which corresponds to 65 V being applied to the electro-optic crystal. A modulation frequency of 1.82 MHz was used such that the 275 ns delay in the chirp resulted in a π phase shift between the sinusoidal chirps of the two beams. Over a quarter period (137 ns), between 275 ns and 411 ns, the frequency difference is swept from 0 MHz to 1000 MHz. If this part of the chirp is synchronised with the lattice pulses we create a lattice accelerating from 0 ms^{-1} to 532 ms^{-1}. Using a sinusoidal chirp means that the lattice velocity is never constant and we need to use a pulse duration equal to a quarter period of the chirp such that the lattice is turned on at rest and off at the maximum velocity of 532 ms^{-1}. If we instead synchronise the portion of the chirp from 0 ns to 137 ns with the pulse we create a lattice which decelerates from 532 ms^{-1} to rest.

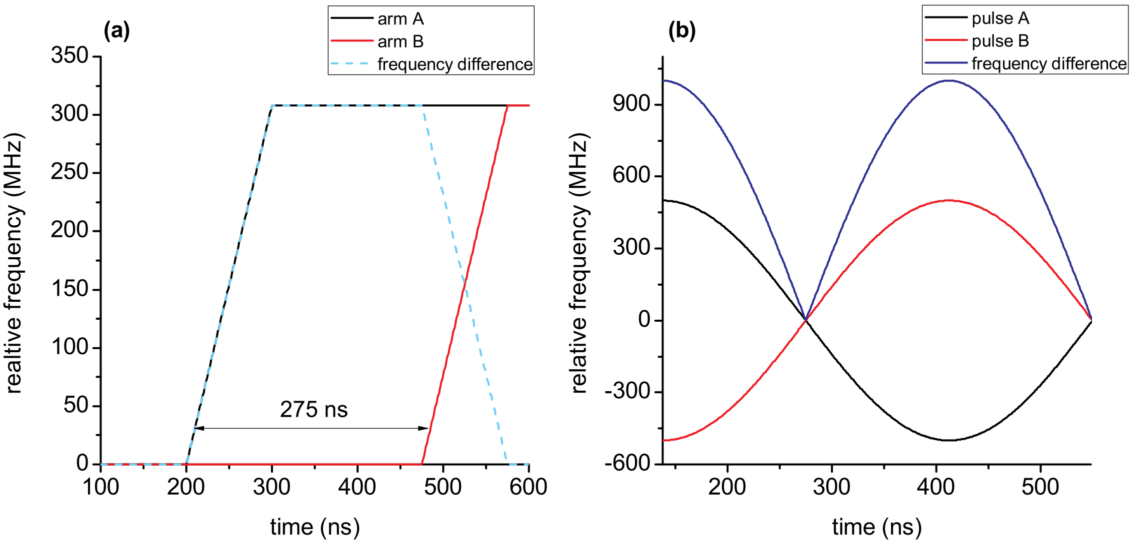

Figure 4.10: Generation of an accelerating lattice with both a linear (a) and a sinusoidal (b) chirp. In (a) the beams are chirped linearly from 0 to 308 MHz in 100 ns. The 275 ns difference between the start times of each beams chirp allows the creation of a frequency difference between them. The sinusoidal waveform used to produce the chirp in (b) has a frequency of 1.82 MHz. The 275 ns delay creates a π phase difference between the chirp of the two beams which maximises the frequency difference between them. In this example the beams are chirped from 0 to 1 GHz.

4.4.4 Analysis of the frequency chirp

In order to monitor the frequency difference between the two output pulses, we pick off a small portion of each pulse and heterodyne (beat) them on a photodiode. The frequency difference between the two pulses governs the beat frequency $\omega(t) = |\omega_A(t) - \omega_B(t)|$. Figure 4.11(a) shows a beat signal that corresponds to a sinusoidal chirp from 0 MHz to 1020 MHz over the pulse duration of 140 ns. This signal was observed on a fast photodiode with a bandwidth 2 GHz. Extraction of the instantaneous frequency $f(t)$ of the beat signal across the pulse duration is not trivial and we use the analysis technique of Fee *et al.* [129]. We assume that the electric fields of the laser pulses from arm A and arm B of the laser system are given by $E_{A,B}(t) = E_{A0,B0}(t)\exp[i(\phi_{A,B}(t) + \omega t)] + c.c.$, where $E_{A0,B0}(t)$ are the electric field amplitudes, ω is the optical oscillation frequency and $\phi_{A,B}(t)$ is the time dependent phase. The derivative of the phase gives the instantaneous frequency $f(t)$. The beat signal observed on the photodiode will follow the form,

$$V \propto |E_A(t)|^2 + |E_B(t)|^2 + E_A(t)E_B^*(t)\exp[i(\phi_A(t) - \phi_B(t))] + c.c. \qquad (4.28)$$

Determining the instantaneous frequency $f(t)$ involves separating the third term from the first two intensity terms and then extracting and measuring how the phase changes with time on top of its oscillation every 2π. The rate of change of the instantaneous phase $\phi(t) = \phi_A(t) - \phi_B(t)$ then gives the instantaneous frequency. In order to isolate the third term in equation 4.28, we first perform a Fourier transform on the beat signal. In most cases the beat frequency is higher than the Fourier components of the first two terms and we can apply a band pass filter to extract the higher frequency Fourier components of the third term. The filtered frequency data are then transformed back into the time domain and the instantaneous phase $\phi(t)$ is determined by measuring the phase angle of this term. Finally, the instantaneous frequency is determined by differentiating the phase with respect to time, $f(t) = d\phi(t)/dt$.

This analysis was carried out in MATLAB. Figure 4.11(b) shows the instantaneous frequency as a function of time resulting from analysis of the beat signal in (a). A super-Gaussian band pass filter, of the form $\exp[-1((-f_0+f)/\Delta f)^{x \gg 2}]$, was used in this analysis. The oscillations in the instantaneous frequency resulting from the analysis are known as Gibb's oscillations and result from the discontinuity and cut-off of the mask in Fourier space, which restricts the range of frequencies [130]. For more details on the beat signal analysis see reference [125].

Determining the instantaneous frequency difference throughout the pulse duration allows us to see how the lattice velocity will change. The lattice corresponding to the beat signal in figure 4.11 will accelerate from 0 ms^{-1} to 542 ms^{-1} and the velocity change will follow the sinusoidal form of the frequency change.

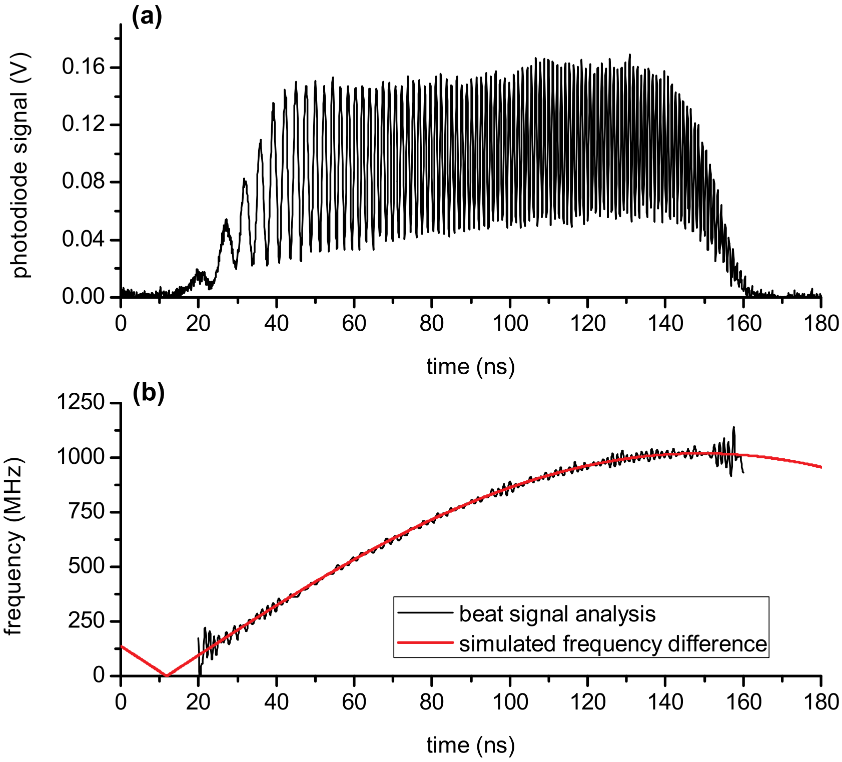

Figure 4.11: (a) Beat signal measured for a sinusoidal chirp from 0 MHz to 1020 MHz applied over the pulse duration of 140 ns. (b) Frequency of the beat signal over the duration of the pulse. The black trace is the frequency determined using the analysis technique described in the text while the red trace is a fit using the function $f(t) = f_0|\cos(\omega t)|$, where f_0 is the amplitude of the chirp and ω is the modulation frequency of the voltage applied to the electro-optic crystal.

4.5 Modeling of deceleration and acceleration

The model of chirped lattice acceleration presented in section 4.3 is useful for gaining insight into the particle acceleration mechanism. However, this model is too simple to accurately simulate experiments as it does not account for intensity variations over the duration of the pulse or allow the simulation of non-linear chirps. To simulate acceleration with experimental lattice parameters we use a Monte Carlo method whereby individual particle trajectories are calculated for many particles. The particles are assigned initial spatial and velocity distributions corresponding to those expected in experiments and by performing the calculation for a large enough sample we can build up the velocity distribution of particles after acceleration.

In order to calculate the trajectory of a particle over the acceleration duration, assuming no collisions, we can solve the equation of motion given by equation 4.16 for a given initial position and velocity. To do this we first rewrite the equation of motion as two coupled equations

$$\begin{aligned} \frac{dv(z,t)}{dt} &= -\frac{\alpha q I(t)}{m\epsilon_0 c}\sin(qz-\phi(t)), \\ \frac{dz}{dt} &= v(z,t) \end{aligned} \tag{4.29}$$

where $\phi(t)$ is the relative phase between the two beams. These coupled equations can then be solved using the fourth order Runge-Kutta method for ideal or experimental temporal intensity profiles and chirps. This modeling method has previously been implemented to model acceleration in one dimension where the particles were equally distributed across 20 μm and assigned a Maxwell-Boltzmann velocity distribution [125]. Although this model predicts the final velocity of the accelerated particles and fraction of particles accelerated, it is not complete. In a three-dimensional lattice the well depth decreases in the radial direction and in the axial direction if the lattice beams are not exactly counter-propagating, as is the case in our experiments. The acceleration force will therefore vary spatially across the lattice. In order to include the effect of the spatially varying force, we have extended the model to include a three-dimensional calculation of the lattice potential.

4.5.1 Calculation of the lattice potential

In order to calculate the lattice potential, given by $U = -\frac{1}{2}\alpha|E|^2$, in three dimensions we need to calculate the interference (i.e. the $|E|^2$ term) of the two lattice beams for a given geometry. We assume the two focused lattice beams have circular Gaussian profiles where, for a beam traveling in the z direction, the electric field in radial coordinates $E(r,z)$ is given by

$$E(r,z,t) = E_0(t)\epsilon\frac{w_0}{w(z)}\mathrm{e}^{i(kz-\phi(t))}\mathrm{e}^{-r^2/w(z)^2}\mathrm{e}^{ikr^2/2R(z)}\mathrm{e}^{-i\zeta(z)}, \tag{4.30}$$

where w_0 is the beam waist at the focus and $w(z)$ is the beam waist at position z. The variable $\zeta(z) \equiv \tan^{-1}(z/z_R)$ is the Gouy phase shift, where $z_R = \pi w_0^2/\lambda$ is the Rayleigh range, and $R(z) = z + z_R^2/z$ is the radius of curvature at plane z. The first term in this equation, $E_0(t)$, is the electric field amplitude, which varies over the lattice duration, and the second term, $w_0/w(z)$, accounts for the decreasing amplitude away from the focus. The third term, $\mathrm{e}^{i(kz-\phi(t))}$, represents the wave traveling in the z direction and the fourth term, $\mathrm{e}^{-r^2/w(z)^2}$, gives the radial Gaussian intensity profile.

In our simulations we want to calculate the potential formed by the spatial overlap of two beams, crossing a small angle, for any given x, y, z coordinate. In order to do this, we rotate our coordinates through an angle θ about the z axis to obtain a new set of Cartesian coordinates x', y', z' where we define z' as the direction of propagation of the laser beam. The new coordinate system is calculated by multiplying the original coordinates by Euler's matrix,

$$\begin{pmatrix} x' \\ y' \\ z' \end{pmatrix} = \begin{pmatrix} \cos\theta & 0 & -\sin\theta \\ 0 & 1 & 0 \\ \sin\theta & 0 & \cos\theta \end{pmatrix} \begin{pmatrix} x \\ y \\ z \end{pmatrix} \tag{4.31}$$

which gives

$$\begin{pmatrix} x' \\ y' \\ z' \end{pmatrix} = \begin{pmatrix} x\cos\theta - z\sin\theta \\ y \\ x\sin\theta + z\cos\theta \end{pmatrix}. \tag{4.32}$$

Figure 4.12 shows the geometry of two overlapped lattice beams, beam 1 propagates along axis z_1' which is at an angle $\theta = \theta_1$ with respect to z while beam 2 travels along axis z_2' which is at an angle of $\theta = \theta_2$. By substituting $z_{1,2} = z_{1,2}'$ and $r_{1,2} = \sqrt{x_{1,2}'^2 + y_{1,2}'^2}$ for the two beams into equation 4.30 we can calculate $|E(x,y,z,t)|^2 = |E_1(x,y,z,t) + E_2(x,y,z,t)|^2$.

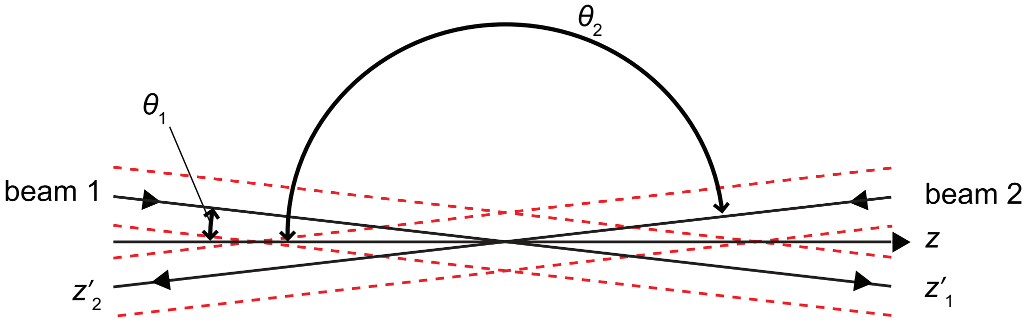

Figure 4.12: Geometry of the overlapped lattice beams which form the lattice. Beam 1 propagates along axis z_1' which is at an angle θ_1 to z. The second lattice beam propagates along z_2' at an angle θ_2 to z. The z axis defines the central axis of the optical lattice.

Figure 4.13 shows a plot of the interference pattern calculated for two equal intensity beams with a focal waist of $w_0 = 50$ μm crossing at a half angle of 82.5°. Although the individual lattice sites cannot be resolved in the plot of the whole lattice it can be seen that the intensity peaks, and therefore the potential well depths, decrease away from the centre of the lattice. Shown inset in the figure are seven individual lattice sites from the centre of the lattice which have a periodicity of approximately 532 nm. In this geometry the lattice has a length of 0.77 mm and has approximately 1450 lattice sites.

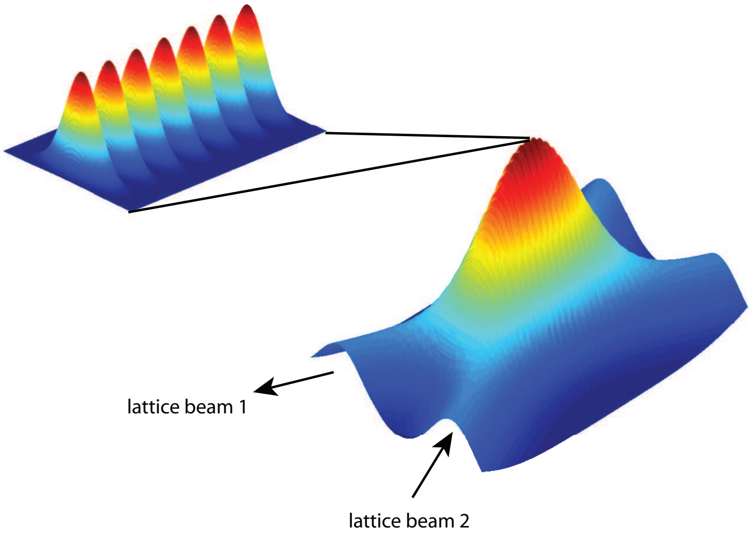

Figure 4.13: Calculated interference pattern of the two lattice beams crossing at half angle of 82.5°.

4.5.2 Acceleration simulations

To incorporate our calculation of the three-dimensional lattice potential into the acceleration simulations we rewrite the coupled equations 4.29 as

$$\begin{aligned} \frac{dv(z,t)}{dt} &= -\nabla U(x,y,z,t), \\ \frac{dz}{dt} &= v(z,t). \end{aligned} \tag{4.33}$$

Although we calculate the potential in three dimensions we only consider the force in the z direction as the radial forces are negligible in comparison, as discussed in section 4.3.1. In order to simplify the computation of these coupled equations, we rewrite the first equation as

$$\begin{aligned} \frac{dv(z,t)}{dt} &= -\frac{\alpha}{2m}\left(\frac{|E(x,y,z-\Delta z,t)|^2 - |E(x,y,z+\Delta z,t)|^2}{2\Delta z}\right), \\ \frac{dz}{dt} &= v(z,t), \end{aligned} \tag{4.34}$$

where the term in brackets in the first equation is the simplified version of the intensity gradient. We solve these coupled equations using the fourth order Runge-Kutta method implemented in MATLAB using the ODE45 solver. Particles are assigned an initial x, y, z coordinate in the lattice and an initial velocity $v(x, y, z)$ and at each time step in the simulation the instantaneous intensity $I(t)$ and phase $\phi(t)$ are used to calculate the potential experienced by the particle. The intensity $I(t)$ can be obtained from either ideal or experimental temporal intensity profiles of the lattice pulses. The phase $\phi(t)$ is determined from an ideal or experimental chirp by integrating the instantaneous relative frequency. We typically run simulations for $N > 50000$ particles to suppress statistical fluctuations. In order to demonstrate our simulations, the following two sections present case studies of acceleration and deceleration with a chirped lattice.

4.5.3 Case study one: acceleration of Ar*

In the introduction to this chapter we discussed the importance of optical Stark acceleration experiments. Here we present the simulation of an experiment to accelerate Ar* atoms initially confined in a MOT to 100 ms^{-1}. This case study is relevant to the next chapter where we present Ar* optical Stark acceleration experiments.

In order to accelerate the stationary Ar* atoms, we generated a lattice which was initially at rest and then accelerated to the desired final velocity. Figure 4.14 shows the lattice pulse characteristics used in the simulation. We used a flat-top pulse with a super-Gaussian form $I(t) = I_0 \exp(-((t_0+t)/\Delta t)^{30})$, where I_0 is the peak intensity, t_0 defines the time at which the pulse is centered and Δt determines the width of the pulse. The pulse had a full width at half maximum (FWHM) duration of 129 ns and a 10-90% rise/fall time of approximately 6 ns. The pulse remained flat once it reached its peak intensity until it began to switch off. A linear frequency chirp from 0 MHz to 188 MHz was applied over a duration of 80 ns. This frequency chirp corresponded to a lattice acceleration from 0 ms^{-1} to 100 ms^{-1} over the chirp duration. The peak intensity of the lattice pulses is 6×10^{12} Wm^{-2} which, from equation 4.20, gives an accelerating well depth of 306 mK. We set the beam waist at the focus of the lattice beams to $w_0 = 65$ μm for our calculation of the lattice potential. In order to create this lattice, beam energies of 5 mJ are required which is well within the capability of out laser system.

We assigned the atoms initial spatial and velocity distributions which corresponded to those measured in the MOT. In the axial direction the atoms were given a Gaussian spatial distribution with a $1/\sqrt{e}$ radius of 360 μm and in the radial direction the atoms were

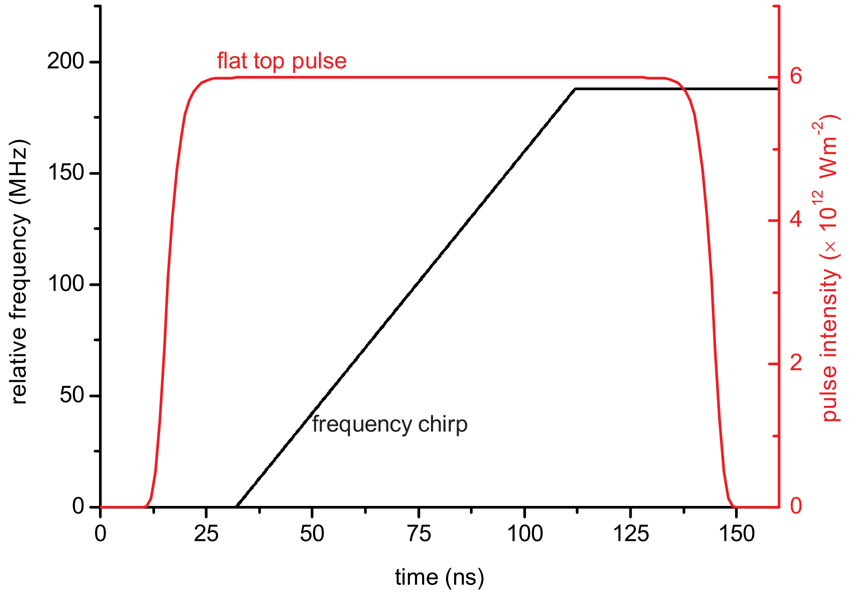

Figure 4.14: Laser pulse characteristics of the lattice beams used in the simulation of Ar* acceleration. The pulse intensity is modeled using a super-Gaussian function to achieve an ideal flat top profile with a 10-90% rise time of 6 ns and a FWHM duration of 129 ns. A linear frequency chirp from 0 MHz to 188 MHz is applied over 80 ns and produces a lattice acceleration from rest to 100 ms^{-1}.

evenly distributed over the lattice as the lattice width was much smaller than the MOT. The initial velocity distribution of the atoms was generated by generating a random normal distribution and multiplying it by $\sqrt{k_B T/m}$ where T was the temperature of the atomic cloud and m was the atomic mass. We calculated the trajectories of 50000 atoms. Figure 4.15(a) shows the initial velocity distribution used in this simulation which corresponded to a temperature of 70 μK.

Figure 4.15(b) shows the velocity distribution of the Ar* atoms after acceleration. The velocity distribution shows an accelerated peak of atoms at a velocity of 100 ms^{-1}. The number of atoms in the peak is 5614 which corresponds to 11% of the total number of atoms in the initial distribution. The velocity width of the accelerated peak is an important charactestic for collision experiments. In this simulation the FWHM velocity width is 10 ms^{-1}. Although the velocity distribution of the accelerated atoms is not thermal it can be instructive to assign a temperature to the atoms. If we assume that a thermal velocity distribution the temperature can be calculated from $v_{FWHM} = \sqrt{\frac{8 \ln 2 k T}{m}}$ which gives a temperature for the accelerated atoms of 87 mK. Again, this is not a true temperature but a useful measure of the energy spread in the accelerated packet. The simulation also shows how the velocity of atoms that are not stably accelerated is perturbed. A large peak at 0 ms^{-1} remains but we see two other low velocity peaks, one at -13 ms^{-1} and the other at approximately 5 ms^{-1}. Over the acceleration time the atoms trapped within the lattice sites are transported by 4 μm and have an acceleration of 1.25×10^9 ms^{-2} ($\sim 10^8 g$).

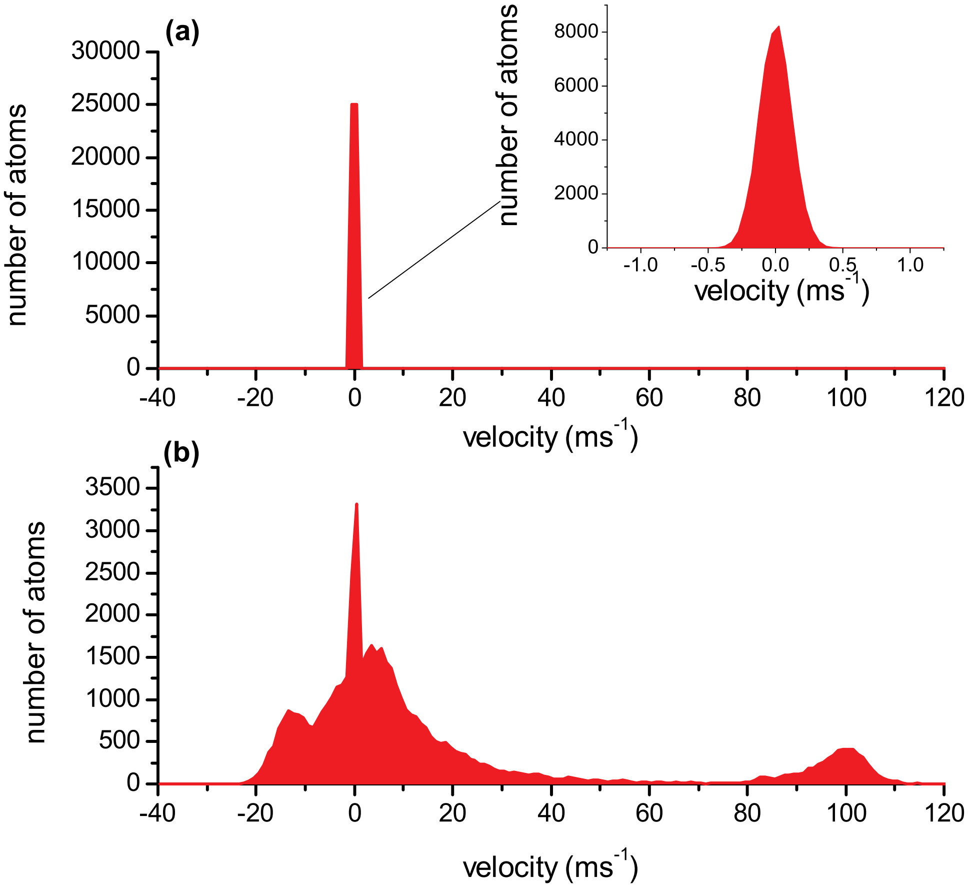

Figure 4.15: Velocity distributions of 50000 Ar* atoms before and after acceleration by the chirped lattice. The initial velocity distribution of the atoms in the MOT is shown in (a) and corresponds to a temperature of 70 μK ($v_{FWHM} = 0.3$ ms^{-1}). The velocity distribution after acceleration is displayed in (b) and shows an accelerated peak of atoms at 100 ms^{-1}. These graphs were produced by binning atoms in 1 ms^{-1} intervals. The inset in figure (a) shows a higher resolution plot of the initial distribution with generated with a binning interval of 0.05 ms^{-1}.

4.5.4 Case study two: deceleration of C_6H_6

In section 4.2 we discussed the deceleration of C_6H_6 to rest in a constant-velocity lattice experiment [64]. It was mentioned that one primary drawback of using a constant-velocity lattice is that the velocity width of the decelerated molecules is at best equal to that in the molecular beam before deceleration. In this simulation we replicate the initial conditions of that experiment where the molecular beam had a mean velocity of 420 ms^{-1} and a temperature of 1.6 K. This allows us to make a comparison of the performance of the two molecular deceleration techniques.

To achieve deceleration we turn on the lattice at the same velocity as the molecular beam and then chirp the frequency difference to zero. Figure 4.16 shows the relative frequency and the intensity profile of the lattice pulses used in the simulation. A super-Gaussian temporal intensity profile with a FWHM duration of 156 ns was used. A sinusoidal chirp was simulated to show that a non-linear chirp can also be used for acceleration/deceleration. The initial frequency difference when the lattice was switched on was set to 789 MHz such that the lattice velocity was 420 ms^{-1}. The polarisability to mass ratio for C_6H_6 ($\alpha = 11.6$ Cm^{2}V^{-1}, $m = 78$ a.m.u.) is less favourable to acceleration/deceleration than for Ar* and higher intensity lattice pulses are required for equivalent accelerations/decelerations. Simulations were carried out with peak pulse intensities in the range 2×10^{14}-3×10^{14} Wm^{-2}. The beam waist at the focus of the lattice beams was set at $w_0 = 50$ μm for the simulation of the lattice. Such a lattice can be created experimentally with pulse energies of 370 mJ or less which is within the capability of our laser system.

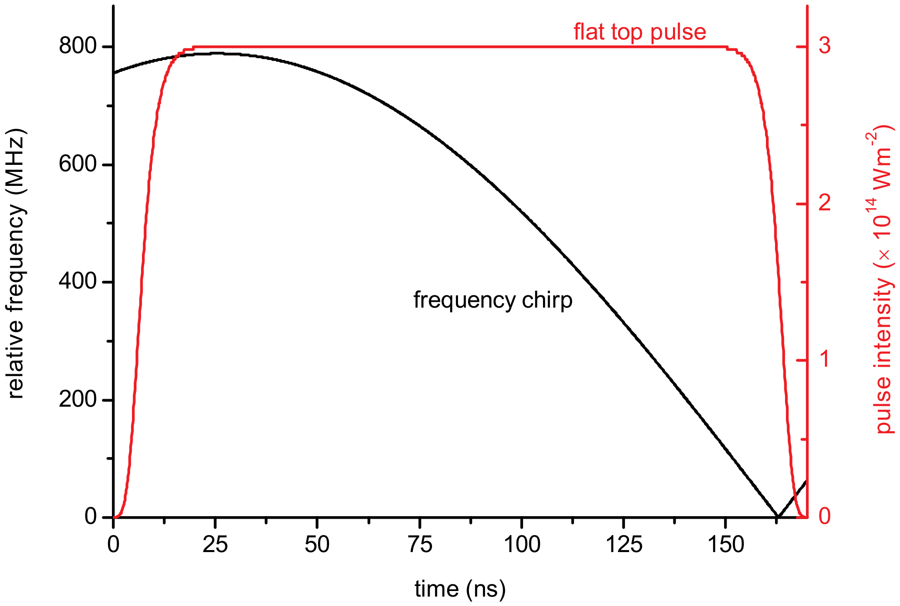

Figure 4.16: Lattice beam characteristics used to simulate the deceleration of C_6H_6. The intensity profile follows a super-Gaussian form with a FWHM duration of 156 ns. A sinusoidal chirp from 789 MHz to zero is applied over the pulse duration which corresponds to a lattice deceleration from 420 ms^{-1} to rest.

The molecules were initially distributed evenly across the lattice in all directions as the spatial extent of the molecular beam is considerably larger than the lattice dimensions in experiments. The trajectories of 100,000 atoms were calculated in this simulation. Figure 4.17(a) shows the initial velocity distribution of the molecules which corresponds to a 1.6

K molecular beam with a velocity of 420 ms^{-1}. Figures 4.17(b)-(d) show velocity distributions after deceleration for three different pulse intensities. The distribution in figure 4.17(b) was produced with pulse intensities of 3×10^{14} Wm^{-2} which gives a decelerating well depth of 6.0 K. A portion of the initial distribution has been decelerated to rest. The velocity distribution of the undecelerated molecules is a large peak, similar in shape to the initial distribution, centred at 430 ms^{-1} and with a much larger velocity width ($\Delta v_{FWHM} = 90$ ms^{-1}) than the initial distribution ($\Delta v_{FWHM} = 31$ ms^{-1}). The number of molecules in the decelerated peak is 3160 which equates to 3% of the total number in the initial distribution. The FWHM velocity width is 26 ms^{-1} which corresponds to a temperature of 1.1 K. Thus, the energy spread in the decelerated peak is narrower than in the initial molecular beam which would have been impossible using a constant-velocity lattice. Over the deceleration duration the particles trapped within the lattice sites are transported by 29 μm and undergo acceleration approximately 3×10^8 times that of gravity.

Although the velocity width in figure 4.17(b) is narrower (1.1 K) than that in the initial distribution (1.6 K) for some applications (e.g. collisional experiments) it may be desirable to have a narrower energy spread. In order to show that narrower energy spreads can be achieved, we simulated deceleration with lower beam intensities. Figures 4.17(c) and 4.17(d) show the C_6H_6 velocity distribution after deceleration with lattice beam intensities of 2.5×10^{14} Wm^{-2} and 2×10^{14} Wm^{-2} respectively. These intensities correspond to well depths of 9.0 K (c) and 6.0 K (d) in the decelerating frame. The fraction of molecules decelerated drops to 1.5% in (c) and 0.5% in (d). More importantly however, the velocity spread in the decelerated peak also becomes smaller. For lattice beam intensities of 1.25×10^{14} Wm^{-2} the velocity width is 23 ms^{-1} which corresponds to a temperature of 908 mK. At lower intensities of 1.0×10^{14} Wm^{-2} the velocity width is 17.6 ms^{-1} and the temperature is 527 mK. This ability to tune the final energy width of the decelerated/accelerated particles is an important feature of this technique.

In previous one-dimensional simulations of the deceleration of C_6H_6 to rest from a 2 K molecular beam at 400 ms^{-1}, 9.6% of the initial distribution was decelerated for lattice beam intensities of 1.0×10^{14} Wm^{-2} [125]. The velocity width of the decelerated packet of molecules was 34 ms^{-1}. In our three-dimensional simulation the numbers for both the portion decelerated and the velocity width are smaller even though we use larger

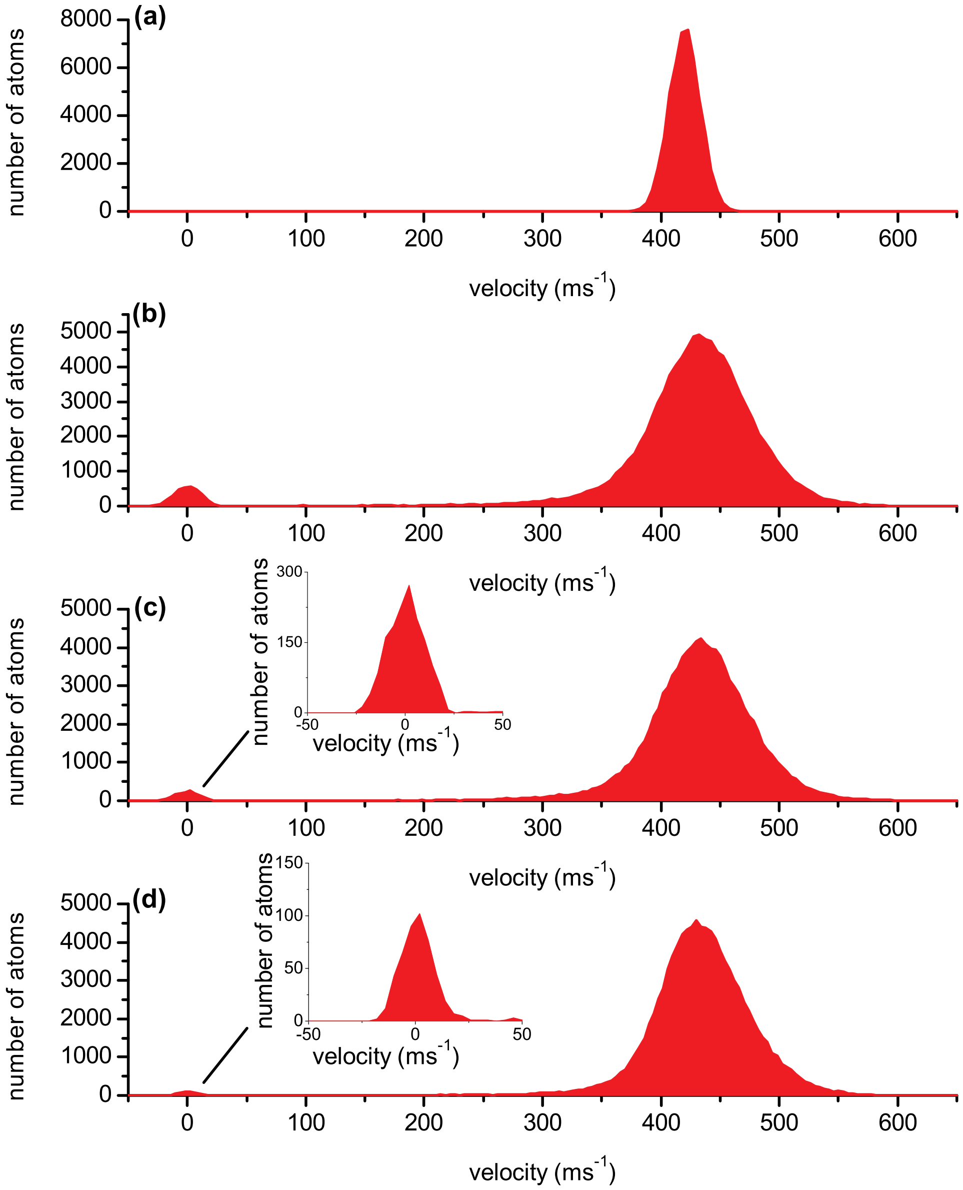

Figure 4.17: Velocity distributions of 100000 C_6H_6 molecules before and after deceleration by the decelerating lattice. Figure (a) shows the velocity distribution of a 1.6 K molecular beam with a mean velocity of 420 ms^{-1}. Figures (b)-(d) show the velocity distributions after the lattice has been applied for lattice beam intensities of (b) 3×10^{14} Wm^{-2}, (c) 2.5×10^{14} Wm^{-2} and (d) 2×10^{14} Wm^{-2}. Reducing the lattice beam intensity results in fewer molecules being decelerated but also produces narrower velocity distributions in the decelerated peaks as discussed in the text. These graphs were produced by binning molecules in 4 ms^{-1} intervals.

intensities. This would be expected due to the radial and axial decrease in potential well depth. This three-dimensional model allows us to more accurately model experiments for given lattice beam intensities.

4.6 Summary

In the next chapter we will present experiments on optical Stark acceleration of Ar* atoms. The material covered in this chapter acts as an in-depth background to these experiments. As well as the theory behind acceleration with a chirped lattice we have also discussed the laser system that has been developed to accelerate/decelerate atoms and molecules. This laser system plays a crucial role in the next chapter and the details provided here as well as the chirp analysis technique will be particularly relevant. The model used to simulate acceleration will also be important in the next chapter. In this chapter we have presented case studies of both acceleration and deceleration where the velocity distribution of the particle sample was calculated. The model of acceleration can be extended to fit experimental data by considering the physical details of the experimental measurement.

Chapter 5

Optical Stark acceleration of Ar*

In order to test chirped optical Stark acceleration, we applied the technique to accelerate Ar* atoms initially confined in the MOT. The Ar* MOT atoms offered a useful test sample for acceleration as they had a favourable polarisability to mass ratio ($\alpha = 47.9 \times 10^{-40}$ Cm^{2}V^{-1}, $m = 40$ amu), a narrow initial velocity distribution and could readily be detected using the experimental set-up described in chapter 3. Also, the close proximity of Ar* atoms to the ionisation potential (4.2 eV) allowed us to evaluate the technique on an easily ionised species which could not be accelerated using the constant-velocity lattice scheme, due to the high intensities required (see section 4.2).

Figure 5.1 shows a schematic diagram of the experimental set-up for chirped lattice acceleration. The lattice pulses from the chirped laser system (see section 4.4) were overlapped at their foci and superimposed on the MOT atoms to create the deep periodic lattice potential. The frequency difference was initially set to zero and then chirped to create a lattice that was initially stationary and then accelerated to a final velocity determined by the final frequency difference. The accelerated atoms were detected using fluorescence imaging and time-of-flight techniques. This chapter discusses the experimental details of our acceleration experiments, detail the simulation of our measurements and present the experimental results alongside corresponding simulations.

5.1 Setting up the experiment

5.1.1 Pointing stability of the chirped laser system

A number of procedures were carried out to prepare the experiment for Ar* acceleration. The chirped laser system and the MOT apparatus were located in two adjacent laborato-

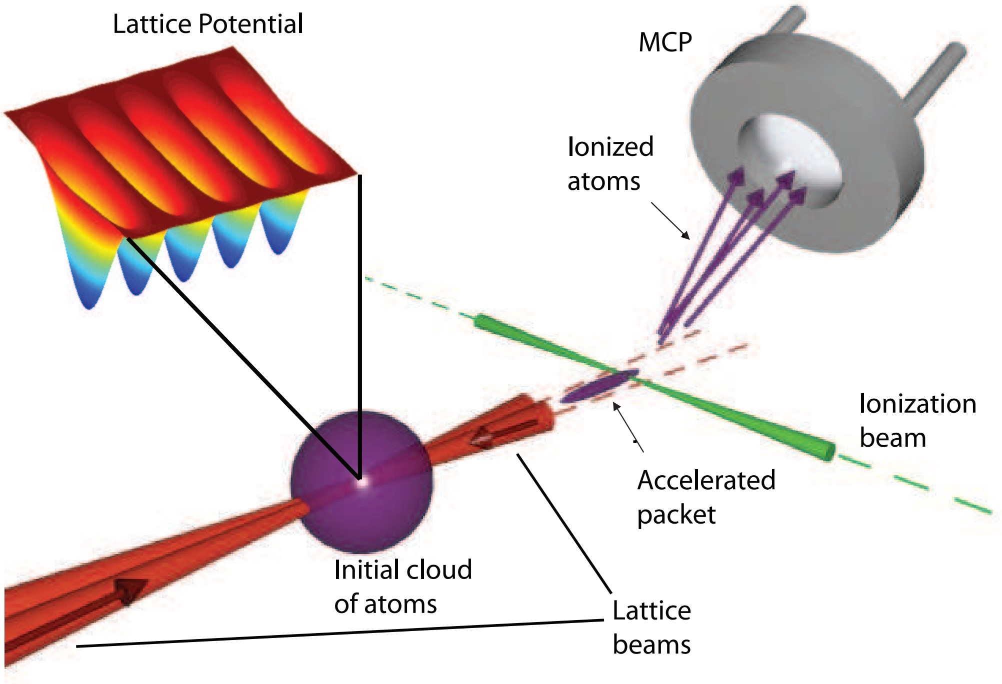

Figure 5.1: Schematic diagram of the experimental set-up for optical Stark acceleration of Ar* atoms. The focused lattice beams were overlapped and then superimposed on the MOT atoms to create the deep optical potential. After acceleration the atoms were detected by imaging their fluorescence after resonant excitation at 811.5 nm on an EMCCD camera and by rapid ionisation with a focused, intense 532 nm laser pulse and detection on a MCP.

ries. The lattice beam path length from the output of the laser system to the MOT was approximately 11 m. The pointing stability of the laser was investigated by aligning one of the output beams over an equivalent path length and focusing it onto a CCD camera. The beam was heavily attenuated and the position of the beam on the camera was monitored over several pulses. Figure 5.2 shows the scatter in the centre point of 20 laser pulses in a 15 μm × 15 μm area. The centre points were determined by fitting Gaussian profiles to the images obtained on the CCD camera in both the horizontal (x) and vertical (y) directions. The data displayed in the figure were normalised such that the mean position of the laser beam was (0,0). The standard deviation in the scatter was 5.1 μm in the x direction and 4.5 μm y direction. The pulses were focused with a 30 cm focal length lens and had a $1/\sqrt{e}$ radius of 51 ± 1 μm. As the standard deviation of the beam position scatter was less than 10% of the beam waist the pointing stability was deemed suitable to use in optical Stark acceleration experiments 11 m from the output of the laser system.

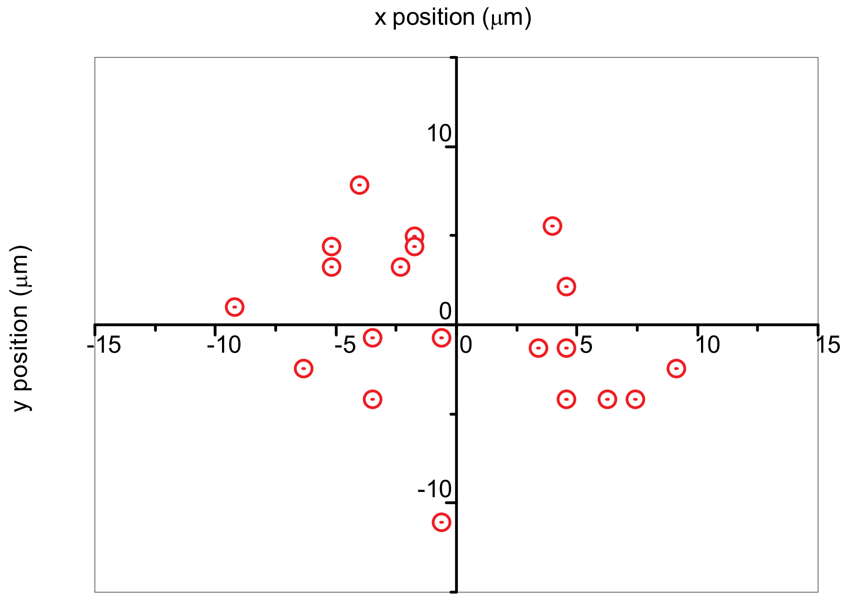

Figure 5.2: Scatter in the central position of 20 laser pulses from the chirped laser system in a 15 μm × 15 μm area measured on a CCD camera. The pulses traveled along a path length of approximately 11 m from the output of the laser system to the CCD camera. The mean position of the laser pulses was (0,0) and the standard deviation of the scatter was 5.1 μm in the x direction and 4.5 μm y direction.

5.1.2 Alignment of the lattice beams

The optics diagram in figure 5.3 shows the alignment of the lattice beams through the science chamber in the MOT vacuum apparatus (see section 3.1). The beams traveled from the lab which housed the chirped laser system to the MOT lab via a beam tube which enclosed their path. To achieve equal focal spot sizes for the lattice the beams had to be collimated with the same radii at the focusing lens. The diameter of the beam from arm B of the laser system was approximately 1.5 times that from arm A. This was corrected for by using a lens pair consisting of a 15 cm focal length convex lens and a 10 cm focal length concave lens which reduced the beam width by a factor of 1.5. The lens pair was located in the chirped laser lab and is not shown on the optics diagram. On exiting the beam tube each beam was passed through a 1064 nm half-wave plate and a thin film polariser which allowed us to vary the beam intensities during experiments. The beams were aligned through the designated windows of the science chamber shown in figure 5.3 such that when overlapped the half angle between them was 83.75°. The windows through which the lattice beams passed were coated with an anti-reflection coating for 1064 nm on both surfaces. Both beams were focused into the science chamber with 40 cm focal length lenses which were mounted on single-axis translation stages such that the axial position of the focus could be finely tuned. All optics used were rated for the high intensity of the lattice pulses. During initial alignment the output beams were heavily attenuated such that the pulsed beams could be observed on an IR card.

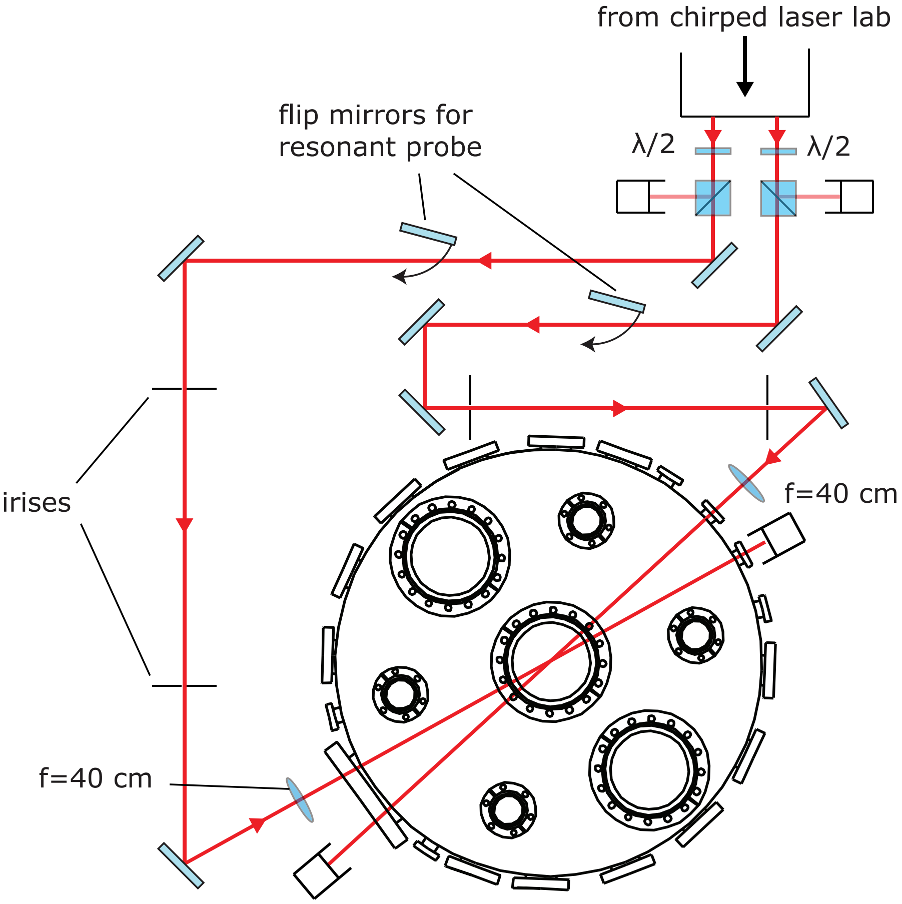

Figure 5.3: Optics diagram for the lattice alignment. The lattice pulses were introduced to the MOT laboratory from the chirped laser laboratory via the beam tube shown. The flip mirrors and irises were used to overlap a probe beam resonant with the Ar* cooling transition during alignment.

A number of diagnostic tools were used to align the lattice beams through the MOT and overlap them with each other. To initially align the beams through the MOT we spatially overlapped a probe beam resonant with the 811.5 nm cooling transition with the path of each lattice beam. This was done by turning up the flip mirrors shown in figure 5.3 and aligning both the probe and lattice beams through the pairs of irises mounted before the final beam steering mirror. When aligned through the MOT the probe beam acted to push atoms out of the MOT via the scattering force leaving a hole in the atomic cloud which could be observed by monitoring the MOT on a CCD camera. Figure 5.4 shows a fluorescence image of the MOT with a probe beam aligned through it. As the lattice beams and probe beams were aligned along the same path, the lattice beams should also have been aligned through the MOT.

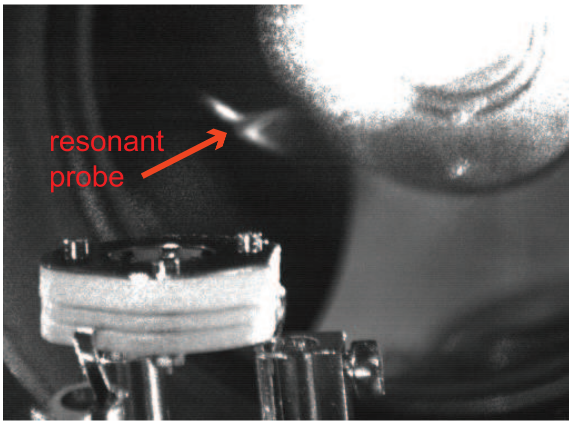

Figure 5.4: Alignment of probe beam resonant with the 811.5 nm cooling transition through the MOT. The beam acts to push beams out of the MOT and is used as an alignment tool for setting up the lattice. Also shown in the bottom left of the image is the MCP detector.

Confirmation that the lattice beams were aligned through the MOT could be obtained by observing an ion signal on the MCP. When the intensity of the lattice beams was high enough they ionised a portion of the atoms in the MOT via the non-resonant three and four photon transitions shown in figure 3.16. The ion signal detected was maximised by adjusting the alignment of the lattice beams to ensure that the beams passed through the centre of the MOT. Even when both lattice beams produced an ion signal it was not certain that they were overlapped as the beam waist of the lattice beams was smaller than the MOT dimensions. In order to verify that the beams were overlapped, we turned the intensity of one of the beams down such that it produced a small ion signal which was recorded. We then recorded the signal from the second beam which had a higher intensity and produced a considerably larger ion signal. We then recorded the ion signal when both beams were on and compared it with the magnitude of the previous two signals as shown in figure 5.5. The magnitude of the ion signal when the lattice beams were both on is clearly larger than the sum of the ion signals from each individual beam. This provides confirmation that the lattice beams were both overlapped with each other and the MOT. The next step in preparing the experiment was then to set up the frequency chirp to produce an accelerating lattice.

5.1.3 Synchronising the chirp with the lattice pulses

In section 4.4.3 we showed how an accelerating lattice could be created by synchronising the chirp with the lattice pulses. In experiments we trigger the waveform generator which

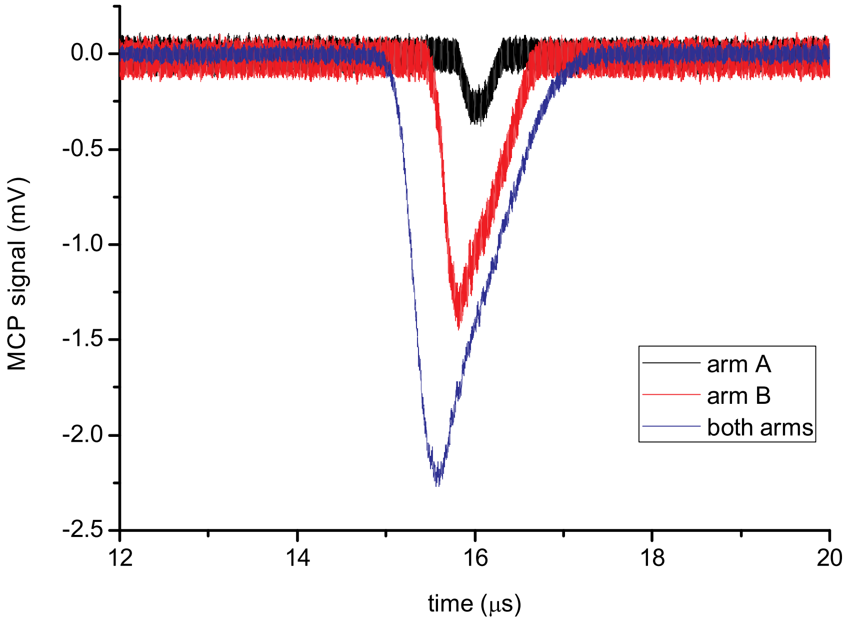

Figure 5.5: Ion signals measured on the MCP when arm A, arm B and both arms were incident on the MOT cloud. The intensity of arm A was turned down so that it was just above the ionisation threshold.

applies the voltage ramp to the electro-optic crystal from the master trigger in the chirped laser system. By then varying the delay to the triggering of the voltage ramp we can synchronise the chirp to the output pulses. We used both linear and sinusoidal chirps in our experiments. A linear chirp is more efficient but, due to equipment limitations at the time, a sinusoidal chirp was required for acceleration to larger velocities, which required larger chirps. It was mentioned earlier that the efficiency of the chirp produced by the electro-optic crystal was 15.4 MHzV^{-1} and that the waveform generator used to apply the voltage to the crystal had a maximum output of 20 V. This means that the largest chirp that could be achieved just using the waveform generator was 308 MHz, which corresponds to a final lattice velocity of 164 ms^{-1}. When we were carrying out experiments even this chirp was not achievable with the waveform generator due to degradation of the electric contacts through which the voltage was applied to the crystal. The efficiency could be improved by moving the electrical contacts but this changed the output of the microchip laser which sometimes then necessitated re-setting up the injection locking of the slave diode (see section 4.4). This was only done when the chirping efficiency became very poor (< 5 MHzV^{-1}) and during our experiments the efficiency was typically $5 - 12$ MHzV^{-1}. In order to achieve larger chirps, we set up the waveform generator to give out a sinusoidal waveform which we then amplified using a tank circuit before applying it to the electro-optic crystal. This section will discuss how both the linear and sinusoidal chirps were set up in experiments.

Linear chirp

In order to produce a linear chirp, we applied a voltage waveform to the crystal with a 70 ns linear ramp. The waveform generator was set up such that it fired one pulse of the desired waveform when triggered from the master trigger in the chirped laser system. Figure 5.6(a) shows the voltage waveform applied to the crystal. In this example the voltage increases from 0 V to 10 V in 70 ns then remains constant for 140 ns before rapidly dropping back to 0 V in 20 ns. Figures 5.6(b) and 5.6(c) show the temporal position of the chirp, corresponding to the voltage ramp in figure 5.6(a), on arm A and arm B of the laser system after the time delay had been introduced by the different length fibres. A chirping efficiency of 15.4 MHzV^{-1} has been assumed for the purposes of this discussion. In order to create an accelerating lattice, we synchronised the chirp such that the linear part of the frequency chirp on arm B coincided with the lattice pulses. Figure 5.6(d) shows the temporal position of the 140 ns lattice pulse which coincides with the linear chirp. As the lattice duration was longer than the chirp duration we created a lattice which was initially stationary for 20 ns, then accelerated for 70 ns before traveling at a constant velocity for the final 20 ns.

If we compare figures 5.6(b) and (c) we can see that there are a number of different times when the frequency difference between the two beams is chirped. The first chirp region is the 70 ns linear chirp on arm B which we want to synchronise with our lattice pulses. At 320 ns we have another chirp where the frequency difference is rapidly chirped back to 0 MHz in 20 ns. At 385 ns the linear ramp is applied to arm A and the frequency difference is again ramped up over 70 ns. Finally, the frequency of arm B is chirped back to 0 MHz at 600 ns. When initially setting up the chirp we monitored the beat signal between the two pulses to make sure we synchronised the desired chirp region with the lattice pulses. By moving the timing of the chirp with respect to the lattice pulses we could map out the different chirp regions and then synchronise the desired chirp region with the lattice pulses. Figure 5.7 shows a beat signal corresponding to a linear chirp from 0 MHz to 80 MHz in 70 ns which has been synchronised in this way. This frequency chirp would produce a lattice with a final velocity after acceleration of 42.5 ms^{-1}. Although this beat signal is useful for aligning the chirp it is not suitable for carrying out the Fourier analysis described in section 4.4.4. This is because the chirp contains low frequency components

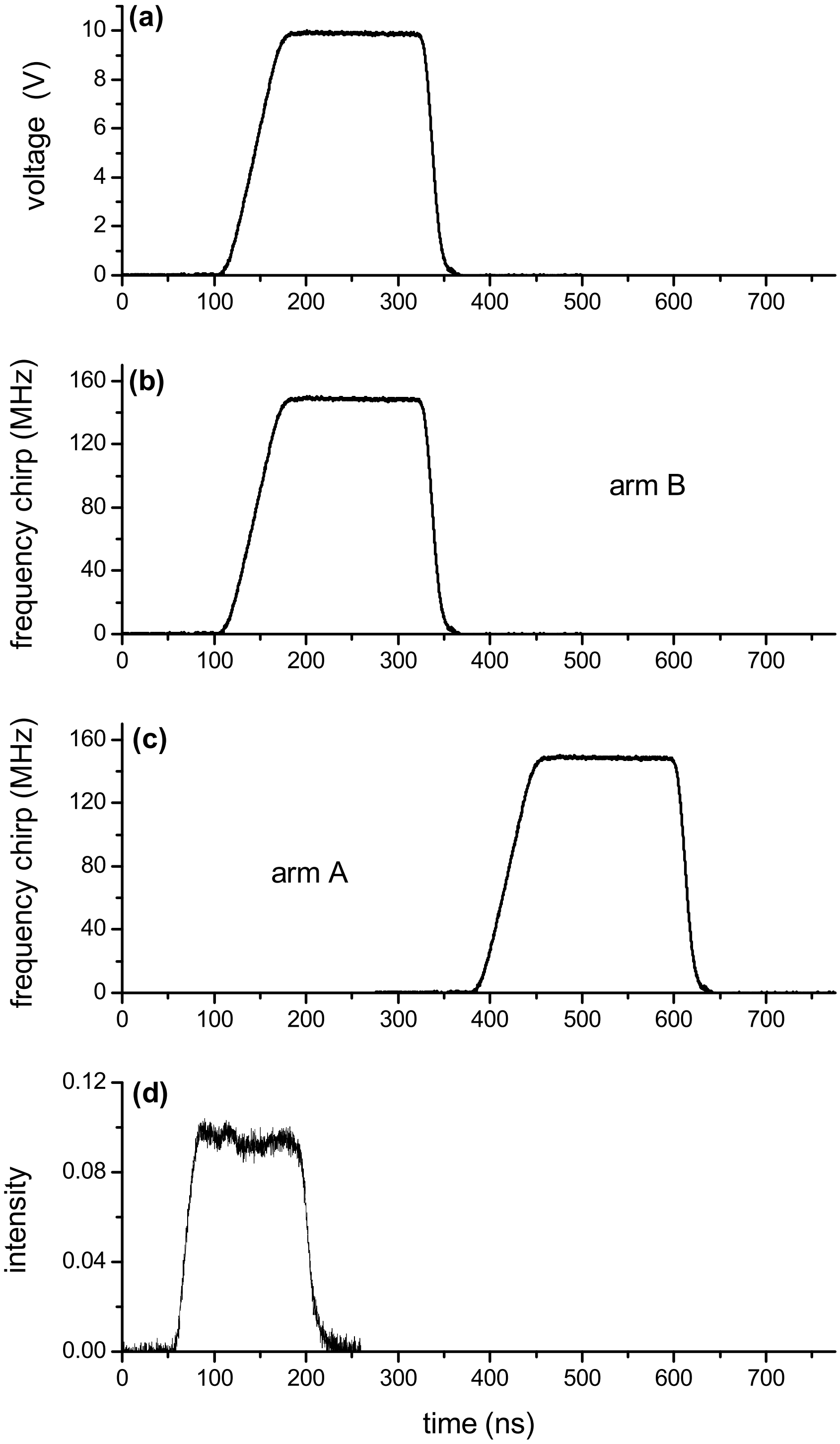

Figure 5.6: Synchronisation of the frequency chirp with the lattice pulses to create an accelerating lattice. (a) The voltage ramp applied to the electro-optic crystal. The voltage increases linearly from 0 V to 10 V over 70 ns and then remains constant for 140 ns before rapidly ramping back down to 0 V in 20 ns. (b) The frequency chirp of arm B of the laser system (the arm from the short fibre) generated by the voltage ramp assuming a chirping efficiency of 15.4 MHzV^{-1}. (c) The frequency chirp of arm A which is delayed by 275 ns. (d) The temporal position of the 140 ns lattice pulses. In this example the chirp has been synchronised such that the linear voltage ramp occurs over the duration of the pulse. This creates an accelerating lattice.

which are not easily separated from the low frequency components which are present in the shape of the optical pulse. In order to separate the beat frequencies, we added an offset of approximately +80 MHz to the frequency of the portion of arm B used to generate the beat signal. This was done be aligning the beam through an 80 MHz AOM.

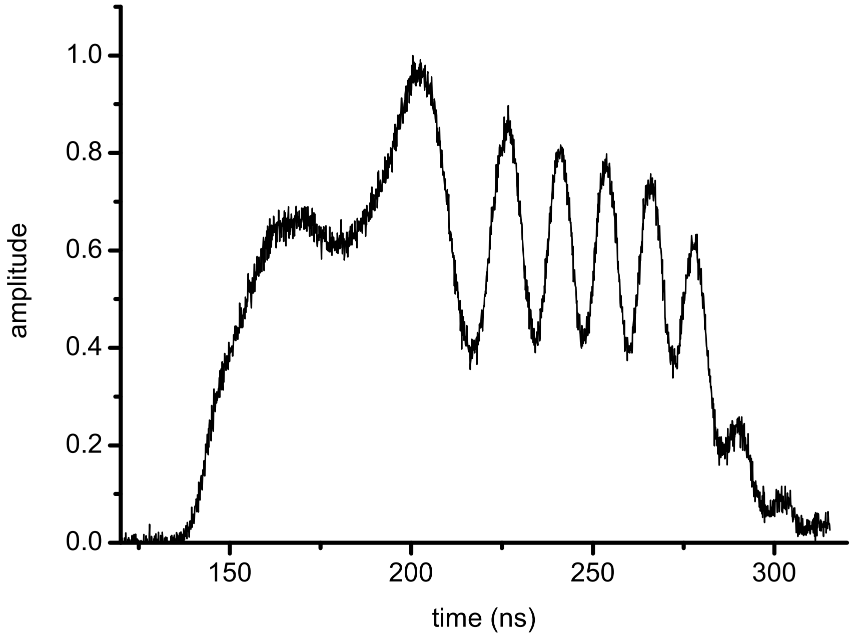

Figure 5.7: Heterodyne signal corresponding to a 70 ns linear chirp from 0 MHz to 80 MHz.

The addition of the 80 MHz frequency offset enabled us to use another diagnostic for synchronising the chirp with the lattice pulses. We used the oscilloscope (LeCroy WavePro 7300) on which we monitored the beat signal to perform a fast Fourier transform (FFT) of the beat signal. This allowed us to observe the frequency components of the chirp as we set it up. Figure 5.8 shows an example of a beat signal observed on the oscilloscope and the corresponding FFT of the signal. The beat signal was produced by a linear chirp from 0 MHz to 110 MHz over 70 ns with an offset of +89 MHz added to arm B. The double-peaked feature in the FFT corresponds to the frequency components in the chirp. The two peaks represent the starting and finishing frequencies of the chirp. As the frequency difference is constant for the first and final 20 ns of the lattice pulses these frequencies have larger amplitudes than the frequencies during the linear chirp. We used this FFT to synchronise the chirp by adjusting the temporal position of the chirp until the two peaks had approximately equal amplitudes as shown in figure 5.8(b). This indicated that the chirp was temporally centred on the lattice pulses. The other chirp regions produced by the voltage ramp in figure 5.6(a) have distinctly different beat and FFT signals. For example, when the linear ramp is applied to arm A (at 400 ns in figure 5.6) the beat signal will decrease in frequency and pass through zero before reaching a final frequency of $f = |\Delta f - f_{offset}|$, where Δf is the frequency magnitude of the chirp and f_{offset} is the frequency offset on arm A. This occurs because the frequency chirp of arm A is negative relative to the frequency offset on arm B. If this portion of the chirp is synchronised with the lattice pulses an accelerating lattice will be created that moves in the opposite direction to the one we use.

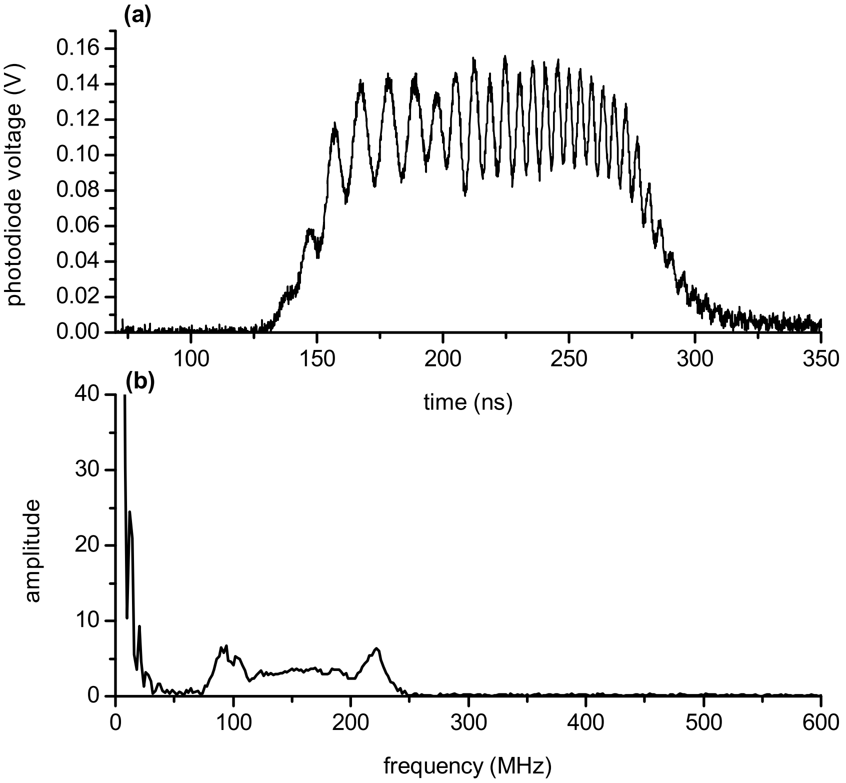

Figure 5.8: Experimental diagnostic for synchronising the chirp with the lattice pulses. (a) Beat signal observed on the oscilloscope for a 70 ns linear chirp from 0 MHz to 110 MHz. A frequency offset of 89 MHz has been added to arm B meaning that a zero frequency difference between the lattice beams is observed as an 89 MHz beat signal. (b) FFT of the beat signal in (a). The double-peaked feature connected by a plateau represents the frequency components in the chirp.

Sinusoidal chirp

A sinusoidal voltage ramp was used to apply voltages larger than 20 V to the electro-optic crystal by passing the output from the signal generator through a tank circuit. The frequency of the sinusoidal signal input was 1.82 MHz such that the 275 ns delay between the chirp of both arms of the laser system resulted in a π phase shift of the sinusoidal chirp (see section 4.4.3). At this frequency the tank circuit gave an amplification of approximately 3.5. Figure 5.9 shows the voltage signal output from the tank circuit after it has been passed through a 666:1 high voltage attenuator. The peak-to-peak voltage of the input waveform was 20 V and, taking into account the voltage attenuation, we can see that the output voltage was ≈ 70 V. The tank circuit output signal in figure 5.9 shows that it takes five oscillations of the sinusoidal waveform for the tank circuit to build up to full amplification. We set up the waveform generator such that it output a burst of 20 sinusoidal oscillations and during experiments made sure we synchronised the chirp such that we used a portion of one of the oscillations with maximum amplification.

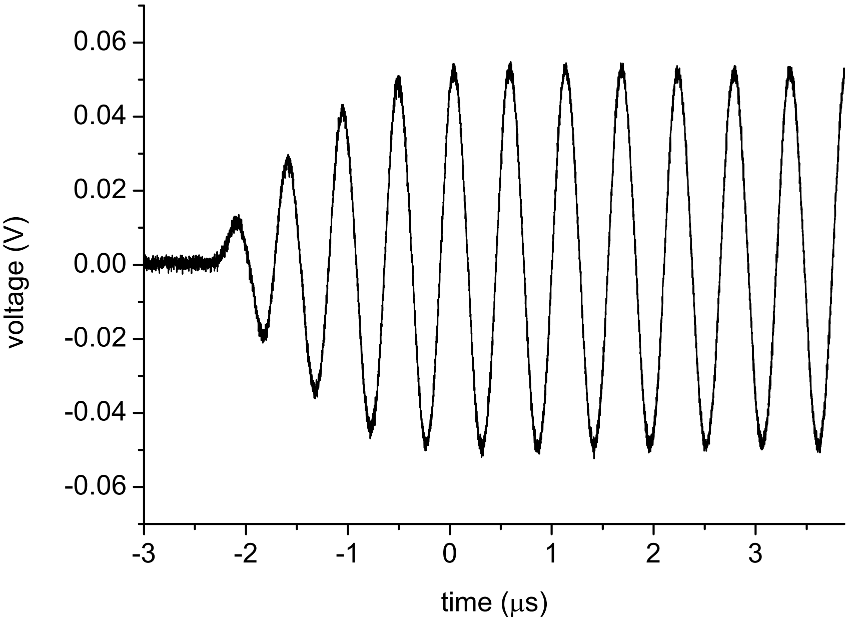

Figure 5.9: Voltage output from the tank circuit when a 1.82 MHz 20 V peak-to-peak signal was input to the circuit. The output has been passed through a 666:1 high voltage attenuator.

The sinusoidal chirp was also synchronised with the lattice pulses by monitoring the beat signal and corresponding FFT on the oscilloscope. Figure 5.10 shows the beat signal produced by a sinusoidal chirp from 0 MHz to 370 MHz with the addition of the 89 MHz offset and the corresponding FFT signal. It also shows the modeled frequency between the two lattice beams which shows the temporal position of the chirp. A sinusoidal chirp has a different characteristic FFT signal to a linear chirp. Figure 5.10(b) shows that with the sinusoidal chirp the rate of change of frequency is higher at the beginning of the chirp than at the end. Thus the higher frequency components in the chirp will have a larger amplitude in the FFT than the lower frequencies. This can be seen in the FFT in figure 5.10(c). The frequency components in the chirp begin at 89 MHz with a relatively small amplitude. The amplitude increases with increasing frequency as the rate of change of the frequency drops off. The peak at the high frequency end of the chirp Fourier components, at approximately $470 \approx 380 + 89$ MHz, is due to the fact that the chirp is almost flat at the end of the optical pulse, as can be seen by comparing figures 5.10(a) and 5.10(b). This FFT signal is a signature of a well set up chirp and during experiments we synchronised the chirp by changing the temporal position of the chirp until this signal was observed.

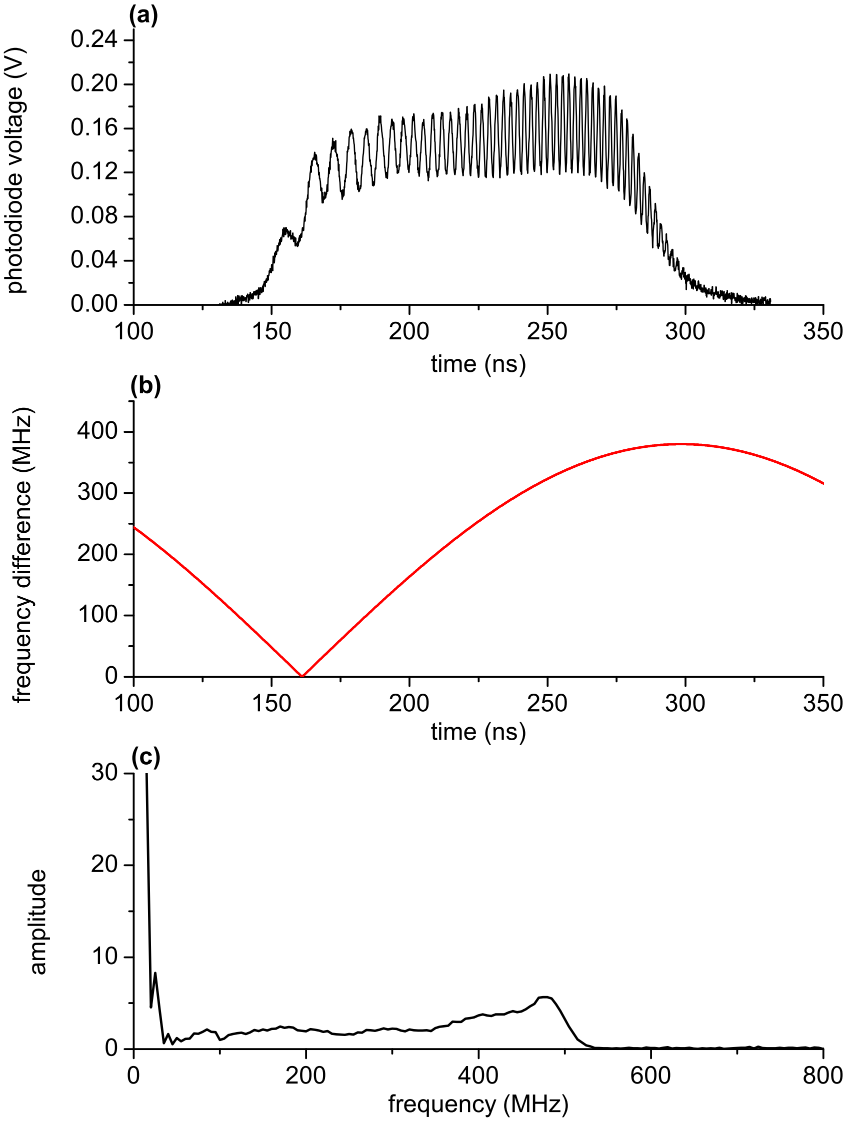

Figure 5.10: Experimental diagnostic for temporally overlapping the sinusoidal chirp with the lattice beams. (a) Beat signal observed on the oscilloscope for a sinusoidal chirp from 0 MHz to 370 MHz with a 89 MHz offset. (b) Modeled frequency difference produced by the chirp which shows the temporal position of the chirp. (c) FFT of the beat signal which shows the characteristic signal of a sinusoidal chirp which has been synchronised with the lattice pulses.

With the lattice beams aligned with the MOT and the frequency chirp synchronised to produce an accelerating lattice, the final step in setting up the experiment was to implement an experimental timing sequence for acceleration.

5.1.4 Experimental sequence

All experimental equipment was synchronised to the master trigger from the chirped laser system using the digital delay pulse generator described in section 3.5.5. The 10 Hz repetition rate of the chirped laser set our acquisition rate. During experiments we switched off all the MOT laser and magnetic fields before acceleration so that the only perturbation on the atoms was from the accelerating lattice. Before the experimental sequence was initiated the MOT was loaded for a few seconds. The experimental sequence began by switching off the Zeeman slower laser beam to minimise the background light during image acquisition. After a delay of 2 ms we then switched off the MOT magnetic field coils which loaded the atoms into an optical molasses. After 2 ms of the optical molasses phase the MOT laser beams were switched off. This sequence for switching off the MOT fields was used as it was the least perturbative to the trapped atoms. The lattice pulses arrived 1 ms after all the MOT fields had been switched off. Once the atoms were accelerated they were imaged by simultaneously switching back on the MOT laser beams and triggering the EMCCD camera. The imaging time was set by considering the expected acceleration in a given experiment. For example, when setting up the experiment for acceleration to 45 ms^{-1} images were acquired 50 μs after the lattice was applied. In this time the accelerated atoms would travel a distance of 2.2 mm and remain well within our 14 mm $\times$ 14 mm imaging region. The image exposure time was typically $15 - 30$ μs. The MOT beams remained on after the image exposure and the rest of the MOT fields were switched back on after a short delay to recapture the atoms.

5.1.5 Detecting acceleration

With the lattice beams aligned with the MOT, the chirp working as outlined previously and the timing sequence initiated we looked for acceleration by monitoring the atomic fluorescence on the EMCCD camera. We initially set the lattice pulse energies to 20 mJ which gave peak intensities of approximately 4.5×10^{12} Wm^{-2}. The frequency excursion of the chirp was initially set to 80 MHz which corresponds to a final lattice velocity of 43 ms^{-1}. When looking for the first signal the key experimental parameter adjusted was the position of the focus of the lattice beams. Once the beams were overlapped at their foci we observed an acceleration signal. Figure 5.11 shows a typical image of accelerated Ar* atoms with the accelerated portion of atoms protruding from one side of the atomic cloud. This image was acquired at a delay of 25 μs after the lattice was applied and is an accumulation of 1000 individual images acquired with an exposure time of 15 μs. The magnitude of the signal from the accelerated atoms was maximised by adjusting the position of the lattice beams while observing fluorescence in real time using a longer exposure time of 50 μs, 8×8 pixel binning and performing a 10 frame running average. Once we had observed acceleration we started making measurements of the accelerated packet, initially using this fluorescence imaging technique.

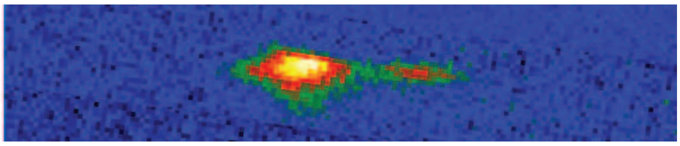

Figure 5.11: Image of accelerated atoms 25 μs after acceleration by the lattice. This image is an accumulation of 1000 individual images acquired with an exposure time of 15 μs.

5.2 Fluorescence imaging of Ar* acceleration

Our first acceleration measurements were made using fluorescence imaging. We measured the velocity of the accelerated packet of atoms by acquiring fluorescence images of the atoms at different delays after applying the accelerating lattice and determining the position of the packet. Figure 5.12 shows fluorescence images of the packet at delays between 25 μs and 125 μs as well as an image of the MOT which shows the initial position of the atoms. The images clearly show a discrete, well collimated ensemble of atoms moving away from their initial position in the MOT cloud. This acceleration was achieved using lattice beam intensities of 3.0×10^{12} Wm^{-2} and the 70 ns linear chirp from 0 MHz to 80 MHz which produced the beat signal in figure 5.7. This chirp was generated by applying a 12 V voltage ramp to the electro-optic crystal. The spatial position of the accelerated packet was measured by plotting the fluorescence from atoms along the axis of acceleration. Figure 5.13 shows the fluorescence recorded from atoms along the axis of acceleration for the image acquired at a delay of 75 μs. In this image the accelerated atoms had moved 3330 μm from their initial position.

The velocity of the atoms can be calculated from $s = \frac{1}{2}at_1^2 + vt_2$, where t_1 is the acceleration time, t_2 is the time between lattice switch off and the middle of the exposure and v is the velocity of the accelerated packet. As the acceleration time (140 ns) is much shorter than the time we allow the atoms to freely propagate before imaging ($t_1 \ll t_2$) we can rewrite this equation as $s = \frac{1}{2}at_1^2 + vt_2 \approx vt_2$. By analysing each image and plotting s against t_2 we determined the velocity of the packet to be 45.5 ± 1.2 ms^{-1}. In these images the axial length of the accelerated packet of atoms appears larger than the width of the initial cloud. However, these images do not display the true spatial extent of packet due to blurring caused by the atoms motion over the long exposure time. If we consider that the atoms have a velocity of 45.5 ms^{-1} and the exposure time is 15 μs the atoms will travel a distance of 0.68 mm over the imaging duration.

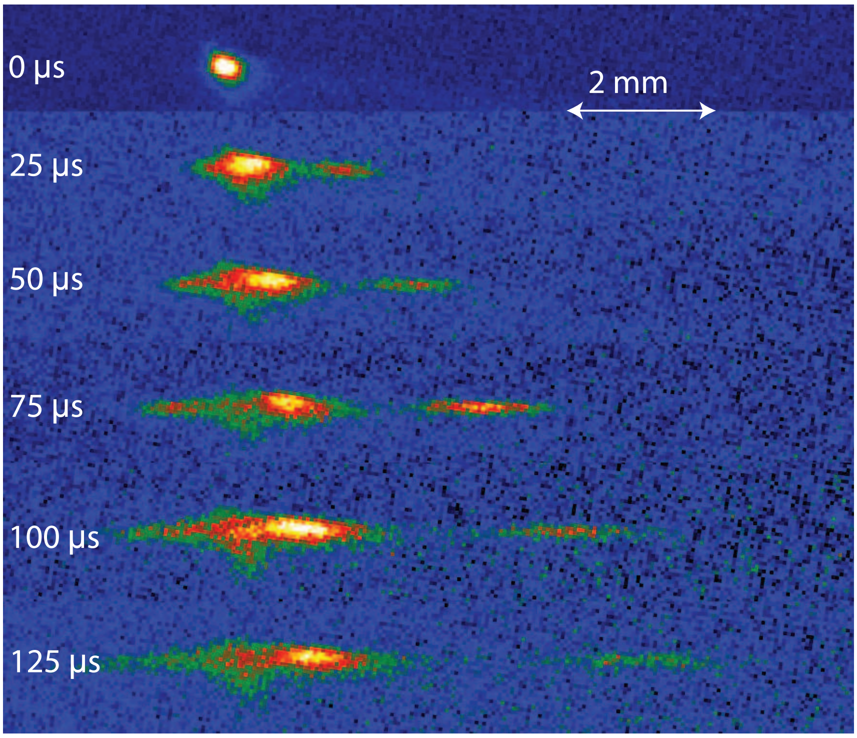

Figure 5.12: Images of accelerated atoms at different delays after acceleration by the lattice. The velocity of the accelerated packet was measured to be 45.5 ± 1.2 ms^{-1}. These images are an accumulation of 1000 individual images acquired with an exposure time of 15 μs. The images of the packet at longer delays are less bright because the atoms are in a less intense region of the MOT light field and fluoresce less.

The images in figure 5.12 also allow us to observe how the atoms which are not successfully accelerated are perturbed. We can see that few atoms remain stationary and that there is a second, much lower velocity, accelerated peak which slowly moves away from the initial MOT position. A small fraction of the atoms is also accelerated in the opposite direction. If we refer back to the simulation of Ar* acceleration presented in section 4.5.3 in the previous chapter we can see that our simulation predicts these low velocity peaks traveling in both directions.

To demonstrate the tunability of the final velocity we acquired images at the same delay

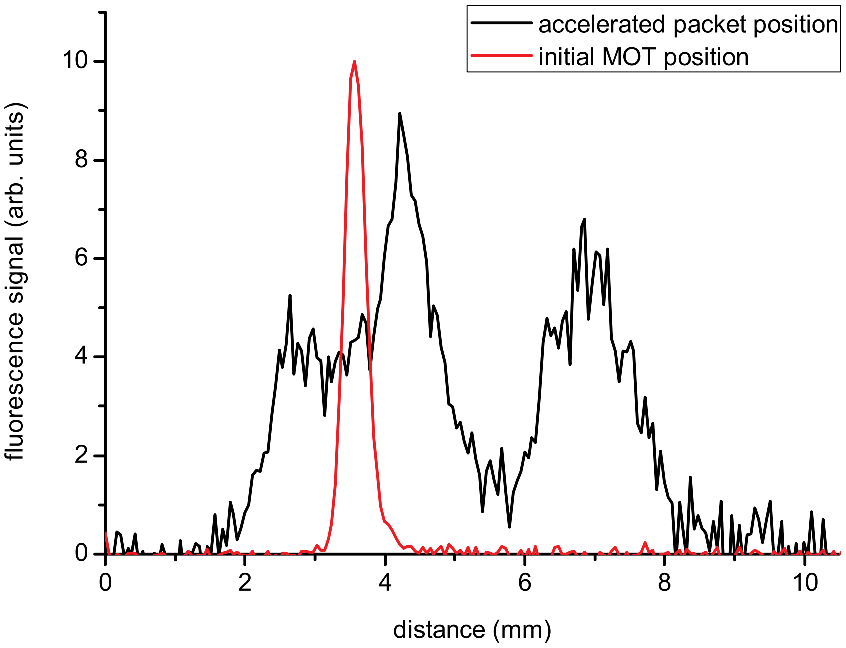

Figure 5.13: Fluorescence recorded from atoms along the axis of acceleration 75 μs after acceleration. Also shown is the initial position of the MOT cloud. The fluorescence counts from MOT cloud have been normalised so that the position of the accelerated packet relative to the MOT can be seen on a comparable scale.

after applying the chirp but with different voltages applied to the electro-optic crystal. Figure 5.14 shows fluorescence images of acceleration achieved by applying sinusoidal voltage waveforms of between 3 V and 12 V to the electro-optic crystal. The images were acquired at the same delays after acceleration and with the same exposure times. The larger voltages produce higher final lattice velocities and it can be seen that the atoms accelerated by larger chirps have moved further from their initial position. The voltages applied to the crystal were 3 V, 5 V, 7 V, 10 V and 12 V and the distances traveled by the atoms were 651 μm, 945 μm, 1239 μm, 1575 μm and 1890 μm. Considering the time until the middle of the camera exposure was $t_2 = 45$ μs, the corresponding velocities are 14.5 ms^{-1}, 21.0 ms^{-1}, 27.5 ms^{-1}, 35.0 ms^{-1} and 42.0 ms^{-1}. The final velocity of the atoms increased linearly with applied voltage with a slope of 2.9 ± 0.9 ms^{-1}V^{-1}. If we assume that the final velocity of the atoms corresponds to the final lattice velocity we get a chirping efficiency of 5.62 ± 0.17 MHzV^{-1}. In these measurements the lattice beam intensities remained the same which meant that the accelerating well depth was shallower for larger chirps. This meant that fewer atoms were accelerated when the larger chirps were applied as can clearly be seen in figure 5.14.

As well as allowing the determination of the velocity of the accelerated atoms the fluorescence images were also used to determine the portion of atoms accelerated. Figure

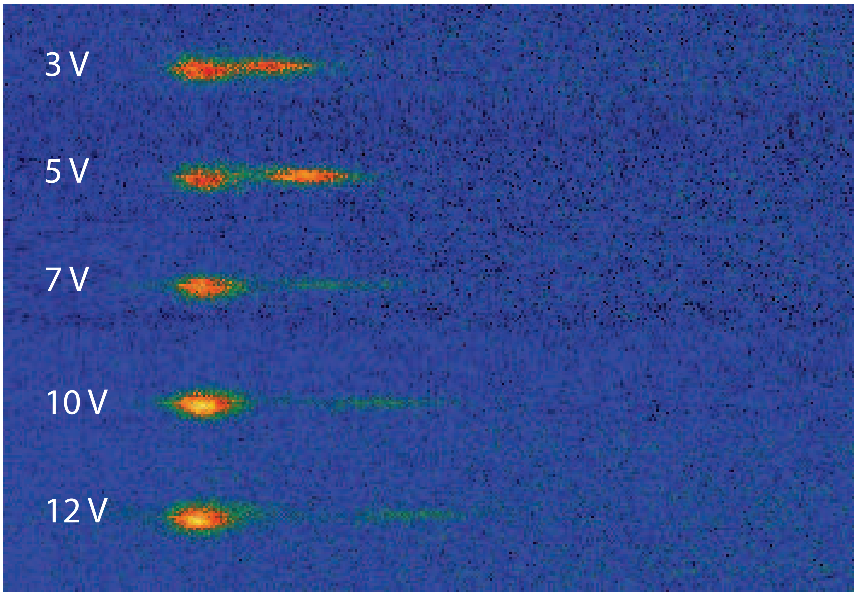

Figure 5.14: Fluorescence images of accelerated atoms for different voltage sinusoidal waveforms applied to the electro-optic crystal. All the images were acquired at a delay of 30 μs and a 30 μs exposure time and are the accumulation of 1000 individual images.

5.15 shows acceleration with different pulse energies and lattice potential well depths. Both images correspond to acceleration to 45.5 ± 1.2 ms^{-1} and were acquired at delays of 75 μs. In image (a) the beam energy was 25 mJ and in (b) energies of 100 mJ were applied. These energies correspond to peak intensities of approximately 3.0×10^{12} Wm^{-2} and 1.2×10^{13} Wm^{-2} respectively. Analysis of the images showed that fraction of the total number of atoms accelerated was increased from 28% to 50% by increasing the intensity.

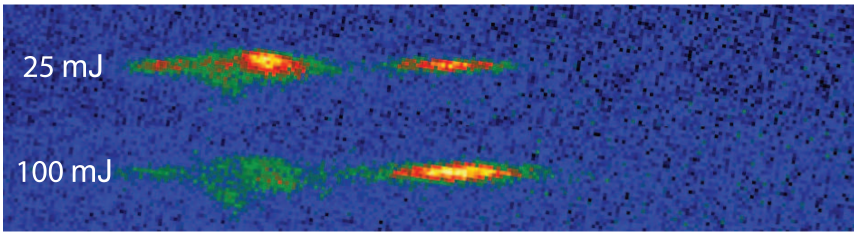

Figure 5.15: Fluorescence images of acceleration with different potential well depths. In image (a) the pulse energies of 25 mJ were applied while in (b) the beam energies were 100 mJ, four times larger.

Although fluorescence imaging proved useful for carrying out the measurements presented here the blurring effect precluded its use in certain measurements. At higher velocities the atoms travel a greater distance over the imaging time which makes the blurring worse. We attempted to acquire images using shorter exposure times so that we could freeze the atomic motion but encountered problems with signal strength and switching of the equipment. Another limitation of using fluorescence was that there was no accurate way to extract the velocity width of the accelerated atoms which is an important characteristic for certain applications. In order to extend the scope of our measurements, we used a time-of flight method involving ionisation of the accelerated atoms.

5.3 Time-of-flight measurements

In order to make more accurate measurements of the atomic velocity distributions at higher velocities, we ionised the atoms at a well-defined distance from the MOT with a focused probe beam and detected the ions produced on the MCP. A pulsed, frequency-doubled Nd:YAG laser (Continuum lasers) operating at 532 nm was used as an ionisation probe beam. The 532 nm pulses ionised Ar* via the non-resonant two-photon process discussed in section 3.5.4. Figure 5.16 shows the temporal profile of a typical output pulse from the laser which had a duration of $\tau_{FWHM} = 10$ ns. The probe beam was focussed into the science chamber with a 40 cm focal length lens along an axis perpendicular to the motion of the atoms, as shown in figure 5.1. The beam was expanded to a diameter of 1.2 cm before being focussed so that we could obtain a narrow 20 μm ionisation region. We overlapped the ionisation beam with a 811.5 nm resonant probe to initially align the beam with the MOT, as was done to align the lattice beams (see section 5.1.2). We then observed a MOT ionisation signal produced by the 532 nm pulse to confirm it was aligned through the atomic cloud. The beam was then moved away from the MOT in the direction which the accelerated atoms would travel if the lattice was applied. When the accelerating lattice was switched on we observed an ion signal from the accelerated atoms which was maximised up by adjusting the vertical position of the beam.

The ionisation probe laser was operated at 10 Hz and triggered from the chirped laser system master trigger. The MOT fields were switched off in the same way as during our fluorescence imaging experiments and the lattice pulses were again applied 1 ms after all the MOT fields were switched off. The ionisation probe beam was applied at different delays after acceleration and the ionisation signal detected by the MCP was recorded on an oscilloscope. The MOT fields were turned back on 1 ms after the lattice was applied. By changing the delay between the ionisation probe and the acceleration pulses we were able to build up time-of-flight (TOF) distributions of the accelerated atoms. The delays at which ion signals were obtained depended on the expected acceleration for a given experiment. For example, if we expected the velocity of the accelerated atoms to be 100

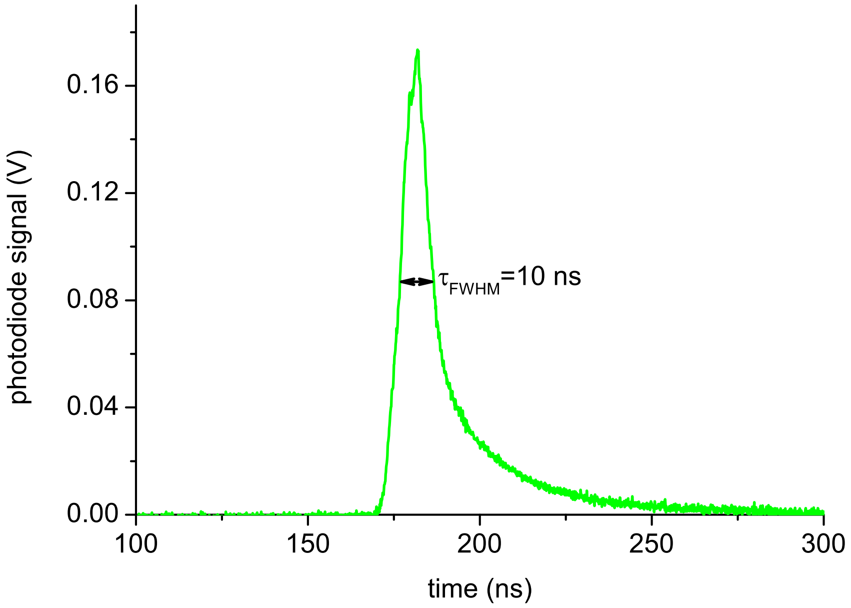

Figure 5.16: Temporal profile of the 532 nm ionisation probe used to detect the accelerated Ar* atoms. The pulses had a FWHM duration of $\tau_{FWHM} = 10$ ns.

ms^{-1}, delays in the range of 28-360 μs would allow us to detect velocities from 120-10 ms^{-1} for an ionisation probe beam 3.6 mm from the MOT.

Figure 5.17(a) shows a TOF signal measured for a chirp from 0 MHz to 80 MHz. The signal clearly shows a peak at shorter time delays, which corresponds to the detection of atoms with faster velocities, followed by a slowly rising tail of atoms which have had their velocity perturbed by the lattice but have not been stably accelerated. Each data point in the TOF distribution was the average of 256 experimental shots. The error bars were derived from the residual scatter on the averaged ion signals analysed, primarily caused by RF interference originating from the RF discharge. This scatter gave an uncertainty in measuring the magnitude of the ion signals. The magnitude of the error bars was the 2σ width of the scatter on the ion signals.

The simplest method for extracting velocity information from a TOF signal involves converting the time axis to velocity and calibrating the magnitude of the MCP signals to take into account the decrease of the velocity width being sampled with time. The time axis of the TOF can be converted to velocity according to $v = s/t$, where s is the distance between the MOT and the ionisation probe and t is the delay between the lattice pulses and the ionisation probe. The position of the ionisation probe beam sets the displacement s and was determined by recording the fluorescence induced on the accelerated atoms by the resonant probe beam which was overlapped with the ionisation probe. By analysing

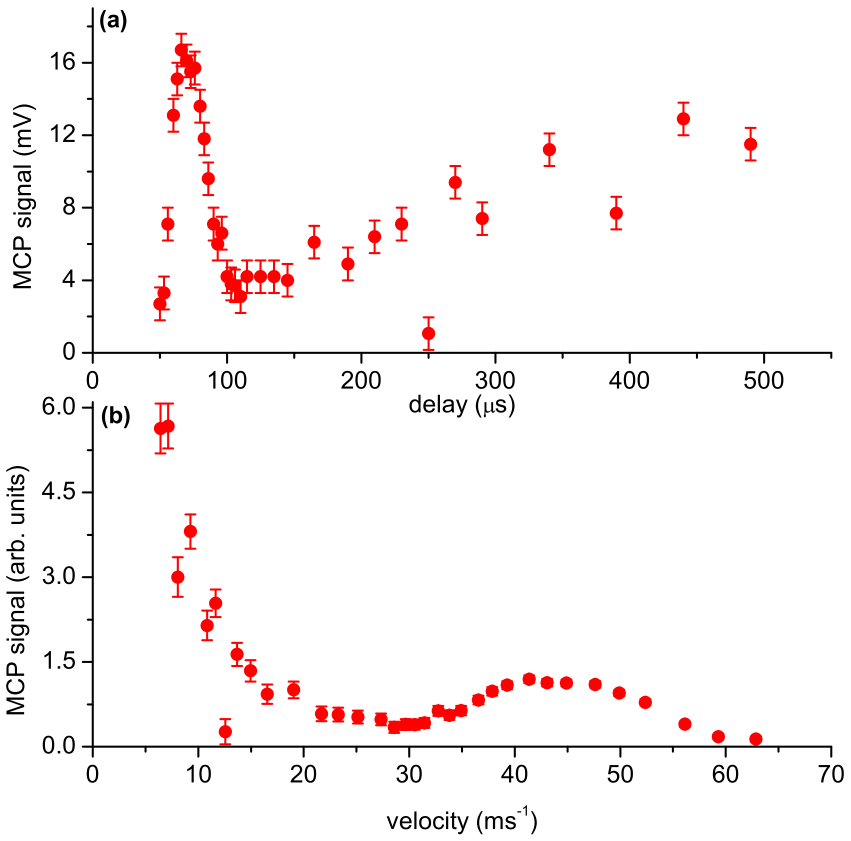

Figure 5.17: (a) TOF distribution of accelerated atoms measured by detecting ions produced by the 532 nm probe on the MCP. The ionisation probe was 3.6 mm from the MOT and each data point was averaged over 256 experimental shots. (b) TOF distribution from (a) converted to a velocity distribution using the method described in the text.

the fluorescence images acquired and fitting a Gaussian profile to the fluorescence signal the position of the resonant probe, and therefore the ionisation probe, was measured. For the data in figure 5.17 the distance between the MOT and the ionisation probe was measured to be 3.1 ± 0.1 mm. The magnitude of the MCP signal must be calibrated when converting from TOF to velocity distribution as the velocity width being sampled decreases with time. Consider a probe region with a width Δz at a distance s from the initial position of the atoms. If the number of atoms in the probe region is measured at a time t, the velocity of atoms at the beginning of the probe region will be $v_1 = \frac{s-\Delta z/2}{t}$ and the velocity of atoms at the end of the probe region will be $v_2 = \frac{s+\Delta z/2}{t}$. The velocity width measured is then given by $\Delta v = v_2 - v_1 = \frac{\Delta z}{t}$, and decreases with t. When converting the TOF distribution to a velocity distribution the magnitude of the MCP signals must then be multiplied by t.

Figure 5.17(b) shows the TOF data from figure 5.17(a) with the time axis converted to velocity. This shows a peak of the accelerated atoms at 44.5 ms^{-1} and that the FWHM velocity width of the peak is approximately 19 ms^{-1}. This velocity distribution, however, does not represent the actual velocity distribution of the accelerated atoms as it neglects important experimental considerations. This model would only be accurate if the atoms began at an identical axial position which is not the case in our measurements. To obtain more accurate measurements of the velocity distribution of the accelerated atoms we followed a different approach whereby we simulated, and fitted, the TOF data.

5.3.1 Simulating the TOF data

In order to simulate our TOF distributions, we extended our Monte Carlo model of acceleration described in section 4.5.2. This model calculated the atomic spatial and velocity distributions after the acceleration process. The TOF profiles were then calculated from the final positions and velocities of the atoms by calculating the position of each particle at different delays after acceleration and counting the number of atoms within the ionisation probe region. The position of the ionisation probe region in the simulation was set to that measured in the experiment and its width was the diameter of the focused beam. The atoms were assigned initial spatial and velocity distributions corresponding to those measured in the MOT and the lattice potential was calculated using experimentally measured lattice beam intensity profiles and relative frequencies. The simulation was run for many particles to suppress statistical fluctuations.

Prior to simulating our TOF data we tested our numerical model by comparing it with an analytical model. In both cases we simulated a simple case of an accelerated packet of atoms with a Gaussian initial spatial distribution and a thermal velocity spread. If we assume an accelerated atomic cloud with a temperature T, a mean velocity v and an initial Gaussian spatial width σ_0, the spatial distribution along the z axis will evolve with time according to

$$f(z,t) = \frac{1}{\sigma(t)\sqrt{2\pi}} \mathrm{e}^{-\frac{1}{2}\left(\frac{z-vt}{\sigma(t)}\right)^2}, \tag{5.1}$$

where

$$\sigma(t)^2 = \sigma_0^2 + \frac{kT}{m} t^2 \tag{5.2}$$

is the expanding width of the cloud. In order to determine the TOF spectrum from equation 5.1, we integrate over the following limits

$$TOF(z,t) = \int_0^\infty \int_{z_p-w_0}^{z_p+w_0} f(z,t)\, dz dt \tag{5.3}$$

z_p is the central position of the ionisation probe beam and w_0 is the radius of the beam. We compared the TOF profiles produced by this analytical model with those produced by our numerical model for different temperatures. Figure 5.18 shows the TOF profiles simulated for accelerated packets with a mean velocity of 31.8 ms^{-1} and temperatures of 0 mK, 20 mK and 50 mK. The atomic cloud was assumed to have an initial $1/\sqrt{e}$ radius of 360 μm. These profiles were produced by an ionisation probe with a beam waist $w_0 = 20$ μm at a distance of 7.6 mm from the initial position of the atomic cloud. The numerical data were produced by calculating the trajectories of 10000 atoms. Figure 5.18 shows that the numerical and analytical simulations agree very well for the three temperatures simulated.

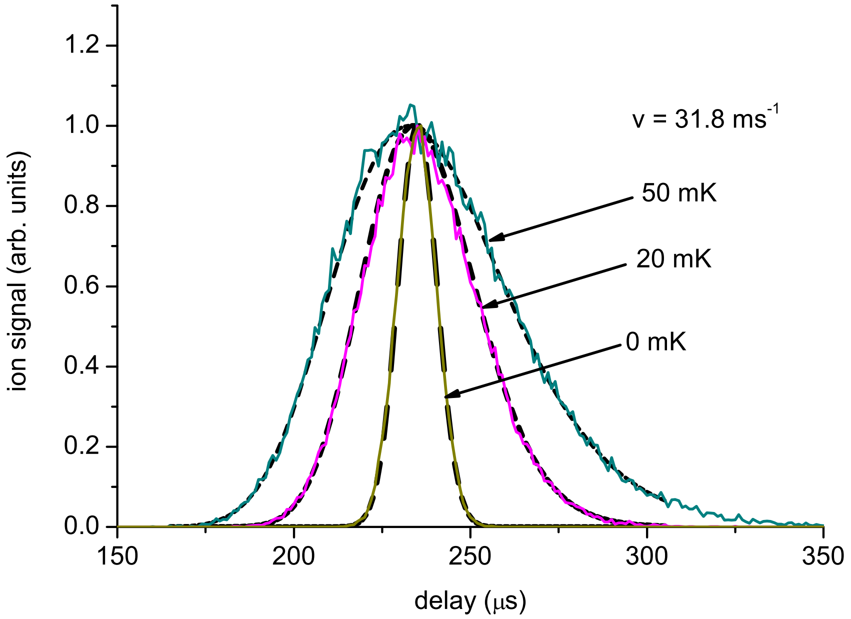

Figure 5.18: Simulated TOF profiles of an atomic packet with a mean velocity of 31.8 ms^{-1} and temperatures of 0 mK, 20 mK and 50 mK. The dashed line profiles were calculated using the analytical model while the numerical model was used to produce the solid line profiles. The ionisation probe distance was set at 7.6 mm and the beam width was $w_0 = 20$ μm.

Figure 5.18 also shows that even if all of the particles have the same velocity (i.e. the 0 mK case) the TOF distribution still has a finite width and converting the time axis to velocity will not give the true velocity distribution. We investigated the difference between the true velocity distribution and that converted from the TOF further using our numerical model. We simulated an atomic ensemble with a mean velocity of 150 ms^{-1}, a temperature of 50 mK and a $1/\sqrt{e}$ radius of 360 μm. Figure 5.19 shows the velocity distribution produced from the simulated TOF measurement and the true velocity distribution of the atoms. It is clear that the velocity distribution converted from the TOF data represents a poor measurement of the true velocity distribution. Although the mean velocity from the converted TOF distribution (150.8 ms^{-1}) is accurate to within 1% of the actual velocity, the width of the velocity distribution is a poor measure of the actual width. The real velocity distribution has a velocity width of $\Delta_{FWHM} = 7.68$ ms^{-1} while the converted TOF distribution has a larger velocity spread of $\Delta_{FWHM} = 11.36$ ms^{-1} which corresponds to a temperature of 112 mK, over double the actual temperature. This study validates our decision to determine the velocity width of the accelerated atoms by simulating the TOF data rather than simply converting the data to a velocity distribution.

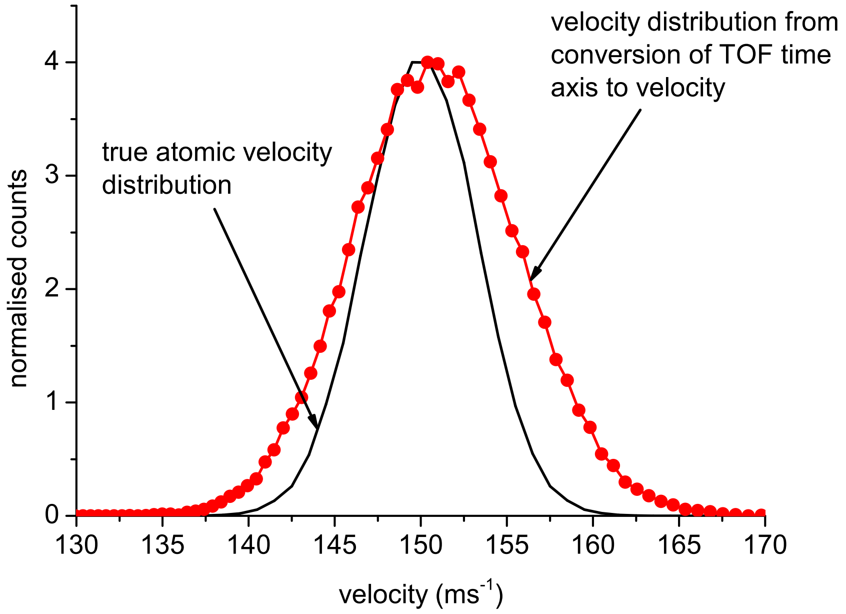

Figure 5.19: Velocity distribution of a 50 mK atomic sample with a mean velocity of 150 ms^{-1} and a simulation of the velocity distribution measured by obtaining TOF data with the ionisation probe and converting the data to a velocity distribution. The ionisation probe was at a distance of 7.6 mm with a beam width of $w_0 = 20$ μm.

The modeling method described in this section will be important in the next section where we will present our ion imaging experimental results. Simulations will be used to infer the velocity distributions of the accelerated atoms by fitting the experimental TOF data.

5.3.2 TOF experimental results and simulations

We carried out acceleration experiments using linear and sinusoidal chirps to accelerate Ar* atoms to different final velocities. As well as recording the MCP signals to produce the TOF profiles, we also recorded the temporal intensity profile of the lattice pulses and the beat pattern produced by heterodyning a small portion of each beam. The beat signals were analysed using the analysis technique described in section 4.4.4 to determine the frequency difference between the pulses over the duration of the pulse. The measured frequency difference and the lattice pulse intensity profiles were used in the simulations used to fit the experimental TOF data.

Figures 5.20(a)-(d) show the measured TOF distributions for four different chirps. The data in (a) and (b) were obtained with a linear chirp but a sinusoidal chirp was required to obtain measurements (c) and (d) where the final frequency difference produced by the chirp was larger. The TOF profiles show a discrete accelerated peak followed by a slow rising tail of atoms at lower velocities which were not stably accelerated but had their velocities perturbed by the moving lattice potential. This lower velocity tail was also seen in the fluorescence images shown in figure 5.12. Superimposed on the TOF data are simulated TOF distributions generated using the model described in sections 4.5.2 and 5.3.1. These TOF distributions were simulated using measured spatial and velocity distributions. The MOT $1/\sqrt{e}$ radius was 180 μm and the velocity distribution corresponded to an atomic cloud with a temperature of 70 μK. Figures 5.20(i)-(iv) show the velocity distributions derived from the TOF fits, (i)-(iv) correspond to (a)-(d) respectively. From these velocity distributions we can determine that the accelerated packets had velocities of (a, i) 71 ± 1 ms^{-1}, (b, ii) 95 ± 1 ms^{-1}, (c, iii) 119 ± 1 ms^{-1} and (d, iv) 191 ± 1 ms^{-1}. The FWHM velocity widths of the accelerated peaks were (a, i) 7 ± 1 ms^{-1}, (b, ii) 6 ± 1 ms^{-1}, (c, iii) 8 ± 1 ms^{-1} and (d, iv) 11 ± 1 ms^{-1} which correspond to temperatures of 43 mK, 31 mK, 56 mK and 105 mK respectively. The fraction of atoms in the accelerated packet in the velocity distributions in figures 5.20(i)-(iv) were 10.8%, 3.1%, 1.9% and 0.7% respectively. These fractions are not absolute as we only experimentally measure a portion of the velocity distributions (i.e. the solid parts of the distributions in the figures 5.20(i)-(iv)). The fluorescence images presented in the previous section are better for measuring the fraction of atoms accelerated as they detect all atoms in the distribution.

Measured lattice beam parameters were used in the acceleration simulations presented

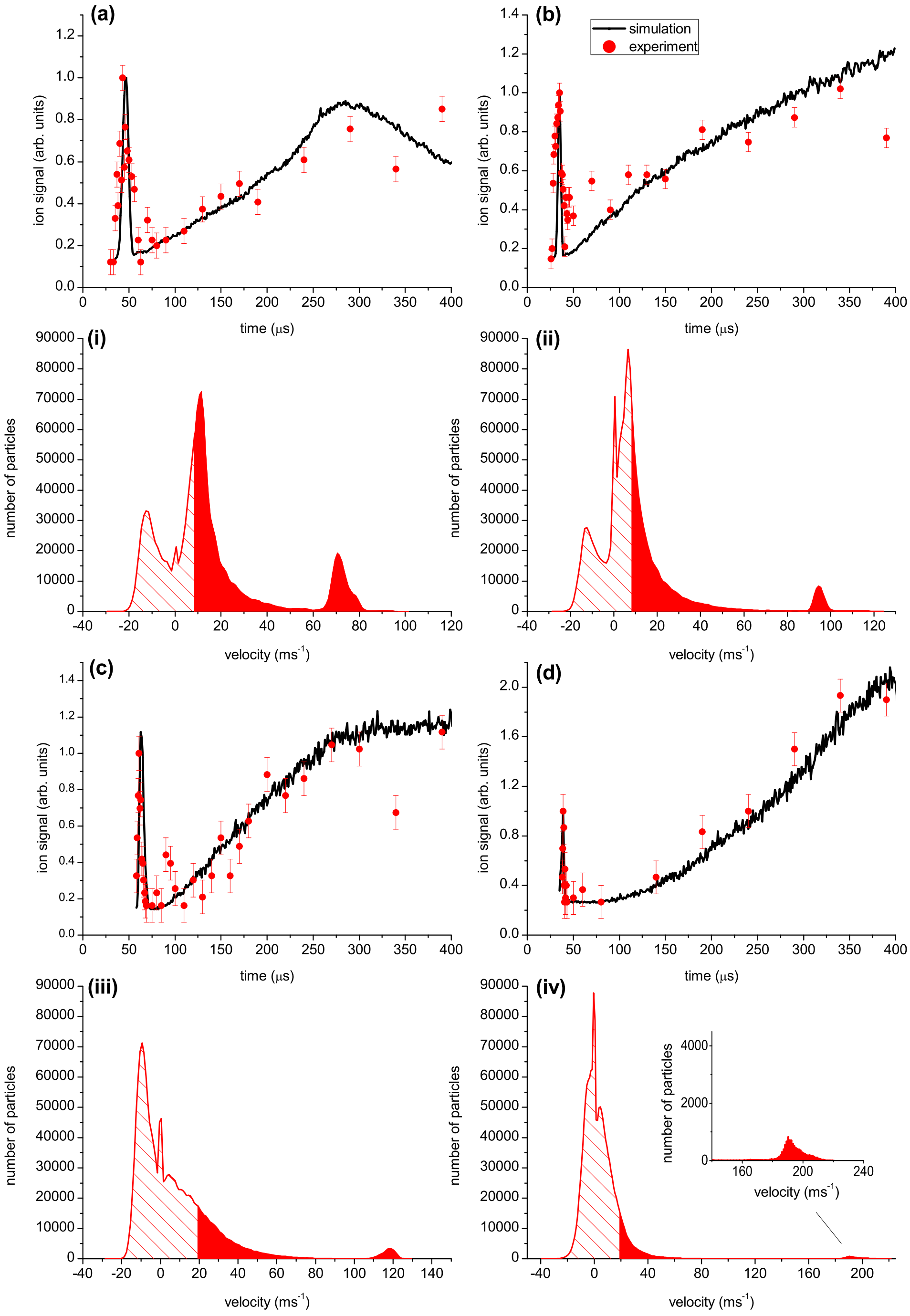

Figure 5.20: TOF measurements of the accelerated atomic packets for different chirps and comparisons with simulations. (a)-(d) TOF profiles and those from simulations corresponding to measured final velocities of (a) 71 ± 1 ms^{-1}, (b) 95 ± 1 ms^{-1}, (c) 119 ± 1 ms^{-1} and (d) 191 ± 1 ms^{-1}. A linear chirp was used to obtain (a) and (b) while the sinusoidal chirp was required to reach the final velocities in (c) and (d). Data were obtained at ionisation probe distances of 3.4 mm (a,b) and 7.6 mm (c,d). Superimposed on the TOF data are simulated TOF distributions generated using the model described in the text. (i)-(iv) Velocity distributions inferred from the TOF fits. The solid parts of the distributions correspond to the portions contributing to the simulated TOF profiles while the shaded portion is the predicted distribution at lower velocities.

in figure 5.20. Figure 5.21 shows the measured lattice pulse characteristics used to simulate the TOF distribution in figure 5.20(b). Figure 5.21(a) shows the $\sqrt{I_1(t)I_2(t)}$ term used to calculate the potential and 5.21(b) shows the measured beat signal from heterodyning the two lattice pulses with a frequency offset added to arm B. This beat signal was analysed to determine the frequency difference between the pulses over the duration of the lattice. Figure 5.21(c) shows the measured frequency difference from the analysis and a fit to the measured data. The frequency difference is initially constant at 91 ± 5 MHz and then increases to 265 ± 10 MHz in 70 ns. The uncertainty on the measured frequency values comes from Gibb's oscillations observed on the data from the frequency analysis (see section 4.4.4). We subtracted the frequency offset from the fit to the chirp and used this in our simulations. When fitting the experimental data with the fit the final frequency difference was adjusted slightly, within the confines of the uncertainty on the measured final frequency difference. The intensity in the simulations was set by considering the energy of the lattice pulses, their duration and their beam waist at the focus. The pulse energies were measured using a power meter with an uncertainty of 10%. Their duration was measured from the temporal pulse profile recorded on a photodiode. The radii of the lattice beams were estimated by measuring the width of the accelerated packet in the fluorescence images. As the width of the packet was less than that of the MOT its form in the radial direction was governed by the lattice beams. By measuring the accelerated packet width from a number of fluorescence images we determined the $1/\mathrm{e}^2$ radius of the lattice beams to be 160 ± 25 μm. In the experiment which produced the results shown in figure 5.20(a), where the atoms were accelerated to 71 ± 1 ms^{-1}, the lattice pulse energies were $E = 50 \pm 5$ mJ and the pulse duration was $\tau = 138 \pm 5$ ns. The intensity of the lattice pulses in this case was calculated to be $(4.5 \pm 1.5) \times 10^{12}$ Wm^{-2}. The large uncertainty is due to the uncertainty in the width of the lattice beams. When simulating the experimental results in figure 5.20(a) the intensity was initially set to 4.5×10^{12} Wm^{-2} and then varied within the uncertainty of the measurement to fit the data. Table 5.1 shows the results from the beat signal analysis for each data set in figure 5.20. Also shown are the final frequency differences and the single beam lattice pulse intensities used in the simulations.

From table 5.1 we can see that the final lattice velocity in the simulations does not exactly correspond to the measured velocity of the accelerated peak. In the case of a linear

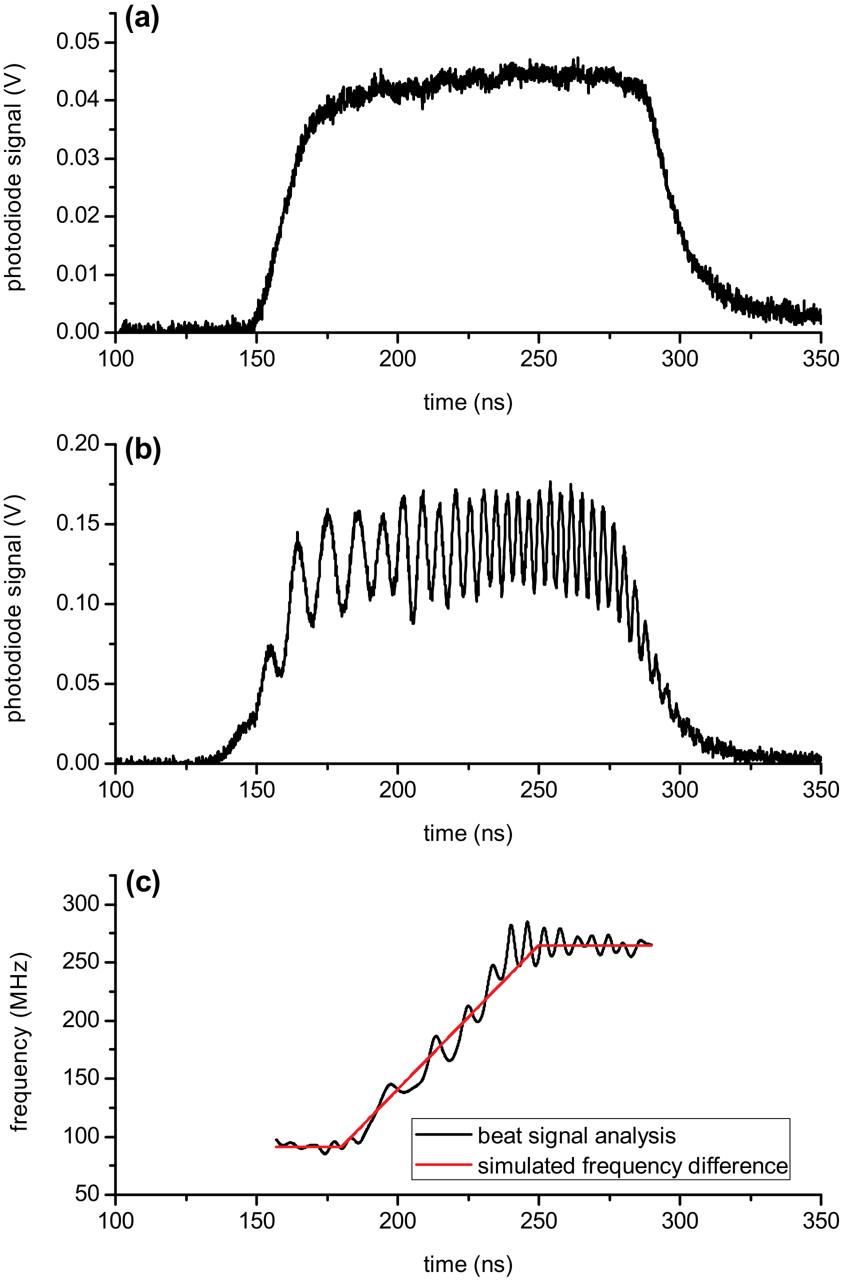

Figure 5.21: Measured lattice pulse characteristics used in simulations shown in figures 5.20(b) and (ii). (a) Square root of the product of the two individual lattice beam temporal profiles (i.e. the $\sqrt{I_1(t)I_2(t)}$ term used to calculate the lattice potential). (b) Beat signal measured by heterodyning the two lattice pulses on a photodiode. (c) Frequency difference as a function of time determined by analysing the beat signal in (b). The red trace is a simulated chirp fitted to the data from the analysis. The frequency difference was chirped from 91 ± 5 MHz to 265 ± 10 MHz in 70 ns. The initial frequency difference is due to the offset added by the AOM.

chirp (i.e. data sets (a,i) and (a,ii) in figure) this is due to the dynamics of the atoms in the lattice sites over the lattice duration. A 70 ns linear chirp was used which ended approximately 20 ns before the lattice switched off and therefore the lattice had a constant velocity for the final 20 ns. In chapter 4 we discussed how the potential well depth in the

Data set (from figure 5.20)	(a,i)	(b,ii)	(c,iii)	(d,iv)
Packet velocity (ms^{-1})	71 ± 1	95 ± 1	119 ± 1	191 ± 1
FWHM velocity width (ms^{-1})	7 ± 1	6 ± 1	8 ± 1	11 ± 1
Measured Δf_{final} (MHz)	138 ± 10	179 ± 10	222 ± 15	371 ± 20
Simulation Δf_{final} (MHz)	147	189	235	368
Simulation final $v_{lattice}$ (ms^{-1})	78	101	125	196
Simulation I ($\times 10^{12}$ Wm^{-2})	3.3	3.1	2.7	5.4

Table 5.1: Summary of measurements from TOF data, analysis of chirp and key simulation parameters.

lattice becomes shallower during acceleration so when the chirp stops, and the lattice has a constant velocity, the well depth increases. During acceleration the atoms become spatially bunched on one side of the lattice sites and when the wells becomes deeper, after the chirp ends, they will move back towards the potential minimum. The atoms will then oscillate in the moving potential wells until the lattice is switched off. As the atoms move back and forth across the constant-velocity lattice sites their velocity will vary about the lattice velocity. The final velocity of the atoms will then vary depending on when the lattice is turned off.

A sinusoidal chirp was used to obtain data sets (c,iii) and (d,iv). The accelerated packet velocity was not equal to the final lattice velocity expected from the amplitude of the chirp as the lattice was switched off before the chirp had achieved the maximum frequency difference. Thus the lattice velocity, and hence the velocity of the accelerated particles, was less than the maximum possible for the chirp used. The particle dynamics over the lattice duration will be studied in more detail in the next chapter.

5.4 Doppler imaging of accelerated atoms

The final measurement technique we used in our acceleration experiments was a Doppler imaging technique which used a resonant laser beam counter-propagating to the accelerated atoms to obtain velocity-selective fluorescence measurements. The probe beam was resonant with the 811.5 nm Ar* transition and was red-detuned such that atoms traveling towards the beam were Doppler shifted back on to resonance. If we recall the atomic photon scattering rate from chapter 2,

$$\Gamma_{scatt} = \frac{s_0\Gamma/2}{1 + s_0 + (2(\Delta + \boldsymbol{kv})/\Gamma)^2}, \tag{5.4}$$

we can see that atoms with a velocity $v = \Delta/k$, where Δ is the detuning of the probe beam, will produce the most fluorescence. Thus, by varying the probe beam detuning we can map out the velocity distribution of the atoms. The natural linewidth Γ sets the best possible velocity resolution of the measurement. The 811.5 nm Ar* transition has a linewidth of 5.87 MHz which gives a velocity resolution limit of 4.8 ms^{-1}. The resonant probe beam was taken from the zeroth order of the MOT slave beam AOM (see figure 3.11) and was initially detuned by -160 MHz from resonance. The beam was then aligned in double-pass through an 80 MHz AOM to shift its frequency back towards resonance. By varying the AOM frequency we could obtain probe beam detunings in the range 0-65 MHz. After the AOM the probe beam was passed through a half-wave plate and a polarising beam splitter so that we could control the power of the beam. This allowed us to account for the varying efficiency of the AOM at different frequencies which caused the probe beam power to vary as we tuned the AOM frequency. The power of the probe beam was maintained at approximately 0.1 mW such that the intensity was well below the saturation intensity which prevented power broadening and an associated decrease in the velocity resolution.

The limited tuning range of probe beam (0-65 MHz) restricted us to the measurement of velocities in the range 0-53 ms^{-1}. This limited the use of the technique to low velocity acceleration. The experimental sequence used to acquire the fluorescence images involved switching on an imaging pulse from the resonant probe laser beam after acceleration while all other fields were switched off. The probe beam was switched using a commercial RF switch, as described in section 3.5.1, and was only on for the duration of the camera exposure. Each image was acquired with a 30 μs exposure time and was an accumulation of 1000 experimental shots. The delay between acceleration and the imaging time was carefully chosen such that the atoms with a velocity corresponding to the probe detuning had moved away from the initial MOT position by the time the image was acquired. This was done because the large number of unaccelerated atoms which remained in approximately the initial MOT position produced a fluorescence signal at most detunings. The fluorescence in a well-defined spatial region of interest was then measured to determine the number of atoms in that velocity class. Each fluorescence image had its background subtracted using images acquired when the MOT magnetic field coils were switched off. All laser beams used in the experiment followed their usual sequence.

We carried out a Doppler measurement on an accelerated packet produced by a lattice with a 70 ns linear chirp from 0 ± 5 MHz to 82 ± 5 MHz and a corresponding final velocity of 43.6 ± 2.7 ms^{-1}. Pulse energies of 10 mJ were used which gave intensities of approximately $(9 \pm 3) \times 10^{12}$ Wm^{-2}. Figure 5.22(a) shows the measured velocity distribution and a simulation of the measurement. The distribution shows an accelerated peak with a velocity of 38 ms^{-1} and a FWHM velocity spread of 14 ms^{-1}. As each data point was the accumulation of 1000 images, statistical fluctuations in the data, from sources such as MOT atom number fluctuation and laser intensity fluctuations, were strongly reduced. The main source of uncertainty in the measurement of the fluorescence at each detuning was from the probe beam intensity. Although we attempted to maintain a constant probe power across all detunings measured it was difficult to do so due to misalignment of the half-wave plate or inaccuracies in the measurement of the AOM efficiency. We estimated that we could maintain the probe beam power to within ±5%. At the intensities we operate at (≈ 0.1 mWcm^{-2}), a 5% uncertainty in the laser power translates almost equivalently to a 5% uncertainty in the atomic photon scattering rate, thus, our error bars in figure 5.22(a) are 5% of the measured fluorescence values.

The simulation of the Doppler measurement was performed using an extended version of the model discussed in section 4.5.2. Once the velocity distribution was calculated, using the model previously introduced, the signal that would be observed using the Doppler imaging technique was then simulated. This was done by summing the fluorescence from each atom, calculated using equation 5.4, at the detunings used in the experimental measurement. The simulation of the acceleration again used measured MOT spatial and velocity distributions and measured lattice beam parameters. The trajectories of 50000 atoms were calculated

In order to determine the velocity resolution of our measurement, we measured the fluorescence from the MOT atoms as a function of detuning, which in an ideal experiment would correspond to a measurement of the natural linewidth of the transition Γ. The measurement was carried out under identical conditions to the Doppler measurement. Figure 5.22(b) shows the measured fluorescence data and a Lorentzian fit which gave a measured linewidth of $\Gamma = 12.9$ MHz, over double the natural linewidth. The primary source for the broadening of the linewidth was the frequency jitter of our MOT laser system discussed in section 3.3. The oscillation in the frequency acted to broaden the

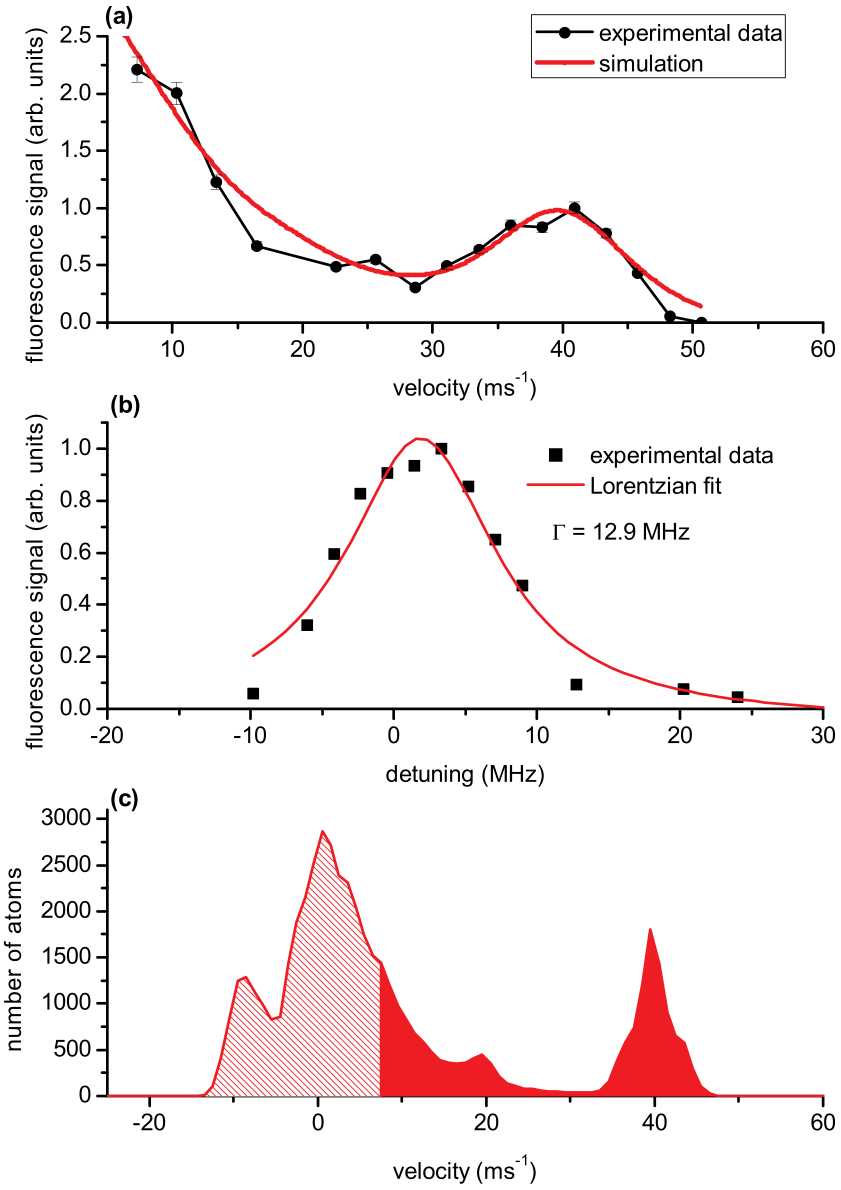

Figure 5.22: (a) Doppler measurement of an accelerated packet of atoms with a velocity of 38 ms^{-1} with an overlaid simulation of the measurement. (b) Fluorescence measurements of the MOT at different detuning's from resonance. The measurement was carried out under the same conditions as the Doppler measurement and was used to test the velocity resolution of the Doppler measurement. (c) Simulated velocity distribution used to simulate the Doppler measurement in (a). The distribution contains 50000 atoms and was generated by binning atoms in 1 ms^{-1} velocity intervals.

linewidth by scanning over a portion of the Lorentzian line shape rather than measuring it at a precise single frequency. In our simulation of the Doppler measurement we used $\Gamma = 12.9$ MHz in the calculation of the fluorescence.

The velocity distribution used to simulate the Doppler measurement in figure 5.22(a) is shown in figure 5.22(c). It is clear that the measured profile is considerably broadened compared with the velocity distribution of the atoms. In the measured profile the accelerated packet is not distinct from the tail of slower atoms that follow, whereas in the simulations we see that the peak is clearly separate from the slower atoms. The accelerated packet in the velocity distribution has a peak velocity of 39.5 ms^{-1} and a FWHM velocity width of 4.0 ms^{-1}. The accelerated peak contained 18% of the atoms in the total distribution, although this number cannot be considered as an absolute measurement as we did not measure the full velocity distribution.

5.5 Discussion

In this chapter we have presented the results from our Ar* optical Stark acceleration experiments. We have demonstrated acceleration to up to 191 ± 1 ms^{-1} while maintaining a narrow velocity spread, of approximately 10 ms^{-1} or less, in the accelerated packet of atoms. The results were obtained using different measurement techniques, each was particularly suited to measuring certain characteristics of the accelerated atomic ensemble. The fluorescence imaging results presented in section 5.2 were used to determine the velocity of accelerated packets at low velocities. We presented a fluorescence imaging data set for an accelerated packet with a measured velocity of 45.5 ± 1.2 ms^{-1} which nicely shows this measurement technique. The main drawback of using fluorescence imaging was that we could not achieve sufficiently short image exposure times to freeze the atomic motion. This resulted in a blurring effect on the images which was accentuated at higher velocities making measurements less precise. However, the fluorescence images had an advantage over the other measurement techniques we used as they imaged all atoms from the initial distribution after acceleration. This was valuable for measurements other than that of the velocity of the accelerated atoms. In particular, determination of the fraction of atoms from initial distribution accelerated was only possible by analysis of these fluorescence images. This allowed us to experimentally verify that by varying the depth of the lattice potential wells we could tune the number of atoms in the accelerated packet. Imaging all atoms in the distribution also allowed us to observe how the velocities of the atoms not stably accelerated were perturbed by the moving lattice potential. From the fluorescence images presented we could see that few atoms remained stationary and that low velocity peaks traveling in both directions were produced, as was predicted by our simulations.

The ion imaging technique presented in section 5.3 enabled us to make precise measurements of the accelerated packet velocity at higher velocities than was possible using fluorescence imaging. Simulations of the acceleration process were used to fit the experimental data and allowed us to determine the velocity, and also the velocity width, of the accelerated packet of atoms. Final velocities of 71 ± 1 ms^{-1}, 95 ± 1 ms^{-1}, 119 ± 1 ms^{-1} and 191 ± 1 ms^{-1} were measured with corresponding velocity spreads of 7 ± 1 ms^{-1}, 6 ± 1 ms^{-1}, 8 ± 1 ms^{-1} and 11 ± 1 ms^{-1}. These velocity spreads correspond to temperatures in the range 30-100 mK. It was mentioned in section 5.3.2 that the measured velocities were not equivalent to the final lattice velocities and it was briefly explained that this was due to the dynamics of the atoms in the lattice potential wells. In the next chapter we will study the atomic dynamics over the acceleration period in more details using our acceleration simulations.

The final measurement technique we used was a Doppler imaging method which allowed us to obtain velocity-selective fluorescence measurements of the accelerated atoms. A frequency tunable laser beam counter-propagating to the accelerated atoms was used to induce fluorescence in atoms within a specific velocity class. This technique was limited to measuring low velocity atoms (< 50 ms^{-1}) due to the limited tuning range of the probe beam frequency. Furthermore, the velocity resolution of this technique was limited by the frequency jitter of the probe laser beam.

Our measurements show that optical Stark acceleration can be used to tune the velocity of the accelerated atoms while maintaining a narrow velocity spread, which is an important feature of the technique. The velocity spreads measured represent an improvement on those measured in constant-velocity lattice molecular deceleration experiments (≈ 80 ms^{-1}) although it is not possible to make a direct comparison as the initial velocity distributions in the constant-velocity lattice experiments were much broader than those in the experiments presented in this chapter. Other techniques for producing controlled atomic and molecular beams achieve comparable velocity spreads. Stark decelerators have been used to produce velocity controlled beams for a wide range of molecular species including CO [51] and NO [131] beams with velocity spreads of 4 ms^{-1} and 3 ms^{-1} respectively. The Zeeman deceleration technique has been applied to Ne atoms initially traveling in a supersonic beam to produce beams with velocities of 55-222 ms^{-1} and velocity spreads of 13-20 ms^{-1}.

5.6 Conclusions

In this chapter we have demonstrated that optical Stark deceleration is capable of producing a tunable velocity particle beam while maintaining a narrow velocity spread. The ability to tailor the optical potential to achieve control over the number of particles in the accelerated beam has also been shown. The measured performance, in terms of velocities and velocity spreads achieved, is comparable with other similar methods (e.g. Stark and Zeeman deceleration) but optical Stark acceleration has the advantage that it can be applied to any polarisable particle. The use of a chirped lattice in our experiments represents a significant improvement over the previously demonstrated constant-velocity lattice deceleration technique as velocity tuning is achieved through simply varying the frequency chirp and the switching of the optical fields is less critical. Furthermore, less intense laser fields are required which broadens the potential application of the method.

By accelerating Ar* we have demonstrated two major advantages of chirped optical Stark acceleration. Firstly, this shows that this method can be applied to atomic and molecular species close in energy to the ionisation potential. Also, Ar* atoms have a polarisability 27 times larger than that of ground state Ar atoms which shows the potential to boost the acceleration force by manipulation of the internal quantum states of the target species. This could feasibly be achieved for any atomic or molecular species as long as the lifetime of the of the excited state is greater than the acceleration period.

Chirped optical Stark acceleration acceleration has a number of potential applications. In our experiments we will use the technique to produce cold stationary molecules for sympathetic cooling experiments. The tunable nature and narrow velocity spread of the beams produced make them ideal for use in high-resolution collision experiments. The high energy resolution provided by the narrow velocity spreads will allow for the study of tunneling and resonance phenomena in interactions which are normally masked by the wide energy spread of conventional molecular beams. It has also been suggested that the technique could be used to study cold ion-molecule interaction crossing a Coulomb crystal with controlled neutral particle beams, or in low energy surface chemistry studies [132]. Another proposal involves the acceleration of positronium (ps) which has a very favourable polarisability-to-mass ratio ($\alpha = 5.93 \times 10^{-40}$ Cm^{2}V^{-1}, $m = 1.1 \times 10^{-3}$ amu) [133]. Positronium beams have application in precise measurement of ps-atom/molecule cross-sections (e.g ps-Ar cross-section measurement [134]) or for use as a probe in condensed matter physics.

Chapter 6

Acceleration dynamics and future experiments

In the previous chapter we presented results from our Ar* optical Stark acceleration experiments where the atomic dynamics inside the individual lattice sites had an important influence on the final atomic velocity distribution. In order to further understand these dynamics, simulations of the acceleration dynamics in our Ar* experiments, and also in planned future experiments, have been carried out. This chapter presents the results from these simulations and discusses the insight gained from them.

6.1 Simulation of Ar* acceleration dynamics for a linear chirp

In order to study the acceleration dynamics, we used the simulations detailed in section 4.5.2. While previously we were only interested in the final velocity distribution of the atoms, we now turn our attention to how the velocity distribution evolves over the accelerating lattice duration. By extracting the velocity distribution at 1 ns intervals in our simulation we can study its evolution during acceleration. Figure 6.1 shows the results from a simulation used to study the acceleration dynamics. This simulation corresponds to that used to fit the 95 ms^{-1} peak in figure 5.20 and was run for 50000 atoms. Figure 6.1(a) shows the lattice beam characteristics used in the simulation. The frequency difference was linearly ramped from 0 MHz to 189 MHz in 70 ns which creates a lattice accelerating to a final velocity of 101 ms^{-1}. Figure 6.1(b) shows temporal evolution of the atomic velocity distribution over the lattice duration from which we can gain insight into the acceleration dynamics. The dashed white line shows the velocity of the lattice.

When the lattice is switched on it is stationary and the atoms are attracted to the local potential minimum. This accelerates the atoms and they begin to oscillate across the lattice sites. This oscillation can be observed in the variation of the atomic velocity distribution with time. The velocity distribution is first broadened when the atoms are accelerated towards the potential minimum. This broadening occurs because the atoms have different initial positions in the lattice sites and therefore when they reach the potential minimum have a broad range of velocities. After a half oscillation across the lattice site they will be stationary again but on the opposite side of the lattice site to where they were initially. From figure 6.1(b) it can be seen that most atoms complete a half oscillation 30 ns after the lattice is switched on and that the velocity distribution has become narrow again. The frequency chirp begins at 50 ns and the lattice begins to accelerate transporting a small fraction of the atoms with it. The trapped atoms undergo oscillations in the lattice during the accelerating phase as well. However, the potential depth in the accelerating lattice is shallower and the oscillations do not have as much of an effect on the velocity distribution as they did in the stationary lattice. The chirp ends at 110 ns and the lattice moves with a constant velocity of 101 ms^{-1} until it is switched off. During acceleration the atoms become spatially bunched up on one side of the lattice sites. When the lattice stops accelerating the potential wells become deeper again and the atoms begin to oscillate in the constant-velocity lattice. This causes the velocity of the accelerated atoms to vary about the final lattice velocity until the lattice is switched off. The final velocity of the accelerated packet is then determined by the lattice switch off time in relation to the atoms oscillation in the constant-velocity lattice.

Successful acceleration depends on the initial velocity and position an atom when the chirp is induced. Those with the wrong initial position or velocity are not stably accelerated but have their velocities perturbed by the subsequent passing optical waves. The density fringes observed in 6.1(b) at low velocities result from this perturbation by the moving lattice. At later times the fringes become closer together as the passing lattice sites gain velocity and pass more frequently. The low velocity peaks observed in the fluorescence images in section 5.2, and predicted by earlier simulations, are a result of untrapped atoms being perturbed by the moving lattice.

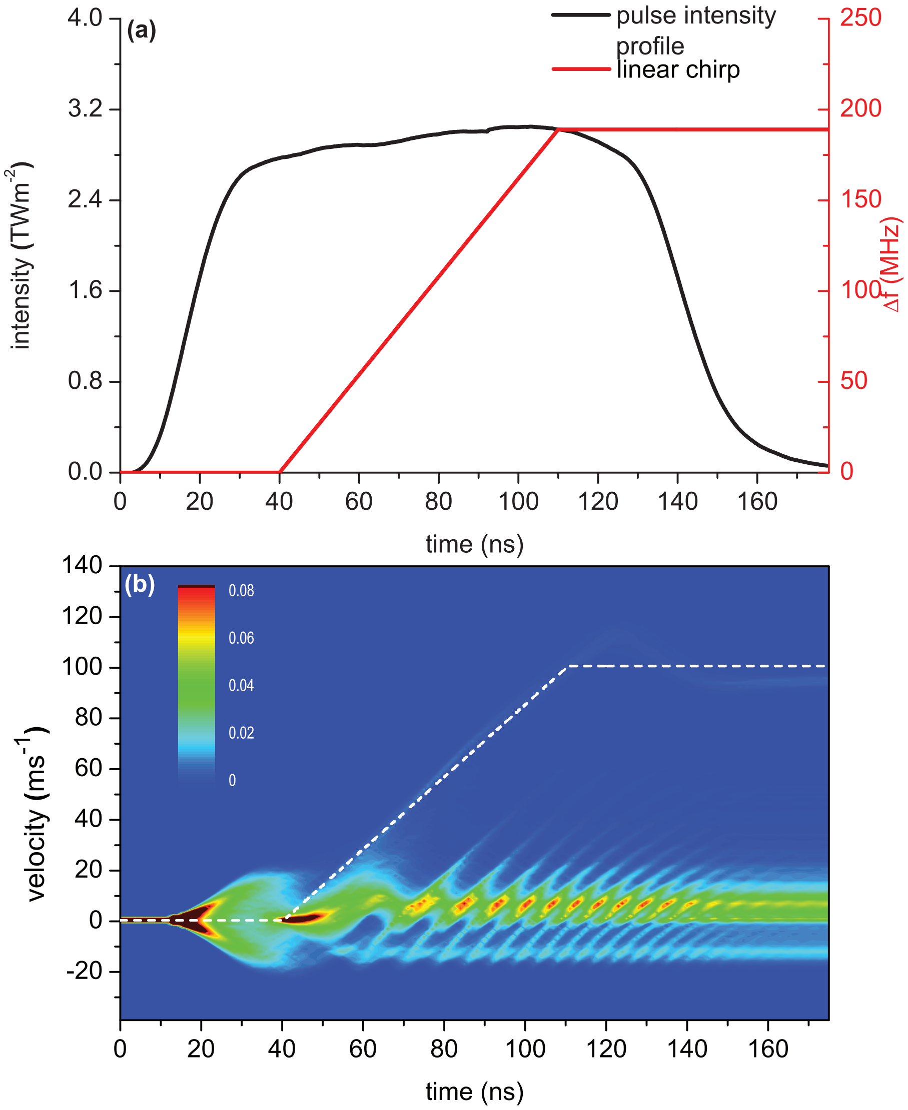

Figure 6.1: Simulation of acceleration dynamics for acceleration to 95 ms^{-1}. This simulation is the same as that used to fit the experimental data in figure 5.20(b). (a) Linear chirp to a frequency difference of 189 MHz and the temporal intensity profile of a single lattice beam. (b) Velocity evolution of the atoms over the lattice duration. This shows the perturbation of the initial velocity distribution caused by first ramping up the lattice intensity and then applying the chirp over 70 ns before switching the lattice off. The dashed white line shows the lattice velocity and the colour bar corresponds to the fraction of the total atoms.

6.1.1 Influence of chirp timing

In the previous section we stated that the delay between the end of the frequency chirp and the lattice switch off was important in determining the final velocity of the accelerated atoms. In order to study this effect further, we carried out a simulation varying the time at which the 70 ns chirp started. The velocity distributions of the accelerated atoms were used to study the influence of the timing of the chirp. Figure 6.2(a) shows the temporal intensity profile of the lattice pulses used in the simulation and the range of temporal chirp positions studied. We used ideal, super-Gaussian lattice pulse intensity profiles in the simulation so that we only studied the effects of varying the chirp position and did observe effects due to intensity variations in the pulse profile. The final frequency difference produced by the chirp was 189 MHz, the same as in the simulation in the previous section. This gave a final lattice velocity of 101 ms^{-1}. Each simulation was run for 50000 atoms and the final velocity distributions were derived from the simulations. Figure 6.2(b) shows a plot of the final velocity of the accelerated packet against start of the chirp. We can see that the final velocity of the accelerated atoms varies by approximately ± 10 ms^{-1} from the final lattice velocity of 101 ms^{-1} depending on the time at which the chirp began.

The velocity width of the accelerated packet also varied with the start time of the chirp. Figure 6.2(c) shows a plot of the FWHM velocity of the accelerated atoms against the temporal position of the chirp. The velocity width varies from between 9 ms^{-1} and 32 ms^{-1}. This variation was dependent on the Ar* velocity distribution when the chirp was applied. As mention earlier turning on the stationary lattice caused the atoms to oscillate in the lattice sites which meant that the atomic velocity distribution varied with time. If the chirp was applied when the initial Ar* velocity distribution was broad then the velocity distribution of the accelerated atoms was also broad.

The fraction of atoms accelerated was also dependent on the velocity distribution when the chirp was applied. This was also investigated using our simulations. Figure 6.3(a) shows the lattice pulse characteristics used in the simulation. Figure 6.3(b) shows the velocity evolution of the atoms in a stationary lattice when no chirp is induced. This has been plotted so that the velocity distribution at the different times at which the chirp starts can be seen. The velocity distribution is narrowest after the atoms have undergone a half oscillation across the lattice sites and are stationary again. From figure 6.3(b) we can see that half an oscillation takes approximately 25 ns. As the depth of the potential wells varies in both the radial and axial directions the atoms have different oscillation frequencies. This causes their oscillations in the lattice sites to fall out-of-phase with each other and the broadening and narrowing of the velocity distribution is no longer observed. Figure 6.3(c) shows the fraction of atoms accelerated plotted against the chirp start time. The fraction accelerated peaks at a chirp start time of 42 ns. From figure 6.3(b) we can see that at this time the velocity distribution is narrow. At earlier and later chirp start times the velocity distribution is much broader when the chirp is applied and the fraction

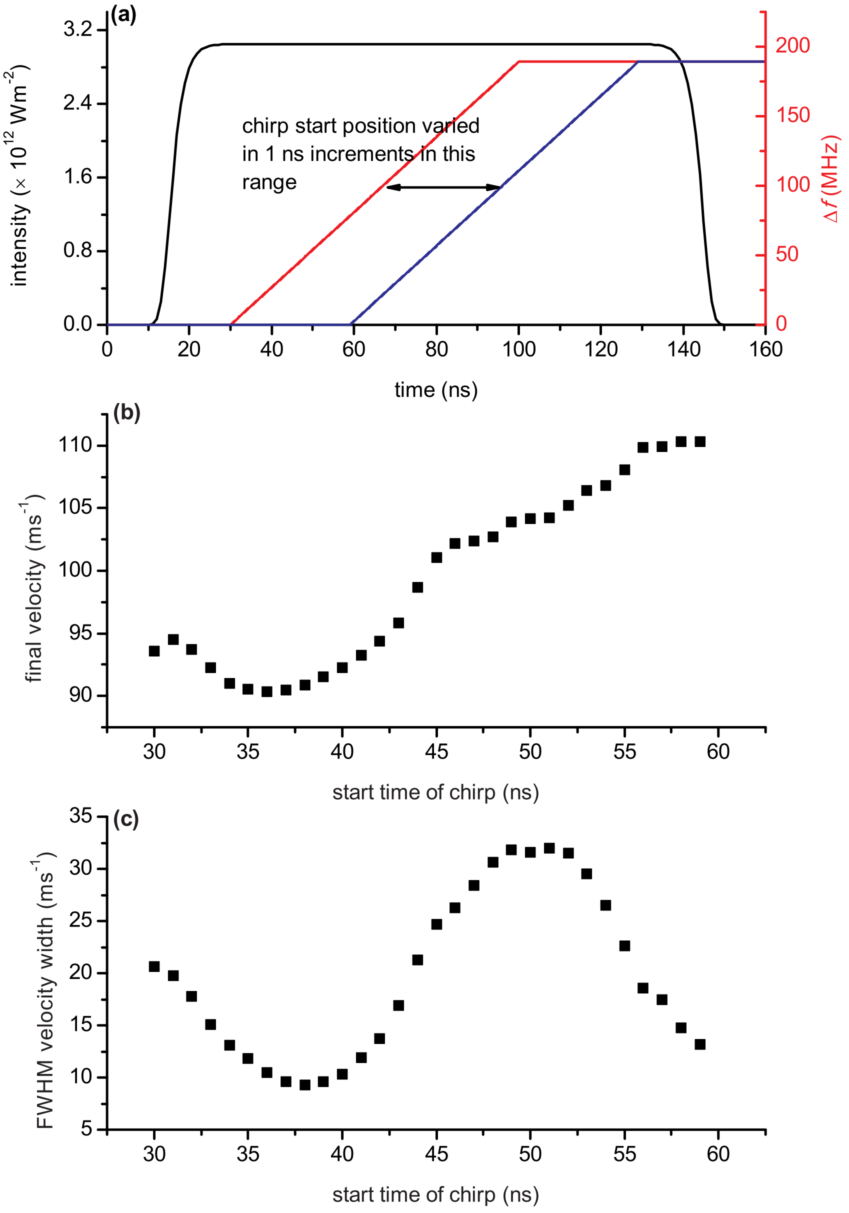

Figure 6.2: Study of the influence of the temporal position of the chirp on the velocity distribution of the accelerated particles. (a) Temporal intensity profile of the lattice pulses used in the simulation and the temporal position of the chirp. The chirp position was varied in 1 ns increments between the red and blue chirp positions shown. (b) The velocity of the accelerated packet of atoms plotted against the temporal position of the chirp. (c) The FWHM velocity width of the accelerated packet plotted against each chirp position.

accelerated is considerably less. By comparing figures 6.2(c) and 6.3(c) we can see that if the chirp is applied when the velocity distribution is narrowest (42 ns) the FWHM velocity width is narrow and the fraction accelerated is greatest. This is the ideal combination in experiments.

In this section it has been shown that when using a linear chirp to accelerate MOT atoms the starting time of the chirp with respect to the lattice beams switch on has a strong influence on the characteristics of the accelerated ensemble of atoms. In the next

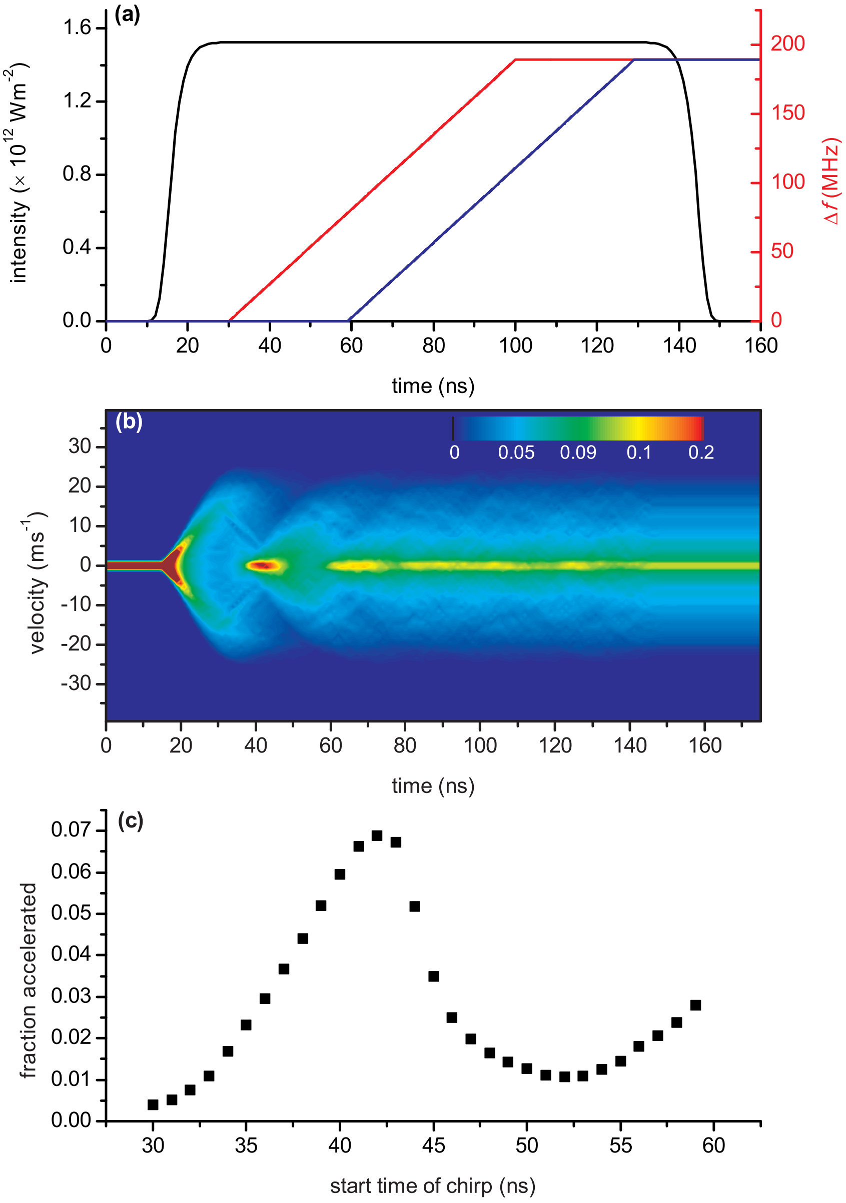

Figure 6.3: Study of the influence of the temporal position of the chirp on the fraction of atoms transported. (a) Temporal intensity profile of the lattice pulses used in the simulation and the temporal position of the chirp. The chirp position was varied in 1 ns increments between the red and blue chirp positions shown. (b) Velocity evolution of the atoms in the lattice when no chirp is applied. This allows us to see the initial velocity distribution of the atoms at the different times when the chirp is applied. (c) Fraction of atoms transported plotted against time at which chirp began.

section we will look at the velocity evolution of atoms when using a sinusoidal chirp.

6.2 Simulation of Ar* acceleration dynamics for a sinusoidal chirp

In the previous chapter the experimental results presented for acceleration of Ar* to 119 ms^{-1} and 191 ms^{-1} required the use of a sinusoidal chirp due to the limitations of the equipment at the time. The acceleration dynamics when accelerating with a sinusoidal chirp are different compared with when a linear chirp is used. Figure 6.4(a) shows the sinusoidal chirp and lattice beam temporal intensity used in the experiment to accelerate to 119 ms^{-1}. When using a sinusoidal chirp the frequency difference between the beams is only zero for a very short period and therefore the lattice is only briefly stationary. The chirp was aligned with the lattice pulses so that the lattice was stationary once the lattice beams reached approximately maximum intensity. This meant that when the lattice was being switched on the frequency difference was decreasing and the lattice was decelerating. The lattice pulse characteristics in figure 6.4(a) were used to simulate the velocity evolution of 50000 Ar* atoms over the lattice duration. Figure 6.4(b) shows how the velocity distribution is perturbed by the lattice. The acceleration is largest initially, when the chirp rate is fastest, and reduces over the duration of the lattice as the chirp progresses towards its maximum. From 6.4(b) we can see that the form of the acceleration follows that of the chirp. The decreasing chirp rate results in an increase in the potential well depths in the accelerating lattice. As the wells deepen towards the end of the acceleration period we can see that the velocity of the accelerated atoms begins to vary about the lattice velocity. This can lead to some deviation between the final lattice velocity and the velocity of the accelerated packet, as was the case for a linear chirp. The increase in well depth also acts to broaden the velocity distribution of the accelerated atoms. For these reasons a sinusoidal chirp is not ideal and future experiments would be better served by a linear chirp, which is also more efficient. In the next section we will look at an ideal chirp for future experiments drawing on what we have learned by studying the acceleration dynamics in our Ar* experiments.

6.3 Ideal chirp for future experiments

The work presented thus far in this thesis has shown that although the chirps we used in our Ar* acceleration experiments were suitable for achieving acceleration the precision of

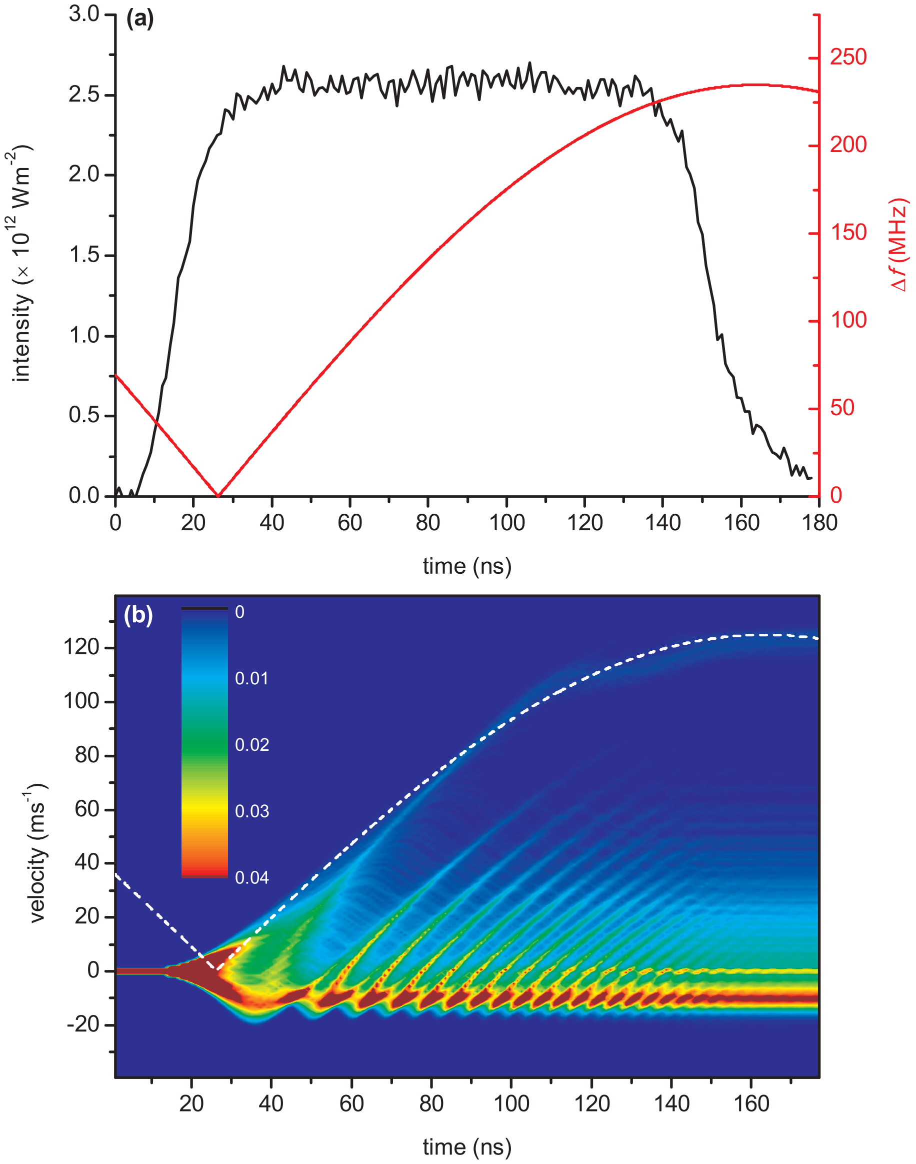

Figure 6.4: Acceleration dynamics when using a sinusoidal chirp to accelerate to 119 ms^{-1}. (a) Temporal intensity profile of a lattice pulse and sinusoidal chirp used in experiment to accelerate Ar* to 119 ms^{-1} and in the simulation of the acceleration dynamics. (b) Temporal evolution of the Ar* velocity distribution.

the final packet velocity, the fraction accelerated and the atoms velocity spread could be improved by varying the timing of the chirp. In this section we will look at acceleration with an ideal chirp which could be applied in future experiments. An ideal chirp is linear, as this is most efficient for acceleration and the depth of the potential wells remains constant over the acceleration duration. In the ideal case, the chirp would begin as soon as the lattice is turned on and end just before the lattice is switched off. Applying the chirp as soon as the lattice is switched on ensures that velocity distribution has not been broadened by the oscillatory motion of the atoms in the lattice when the chirp is applied. Also, by ending the chirp as the lattice is turned off the oscillatory motion which caused a mismatch between the final lattice velocity and the accelerated packet velocity when we used a 70 ns chirp would no longer be a problem. Furthermore, using a chirp which is applied over the full lattice duration means that the chirp rate is the lowest possible which reduces the intensity requirements of the lattice beams.

We studied acceleration with an ideal chirp which produced the same final frequency difference (189 MHz) as the 70 ns linear chirp studied earlier. Figure 6.5(a) shows the chirp and temporal intensity profile of the lattice pulses use in the simulation. Figure 6.5(b) shows the evolution of the atomic velocity distribution over the acceleration duration and 6.5(c) shows the final velocity distribution. From the evolution of the velocity distribution we can see that acceleration continues until the lattice is switched off. The peak of accelerated atoms in the final velocity distribution is at 103 ms^{-1} and the final lattice velocity was 101 ms^{-1}. By removing the 20 ns constant-velocity lattice phase which was present when the 70 ns linear chirp was used we will be able to more precisely tune the final packet velocity in future experiments. The final velocity distribution shows a series of smaller peaks at lower velocities. These are produced by atoms which are not trapped in the lattice site where they are initially located but are accelerated by one of the following passing optical waves. The acceleration of atoms in these smaller peaks can also be seen from the plot of the evolution of the velocity distribution. The fraction of atoms accelerated in this simulation was 16.1%. If we consider that the lattice beam intensities were 2.0×10^{12} Wm^{-2} we can show that using the longer chirp is much more efficient. This is compared with the 3.1% accelerated when using the 70 ns chirp with the higher lattice beam intensities of 3.1×10^{12} Wm^{-2}.

6.4 Deceleration of H_2 molecules

Thus far we have studied acceleration of Ar* atoms with a very narrow initial velocity distribution, corresponding to a temperature of 70 μK. This narrow velocity distribution is strongly perturbed by the lattice even before we apply a chirp. In future experiments we will use optical Stark acceleration/deceleration on samples which have a much broader initial distribution. To understand how this will work in a future experiment to decelerate H_2 molecules from a molecular beam the deceleration has been simulated. Molecular hydrogen is an attractive species for the first molecular deceleration experiments as it has a favourable polarisability to mass ratio ($m = 2$ amu, $\alpha = 5.2 \times 10^{-40}$) and can efficiently

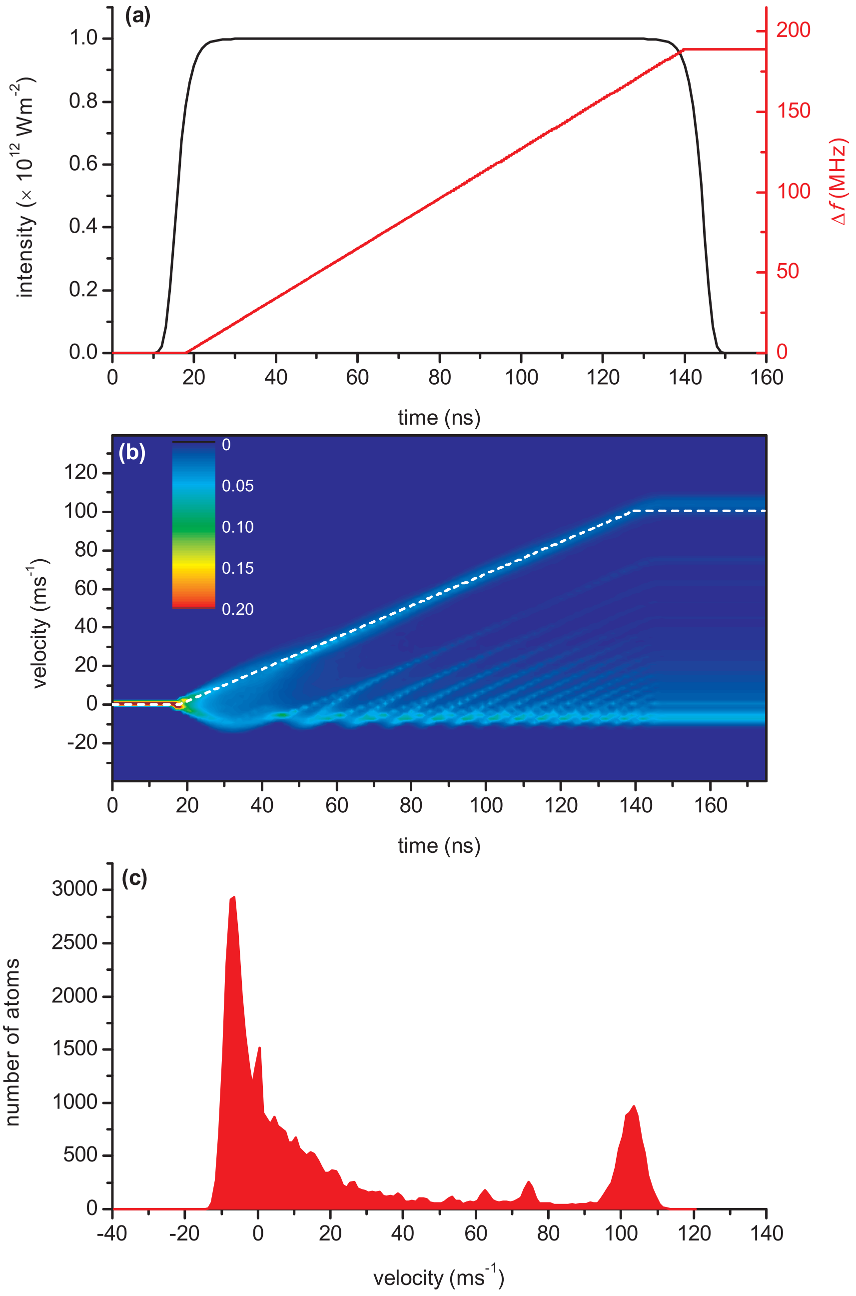

Figure 6.5: Simulation of acceleration of Ar* atoms with an ideal chirp. (a) Lattice beam pulse profiles and ideal linear chirp from 0 MHz to 189 MHz. (b) Velocity evolution of the atomic velocity distribution over the acceleration duration. (c) Final velocity distribution of the accelerated atoms.

be decelerated. This work is being carried with collaborators from Dr Michael Tarbutt's research group at Imperial College London who have developed an apparatus capable of producing a H_2 beam with temperatures on the order of 100 mK. The chirped laser system has been further developed since our Ar* acceleration experiments and can now produce linear ramps over large frequency excursions (> 1 GHz). This has been made possible by the addition of a high voltage amplifier (A-303 A. A. Lab Systems) which is capable of amplifying fast linear ramps and allows the application of large voltage ramps to the electro-optic crystal. In this section a simulation of this experiment will be presented which will allow us to compare the acceleration dynamics in an experiment where the initial velocity distribution is much larger than in a MOT. The simulation will also allow us to determine the lattice beam energies required for this future experiment.

In order to simulate the experiment, we used spatial and velocity distributions for the H_2 beam corresponding to those which were measured by our collaborators during characterisation of their apparatus. The H_2 beam has a forward velocity of 248 ms^{-1} and velocity width of 68 ms^{-1} which corresponds to a temperature of 200 mK. In the simulation the molecules were distributed evenly over the lattice dimensions as in the experiment the spatial extent of the lattice will be much smaller than that of the molecular beam. Figure 6.6(a) shows the lattice beam parameters used in the simulation. The initial frequency difference was 466 MHz such that the initial velocity of the lattice was 248 ms^{-1}, equal to that of the molecular beam. The lattice was then decelerated to rest over the pulse duration by linearly ramping down the frequency difference to zero. Figure 6.6(b) shows the evolution of the molecules' velocity distribution produced by the simulation and figure 6.6(c) shows the final velocity distribution. These figures were produced by simulating the trajectories of 50000 H_2 molecules. The final velocity distribution shows a discrete peak at 0 ms^{-1} which has a velocity width of 24.5 ms^{-1} corresponding to a temperature of 26.2 mK. The fraction of atoms in the decelerated peak is 10.9%. The velocity evolution plot shows that decelerating lattice traps a portion of the initial distribution and smoothly transports it to 0 ms^{-1}. From this plot we can also see that the distribution of the unaccelerated atoms is not as strongly perturbed as in the Ar* acceleration experiments where the initial distribution was much narrower.

In the simulation lattice beams with a diameter of 100 μm were used and considering the peak intensity of the pulses was 4×10^{12} Wm^{-2} lattice pulse energies of approximately 18 mJ will be required in the experiment to replicate the results of our simulation. These pulse energies are well within the capability of our laser system.

This experiment will allow us to demonstrate an important feature of optical Stark acceleration/deceleration which was not observed in our Ar* acceleration experiments due to the narrow initial distribution of the atoms. When this technique is applied to samples with a broader initial distribution it can be used to select a portion of the sample with a

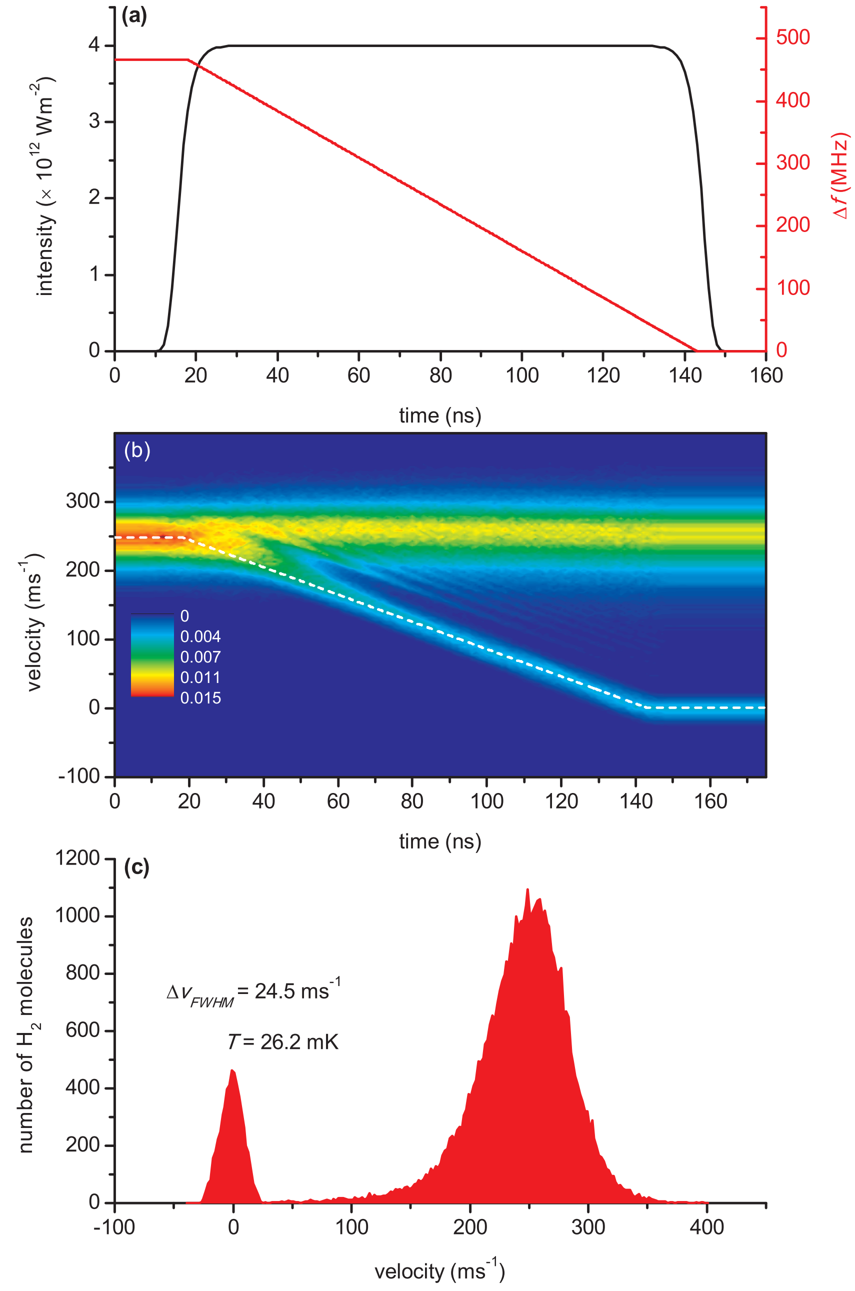

Figure 6.6: Simulation of deceleration of H_2 molecules from a molecular beam with a forward velocity of 248 ms^{-1} and a velocity width of 68 ms^{-1} corresponding to a temperature of 200 mK. (a) Lattice beam parameters used in simulation. (b) Evolution of the H_2 velocity distribution over the lattice duration. (c) Final velocity distribution of the H_2 molecules with a discrete decelerated peak at 0 ms^{-1}. The peak has a velocity width of $\Delta v_{FWHM} = 24.5$ ms^{-1} which corresponds to a temperature of 26.2 mK.

narrower velocity distribution than in the initial distribution. In the simulation we have presented in this section the velocity width of the decelerated molecules (24.5 ms^{-1}) was considerably narrower than in the initial distribution (68 ms^{-1}). The velocity spread of the decelerated molecules could be decreased further in experiments by reducing the pulse intensities and reducing the potential well depths.

6.5 Conclusions

In this chapter the dynamics of particles in accelerating and decelerating chirped optical lattices have been studied. Simulations were used to look at the evolution of the atomic velocity distribution over the acceleration duration. This investigation showed that although the chirps we used in our Ar* acceleration experiments could readily achieve acceleration they had some disadvantages. When the 70 ns linear chirp was used the lattice had a constant velocity for the final 20 ns before it was switched off. Oscillations of the accelerated atoms in the constant-velocity lattice sites caused a mismatch between the final lattice velocity and the velocity of the accelerated packet. In future experiments where precise tuning of the atomic packet velocity over a wide range is required this would be a disadvantage. The influence of the timing of the chirp was further investigated. It was found that the final velocity, the velocity spread and the fraction of atoms accelerated were all strongly affected by the timing of the chirp with respect to the lattice beams. We also studied the acceleration dynamics using a sinusoidal chirp where the chirp rate decreases over the lattice duration and the accelerating potential well depths increase. The atoms oscillate in the deeper potential wells which causes a variation of the atomic velocity about the lattice velocity. The increasing well depth also acts to broaden the velocity spread of the accelerated packet. In future experiments these disadvantages could be negated by using a linear chirp which begins as the lattice is being turned on and ends when the lattice is being switched off. We simulated Ar* acceleration with such a chirp. The acceleration continued until the lattice was switched off and the final packet velocity (103 ms^{-1}) was approximately equal to the final lattice velocity (101 ms^{-1}).

We have also studied the acceleration dynamics in an H_2 deceleration experiment currently under preparation where the initial velocity spread ($\Delta v_{FWHM} = 68$ ms^{-1}) of the sample was much broader than in our Ar* experiments. The perturbation of the velocity distribution by the lattice was much less pronounced than in the Ar* experiments. This simulation also showed that with modest beam energies 10.8% of the H_2 molecules could be decelerated to rest to produce a stationary molecular sample with a temperature of 26.2 mK.

Chapter 7

Ar* QUEST

This chapter describes the trapping of metastable argon in a quasi-electrostatic trap (QUEST). The motivation behind this experiment was to study optical trapping of Ar* in a more simply implemented QUEST than one formed in a high finesse build-up cavity, which will be required for sympathetic cooling experiments.

7.1 Introduction

The QUEST was introduced in section 2.5.2 and uses optical fields that are detuned very far from resonance to form a potential given by $U = -\frac{1}{2}\alpha_{stat}|\epsilon|^2$. The simplest QUEST can be formed at the focus of a single focused Gaussian laser beam [94] where the optical potential is given by

$$U(r,z) = -\frac{\alpha P}{\pi\epsilon_0 c w^2(z)} \exp\left(-\frac{2r^2}{w^2(z)}\right), \tag{7.1}$$

where r is the radial coordinate and P is the power of the laser beam. The $1/\mathrm{e}^2$ beam radius $w(z)$ varies with z as $w(z) = w_0\sqrt{1-(\frac{z}{z_R})^2}$, where $z_R = \frac{\pi {w_0}^2}{\lambda}$ is the Rayleigh range. Figure 7.1 shows a sketch of a single beam QUEST illustrating the intensity gradients in the radial and axial directions which give rise to 3D confinement. In order to produce sufficient trap depths in a single beam QUEST, high power lasers are required. CO_2 lasers are often used as they offer sufficient laser powers at a wavelength of 10.6 μm, far from any atomic resonances. The atomic spontaneous photon scattering rates from CO_2 laser fields are very low, typically on the order of 10^{-3} s^{-1}, and therefore scattering induced heating of the trapped sample is negligible. CO_2 lasers have been used in a number of cold alkali atom trapping experiments [135, 136] and in the all optical production of a Bose-Einstein condensate [137] and a Fermi degenerate gas [138]. In this chapter we will discuss the set up of a QUEST for Ar* atoms produced using a 100 W CO_2 laser.

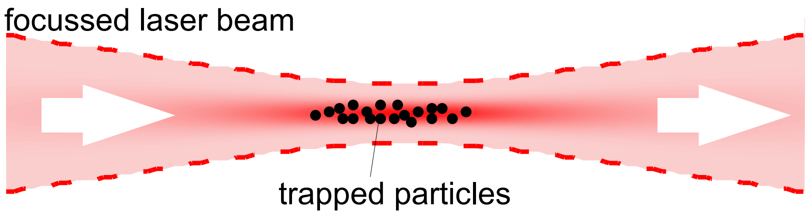

Figure 7.1: Sketch of an optical dipole trap formed at the focus of a Gaussian laser beam. The red shading represents the local intensity in the beam and illustrates the gradients which provide 3D confinement.

7.2 The CO_2 laser

The CO_2 laser used in this experiment was previously used in Rb trapping experiments at Durham University [139, 140]. The laser was a Coherent DEOS GEM Select 100 which was specified to give a 100 W, TEM_{00} output at 10.6 μm with a $1/e^2$ beam diameter of 3.8 mm. In our CO_2 laser the discharge was driven by a 2 kW, water-cooled RF power supply. Although the laser was specified to give an output power of 100 W we measured an output of approximately 120 W after removing some internal mirrors from the laser and moving the position of the laser output window. Due to the far infrared wavelength few materials transmit CO_2 laser light and ZnSe optics are used for all windows and lenses.

Alignment of the laser output beam was not straightforward due to the associated dangers of working with high intensity lasers and the fact that there were no convenient methods for detecting the beam position because of its far infrared wavelength. At full power the only way to determine the beam position is by burning objects or using an expensive thermal imaging camera. At low power the beam can be aligned much more safely using a UV torch and thermal imaging plate or using burn paper. In order to reduce the operating power of the laser during alignment, we operated the laser in a pulsed mode by running the RF power supplied to the discharge on a duty cycle. Applying a 0.1 ms TTL signal at 10 Hz to the relevant control pin in the RF power supply enabled reduction of the average output power to 0.1% of the CW output. The average beam power could be controlled by varying the width of the TTL signal. Figure 7.2 shows the average laser output power at a different duty cycles measured using a water-cooled power meter (Coherent, part no.: 0217-722-00). Although this method was very useful for rough beam path alignment the beam quality was poor in pulsed mode making alignment of lenses

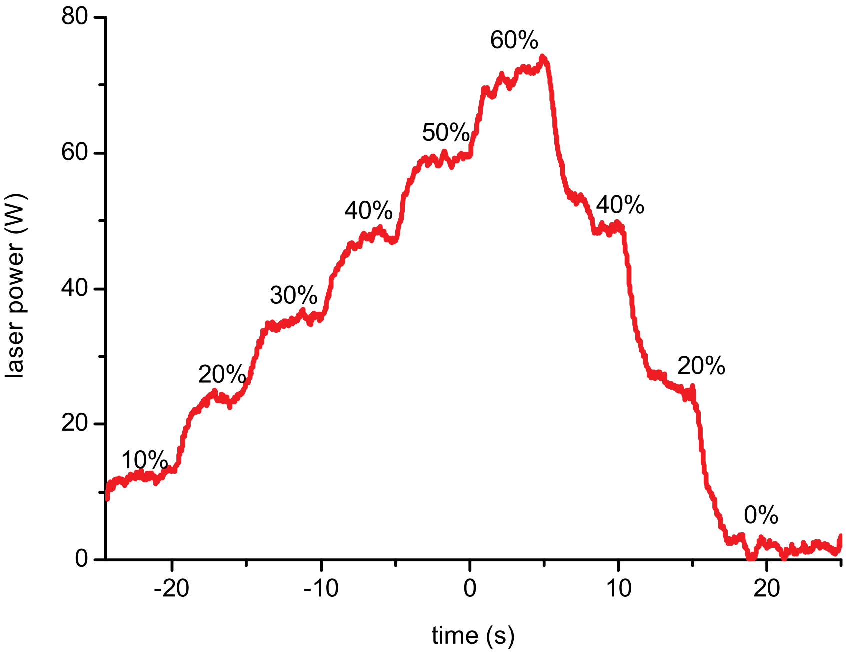

Figure 7.2: CO_2 laser output power at different RF power duty cycles. A TTL signal was applied to the RF power supply at a frequency of 10 Hz and the percentages shown on the graph indicate the width of the TTL signal as a fraction of the 100 ms period.

and telescopes impractical. This problem arose because when the laser was first switched on it took over a second for the cavity to thermally stabilise and during the stabilisation period a number of TEM modes were present in the output beam. In pulsed mode the cavity does not thermally stabilise to the correct length and the output beam contains higher-order TEM modes. In order to produce a low power TEM_{00} beam, we operated the laser at full power in continuous mode and inserted a rotating Brewster angle CO_2 laser beam attenuator in the beam path at the output of the laser. Manual rotation of the attenuator was then used to control the beam power during alignment. When strongly attenuating the beam the attenuator got very hot and we cooled it using an electrical fan. Once the laser was operating at low power we used a UV torch and thermal imaging plate and burn paper for alignment.

7.3 QUEST alignment

The optical set-up for the QUEST, shown in figure 7.3, was relatively simple and required only a few optical elements. The CO_2 laser was mounted on a small optical table such that output window was the same height as the MOT and no adjustment of the beam height was required. The output beam from the laser was expanded to a diameter of 19 mm by two lenses before being focused in to the science chamber with a 345 mm focal length lens. The beam path between the two telescope lenses was enclosed in a stainless steel tube as protection from the high intensity focus. All lenses and windows were made from ZnSe and AR coated on both surfaces.

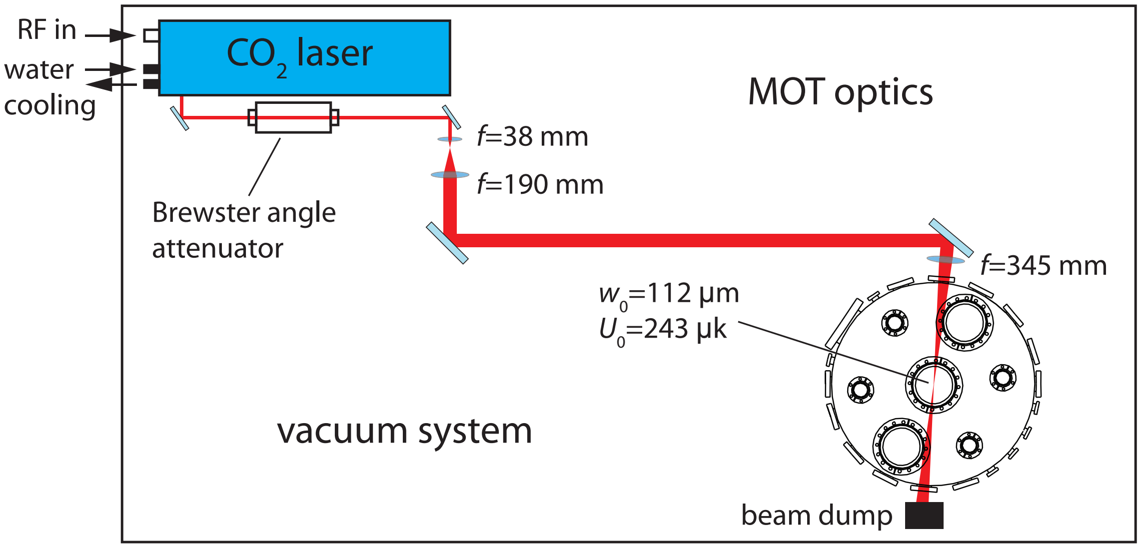

Figure 7.3: Schematic of the QUEST optical set-up showing how the CO_2 laser and associated optics were incorporated with the rest of the experiment.

In order to the characterise the focus of our trapping beam, the waist was measured using the knife edge technique. This method involves moving a razor blade mounted on a translation stage through the beam in well-defined increments and monitoring the transmission of the beam on a power meter. Assuming the beam is Gaussian the power measured should follow

$$P = P_0 \left[1 - \operatorname{erf}\left(\frac{\sqrt{2}}{w}(z - z_0) \right) \right] \tag{7.2}$$

where P_0 is the power of the beam, w is the beam waist, z is the position of the razor blade, z_0 is the offset from $z = 0$ and erf is the error function. We replicated the beam path shown in figure 7.3 when making the knife edge measurement by aligning the beam through the 345 mm lens and then a ZnSe window identical to the one on the science chamber. Figure 7.4 shows data from a knife edge measurement at the beam focus and the corresponding fit obtained using equation 7.2 which gave a beam waist of 112 ± 3 μm. The focus of the beam was found by measuring the waist at different axial positions and finding the minimum. Importantly, the position of the focus was found to be at a distance of 358 mm from the lens, probably due to imperfect collimation of the beam before hitting the lens. The laser power was measured on the other side of the vacuum chamber to be 62.5 W giving a trap depth for Ar* of 215 μK. This estimate does not take into account attenuation of the laser through the final window, after the trapping region, which contained rubidium deposits on its surface from a previous experiment [139] and it is likely that the trap was deeper.

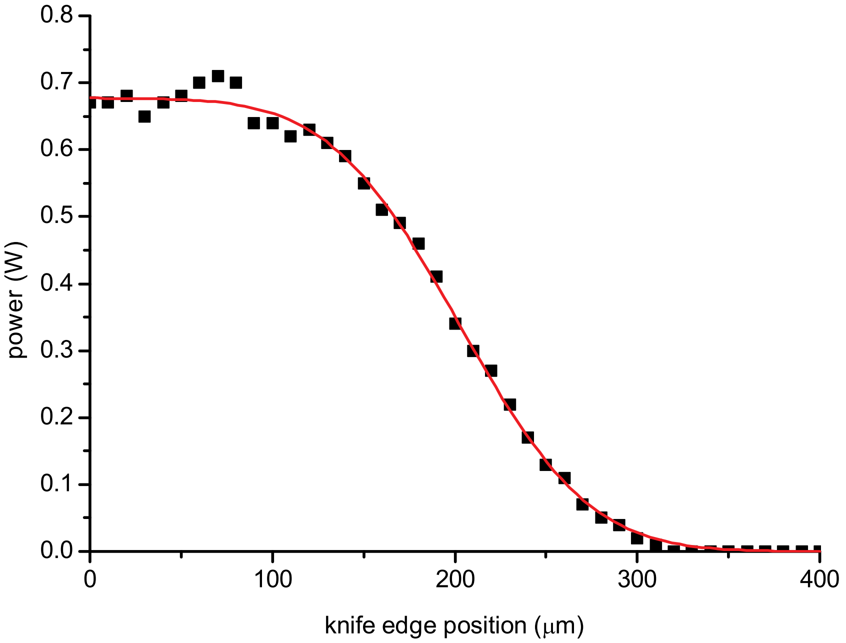

Figure 7.4: Knife edge measurement at focus of the CO_2 laser beam. The red line is a fit to the data obtained using equation 7.2 which gave a beam waist of 112 ± 3 μm.

In order to successfully load atoms from the MOT to the QUEST, there must be a good spatial overlap between the MOT and the focus of the CO_2 laser beam. The focused beam had no observable effect on the MOT behaviour under normal operation and in our experiment there was no simple diagnostic to determine whether or not the two were overlapped. In other QUEST experiments alignment was carried out by Stark shifting atoms in a diffuse MOT out of resonance with the MOT beams and looking for a dark stripe in the fluorescence signal from the atomic cloud [139]. This method is not suitable when working with Ar* as the polarisabilities of the ground and excited state of the cooling transition are very similar and the optical Stark shift induced by our CO_2 trapping beam was less than 1 MHz. Resonant probe beams, used successfully in alignment of the optical lattice with the MOT in the Ar* acceleration experiments, could not be used either. The different refractive indices of ZnSe for 10.6 μm and 811.5 nm resulted in large deflection of the resonant probe with respect to the trapping beam when passing through any ZnSe optics and made overlapping the two very difficult.

Our approach to trap alignment was to set up an experimental sequence to transfer atoms to the QUEST and translate the focus of the trapping beam until a trap signal was observed. In the first stage of the experimental sequence the MOT was loaded for 2.5 seconds before the Zeeman slower laser beam and atomic beam shutters were closed. This lowered the pressure in the science chamber from 1.3×10^{-8} mbar to 6.4×10^{-9} mbar and reduced the background light during imaging. The MOT atoms were then loaded into a 3D molasses for 5 ms before switching off the MOT cooling beams and allowing the atoms to expand freely or become trapped in the QUEST. An image of the atomic cloud was acquired after 10 ms expansion by switching the cooling beams back on and triggering the EMCCD camera. Images were acquired with a 3 ms exposure time. The CO_2 laser beam was on continuously throughout this sequence.

With the experimental sequence running the trap focusing lens was translated in the horizontal and vertical directions through a grid of points as we looked for a trapping signal. The first alignment attempt was carried out before we had performed the knife edge measurement and no signal was observed. After we had measured the position of the focal spot the trap focusing lens was carefully positioned 358 mm from the centre of the science chamber and we searched for a signal again, this time with success. Figure 7.5 shows a typical trapping signal which has been maximised by further translation of the lens in the horizontal and vertical directions. In the image shown approximately 43 % of the MOT atoms were transferred to the QUEST.

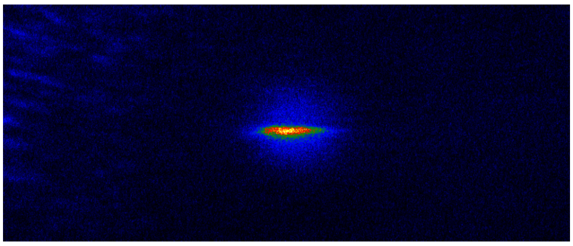

Figure 7.5: Fluorescence image of Ar* atoms trapped in QUEST 10 ms after loading from the MOT. This image was the accumulation of 20 individual images with an exposure time of 3 ms.

7.4 Penning ionisation and trap loss

Trap loss in cold atomic traps can result from one-body, two-body and many-body collisional processes. In our work the densities were not high enough for many body losses to become significant and they will be ignored from this discussion [82]. One-body losses arise from collisions between atoms in the background gas and those in the trap and are independent of the trap density. Two-body collisional losses are the result of intra-trap collisions and are density-dependent. The two-body loss channel dominates in metastable rare gas experiments as the large internal energy of the atoms makes them inherently fragile [82]. If we consider an Ar* atom in the $4s[3/2]_2$ metastable state its internal energy is 11.5 eV which is more than half the ionisation potential (15.8 eV). An inelastic collision with another Ar* atom can lead to one of two ionisation processes, either Penning ionisation (PI) or associative ionisation (AI)

$$\mathrm{Ar}^* + \mathrm{Ar}^* \rightarrow \begin{cases} \mathrm{Ar} + \mathrm{Ar}^+ + \mathrm{e}^- \\ \mathrm{Ar}_2^+ + \mathrm{e}^-. \end{cases} \tag{7.3}$$

The first process is PI and the products of the collision are one ground state argon atom, one argon ion and a free electron which carries away the excess energy from the reaction. AI produces one diatomic molecular argon ion and a free electron. Both processes result in two Ar* atoms being lost from the trap per collision. These collisional trap loss processes can be investigated by analysing the decay of the number of atoms in the trap $N(t)$ which will follow the trap loss equation given by,

$$\frac{dN(t)}{dt} = -\alpha N(t) - \beta \int_V n^2(\boldsymbol{r}, t)\mathrm{d}^3 r \tag{7.4}$$

where α is the one-body loss coefficient, β is the two-body loss coefficient and $n(\boldsymbol{r}, t)$ is the local atomic density at $(\boldsymbol{r}, t)$. Two-body trap loss has already been investigated for cold Ar* in a MOT by Busch *et al.* [141] who determined a loss rate of $\beta = 5.8 \times 10^{-10}$ $\mathrm{cm}^3\mathrm{s}^{-1}$. They also looked at the relative contributions to the loss rate from PI and AI, by analysing ions ejected from the MOT in a quadrupole mass spectrometer, and found PI to be the dominant process producing approximately 10^2 times as many ions as AI. The measurements in this work were carried out while the atomic cloud was being illuminated by the MOT light which can lead to light-assisted collisions and different ionisation processes than PI and AI. Photoassociative collisions become important when two colliding atoms are excited to a quasimolecular state from which alternative loss channels, such as autoionisation, exist. Our Ar* QUEST presents an opportunity to make the first measurement of the two-body loss rate β in a dark Ar* sample where PI and AI are the only collisional loss mechanisms.

7.4.1 Trap lifetime measurement

In order to investigate the trap decay in our Ar* QUEST, we analysed fluorescence images of the trapped atoms at varying delays after loading the trap. Figure 7.6(a) shows fluorescence images of the evolving QUEST and figure 7.6(b) is the corresponding trap decay curve which was produced by analysing the fluorescence in the QUEST region. The images show the atoms spreading out into the QUEST in the axial direction and also the untrapped atoms expanding away from the trapping region. The trap lifetime was determined by fitting a double exponential to the decay curve, one curve to account for the untrapped background atoms expanding away from the trapping region and the other for the decay of atoms in the QUEST. The two curves had time constants of 2.8 ± 0.2 ms and 18.3 ± 0.3 ms respectively. We started to investigate the trap decay with a view to measuring the two-body trap loss coefficient but soon realised that the trap lifetime was too short to be due to intra-trap collisions alone. The dominant process removing atoms from the trap was most likely parametric excitation induced by vibration of the CO_2 laser beam. The mechanical resonances in our set-up discussed in section 3.3 caused vibration of the mirrors used to align the CO_2 laser beam into the science chamber which resulted in the trap being shaken. Parametric excitation has been studied in optical dipole traps where the intensity of the trapping laser beam was modulated rather than the spatial position of the trapping beam(s) [142, 143]. Primary heating resonances have been observed when the modulation frequency of the trapping laser beam was f and $2f$, where f is the oscillation frequency of the atoms in the trap, while higher-order resonances have also been observed. At these frequencies the kinetic energy of the atoms increases exponentially and they are heated out of the trap [142]. Intensity fluctuations of the trapping laser can lead to parametric excitation; however, this is not generally a problem when using CO_2 lasers as the output power tends to be very stable [136].

The trap frequencies in our QUEST can be estimated by assuming that the trapping potential is a simple cylindrically symmetric harmonic oscillator. This approximation holds if the temperature of the trapped atoms is small compared with the depth of the trapping potential ($T \ll U_0/k_\mathrm{B}$). The potential produced by a cylindrically symmetric, harmonic oscillator is given by

$$U(r,z) \approx -U_0 \left(1 - 2\frac{r^2}{w_0^2} - \frac{z^2}{z_R^2}\right) \tag{7.5}$$

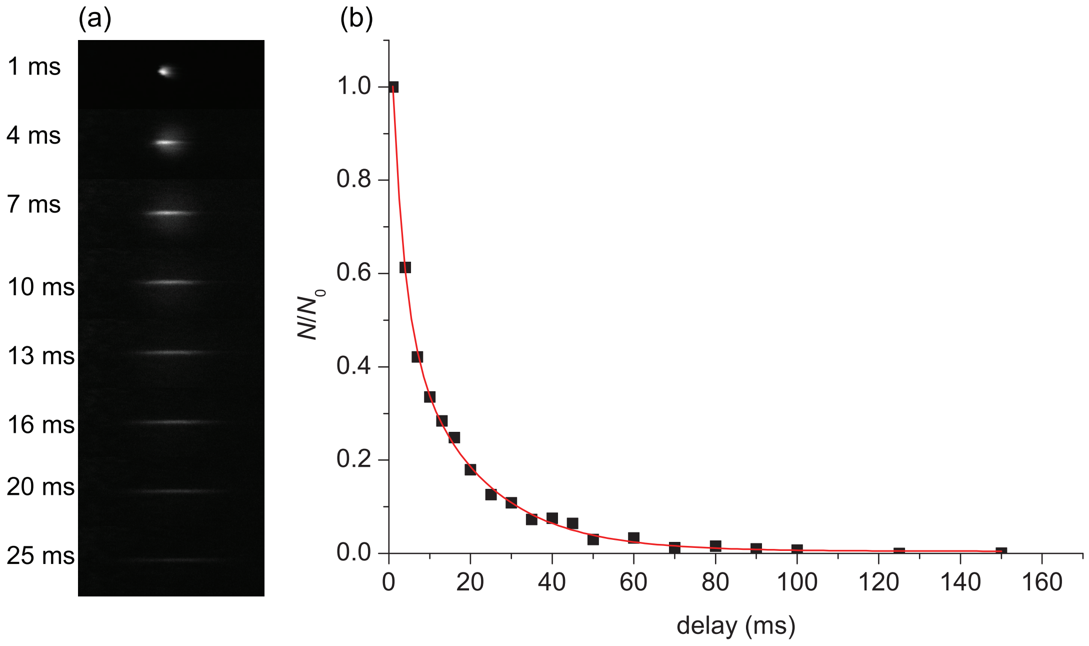

Figure 7.6: Study of decay of atoms in the Ar* QUEST. (a) Images of the QUEST at different delays after switching off the MOT. The images are the accumulation of 20 individual images acquired with an exposure time of 3 ms. (b) Trap decay curve obtained by analysing the images of the QUEST. The red curve is a fit obtained using a double exponential function. The time constants of the two decay curves are 2.8 ± 0.2 ms and 18.3 ± 0.3 ms. The fast decay is due to the untrapped atoms which expand away from the region of interest while the longer curve is the decay of the QUEST.

and the radial and axial trap frequencies are

$$\omega_{rad} = \sqrt{\frac{4U_0}{mw_0^2}}, \qquad \omega_{ax} = \sqrt{\frac{2U_0}{mz_R^2}}. \tag{7.6}$$

Our trapping beam was focused to a waist of $w_0 = 112$ μm, had a measured power of 62.5 W and a Rayleigh range of $z_R = 3.7$ mm. The oscillation frequencies can be estimated to be $\omega_{rad} = 2\pi \times 588$ Hz and $\omega_{ax} = 2\pi \times 13$ Hz. Parametric heating is most effective at the $2f$ resonance frequency which is approximately 1.2 kHz in the radial direction. In section 3.3 the frequencies of the mechanical resonances driven by the turbomolecular pumps were measured and one of the two main vibration frequencies was found at 1.4 kHz, close to twice the radial trap frequency. In our estimation of the trap frequencies the power used for the trapping beam was measured after the beam had passed through the final window on the science chamber. It is likely that the power in the trapping region was higher and that the trap frequencies were higher which would make the 1.4 kHz vibration closer to the $2f$ parametric resonance. This, coupled with the fact that the parametric resonances can be intrinsically quite broad, make parametric excitation the most probable dominant trap loss mechanism.

7.5 Future experiments

Experiments with the Ar* QUEST described in this chapter are ongoing. At the moment work is being carried out to vibrationally isolate the turbomolecular pumps from the rest of the experiment by installing vibrational damping flanges between the pumps and the vacuum chambers. This should reduce parametric excitation as a loss mechanism leaving two-body collisions as the dominant loss channel. If this is successful the Ar* QUEST offers a good opportunity to measure the two-body loss coefficient β in a dark Ar* sample for the first time.

In other cold metastable rare gas experiments much work has gone into suppressing the two-body loss rate through spin polarisation of the atomic sample. This technique is crucial in BEC experiments where a 'good' ratio of elastic to inelastic collisions is key to successful evaporative cooling [144, 145]. Penning ionisation should conserve the total spin of the system and by polarising the atomic sample such that this is not possible loss rates can be reduced. Below is a Penning reaction between two unpolarised Ar* atoms,

$$\begin{array}{rccccccccc} & \mathrm{Ar}^* & + & \mathrm{Ar}^* & \rightarrow & \mathrm{Ar} & + & \mathrm{Ar}^+ & + & \mathrm{e}^- \\ \text{Spin}: & s_a = 1 & & s_b = 1 & | & s_a = 0 & & s_b = \frac{1}{2} & & s_c = \frac{1}{2} \\ \text{Total spin}: & & S_R = 0,1,2 & & | & & & S_P = 0,1 & & \end{array}$$

where the second row shows the individual particle spins and the third row is the possible total spins. We can see that the total spin can only be conserved when the total spin of the reactants is $S_R = 0$ or 1. Assuming that spin conservation in collisions holds, polarising the atomic sample such that $S_R = 2$ will greatly suppress the ionisation rate as the reaction can only proceed via the weak spin-spin dipole interaction which involves a spin-flip of one of the electrons. This picture is not complete however and for species heavier than helium the presence of orbital angular momentum complicates the interaction. Table 7.1 shows the measured polarised and unpolarised loss rates for different rare gas species [82]. Loss rate suppression of up to 10^4 has been observed in ^{4}He* and approximately 10^2 for ^{20}Ne and ^{22}Ne in polarised samples while the rates remain unchanged for Kr and Xe. In references [146] and [147] the absence of any ionisation suppression in the heavier species is interpreted as a consequence of spin-flips induced by anisotropic interactions between

Atomic species	^{3}He*	^{4}He*	^{20}Ne*	^{22}Ne*	^{40}Ar*	^{84}Kr*	^{132}Xe*
$\beta_{polarised}$ (10^{-14} cm^{3}s^{-1})	-	2	650	12000	-	40000	6000
Reference	-	[148]	[149]	[149]	-	[150]	[146]
$\beta_{unpolarised}$ (10^{-11} cm^{3}s^{-1})	38	20	50	100	58	40	6
Reference	[151]	[151]	[152]	[153]	[141]	[150]	[146]

Table 7.1: Measured polarised and unpolarised loss rates for metastable rare gas atoms. All measurements were carried out on dark samples apart from the Ar* measurement.

colliding atoms.

No measurements have yet been reported on a spin polarised Ar* sample and the set-up described in this chapter offers a good opportunity to investigate such collisions. The only addition to the experimental sequence required is a spin polarisation stage which involves applying a uniform magnetic field to the atomic cloud and optically pumping all atoms to the $m_J = 2$ metastable substate. The outcome of such a study could be important in furthering our understanding of these reactions as loss suppression has been observed for the lighter rare-gas species but not for the heavier elements.

Chapter 8

Conclusions

This thesis describes the construction and characterisation of a unique cold argon atom source for sympathetic cooling of molecules. It also describes the use of this source to demonstrate chirped optical Stark acceleration for the first time. This chapter will summarise the apparatus constructed to produce ultracold argon atoms and discuss the principal results from the experiments carried out. Future research directions for the project are also outlined.

8.1 Source of ultracold argon atoms

8.1.1 Summary of experiment

A large portion of the work presented in this thesis was based on the construction of a source of ultracold ground state argon atoms. The preparation of the argon atoms was a two stage process. The atoms were first laser cooled and trapped in a MOT while in a high-lying metastable state before being optically quenched back to their absolute ground state. The atoms could not be cooled from their ground state as the nearest transitions are in the vacuum ultra violet. We cooled argon from its lowest lying metastable state using the $4s[3/2]_2 \rightarrow 4p[5/2]_3$ transition at 811.53 nm. Cooling of the Ar* atoms was carried out using an external-cavity diode laser which was stabilised to the cooling transition using a magnetic dichroism technique. This was the first application of this technique to a plasma operated at our pressures where the applied magnetic field affected the behaviour of the gas [154]. The MOT confined Ar* atoms at a density on the order of 10^9 cm^{-3} and a temperature of 70 μK. This is one of very few Ar* MOTs which have been produced. These systems have been used to study ultracold collisions [141], to perform Ar* lifetime measurements [9] and in atom optics experiments [114]. The Ar* MOT that we have produced is the first rare-gas MOT which has been produced with the aim of trapping and studying the atoms in their ground state. The MOT apparatus constructed could also be used to cool and trap Kr* as its laser cooling wavelength is at 811.3 nm.

8.1.2 Improvements to the system

The Ar* MOT constructed was well suited for the experiments presented in this thesis. Work is now ongoing to make improvements for future experiments. One potential problem could be that the pressure in the science chamber is not low enough for sympathetic cooling experiments. A very low pressure will be required for these experiments so that the co-trapped atoms and molecules can thermalise before the trapped sample is depleted by collisions with atoms in the background gas. A potential solution to this could be to reduce the gas load on the science chamber. This could be achieved by moving the science chamber off-axis from the atomic beam and guiding the Ar* atoms in the beam through the science chamber skimmer. This would reduce the number of atoms entering the chamber by approximately 10^4. Directing the Ar* atoms into the science chamber could be achieved using either a 2D MOT [116] or a magnetic guide [117]. The gas load could also be reduced using a double MOT system [118] where the first MOT acts as an atomic source for the second which would be located in the science chamber.

Another improvement to the system, which is currently being implemented, involves vibrational isolation of the turbomolecular pumps (TMPs) from the rest of the experiment. The TMPs drive mechanical resonances on the optical table which had a deleterious effect on the short term frequency stability of the ECDL when locked. We measured a square root Allan variance of 3.2 MHz at an averaging time of $\tau = 3 \times 10^{-4}$ s. By installing vibrational damping flanges between the TMPs and the vacuum system we should be able to reduce the effects of the mechanical resonances on the experiment and improve the short term stability of the laser lock.

Since the experiments in this thesis were completed the MOT cloud density diagnostic has been improved. The density measurement presented in this thesis used a fluorescence imaging technique. This method relies on calibrating the camera to determine the number of photons captured by the camera for a given MOT image. The precision of the measurement is limited by how well the calibration can be carried out. A more precise method involves measuring the absorption of a weak probe beam passing through the atomic cloud. The Beer-Lambert law can then be used to determine the number of atoms in the MOT from the absorption signal. This absorption method has now been implemented in our experiment and will be important for future experiments, such as collisional studies where knowledge of the density of the trapped sample is crucial in making precise measurements.

8.1.3 Conclusions

The metastable argon MOT described in this thesis will form an integral part of future molecular sympathetic cooling experiments. The trapped atomic cloud was measured to have a density of 3.93×10^9 cm^{-3} and a temperature of 73.2 ± 0.4 μK. The simulations of sympathetic cooling for Ar-H_2 and Ar-C_6H_6 carried out by Barletta *et al.* [90] assumed an initial argon temperature of 100 μK and a density of 10^{14} cm^{-3}. The temperature of the MOT atoms therefore should be suitable for cooling to ultracold temperatures, even when the heating due to the quenching process is taken into account. The density however, is considerably less than that assumed in the simulation. The Ar* MOT density is limited by trap loss due to ionising intra-trap collisions. Sympathetic cooling experiments will use ground state argon atoms trapped in a conservative optical potential where this loss channel will not exist. We should therefore be able to achieve much higher densities in the optical potential by continually quenching Ar* MOT atoms into the trap. A similar loading scheme has been used to achieve rubidium densities on the order of 10^{13} cm^{-3} in an optical lattice [155]. Quenching of the ultracold Ar* atoms to their ground state has also been demonstrated using a laser at 801.48 nm. This represents the completion of one of the key experimental elements, the ultracold argon source, for molecular sympathetic cooling experiments.

8.2 Optical Stark acceleration of Ar*

8.2.1 Summary of results

In this thesis we presented the first chirped optical Stark acceleration experiments. Metastable argon atoms, initially confined in the MOT, were accelerated to velocities of up to 191 ± 1 ms^{-1} while maintaining narrow energy spreads (30-100 mK). Fluorescence images of the atoms, acquired after acceleration, showed a discrete packet of accelerated atoms moving away from their initial position in the MOT. Precise measurements of the atomic packet velocity were made by carrying out time-of-flight measurements and fitting the distributions obtained using a Monte Carlo numerical simulation of acceleration. One advantage of the optical Stark accelerator is that the number of atoms in the accelerated beam can be controlled. We demonstrated this capability by tailoring the depth of the optical potential to vary the fraction of atoms from the MOT accelerated. Using Ar* we have demonstrated that optical Stark acceleration can be applied to a species close to the ionisation potential (4.2 eV) which would not have been possible using the constant-velocity lattice optical Stark acceleration scheme. Also, a major advantage of the optical linear accelerator is that the acceleration potential is dependent on the polarisability of the target species and thus also dependent on its electronic state. In its metastable state argon has a polarisability 27 times larger than in the ground state. State-dependent polarisability therefore presents the option to select the initial quantum state of the acceleration species and to boost the acceleration force. This is even true for molecules with excited-state lifetimes (τ) on the timescale of hundreds of nanoseconds, as long as τ is greater than the acceleration period.

8.2.2 Improvements for future experiments

From the results of the acceleration experiments it was observed that the final velocity of the atomic packet was not equal to that of the lattice. This would be undesirable in future experiments where precise tuning of the velocity is required. Simulations of the atomic dynamics over the acceleration duration showed that the chirp used in our experiments caused this velocity mismatch. In the experiments the chirp ended 20 ns before the lattice was switched off. For the final 20 ns of the lattice it had a constant velocity and deeper potential wells. Oscillation of the accelerated atoms in these deeper wells meant that the velocity of the packet was not equal to the velocity of the lattice when the chirp was switched off. An ideal chirp for future acceleration or deceleration experiments was proposed. This chirp would be applied when the lattice is turned on and end when the lattice is switched off. Acceleration with this chirp was simulated and the velocity of the accelerated atoms matched that of the lattice until the lattice was switched off. This should allow more precise tuning of the accelerated atoms in future experiments.

8.2.3 Conclusions

The Ar* optical Stark acceleration experiments presented in this thesis have shown that this technique is capable of producing a particle beam with a tunable velocity and a narrow velocity spread. These experiments represent a significant improvement over previous optical Stark acceleration experiments with a constant-velocity lattice as velocity control is achieved by simply varying the frequency chirp and precise switching of the optical fields is less critical. These experiments have also demonstrated the feasibility of using this technique for molecular deceleration which will be crucial in future sympathetic cooling experiments. Optical Stark deceleration could become an important technique in cold molecule research as it can be applied to any molecule regardless of whether it has a permanent electric or magnetic dipole moment. Important applications include reactive scattering experiments [119] and atomic nanofabrication [120]. It has also been proposed that the technique could be used to study cold ion-molecule interactions by crossing a Coulomb crystal with controlled neutral particle beams, or in low energy surface chemistry studies [132].

8.3 Ar* QUEST

The final experiment presented in this thesis involved trapping of the ultracold Ar* atoms in a quasi-electrostatic trap (QUEST) formed at the focus of a 100 W laser beam with a wavelength of 10.6 μm. Parametric excitation, caused by vibration of the trapping beam, is believed to have resulted in trap loss and prevented the study of collisions between the trapped Ar* atoms. The work currently being carried out on our experiment to vibrationally isolate the TMPs from the rest of the apparatus should allow further experiments with the Ar* QUEST to be carried out. If successful, this should reduce parametric excitation as a trap loss mechanism. The QUEST would then present a good opportunity to measure the two-body loss rate, β. Two-body trap loss has been investigated for ultracold Ar* in a MOT by Busch *et al.* [141] who determined a loss rate of $\beta = 5.8 \times 10^{-10}$ cm^{3}s^{-1}. However, the measurements in their work were carried out while the atoms were being illuminated by the MOT lasers which can lead to light-assisted collisions. Measurements of β for the other rare gas species have been carried out using dark atomic samples and our QUEST could be used to measure β for Ar* for the first time in the dark. In other cold metastable rare gas experiments much work has gone into suppressing the two-body loss rate through spin polarisation of the atomic sample. This has been investigated for helium, neon, krypton and xenon but not yet for argon. Our QUEST should also allow the investigation of trap loss in a spin polarised sample of ^{40}Ar*. The outcome of such a study could be important in furthering our understanding of these reactions as loss suppression has been observed for the lighter rare gas species but not for the heavier elements.

8.4 Concluding Remarks

The work presented in this thesis will form the foundation of future molecular sympathetic cooling experiments. The apparatus constructed will provide the source of ultracold ground state argon atoms and the Ar* optical Stark acceleration experiments have demonstrated the feasibility of using this technique for molecular deceleration. Work on this project is ongoing and an experiment is currently under development to decelerate H_2 molecules to rest from a molecular beam. The completion of this experiment will represent another milestone in the project as optical Stark deceleration is essential to our sympathetic cooling scheme. Another experiment is being prepared to trap ultracold, ground state argon atoms in a QUEST formed at the centre of a high-finesse optical cavity. It will be interesting to discover the densities that can be accumulated in the trap and whether any evaporative cooling takes places. Once these experiments have been completed focus will switch to combining them to load both atoms and molecules into the QUEST which will facilitate sympathetic cooling of the molecules. If successful this method should allow the cooling of a wide range of complex molecules to ultracold temperatures. This will open up the opportunity to perform a wide range of experiments studying how these molecules interact in a temperature regime where quantum mechanical effects become important.

Bibliography

[1] T. Hänsch, A. Schawlow, *Optics Communications* **13**, 68 (1975).

[2] E. L. Raab, M. Prentiss, A. Cable, S. Chu, D. E. Pritchard, *Phys. Rev. Lett.* **59**, 2631 (1987).

[3] K. B. Davis, M.-O. Mewes, M. A. Joffe, M. R. Andrews, W. Ketterle, *Phys. Rev. Lett.* **74**, 5202 (1995).

[4] M. Lewenstein, *et al.*, *Advances in Physics* **56**, 243 (2007).

[5] I. Bloch, J. Dalibard, W. Zwerger, *Rev. Mod. Phys.* **80**, 885 (2008).

[6] J. Ye, H. J. Kimble, H. Katori, *Science* **320**, 1734 (2008).

[7] J. Weiner, V. S. Bagnato, S. Zilio, P. S. Julienne, *Rev. Mod. Phys.* **71**, 1 (1999).

[8] T. D. Ladd, *et al.*, *Nature* **464**, 45 (2010).

[9] H. Katori, F. Shimizu, *Phys. Rev. Lett.* **70**, 3545 (1993).

[10] A. L. de Oliveira, M. W. Mancini, V. S. Bagnato, L. G. Marcassa, *Phys. Rev. A* **65**, 031401 (2002).

[11] M. Zinner, P. Spoden, T. Kraemer, G. Birkl, W. Ertmer, *Phys. Rev. A* **67**, 010501 (2003).

[12] G. Wilpers, *et al.*, *Phys. Rev. Lett.* **89**, 230801 (2002).

[13] M. H. Anderson, J. R. Ensher, M. R. Matthews, C. E. Wieman, E. A. Cornell, *Science* **269**, 198 (1995).

[14] B. DeMarco, D. S. Jin, *Science* **285**, 1703 (1999).

[15] M. R. Andrews, *et al.*, *Science* **275**, 637 (1997).

[16] I. Bloch, *Nat Phys* **1**, 23 (2005).

[17] M. Greiner, O. Mandel, T. Esslinger, T. W. Hansch, I. Bloch, *Nature* **415**, 39 (2002).

[18] B. Paredes, *et al.*, *Nature* **429**, 277 (2004).

[19] H. Katori, *Nat Photon* **5**, 203 (2011).

[20] M. Anderlini, *et al.*, *Nature* **448**, 452 (2007).

[21] L. D. Carr, D. DeMille, R. V. Krems, J. Ye, *New Journal of Physics* **11**, 055049 (2009).

[22] J. J. Gilijamse, S. Hoekstra, S. Y. T. van de Meerakker, G. C. Groenenboom, G. Meijer, *Science* **313**, 1617 (2006).

[23] B. C. Sawyer, B. K. Stuhl, D. Wang, M. Yeo, J. Ye, *Phys. Rev. Lett.* **101**, 203203 (2008).

[24] R. V. Krems, *Phys. Chem. Chem. Phys.* **10**, 4079 (2008).

[25] J. M. Hutson, *Science* **327**, 788 (2010).

[26] L. P. Parazzoli, N. J. Fitch, P. S. Żuchowski, J. M. Hutson, H. J. Lewandowski, *Phys. Rev. Lett.* **106**, 193201 (2011).

[27] S. Ospelkaus, *et al.*, *Science* **327**, 853 (2010).

[28] J. Eschner, G. Morigi, F. Schmidt-Kaler, R. Blatt, *J. Opt. Soc. Am. B* **20**, 1003 (2003).

[29] J. van Veldhoven, *et al.*, *Eur. Phys. J. D* **31**, 337 (2004).

[30] S. Y. T. van de Meerakker, N. Vanhaecke, M. P. J. van der Loo, G. C. Groenenboom, G. Meijer, *Phys. Rev. Lett.* **95**, 013003 (2005).

[31] J. J. Gilijamse, *et al.*, *The Journal of Chemical Physics* **127**, 221102 (2007).

[32] M. R. Tarbutt, J. J. Hudson, B. E. Sauer, E. A. Hinds, *Faraday Discuss.* **142**, 37 (2009).

[33] B. C. Regan, E. D. Commins, C. J. Schmidt, D. DeMille, *Phys. Rev. Lett.* **88**, 071805 (2002).

[34] M. Ziskind, C. Daussy, T. Marrel, C. Chardonnet, *The European Physical Journal D - Atomic, Molecular, Optical and Plasma Physics* **20**, 219 (2002).

[35] K. Góral, L. Santos, M. Lewenstein, *Phys. Rev. Lett.* **88**, 170406 (2002).

[36] D. DeMille, *Phys. Rev. Lett.* **88**, 067901 (2002).

[37] K. M. Jones, E. Tiesinga, P. D. Lett, P. S. Julienne, *Rev. Mod. Phys.* **78**, 483 (2006).

[38] T. Köhler, K. Góral, P. S. Julienne, *Rev. Mod. Phys.* **78**, 1311 (2006).

[39] P. D. Lett, *et al.*, *Phys. Rev. Lett.* **71**, 2200 (1993).

[40] A. N. Nikolov, *et al.*, *Phys. Rev. Lett.* **84**, 246 (2000).

[41] J. M. Sage, S. Sainis, T. Bergeman, D. DeMille, *Phys. Rev. Lett.* **94**, 203001 (2005).

[42] M. Viteau, *et al.*, *Science* **321**, 232 (2008).

[43] J. G. Danzl, *et al.*, *Science* **321**, 1062 (2008).

[44] K.-K. Ni, *et al.*, *Science* **322**, 231 (2008).

[45] J. Deiglmayr, *et al.*, *Phys. Rev. Lett.* **101**, 133004 (2008).

[46] S. Jochim, *et al.*, *Science* **302**, 2101 (2003).

[47] J. M. Doyle, B. Friedrich, J. Kim, D. Patterson, *Phys. Rev. A* **52**, R2515 (1995).

[48] J. D. Weinstein, R. deCarvalho, T. Guillet, B. Friedrich, J. M. Doyle, *Nature* **395**, 148 (1998).

[49] W. C. Campbell, E. Tsikata, H.-I. Lu, L. D. van Buuren, J. M. Doyle, *Phys. Rev. Lett.* **98**, 213001 (2007).

[50] S. Y. T. van de Meerakker, H. L. Bethlem, G. Meijer, *Nat Phys* **4**, 595 (2008).

[51] H. L. Bethlem, G. Berden, G. Meijer, *Phys. Rev. Lett.* **83**, 1558 (1999).

[52] H. L. Bethlem, F. M. H. Crompvoets, R. T. Jongma, S. Y. T. van de Meerakker, G. Meijer, *Phys. Rev. A* **65**, 053416 (2002).

[53] S. Y. T. van de Meerakker, P. H. M. Smeets, N. Vanhaecke, R. T. Jongma, G. Meijer, *Phys. Rev. Lett.* **94**, 023004 (2005).

[54] J. R. Bochinski, E. R. Hudson, H. J. Lewandowski, G. Meijer, J. Ye, *Phys. Rev. Lett.* **91**, 243001 (2003).

[55] E. R. Hudson, *et al.*, *Phys. Rev. A* **73**, 063404 (2006).

[56] S. Jung, E. Tiemann, C. Lisdat, *Phys. Rev. A* **74**, 040701 (2006).

[57] H. L. Bethlem, *et al.*, *Nature* **406**, 491 (2000).

[58] N. Vanhaecke, U. Meier, M. Andrist, B. H. Meier, F. Merkt, *Phys. Rev. A* **75**, 031402 (2007).

[59] E. Narevicius, *et al.*, *Phys. Rev. Lett.* **100**, 093003 (2008).

[60] E. Narevicius, *et al.*, *Phys. Rev. A* **77**, 051401 (2008).

[61] R. Fulton, A. I. Bishop, M. N. Shneider, P. F. Barker, *Nat Phys* **2**, 465 (2006).

[62] P. F. Barker, M. N. Shneider, *Phys. Rev. A* **66**, 065402 (2002).

[63] R. Fulton, A. I. Bishop, M. N. Shneider, P. F. Barker, *Journal of Physics B: Atomic, Molecular and Optical Physics* **39**, S1097 (2006).

[64] A. I. Bishop, L. Wang, P. F. Barker, *New Journal of Physics* **12**, 073028 (2010).

[65] N. Coppendale, L. Wang, P. Douglas, P. Barker, *Applied Physics B: Lasers and Optics* **104**, 569 (2011).

[66] C. Maher-McWilliams, P. Douglas, P. F. Barker, *Nat Photon* **6**, 386 (2012).

[67] E. S. Shuman, J. F. Barry, D. DeMille, *Nature* **467**, 820 (2010).

[68] M. D. Di Rosa, *The European Physical Journal D - Atomic, Molecular, Optical and Plasma Physics* **31**, 395 (2004).

[69] W. Lu, Y. Zhao, P. F. Barker, *Phys. Rev. A* **76**, 013417 (2007).

[70] P. Maunz, *et al.*, *Nature* **428**, 50 (2004).

[71] H. W. Chan, A. T. Black, V. Vuletić, *Phys. Rev. Lett.* **90**, 063003 (2003).

[72] C. J. Myatt, E. A. Burt, R. W. Ghrist, E. A. Cornell, C. E. Wieman, *Phys. Rev. Lett.* **78**, 586 (1997).

[73] F. Schreck, *et al.*, *Phys. Rev. A* **64**, 011402 (2001).

[74] G. Modugno, *et al.*, *Science* **294**, 1320 (2001).

[75] P. Soldan, P. S. Zuchowski, J. M. Hutson, *Faraday Discuss.* **142**, 191 (2009).

[76] P. F. Barker, *et al.*, *Faraday Discuss.* **142**, 175 (2009).

[77] M. Lara, J. L. Bohn, D. Potter, P. Soldán, J. M. Hutson, *Phys. Rev. Lett.* **97**, 183201 (2006).

[78] P. S. Żuchowski, J. M. Hutson, *Phys. Rev. A* **78**, 022701 (2008).

[79] A. O. G. Wallis, J. M. Hutson, *Phys. Rev. Lett.* **103**, 183201 (2009).

[80] T. E. Mehlstäubler, *et al.*, *Phys. Rev. A* **77**, 021402 (2008).

[81] S. Tokunaga, *et al.*, *The European Physical Journal D - Atomic, Molecular, Optical and Plasma Physics* **65**, 141 (2011).

[82] W. Vassen, *et al.*, *Rev. Mod. Phys.* **84**, 175 (2012).

[83] P. Barletta, J. Tennyson, P. F. Barker, *Phys. Rev. A* **78**, 052707 (2008).

[84] P. Barletta, J. Tennyson, P. F. Barker, *New Journal of Physics* **11**, 055029 (2009).

[85] J. Dalibard, C. Cohen-Tannoudji, *J. Opt. Soc. Am. B* **6**, 2023 (1989).

[86] R. D. Knight, L. G. Wang, *Phys. Rev. A* **32**, 2751 (1985).

[87] Y. Ralchenko, A. E. Kramida, J. Reader, N. A. S. D. Team, *NIST Atomic Spectra Database*, version 4.1 (http://physics.nist.gov/asd) (2011).

[88] A. Mosk, *et al.*, *Opt. Lett.* **26**, 1837 (2001).

[89] S. K. Lee, H. S. Lee, J. M. Kim, D. Cho, *Journal of Physics B: Atomic, Molecular and Optical Physics* **38**, 1381 (2005).

[90] P. Barletta, J. Tennyson, P. F. Barker, *New Journal of Physics* **12**, 113002 (2010).

[91] P. D. Lett, *et al.*, *Phys. Rev. Lett.* **61**, 169 (1988).

[92] P. J. Ungar, D. S. Weiss, E. Riis, S. Chu, *J. Opt. Soc. Am. B* **6**, 2058 (1989).

[93] H. J. Metcalf, P. van der Straten, *Laser Cooling and Trapping* (Springer-Verlag, New York, 1999).

[94] T. Takekoshi, J. Yeh, R. Knize, *Optics Communications* **114**, 421 (1995).

[95] V. Sheveleko, *Atoms and their spectroscopic properties*, Springer series on atoms and plasmas (Springer, 1997).

[96] C. I. Sukenik, H. C. Busch, *Review of Scientific Instruments* **73**, 493 (2002).

[97] C. Y. Chen, *et al.*, *Review of Scientific Instruments* **72**, 271 (2001).

[98] L. Ricci, *et al.*, *Optics Communications* **117**, 541 (1995).

[99] K. L. Corwin, Z.-T. Lu, C. F. Hand, R. J. Epstein, C. E. Wieman, *Appl. Opt.* **37**, 3295 (1998).

[100] Y. Chung, R. Tkach, *Electronics Letters* **24**, 804 (1988).

[101] N. Vansteenkiste, *et al.*, *J. Phys. II France* **1**, 1407 (1991).

[102] H. Katori, F. Shimizu, *Japanese Journal of Applied Physics* **29**, L2124 (1990).

[103] B. Fazio, O. M. Maragó, M. Musso, *J. Opt. Soc. Am. B* **22**, 1325 (2005).

[104] G. Copley, D. Camm, *Journal of Quantitative Spectroscopy and Radiative Transfer* **14**, 899 (1974).

[105] G. Wasik, W. Gawlik, J. Zachorowski, W. Zawadzki, *Applied Physics B: Lasers and Optics* **75**, 613 (2002).

[106] T. Petelski, M. Fattori, G. Lamporesi, J. Stuhler, G. Tino, *The European Physical Journal D - Atomic, Molecular, Optical and Plasma Physics* **22**, 279 (2003).

[107] D. Allan, *Proceedings of the IEEE* **54**, 221 (1966).

[108] S. Kobayashi, T. Kimura, *Quantum Electronics, IEEE Journal of* **17**, 681 (1981).

[109] W. D. Phillips, H. Metcalf, *Phys. Rev. Lett.* **48**, 596 (1982).

[110] Y. B., Ovchinnikov, *Optics Communications* **276**, 261 (2007).

[111] T. P. Meyrath, *Ph.D. Thesis, University of Texas* (2005).

[112] L. P. Maguire, S. Szilagyi, R. E. Scholten, *Review of Scientific Instruments* **75**, 3077 (2004).

[113] R. E. Scholten, *Review of Scientific Instruments* **78**, 026101 (2007).

[114] D. Schneble, *Ph.D. Thesis, Universität Konstanz* (2002).

[115] H. C. Busch, *Ph.D. Thesis, Old Dominion University* (2004).

[116] A. Scholz, M. Christ, D. Doll, J. Ludwig, W. Ertmer, *Optics Communications* **111**, 155 (1994).

[117] J. P. Beardmore, A. J. Palmer, K. C. Kuiper, R. T. Sang, *Review of Scientific Instruments* **80**, 073105 (2009).

[118] K. Dieckmann, R. J. C. Spreeuw, M. Weidemüller, J. T. M. Walraven, *Phys. Rev. A* **58**, 3891 (1998).

[119] M. Qiu, *et al.*, *Science* **311**, 1440 (2006).

[120] D. Meschede, *Journal of Physics: Conference Series* **19**, 118 (2005).

[121] A. Assion, *et al.*, *Science* **282**, 919 (1998).

[122] B. J. Sussman, D. Townsend, M. Y. Ivanov, A. Stolow, *Science* **314**, 278 (2006).

[123] A. Rakonjac, *et al.*, *Opt. Lett.* **37**, 1085 (2012).

[124] U. Eichmann, T. Nubbemeyer, H. Rottke, W. Sandner, *Nature* **461**, 1261 (2009).

[125] N. P. Coppendale, *Ph.D. Thesis, University College London* (2011).

[126] G. Dong, W. Lu, P. F. Barker, *Phys. Rev. A* **69**, 013409 (2004).

[127] P. F. Barker, M. N. Shneider, *Phys. Rev. A* **64**, 033408 (2001).

[128] A. E. Siegman, *Lasers* (University Science Books, 1986).

[129] M. S. Fee, K. Danzmann, S. Chu, *Phys. Rev. A* **45**, 4911 (1992).

[130] C. P. C. Pan, *IEEE Transactions on Signal Processing* **49**, 444 (2001).

[131] S. Y. T. van de Meerakker, G. Meijer, *Faraday Discuss.* **142**, 113 (2009).

[132] A. Osterwalder, *Nat Photon* **6**, 346 (2012).

[133] P. F. Barker, M. Charlton, *New Journal of Physics* **14**, 045005 (2012).

[134] N. Zafar, G. Laricchia, M. Charlton, A. Garner, *Phys. Rev. Lett.* **76**, 1595 (1996).

[135] T. Takekoshi, R. J. Knize, *Opt. Lett.* **21**, 77 (1996).

[136] K. M. O'Hara, *et al.*, *Phys. Rev. Lett.* **82**, 4204 (1999).

[137] M. D. Barrett, J. A. Sauer, M. S. Chapman, *Phys. Rev. Lett.* **87**, 010404 (2001).

[138] S. R. Granade, M. E. Gehm, K. M. O'Hara, J. E. Thomas, *Phys. Rev. Lett.* **88**, 120405 (2002).

[139] P. F. Griffin, *Ph.D. Thesis, Durham University* (2005).

[140] K. J. Weatherill, *Ph.D. Thesis, Durham University* (2007).

[141] H. C. Busch, M. K. Shaffer, E. M. Ahmed, C. I. Sukenik, *Phys. Rev. A* **73**, 023406 (2006).

[142] S. Friebel, C. D'Andrea, J. Walz, M. Weitz, T. W. Hänsch, *Phys. Rev. A* **57**, R20 (1998).

[143] J. Wu, R. Newell, M. Hausmann, D. J. Vieira, X. Zhao, *Journal of Applied Physics* **100**, 054903 (2006).

[144] F. Pereira Dos Santos, *et al.*, *Phys. Rev. Lett.* **86**, 3459 (2001).

[145] A. Robert, *et al.*, *Science* **292**, 461 (2001).

[146] C. Orzel, M. Walhout, U. Sterr, P. S. Julienne, S. L. Rolston, *Phys. Rev. A* **59**, 1926 (1999).

[147] M. R. Doery, E. J. D. Vredenbregt, S. S. Op de Beek, H. C. W. Beijerinck, B. J. Verhaar, *Phys. Rev. A* **58**, 3673 (1998).

[148] A. S. Tychkov, *et al.*, *Phys. Rev. A* **73**, 031603 (2006).

[149] P. Spoden, *et al.*, *Phys. Rev. Lett.* **94**, 223201 (2005).

[150] H. Katori, F. Shimizu, *Phys. Rev. Lett.* **73**, 2555 (1994).

[151] R. G. Dall, K. G. H. Baldwin, L. J. Byron, A. G. Truscott, *Phys. Rev. Lett.* **100**, 023001 (2008).

[152] S. J. M. Kuppens, *et al.*, *Phys. Rev. A* **65**, 023410 (2002).

[153] W. J. van Drunen, *Ph.D. Thesis, Technische Universität Darmstadt* (2008).

[154] P. Douglas, C. Maher-McWilliams, P. F. Barker, *Review of Scientific Instruments* **83**, 063107 (2012).

[155] R. Scheunemann, F. S. Cataliotti, T. W. Hänsch, M. Weitz, *Journal of Optics B: Quantum and Semiclassical Optics* **2**, 645 (2000).